University of Southampton

Faculty of Environmental and Life Sciences

School of Ocean and Earth Sciences

Microbial influences on the resuspension and deposition processes of sediment transport

by

Naiyu Zhang

Thesis for the degree of Doctor of Philosophy

September, 2021

University of Southampton

Abstract

Faculty of Environmental and Life Sciences

School of Ocean and Earth Sciences

Doctor of Philosophy

Microbial influences on the resuspension and deposition processes of sediment transport

by

Naiyu Zhang

The extensive presence of microbial cells in aquatic sediments and the complex interactions/aggregations with sediment particles are found to have substantial effects on the dynamic processes of sediment transport. To date, extensive efforts have been paid to investigate such complex but typically common processes, but we are still far from a clear understanding. Specifically, the three-dimensional (3D) matrices of bio-sediment association, microbial mediation in the enhancement and reduction of sediment stability, and the effects of bio-sediment association on drag and settling velocities, remain to be clearly understood. This thesis seeks for a clearer and more comprehensive understanding of microbial sediment interactions and the influences on the resuspension and deposition processes of sediment transport. To achieve these goals, a new approach has been developed by using X-ray microtomography techniques, which for the first time allows the 3D matrices of biological sediment aggregates (BSA) to be imaged and quantified in their hydrated states. The results show that the microbial development state and the complex microbial sediment interaction/aggregation can significantly affect BSA architectures. As the BSA grow towards a better developed state, with higher organic fractions and larger aggregated sizes, the internal structure of BSA appears to become more compact and interconnected. The BSA at different stages of development in turn have a range of effects on sediment stability. The more fully developed BSA of a high organic fraction are found to biostabilize sediments, while the BSA at a less well developed state with lower organic fractions considerably destabilize sediments. By contrast, the microbial influences on the depositional processes present different patterns, where the volume of pore water plays a more important role in determining settling velocities, compared to the organic matter. These important results reveal the mechanisms and properties that influence microbial moderations of resuspension and deposition processes, providing much needed insight into microbial sediment transport. Predictive relationships for estimating the stability, drag and settling velocities of BSA are also tentatively proposed based on the test data available.

The insights gained suggest important possibilities for future work to achieve a more complete characterization of sediment transport in the presence of microbial mediation.

Table of Contents

List of Figures

List of Tables

List of Symbols

γ	Empirical coefficient in van Rijn's formula of $\tau_{m,crit}$ (dimensionless)
ε	BSA porosity (dimensionless)
η	Biotic drag ratio (dimensionless)
θ_{crit}	Critical Shields parameter (dimensionless)
$\theta_{crit,A}$	Dimensionless critical Shields parameter of BSA
υ	Kinematic viscosity of water (m^2/s)
ρ	Aggregate density (kg/m^3)
ρ_A	Density of BSA, including pore water (kg/m^3)
ρ_b	Density of organic matter (kg/m^3)
ρ_{ci}	Averaged density of each component of BSA (kg/m^3)
ρ_M	Density of BSA matter, excluding pore water (kg/m^3)
ρ_w	Density of water (kg/m^3)
ρ_s	Density of sediment particles (kg/m^3)
$\overline{\tau_b}$	Mean bed shear stress (Pa)
τ_{crit}	Critical shear stress for sediment suspension, or resuspension threshold (Pa)

$\tau_{crit\_abiotic}$	Resuspension threshold of abiotic control sand (Pa)
τ_{crit_BSA}	Resuspension threshold of BSA (Pa)
$\tau_{m,crit}$	Resuspension threshold of sand-mud mixed sediments (Pa)
φ_b	Organic fraction of matter per aggregate (dimensionless)
φ_s	Sediment fraction of matter per aggregate (dimensionless)
A	Projected area (m^2)
C_D	Drag coefficient (dimensionless)
C_{Db}	Biotic drag (dimensionless)
C_{Ds}	Abiotic drag (dimensionless)
c_{gel}	Gelling mass concentration of the fine particles (kg/m^3)
$c_{gel,s}$	Dry bulk density of sand bed by mass (kg/m^3)
D_*	Dimensionless particle diameter
D_{*A}	Dimensionless aggregate diameter
D_p	2D perimeter-based fractal dimension (dimensionless)
D_v	3D volume fractal dimension (dimensionless)
d_{50}	Median grain diameter (m)
d_A	Spherical volume equivalent diameter of V_A (m)

d_x	Maximum aggregate length projected at x-axis direction (m)
d_y	Maximum aggregate length projected at y-axis direction (m)
d_z	Maximum aggregate length projected at z-axis direction (m)
d_f	Diameter of fractal aggregates
d_M	Spherical volume equivalent diameter of V_M (m)
d_p	Primary particle diameter
d_s	Spherical equivalent diameter of V_{s_sum} (m)
d_{sand}	Median particle size of sand grains (m)
E	Turbulent kinetic energy density (Pa)
F_b	Buoyant forces (*N*)
F_d	Drag forces (*N*)
F_g	Gravitational forces (*N*)
g	Gravity acceleration (m/s^2)
L	Equivalent diameter of particle (aggregate) (m)
M_A	Aggregate mass (kg)
M_M	Mass of matter (sediment particles + organic matter) held per aggregate (kg)
M_w	Mass of pore water held per aggregate (kg)

N_f	The number of primary particles per aggregate
Re	Reynolds number (dimensionless)
Re_A	Reynolds number of aggregate (dimensionless)
V	Volume (m^3)
V_A	Sum volume of all the sediment particles, organic matter and pore water enveloped per BSA (m^3)
V_B	Total volume of organic matter per aggregate
V_M	Sum volume of all the sediment particles and organic matter aggregated per BSA (m^3)
V_S	Sum volume of all sediment particles aggregated per BSA (m^3)
V_w	Total volume of water per aggregate
v_{ci}	Total volume of each component per BSA (kg/m^3)
w_s	Terminal settling velocity (m/s)
w_{s-A}	Settling velocity estimated by considering all the three fractions of components: sediment particles, organic matter, as well as pore water (for creeping flow regime, Re<1) (m/s)
w_{s-AD}	Settling velocity estimated by considering all the three fractions, but for fast-settling particles of higher Reynolds number, Re>1 (m/s)
w_{s-M}	Settling velocity estimated by considering the contents of both sediment particles and organic matter (for creeping flow

	regime, Re<1) (m/s)
w_{s-S}	Settling velocity estimated by simply considering the content of sediment particles (for creeping flow regime, Re<1) (m/s)

List of Abbreviations

2D	Two-dimensional
3D	Three-dimensional
ADV	Acoustic Doppler Velocimeter
APS	Acidic polymeric substances
BSA	Biological sediment aggregates
CCA	Cluster-cluster aggregation
CCD	Charged-coupled device
CLSM	Confocal laser scanning microscopy
CMF	Core mini flume
DLVO	Derjaguin−Landau−Verwey−Overbeek theory
EPS	Extracellular polymeric substances
ESEM	Environmental Scanning Electron Microscopy
FIB-nt	Focused Ion Beam Nano tomography
LN2	Liquid nitrogen
LTSEM	Low-temperature Scanning Electron Microscopy
Micro-CT	X-ray micro-computed tomography
MPB	Microphytobenthos
NMR	Nuclear Magnetic Resonance
OBS	Optical backscatter sensor
PSD	Particle size distribution

ROI	Region of Interest
SEM	Scanning Electron Microscopy
SNR	Signal to noise ratio
SPM	Suspended particulate matter
TEM	Transmission electron microscopy
TEP	Transparent exopolymer particles
TKE	Turbulent kinetic energy method

Declaration of Authorship

Print name: Naiyu Zhang

Title of thesis: Microbial influences on the resuspension and deposition processes of sediment transport

I declare that this thesis and the work presented in it is my own and has been generated by me as the result of my own original research.

I confirm that:

1. This work was done wholly or mainly while in candidature for a research degree at this university;

2. Where any part of this thesis has previously been submitted for a degree or any other qualification at this university or any other institution, this has been clearly stated;

3. Where I have consulted the published work of others, this is always clearly attributed;

4. Where I have quoted from the work of others, the source is always given. With the exception of such quotations, this thesis is entirely my own work;

5. I have acknowledged all main sources of help;

6. Where the thesis is based on work done by myself jointly with others, I have made clear exactly what was done by others and what I have contributed myself;

7. Section 2.1 in Chapter has been published as:

Journal article:

Naiyu Zhang, Charlotte E. L. Thompson, Ian H. Townend, Kathryn E. Rankin, David M. Paterson, and Andrew J. Manning, Nondestructive 3D Imaging and Quantification of Hydrated Biofilm-Sediment Aggregates Using X-ray Microcomputed Tomography, Environmental Science & Technology 2018 52 (22), 13306-13313.

Conference presentation:

Naiyu Zhang, Charlotte E. L. Thompson, Ian H. Townend, Kathryn E. Rankin, David M. Paterson, and Andrew J. Manning, Investigating the internal structure of biofilm-sediment aggregates using X-ray micro-tomography. In 2018 AGU Fall Meeting. Washington, DC: 12/10/18-12/14/18

Naiyu Zhang, Charlotte E. L. Thompson, Ian H. Townend, A novel approach to quantifying resuspension resistance of sediment organic matter against coastal flow, EGU General Assembly 2020, Online, 4–8 May 2020, EGU2020-15864.

Acknowledgement

I would like to thank all the people that have shared their experiences, knowledge and contributed their expertise to this PhD research. I would like to give my particular and grateful thanks to my principle supervisor, Dr. Charlie Thompson. Since the first day we started to work together, she has been supportive with me and my research. I truly appreciate all the time, effort and support she has given to guide, inspire and encourage me to pursue PhD and to go through those difficult times. I would not go this far without her guidance and supports. I would also like to thank my second supervisor, Prof. Ian Townend, who went above and beyond in supervising me. No word could ever express how much I am grateful for his guidance and encouragement. Particular thanks also go to Charlie and Ian for their supportive guidance, especially in this strange 2020. They have given me so much time and effort to guide me follow the right track and learn how to think coherently and scientifically. Their directions and supports make me feel confident for future explorations of my interested research topics and building up my own career.

My particular thanks go to Dr. Hachem Kassem, who has been continuously providing help and guidance for laboratory flume maintenance. His expertise and supports make me to run flume resuspension tests smoothly and enjoyed the fun of resuspension experiments. I would also like to thank Prof. David Paterson, who supportively provided feedbacks on my research. Particular thanks to Prof. David Paterson and Dr. Andrew Blight for their hosts of the field BSA sampling from the Tay Estuary. I am also grateful to Dr. Andrew Manning for his generosity of sharing the camera-video system, letting me to test the settling velocities of clay BSA. I would like to thank also the μ-VIS team and special thanks to Dr. Kathryn Rankin, Dr. Orestis Katsamenis, Dr. Nicholas Hale, and Dr. Richard Boardman for their assistance in performing the scans carried out at the μ-VIS X-ray Imaging Centre, University of Southampton. I also gratefully thank Mr. John Ford for his technical support for embedding specimens in

resin, Mr. Daniel Doran and Mr. Mathew Beverley-Smith for their technical support for resin preparation, Dr. John R. Gittins for this technical support for Alcian blue staining solution preparation, and Ben Callow for his helpful advice in image processing. I am also grateful to the team of BLUE-Coast, Prof. Martin Solan and Dr. Rachel Hale. Working with them makes me to enjoy the fun of field sampling campaign and gain valuable experiences.

My special thanks to Dr. Jingjing Zhou, for her unshakable supports, for her enthusiastic encouragement and guidance, and for those forever beautiful memories in Nanjing and Southampton.

Finally, for the unconditional love and supports I want to thank my parents and especially my boyfriend, Danxu. I appreciate his love, understanding, respect and belief during such a long-distance relationship for four years. No matter how difficult the moment was/is/will be, he has always been with me and his love has made me to do everything possible.

Chapter 1 Introduction

1.1 Extensive presence of microbial cells in aquatic sediments

In natural aquatic environments, the majority of sediment particles are to some extent mediated by the attachment, adherence and accumulation of microbial cells and microbiologically-produced organic matter, both during the transport processes in the water column and during periods when resting on the bed. Microorganisms are present in a variety of marine environments, from shallow-water to deep-sea, and from surface water to benthic sediments (Flemming, 2019). The surface ocean, which covers 70% of the planet's surface, has a high microbial cell concentration, being 3-5 orders of magnitude higher than that of bulk ocean water (Wurl et al., 2017). Surface oceanic sediments have a denser cell abundance, which is up to 10^4 orders higher than that of cells in the open ocean water (Probandt et al., 2018). Microorganisms, either in the water column or in seabed sediments, do not live as dispersed, single cells, but instead accumulate at the interfaces and form microbial aggregates, such as flocs, sludge, films and mats (Flemming, 2019; Flemming and Wingender, 2010). The interfaces, where cells attach and accumulate, can be biotic surfaces such as plankton, plants, animals and other microorganisms, and abiotic surfaces of any solid-liquid, liquid-liquid, liquid-gas and solid-gas, such as microplastic particle and fibres, sediment particles (e.g. clay minerals, silts and sand grains) (Flemming, 2019; Flemming and Wingender, 2010).

The settling of non-motile cells needs low and moderate flow velocity to transport the cells to adhere to the surfaces of substratum, whereas motile cells can transport towards and land on the substratum surfaces by actuating their flagella regardless of fluid velocity (Tuson and Weibel, 2013). Upon successful cell landing, initial attachment between the deposited cells and the substratum surfaces occurs rapidly within minutes (Nichols and Nichols, 2008; Tuson and Weibel, 2013). Cells can be regarded as inert colloidal particles and the process can be modelled by surface thermodynamics and

Derjaguin−Landau−Verwey−Overbeek theory (DLVO) (Carniello et al., 2018). Once the microbes are at a closer distance than 1.5 nm, the cells are attached irreversibly and ~~secret~~ excrete extracellular polymeric substances (EPS) to attach to surfaces (Nichols and Nichols, 2008). EPS are mainly polysaccharides, proteins, nucleic acids and lipids (Flemming, 2011). They provide the mechanical stability of biofilms, mediate adhesion to surfaces and form a cohesive three-dimensional (3D) organic polymer network that interconnects the cells and substratum surfaces, forming a biofilm matrix to stabilize microbial cells (Flemming, 2019). Marine sediment particles provide preferential solid-liquid interfaces for microbial cells, including microalgae, diatoms, bacteria, and fungi, to accumulate. By secreting copious amounts of EPS, binding sometimes more than 90% water (Flemming and Wingender, 2010; Schmitt and Flemming, 1999), and adhering sediment particles and the other microbial cells/aggregates, these microorganisms form hydrogel-like aggregates, referred to as Biological Sediment Aggregates (BSA) (Zhang et al., 2018).

1.2 Complex geometries of BSA

BSA are highly hydrated and heterogeneous (Ransom et al., 1998). BSA comprise patches of microbial cell clusters within a matrix of EPS and separated by internal pores and channels (Sutherland, 2001). The presence of sticky EPS results in various structural appearances, including colloidal, capsular, film, or fibrous structures, to occur (Flemming, 2011; Flemming and Wingender, 2010). When EPS are produced after cell colonization, cone/mushroom-shaped structures may be present. Water may channel through the film structures forming the stalks of EPS, leaving the water channels to penetrate within the micro-colonies (Wimpenny and Colasanti, 1997). Such connected water channels and mushroom-like EPS structures may not always form, but instead present as separated micro-colonies attached to each other, and have unconnected pores developed within such micro-colonies (Keevil and Walker, 1992).

The highly heterogeneous internal mass distribution of BSA may challenge the use of

fractal theory to represent the 'true' binding nature of BSA matrices (Wheatland et al., 2017). Scanning Electron Microscopy (SEM) has been used to image EPS strands and plates, however the standard SEM requires dehydrating the hydrated samples, unavoidably resulting in considerable distortion of hydrated biofilm matrix (Paterson, 1995). The preparatory losses of EPS during conventional resin-embedding methods are also found to be considerable, sometimes accounting for 50%-80% (Leppard et al., 1996). Low-temperature SEM (LTSEM) or cryo-SEM requires freezing hydrated biofilm, which has been found to cause considerable artefacts, making it difficult to interpret the internal structures of BSA (Perkins et al., 2006). Transmission electron microscopy (TEM) is another technique for a high-resolution imaging of EPS fibril bundles in BSA, but only for 2D observation (Liss et al., 1996). Focused Ion Beam Nano tomography (FIB-nt) has recently been used for 3D characterization of the structure of suspended flocculated matter (Wheatland, et al., 2017), which has made advanced progress in charactering microbial cells attaching to the aggregates in a 3D matrix and at a high resolution, but as with TEM, requires the aggregates to be fully dehydrated and stabilized in resin blocks. Either SEM or TEM/FIB-nt involves various degrees of desiccation of BSA, and suggests a need for the direct 3D imaging of hydrated BSAs in liquid media. The organic matter in natural BSA are predominantly comprised of water (Schmitt and Flemming, 1999), the majority of the water (up to 98%) (Schmitt and Flemming, 1999) bound by EPS within the microbial matrix can be easily removed (Schmitt and Flemming, 1999). Prior work also shows that biofilms tend to create an environment to retain moisture, when exposed to dry environments (Flemming and Wingender, 2010). The loss of water at the biofilm surface brings polymer sites closer together (Gerbersdorf and Wieprecht, 2015), forming a skin-like protector against further evaporation of the water underneath (Flemming and Wingender, 2010; Gerbersdorf and Wieprecht, 2015). The binding architecture is altered, and the internal pores and channels are distorted. The observed structures of BSA that have undergone desiccation is thus unlikely to be representative of the

structures of the aggregates when they are transported in hydrated form (Paterson, 1995). Given that fluid flow through these pores and channels is a key mechanism for uptake, storage and mineralization of carbon and nutrients from surrounding environments (Romaní et al., 2004), a realistic observation of the internal structures of BSA is crucial for investigating nutrient exchange (Molins, 2015), and understanding the entrapping and accumulation of microbes in such porous media (Gerbersdorf and Wieprecht, 2015). Conducting non-destructive, 3D imaging and quantification of hydrated BSA sustained in liquid medium is therefore important (Keyes et al., 2013). Environmental SEM (ESEM) and confocal laser scanning microscopy (CLSM) in combination with fluorescent staining are two currently available tools for observing a hydrated biofilm matrix (Chu and Lee, 2004). However, ESEM is limited to the surface structure characterization, instead of the 3D internal structure (pores and throats), while CLSM finds it difficult to distinguish the morphologies of sediment particles and pore water in aggregates as neither can be targeted by appropriate staining (Zhao, et al., 2011). These standard specimen preparation techniques have limited aggregate imaging success to date, and it seems direct imaging of hydrated aggregates in liquid media would be a preferable approach, which is however lacking and needing new methods to be developed.

1.3 Microbial influences on the resuspension processes of sediment transport

1.3.1 Microbial mediation of sediment stability: biostabilization

The presence of microbiology and the development of BSA across sediment-water interfaces mediate the resuspension behaviours of sediments to some extent. Positive relationships between sediment stability parameters (e.g. resuspension thresholds, erosion rates) and microbial parameters (e.g. biomass and carbohydrates) are found in previous studies (Friend, et al., 2003; Gerbersdorf et al., 2005; Hope et al., 2020; Sutherland, et al., 1998; Yallop et al., 2000). Amos et al. (2004) found the resuspension

thresholds of in situ sediments were increased by 153-244% by the presence of microbial mediation, and the degree of the mediation was mainly determined by microbial species. Microbial development can mediate sediment stability through binding particles together to enhance adhesion strength among particles, and/or moderating bed roughness and benthic hydrodynamics (Friend et al., 2008). In previous studies, the microbial mediations that generally enhance sediment stability are referred to as 'biostabilization' (de Boer, 1981), which defines 'a decrease in sediment erodibility caused directly or indirectly by biological action' (Paterson and Daborn, 1991).

Two dominant populations of microorganisms that live in benthic sediments, excrete EPS, and influence the resuspension behaviours of sediment transport are heterotrophic bacteria and autotrophic microphytobenthos (MPB) (Lubarsky et al., 2010; Lundkvist et al., 2007). MPB define a generic group of phototrophic algae (e.g. diatoms, dinoflagellates), cyanobacteria and other photosynthetic bacteria that colonize sedimentary substrates (Jesus et al., 2009). These microorganisms frequently colonize sediments and form dense photosynthetic biofilms in coastal environments, and have a variety of ecological and environmental functions and attributes, including mediating nutrient cycling between benthic sediments and the water column (Cabrita and Brotas, 2000), accumulating pollutants (Reid et al., 2016), and affecting the stability of sediments against hydrodynamic forcing (Paterson, 1989).

1.3.1.1 Microphytobenthos (MPB)

MPB are often grouped according to the type of substratum available for microorganisms to colonize. Grain size of sediment particles is found to be a controlling variable for MPB diversity (Jesus et al., 2009; Underwood and Barnett, 2006). Underwood and Barnett (2006) found muddy sediments (<63 μm) appeared to be dominated by diatom biofilms while sandy sediments presented more microbial diversity, including both diatoms and cyanobacteria. This is supported by the work of

Jesus et al. (2009) across Tagus intertidal sediments. where sandy sites presented higher species diversity. De Winder et al. (1999) also provided supportive evidence that diatom biofilms developed on fine-grained sediments, while cyanobacteria preferred to grow on coarser sediment.

The stabilities of MPB-dominated sediments are often found to positively correlate with light and present short-term day-night variations (De Brouwer and Stal, 2001; Lundkvist et al., 2007; Smith and Underwood, 2000). EPS production is dynamic during the day-night cycles. Colloidal EPS were found to secrete during both day and night, while bound EPS production was promoted in the light and reduced at night (Smith and Underwood, 2000; Staats et al., 2000). Field studies also found a clear kinematics of MPB biomass during day-night cycles, where biomass increased in the light during daytime and decreased in the dark at night (Blanchard et al., 2001). Friend et al. (2005) found strong day-night variations, where the bed stabilities were enhanced during the day and reduced by 32% at night. This result was in contrary to Friend et al. (2003), where stabilities of sandy sediments were higher at night and lower during the day. Such contrasting trends between sandy and muddy sediments however cannot be explained by biological parameters of chlorophyll *a* and carbohydrates, as the contents of chlorophyll *a* and carbohydrates were higher during the day than at night, for both sandy and muddy sediments. In addition, no significant correlations were present between sediment stability and biological parameters of chlorophyll *a* and carbohydrates (Friend et al., 2005). This means, beyond diatom migration and EPS production, some other processes might be affecting the microbial mediations during day-night cycles, and need to be considered for bed stability predictions (Friend et al., 2005).

1.3.1.2 Heterotrophic bacteria

Heterotrophic bacteria ubiquitously dominate aquatic sediments, e.g. up to 10^9-10^{12} cells per gram of dry mud (Black et al., 2002). Whilst heterotrophic bacteria are

consumers of organic matter, an increasing body of studies have found that bacteria also produce copious amount of EPS and mediate the resuspension properties of sediment transport (Dade et al., 1996; Gerbersdorf et al., 2009; Lubarsky et al., 2010). For example, the incubation of bacteria within sediments has been found to increase sediment stability between 2 (Gerbersdorf et al., 2008) and 4 times (Dade et al., 1990), and is supported by in situ increases in stability of ~60% (Dade et al., 1996). Similar results were also found by using artificial polymers (xanthan gum) in both sandy and muddy sediments (Tolhurst, et al., 2002).

Some recent studies were conducted to investigate the individual and relative biostabilization capacity of heterotrophic bacteria and autotrophic diatoms. For example, Gerbersdorf et al. (2009) inoculated natural bacteria and diatom cultures from the Eden estuary (Scotland, UK) into sediment composed of fine-grained glass beads, and found that the bacteria-dominated cultures had a stronger biostabilization effect than that of the diatom-dominated cultures. Lubarsky et al. (2010) found similar results, where bacteria created significantly greater bed stability than axenic diatoms (up to a factor of 2). There are also some other observations, in which bacteria made less or negligible contributions to bed stability as compared with microalgae assemblages in the field (Lundkvist et al., 2007). As discussed by Lubarsky et al (2010) and Gerbersdorf et al. (2009), such contrasting results might be due to the different ways of preparing bacterial cultures. In particular, Lubarsky et al (2010) and Gerbersdorf et al. (2009) segregated bacterial assemblages from natural cultures, while Lundkvist et al., (2007) let natural mixed cultures grow under dark to obtain bacterial assemblages.

In addition to the individual stabilizing capacities of bacteria and microalgae, the combined effects of the mixed cultures of bacteria and microalgae were also studied. Gerbersdorf et al. (2009) and Lundkvist et al. (2007) found synergistic effects of the mixed cultures, in which the biostabilizing effects from the mixtures of bacterial and microalgae were even higher than the summation of the two effects. One hypothesized reason is the influence of bacteria and microalgae association. For example, some

microalgae need interations with bacteria to thrive. The nutrient cycling of bacteria can accelerate the growth of microalgae and the production of EPS. Supporting evidence was found in Lubarsky et al. (2010), where microalgae biomass were higher in the mixed cultures, compared with that produced in axenic microalage cultures (Lubarsky et al., 2010). It is often suggested that microalgae excrete a larger proportion of polysacharides, while bacteria produce mainly proteins in their EPS matrices (Flemming and Wingender, 2002). As such, the stronger capacity of stabilizing sediments might be assocaited with the production of protein. The studies of Lubarsky et al. (2010) presented some constrasting results. Similar quatitaties of protein EPS were produced, but distinct effects on the bed stability remained between the bacteria treatment and mixed treatment (bacteria+microalgae). A possible explanation proposed by the authors in that work was the EPS produced between bacteria and microalgae had different machanical characteristics. Whilst the exact differences of the mechanical EPS characteristics remain to be determined, the summary of the above work strongly suggest the quantities of EPS concentrations and/or compositions might not be wholly attributed to microbial mediation of bed stability.

1.3.3 Temporal and spatial variations of microbial sediment stability

1.3.3.1 Temporal variation

The microbial mediation of sediment stability is sensitive to a range of environmental factors, such as temperature, nutrient conditions, physical disturbances (e.g. hydrodynamic forces, rainfall and storm events), the distribution of microbe species and the activities of their predators, leading to high temporal and spatial heterogeneity (Amos et al., 2004; Friend et al., 2003b; Kornman and De Deckere, 1998). Amos et al. (2004) deployed two benthic annular flumes (Sea Carousel and Mini flume) to 24 sites in Venice Lagoon and found bed stabilities were increased up to a factor of 5 in summer, when compared with that in winter. The seasonal patterns of bed stability might be attributed to the variations in microbial activities due to water temperature changes

from 5 to 30ºC (Amos et al., 2004). Underwood and Paterson's (1993) studies in the Severn estuary, UK, showed that sediment concentrations of chlorophyll *a* positively correlated with temperature, while Cammen (1991) observed by contrast a general decrease in chlorophyll *a* during summer months, possibility due to increased consumption by grazers. Laboratory competition experiments between cyanobacteria and benthic diatoms found that the benthic diatom, *Nitzschia sp.* dominated across both sandy and muddy sediments at 10ºC and 15ºC, while cyanobacteria, *Microcoleus chthonoplastes*, prevailed as temperature increased to 25ºC. Friend, et al. (2003b) also found strong seasonal patterns of microbial influences on bed stabilities in a mixed intertidal habitat in Portugal. In the late summer/early autumn, the biostabilization was mainly attributed to cyanobacteria, and colloidal carbohydrate was the best predictor for the resuspension thresholds. The activities of cyanobacteria then largely declined in late winter/early spring, and the best predictor became bed elevation. Chen et al. (2020) observed seasonal patterns in both vegetated saltmarshes and adjacent un-vegetated habitats, where the resuspension thresholds of saltmarsh sediment stability and the adjacent un-vegetated areas increased by 50% and 126% respectively in summer, as compared with that in winter. The promoted biostabilization effect in summer was found to relate to the dense populations of diatoms (Chen et al., 2020). Similar bed stability changes linked to the variations of diatoms were also observed by Kornman and Deckere (1998), where temporal variations of diatoms caused by local grazing activities led the resuspension thresholds in the Dollard Estuary, Netherlands, to vary monthly between 0.1 Pa to 0.5 Pa. Andersen (2001) conducted monthly field surveys in two microtidal mudflats in the Danish Wadden Sea, in which strong seasonal variations in the bed stabilities were also found, together with significant correlations with MPB biomass. By contrast, Andersen et al. (2005) found no such seasonal variations in tidal channel sediments due to the limited availability of light. Gerbersdorf et al. (2005) found strong seasonal variabilities of biological parameters and varying relationships with erosion thresholds across the surface layers of sediments (0.5 cm),

where the resuspension thresholds strongly correlated with colloidal carbohydrates during spring time. Whilst similar quantities of colloidal carbohydrates were produced in winter, the stabilities of sediments from much deeper depths (5-35 cm) presented more general variability with no such seasonal patterns (Gerbersdorf et al., 2005). This might be attributed to biological activities e.g. algal biomass, which prevailed in surficial sediments, but decreased with depth. Seasonal variations in biological activities lead to seasonal changes in biomass, EPS production and correlations with sediment stability to occur. As depth increases, consolidation effects and sediment properties became important in determining sediment stabilities (Gerbersdorf et al., 2005).

Tolhurst et al. (2006) found temporary variations in the microbial influences on sediment stabilities at much shorter time scales during tidal emersion, where weak correlations between sediment stability and colloidal carbohydrates was observed. During the emersion period, the resuspension threshold showed a rapid increase in the beginning of the emersion, while the changes in carbohydrates appeared to be much more gradual. Previous studies discussed that the colloidal carbohydrate was water-soluble and thus might quickly disappear as tides came in, thus contributing to limit the extent of sediment stability (De Winder et al., 1999). It was believed that bound carbohydrates would play a more prominent role in stabilizing sediments, especially during the emersion period (De Winder et al., 1999). However, Tolhurst et al. (2006) found no significant correlations between sediment stabilities and bound carbohydrates, which means the concentrations of either colloidal or bound EPS cannot fully explain the short-term variations of microbial sediment stabilities. Some other mechanisms in addition to the EPS concentrations might be influencing sediment stabilities, such as the structural properties of three-dimensional EPS matrices (De Brouwer et al., 2005; Tolhurst et al., 2006).

Temporal variations of microbial mediations at time scales of 3-5 days were recently found to be present at both sandy and muddy sediments in the Dee estuary, UK, (Hope

et al., 2020). These authors found the variations of sediment stability significantly correlated with the changes of biomass and MPB species, indicating strong contributions of microbial development and activities to the temporal variations. However, one sandy site in a very energetic system subject to frequent hydrodynamic reworking showed negative correlations between sediment stabilities and the biological parameters of chlorophyll *a* and organic contents. Frequent reworking of benthic microbial substances and sediment particles might prevent the establishment of film-like matrices which armour seabed sediments. Instead, a fluffy layer of fragmented biofilm and microbial cells were created at the bed interfaces, mediating sediment stabilities in different ways. For example, the reworking effects of the local energetic hydrodynamics might frequently disturb the biophysical bonds between particles and weaken the resistance strength against hydrodynamic forcing. The negative relationships between biomass and sediment stability challenge the generally held belief that the bed stabilities are always positively correlated with biological parameters and the mechanisms leading to such negative correlations remain to be tested.

1.3.3.2 Spatial variation

Microbial growth, and bio-sediment combinations also present strong spatial heterogeneities. Depending on the history of bed deposition, the processes of consolidation, the development of microbiology, and bio-sediment combinations often present depth variations. For example, Gerbersdorf et al. (2005) found only the surface sediments presented significant seasonal variations with biological parameters. By contrast, the stabilities of sediments at depths (e.g. 5-35 cm) correlated with layer depths, as dominated by consolidation effects (Gerbersdorf et al., 2005). Sutherland et al. (1998) measured the vertical profiles of bulk densities from the sediments at eight stations along a transect in a microtidal estuary. According to the vertical gradients in bulk densities, three sedimentary layers were defined: a biogenic layer (bulk densities $\sim<1000$ kg/m^3), a consolidating layer (bulk densities = 1000-1100 kg/m^3) and an underlying uniform layer. The biogenic layer was associated with high concentrations

of chlorophyll *a* at the sediment surfaces, and the layer became thinner seaward. The consolidating layer showed clearly increasing densities with depth and reached to 11-15 mm below the surface (Sutherland et al., 1998). The results agree with those of Gerbersdorf et al.(2005), who also found that the microbial mediations tend to be stronger in the surficial sediments. As reported by Sutherland et al. (1998), Paterson (1989) and Black et al. (2002)., such a MPB-mediated surfical layer is often limited to very shallow depths, of a few mm.

The deployment of an in situ benthic flume at eight stations at upper south cove, Nova Scotia found both erosion rate and erosion threshold presented significant correlations with biological parameters of chlorophyll *a* and colloidal carbohydrates, indicating the strong effects of microbial development and the interactions with sediment particles for both the surficial and sublayer sediments (Sutherland, et al., 1998). Bio-sediment combinations beneath the bed surface were recently better detected both in the field and laboratory. In the field sediments from the Dee Estuary, UK, peak EPS contents were detected at a depth of 4 mm beneath the bed interface (Malarkey et al., 2015). Chen et al. (2017b) found, as the growth period of bacteria increases, e.g. to a period of one month, biofilm penetrated to depths of 1.8 cm. SEM images showed differently structured matrices of BSA at depths. At surficial layers, sediment particles are well-embedded into film-like matrices with little exposure to surrounding waters, but became increasingly exposed and only attached by small organic patches as the microbial development penetrates downward (Chen, et al., 2017b). The depth distribution of BSA was found to evolve with time, suggesting the important role of the development period in the penetration of EPS in sediment matrices. A pattern of 'hindered' erosion was proposed to characterise the microbial mediations of sublayer sediments, in which, after the removal of surficial biofilm-protection, the penetrated EPS in the sublayers, through binding particles together, continue to protect particles from erosion (Chen, et al., 2017a).

Sutherland et al. (1998) found the net erosion rates of microbiologically-mediated

sediments incorporating sublayer sediments showed stronger variations than the erosion threholds of the surface biogenetic layer, for the same sites. This means that, compared to the surficial sediments, that are dominantly mediated by microbial activities, other processes might be involved in affecting the resuspension of sublayer sediments. During the erosion processes, the initial erosion stage might be dominantly controlled by the surface bio-sediment combinations. As erosion continued to incorporate the sublayer sediments well beneath the topmost 2mm depths, the erosion behaviours start to be determined by the microfabric of the sublayer sediments (Sutherland, et al., 1998). The microfabric properties of the sublayer sediments might depend on the microbial sediment association to some extent (Chen, et al., 2017b), but also the history of bed deposition and the processes of consolidation (Sutherland, et al., 1998).

Due to environmental gradients of sediment particle size, temperature, salinity and hydrodynamics across coastal habitats, MPB biomass and bio-sediment combinations can occur in patchy distributions over varying scales from centimetres to kilometres (Daggers et al., 2020; Jesus et al., 2009). Remote sensing has captured the spatial patchiness of MPB biomass (chlorophyll a), at the microscale (centimetres to meters in size), mesoscale (meters to kilometres in size), and macroscale (kilometres up to scale of an entire estuary) (Daggers et al., 2020; Ibrahim et al., 2014). Daggers et al. (2020) used remote sensing (Sentinel-2 imagery) and found the location of MPB patchiness related with the seasonal heterogeneities of silty particles on tidal flats. The physical properties of the sediments, such as grain size, play a determined role in the dynamics of MPB biomass across tidal flats (Daggers et al., 2020). This observation agrees with previous studies that the meso- and macro-scale MPB patchiness is associated with sediment characteristics (e.g. particle size), and local hydrodynamic conditions (e.g. wind velocities, emersion period) (Orvain et al., 2012; van der Wal et al., 2010). Guarini at al. (1998) found clear seasonal variations in MPB patch size, increasing from winter to summer, while Daggers at al. (2020) found no seasonal variabilities in terms of MPB

patch size, likely due to the differences in local environmental conditions, including irradiance, temperature, nutrient concentration and hydrodynamics (Daggers et al., 2020). Besides the influences of abiotic conditions, other studies of microscale MPB patches demonstrated the controlling role of benthic infauna activities (Rietkerk et al., 2004). Weerman et al. (2011) investigated the structural patterns of MPB distributions at an intertidal mudflat in the Netherlands, where the spatial patterns developed during spring but collapsed in summer. This was caused by an increase of benthic herbivores in summer, inhibiting diatom growth (Weerman et al., 2011). This finding was supported by Orvain et al. (2014), in which the activities of mud snails caused a similar collapse of chlorophyll *a* in summer at Marennes-Oléron Bay, France. Associated with the changes of MPB biomass, film-like matrices were destroyed, and armouring effects by biofilm on bed stability was not shown. Instead, a fluff layer was established and erosion was enhanced. Orvain et al. (2014) also found, in contrast to the majority of studies, high EPS protein correlated with high erodibility, which questions the usage of EPS protein as a bed stability indicator, and suggests a need to account for such infauna disturbances in assessing microbial mediations of sediment stabilities.

As such, the temporal and spatial variations in microbial sediment association are largely mediated by local sedimentary properties, biological activities and environmental conditions, complexing the predictions of microbial sediment stabilities. Whether there would be a unified model establishes relationships between microbial development and sediment stability is challenging but needed. It is generally hypothesized that the mechanisms for biostabilization are through the addition of adhesion to increase the stabilizing forces of microbial sediments against flow erosion (Fang et al., 2017), binding sediment particles into cohesive network which acts as an armour to protect sediments (Vignaga et al., 2013), and/or smoothing the sediment surfaces to reduce drag acting on sediments (De Deckere, et al., 2001; Black et al., 2002) The difficulties of visualisation of the matrices established by bio-sediment association mean these hypotheses are yet to be verified, and the current quantitative

characterization of microbial influences on sediment stability is generally empirical (De Brouwer et al., 2005). The majority of current quantitative relationships are established with a variety of biochemical compositions (Underwood and Paterson, 1993; Yallop et al., 2000). For example, Underwood and Paterson (1993) found sediment stability significantly correlated with water content, chlorophyll a and colloidal carbohydrate, with the latter being the best biochemical predictor for sediment stability (Underwood and Paterson, 1993). Gerbersdorf et al.'s (2008) experiments found close correlations with cell numbers and colloidal EPS protein concentrations, but not with carbohydrate. Yallop, et al. (2000) showed a range of variables, including chlorophyll a, carbohydrate, water content and bacterial cells, can affect sediment stability. Empirical correlations were established for predicting microbial sediment stabilities as a function of the above variables. From the above examples, we can see the correlations between sediment stability and biochemical indicators are variable and may be to some extent controversial. Recent experimental and analytical works provide a different way to quantify the microbial influences on sediment transport (Fang et al., 2014, 2020; Fang et al., 2017). In their work, film water theory was applied to characterize the cohesion among sediment particles, and an empirical adhesion force equation was established to describe the mediations of microbial development. Through force analysis, a revised Shields diagram was proposed which allows the sediment stability mediated by microbial development to be estimate (Fang et al., 2014). Fang et al.(2014, 2017) make great progress in quantifying the microbial influences on sediment transport. However, Fang et al. (2014, 2017) models are derived for the case of microbial mat (biostabilization). The microbial mats were laboratory cultivated under calm water conditions, which may differ from the microbial matrices developed under cyclic resuspensions (Chen et al., 2019). This then suggests a need for future work to quantitatively characterize the stabilities of microbial sediments developed under cyclic flow resuspension and deposition.

1.3.4 Biostabilization or biodestabilization?

At a relatively mature development stage, which can take from a few days to 4-5 weeks, a microbial mat matrix that can be up to a few centimetres thick is usually established (Gerbersdorf and Wieprecht, 2015). This mat matrix is adhesively sticky, embedding a large number of particles, covering the underlying sediment particles and protecting the particles from mobilization by reducing the exposure of the adhered particles to flow-induced bed shear stresses. The establishment of the organic mat acts as an armour to enhance the erosion resistance of the underlying sediments (Paterson et al., 2008; Vignaga et al., 2013). To date, extensive field and laboratory experiments and observations have been conducted to study the influences of the microbial mat matrices on sediment stability (Amos et al., 2004; Black et al., 2002; De Brouwer et al., 2005; Chen et al., 2019; Cuadrado et al., 2014; Droppo et al., 2007; Fang et al., 2015; Flemming, 2019; Friend et al., 2008; Gerbersdorf and Wieprecht, 2015;2008; Grabowski et al., 2011; Lundkvist et al., 2007; Sutherland, et al., 1998). For example, Chen, et al. (2017a) experimentally investigated BSA after different growth periods under calm water conditions. With increasing growth periods, the stability of microbial sediments increases and eventually present biostabilization effects, with a more than 60% increase after growth of 22 days. However, the behaviour of the microbial sediments exhibits distinctly different behaviours in the first growth stage (5 days), where the microbial sediments appear to be more easily eroded than the abiotic control sediments. Such destabilization effects cannot be caused by bioturbation as no seabed fauna are present in their experiments (Chen, et al., 2017a). Reasonable explanations for such destabilization effects are lacking in the current understanding of microbial influences on sediment stability. Gerbersdorf, et al. (2008) conducted resuspension experiments to study the laboratory-incubated microbial community grown on non-cohesive glass beads. Their work also showed, although the stability of the sediments increased significantly when the microbiology at a relatively well-developed stage after the three weeks of incubation, a decrease in sediment stability was observed during the

first week after the settling of microbial cells into seabed sediments. Similarly, a recent study of the motion of microbial aggregates attached sand grains also showed an advanced motion after the microbial attachment (Mariotti et al., 2014). De Brouwer et al. (2005) inoculated sterile sediments with two types of microorganisms, C. closterium and Nitzschia sp. Whilst the stability of sediments generally increases overtime as the microbial matrices become increasingly mature, after cell growth of 2 days, the resuspension tests of the microbial sediments show a reduced stability compared to the abiotic control, for both microorganisms (De Brouwer et al., 2005). Such destabilization effects appear not to be limited to laboratory settings. Their field observation of intertidal sediments of the Zandkreek, Netherlands, from December 1999 to October 2000, presented a reduction of sediment erosion threshold when the field biomass increased in February (De Brouwer et al., 2005). Hope et al., (2020) found microbial biomass and organic matter production played a negative role in the stability of a sandy site in very energetic systems when subject to frequent processes of hydrodynamic reworking. In other words, the increased microbial biomass and organic matter production led to decreased sediment stabilities. This result is in contrary to the generally-held belief that the microbial development enhances sediment stability. It was hypothesized that, due to the frequent turnover and reworking of surface sediments, the establishment of a well-developed film-like organic matrix was prevented. Instead, a fluffy layer of fragmented biofilm and microbial cells was created at the bed surfaces, which mediate the resuspension behaviours of sediments in different ways from the film-like organic matrices.

The explanations/explorations of such destabilization effects are generally lacking, which may be because the destabilization magnitude is small compared to the significant biostabilization effects. From the summary of the above experimental and field studies, the microbial influences on sediment stabilities appear to be controversial. Do the microbial mediations always enhance sediment stability, or are the biostabilization effects restricted to the establishment of a microbial mat?

1.3.5 Measurement of microbial sediment stability

Different devices are available to investigate microbial influences on sediment stability. These include: laboratory and *in situ* annular flumes, e.g. the Sea Carousel (Amos et al., 1992), laboratory and shipboard mini-flumes, e.g. Core-Mini Flume at the University of Southampton (Thompson et al., 2013), cohesive strength meter (CSM) (Paterson, 1989), and microcosms, e.g. Gust (Gust and Müller, 1997). Tolhurst et al.,(2000) compared four in situ devices, (a) a microcosm system (Gust), (Gust and Müller, 1997), (b) SedErode (Sediment Erosion Device), a portable version of Instrument for Shear stress In-Situ (ISIS) developed at HR Wallingford (Mitchener et al., 1996) , (c) *in situ* erosion flume (ISEF) (Houwing and van Rijn, 1997), and (d) CSM (Paterson, 1989), for determining resuspension thresholds of intertidal sediments. The microcosm is a circular flume, with a diameter of 30 cm. There is a rotating disc sitting on a removable lid, and water is pumped in and out from the chamber though a 10 mm tube from the central rotating axis. The flow rate is controlled by a flowmeter with a valve at different pumping rates (Thomsen and Gust, 2000). The microcosm can obtain sediment stability in the form of critical shear stresses, τ_{crit} (Pa) (Tolhurst et al., 2000). SedErode consists of a bell head, a pump and control system, and was designed to measure bed stability of cohesive sediments (Mitchener et al., 1996). The bed shear stress was generated by pumping water from a channel between the bottom of bell head and the surface of the underlying sediments. This measurement also allows calculation of critical shear stresses, τ_{crit} (Pa) for sediment resuspension. The ISEF is a 'vertical standing' annular flume at the seabed surface, allowing through the measurement of flow velocity and turbidity the determination of the critical shear stresses for sediment entrainment. The CSM generates a vertical jet of water at the bed surface to suspend sediments (Tolhurst et al., 2000). The measurement returns an erosion pressure, from which critical shear stresses can be calculated (Tolhurst et al., 1999, 2000). Compared to the other four devices, CSM can be quickly deployed and requires short measurement duration,

beneficial to the measurement of short-term temporal variations in sediment stability such as the variations of bed stabilities during tidal immersion (Friend, et al., 2003). It is worth noting that each device uses a different method to exert an eroding force at the sediment-water interface. These four devices were deployed to test the erosion threshold and erosion rate at Skeffling intertidal mudflat on the Humber Estuary, UK (Tolhurst et al., 2000). After the standard data normalisation, the erosion thresholds became comparable between devices, while the erosion rate data showed more than an order of differences. It was argued that the big differences between the results might be caused by different device deployment time and the duration of the erosion steps used to determine thresholds. The spatial variation of the tested site could partially contribute to the differences, such as the presence and absence of bioturbation, or the heterogeneous development of biofilm (Tolhurst et al., 2000). Widdows et al. (2007) compared five devices across a range of different intertidal cohesive sediments (from newly-settled mud to the mud at the edges of salt marshes), in terms of both erosion threshold and erosion rate. The devices include annular flumes, mini-annular flumes, CSM and EROMES (Widdows et al., 2007). Significant relationships between annular flumes and mini-flumes for the erosion threshold measurement were presented. Amos et al. (2004) deployed an in situ annular flume (the sea Carousel) and mini annular flume at 24 sites in Venice Lagoon, and the results were compared with the previous measurements by SedErode (Feats and Michener, 1999). The erosion thresholds were comparable between Sea Carousel and Mini flume, while the SedErode provided consistently lower erosion thresholds (by a factor of 2-5) than that from annular flumes. Widdows et al. (2007) found no comparable relationships were revealed from the results presented among annular flumes, CSM and EROMES. No consistent relationships between erosion thresholds and the physical and biological properties of sediments were revealed, possibly due to the spatial variances among the tested sites. The authors suggested the main cause for the measurement differences between devices is their distinct way of applying bed shear stresses to the sediments (Widdows et al.,

2007). Given these previous studies and the poorly comparable results between devices, the direct comparisons of erosion thresholds in existing literature obtained from different devices seem to be impossible, but trends and relationships should be comparable.

1.4 Microbial influences on the deposition processes of sediment transport

Vertical fluxes of suspended particulate matter (SPM) in both shallow-water and deep-sea systems control particle export and flux attenuation, which plays a key role in a range of biogeochemical cycling (Wheatland et al., 2017). For example, the transfer efficiency of organic matter from the surface waters to depths critically determines oceanic carbon burial capacity and the balance of atmospheric carbon dioxide at air-sea interfaces (Cram et al., 2018; Kwon et al., 2009). In coastal habitats, such as tidal flats and marshes, the settling velocities critically determine whether the input sediments keep pace with the erosion rate and thus the fate of these habitats under environmental changes, such as sea level rise (D'Alpaos et al., 2007). Some management strategies that seek to restore tidal marshes thus need precise estimates of SPM settling velocity variations to predict local sediment budget dynamics and assess the strategy feasibility (Ganju et al., 2005). Microorganisms and their produced organic matter are extensively present in aquatic environments, which leads the majority of suspended particles to be microbiologically mediated and creates highly porous and irregular BSA (Droppo et al., 1996; Wheatland et al., 2017; Zhang et al., 2018).

The interaction between microbial cells, the produced organic matter and sediment particles further complicates SPM dynamics and vertical fluxes of particles, through altering aggregate size, structure and settling velocities. For example, the sticky biofilm can to some extent promote aggregation among phytoplankton cells, suspended inorganic sediment particles (e.g. riverine clay minerals, dust), and other microbial cells into aggregates with larger sizes, higher densities and faster settling speeds (Turner,

2015). The importance of minerals in controlling the settling rate of particulate organic matter (POM) has recently been appreciated (Armstrong et al., 2002). The vertical export of POM largely correlates with (ballast) mineral fluxes (Armstrong et al., 2009; Klaas and Archer, 2002), such as through adherence with clay minerals as organo-clay aggregates during the depositional processes (Bauer et al., 2013). The interactions between microbial cells/organic matter and sediment particles creates complexity in the settling behaviours of aggregates. Some contrary observations in terms of size-velocity, and composition-velocity relationships are recorded in the literature and need to be better understood (Iversen and Ploug, 2010; Iversen and Lampitt, 2020; Passow and De La Rocha, 2006). This suggests a need to understand the interactions between microbiology/organic matter and sediment particles, and how such interactions would affect the architecture and settling velocities of the vertical particle fluxes.

1.4.1 Microbial mediation of size-velocity relationships

According to Stokes law, settling velocities of non-porous solid spheres positively correlate with size. Size-velocity relationships are often affected by the presence of microbial development. Iversen and Ploug (2010) found settling velocities increased with size, but only for the aggregates of similar microbiology and mineral composition. Due to the differentiated compositions of microbial species, aggregates of the same sizes develop distinct porosities, structures and densities, which alters and complicates the size-velocity relationship. For example, through the association with high inputs of dust from Sahara (opal, carbonate, and lithogenic), the aggregates formed by the cocolith (*Emiliania huxleyi*) were more compact and dense, compared to the aggregates formed by diatoms (e.g. *Skeletonema costatum)*. The porosities of *Emiliania huxleyi* aggregates were ~ 96%, much lower than that of *Skeletonema costatum* (99%) (Ploug et al., 2008). Also, the cocolith aggregates were found to have a spherical nature, leading to lower drag exerted on these aggregates during the settling processes. As such, compared to diatom aggregates of similar sizes, the cocolith aggregates settled at much faster speeds. Khelifa and Hill, (2006) analysed a large variety of aggregates from

estuarine and coastal systems and showed settling velocity can vary by ~ two orders of magnitude for the same size. Maggi and Tang, (2015) analysed 52 BSA datasets collected from a variety of aquatic environments and found almost invariant settling velocities with size spanning across almost four orders of magnitude. Fifty five sequences of aggregate sizes and settling velocities observed through *in situ* optical measurement by Iversen and Lampitt, (2020), in which only 8 of them showed positive correlations between size and velocities, mainly due to the strong heterogeneities of aggregate composition, density and structures. Laurenceau-Cornec et al. (2020) compiled a large size-velocity dataset collected from both laboratory conditions and in situ measurements. Considerable scatters presented, indicating that the large aggregates do not necessarily settle at faster speed.

As such, the extent to which aggregate settling velocities positively correlate with size, and the application of Stokes law to the estimates of aggregate settling velocities in the presence of microbiology becomes questionable. The strong variabilities of size-velocity relationships suggest there must be some other mechanisms at work, that might better account for settling velocity estimates (Iversen and Lampitt, 2020).

1.4.2 Microbial mediations of composition-velocity relationships

Through the prevailing mixing between organic (e.g. EPS and microbial cells) and inorganic particles (e.g. minerals), aquatic aggregates can comprise a wide range of inorganic fractions from less than 10% to over 90% (Maggi, 2013; Maggi and Tang, 2015). BSA of >90% organic matter are found to settle at similar settling velocities as the BSA comprised of much less organic matter (Boyd and Trull, 2007; Maggi and Tang, 2015). It has been found the addition of minerals into microbial cultures promotes the aggregation process and forms aggregates of smaller sizes and compact structures, compared to the pure phytoplankton aggregates (Hamm, 2002; Laurenceau-Cornec et al., 2020; Passow and De La Rocha, 2006). The vertical fluxes of particulate organic matter (POM) and minerals in the deep sea were found to be related, and the ballast

minerals were suggested to enhance the POM export to depths, such as though enhancing settling velocities, referred to as 'mineral ballasting' (Armstrong et al., 2002; Klaas and Archer, 2002). There is however a debate as to whether the addition of mineral particles will always lead to faster settling velocities (Armstrong et al., 2002; Hamm, 2002; Wilson et al., 2012). Hamm (2002) conducted laboratory incubation experiments to test the effects of minerals on aggregate settling velocities, and found the increase in mineral concentrations did not necessarily accelerate settling velocities. Similar observations were also demonstrated by Passow and De La Rocha (2006). Wilson et al. (2012) analysed the spatial variabilities of POM and minerals and showed the lack of a uniform relationships between POM and mineral fluxes globally, which questions the mineral ballast hypothesis. Maggi and Tang analysed a wide variety of aggregates and demonstrated that the settling velocities remained almost invariant as the mineral fraction of the aggregates largely vary from less than 10% to over 90%. Passow and De La Rocha (2006) suggested alternative interpretations, such that the microbial production of sticky organic matter glues mineral particles and determines the settling velocities of mineral particles, rather than the vice versa. As such, the patterns in which aggregate composition affect settling velocities and the relationships between aggregate composition and settling velocities that account for microbial mediations remain to be determined.

Maggi and Tang (2015) established a settling velocity map which considers the effects of differentiated organic matter fractions on settling velocities, and aids a more precise estimate of vertical fluxes of organic and mineral matter (Maggi and Tang, 2015). However, the majority of the aggregates analysed in Maggi and Tang's (2015) work are relatively slow-sinking aggregates comprised of clay minerals/ silty particles with the sediment particle size of < 10 microns and an average settling velocity of less than 0.1mm/s to 6 mm/s. The applicability to the aggregates, that have fine-grained sand particles attached and settle at much higher speeds (e.g. sand of d_{50} =193 microns can settle at ~23 mm/s in still water) (Jacobs et al., 2011), may be restricted. In natural

environments, the suspended particulate matter comprises both the aggregates developed during the flocculation processes in the water column and the aggregates developed in/at the seabed. Seabed sediments generally comprise a mixture of sediments of different particle sizes, including both clay minerals/silty particles and sand grains. BSA developed through the microbial aggregation with clay and silt particles are found to aggregate with sand grains in both low- and high-energetic coastal sand bars (Virolle, et al., 2019; Duteil et al., 2020). This suggests the studies of microbial mediations on the fast-settling aggregates, e.g. those aggregated with sand grains, are also needed.

1.4.3 Microbial mediations of aggregate structures

Aggregates often form complex internal arrangements and highly porous and irregular geometries, mediating the size-velocity and composition-velocity relationships. For example, the porous structures of aggregates critically determine the properties of internal flow through settling aggregates, through altering the drag forces exerted on the aggregates to mediate settling velocities (Emadzadeh and Chiew, 2020). Meanwhile, aggregate structures reflect the internal arrangement of biofilm and sediment particles, and the porosities of aggregates determine densities, both of which in turn determine the settling velocities, such as demonstrated by Laurenceau-Cornec et al. (2020).

To quantify the complex, irregular and porous aggregate structures, the fractal dimension was introduced (Meakin, 1991; Kranenburg, 1994; Maggi, 2007; Maggi, et al., 2007). Among the various types of fractal dimension used for characterizing aggregate structures and geometries, such as the two-dimensional (2D) perimeter-based fractal dimension, 3D volume fractal dimension, $D_v = \frac{\log N_f}{\log(\frac{d_f}{d_p})}$ (d_p is primary particle diameter, d_f is the diameter of fractal aggregates and, N_f is the number of primary particles per aggregate), is often used and one of the most powerful parameters to

characterize the space-filling capacity of the 3D aggregate structures (Kranenburg, 1994; Maggi, 2007; Meakin, 1991). The larger the volume fractal dimension is, the more compact internal structure the aggregates have (Maggi, 2007). It is believed that aggregate internal structures result from a balance between aggregation and breakup (Van Ledden et al., 2004; Lick et al., 1993; Winterwerp and van Kesteren, 2004). Great progress has been made to relate the morphological parameters of aggregates, settling velocities and the kinematic processes of particle aggregation and breakup, to the volume fractal dimension, which allows numerical modelling and simulation of aggregation dynamics (Tang, 2017). There are however many difficulties in direct measurements of 3D volume fractal dimension with the usage of existing image methods (Vahedi and Gorczyca, 2011). Widely applied optical microscopic and video camera tracking systems capture two-dimensional surfaces of aggregate geometry, from which it is difficult to extract the real volume structures. Maggi and Winterwerp (2004) proposed an indirect method, using the measurements of perimeter-based fractal dimension, D_p, and the 2D projected area of floc, which enables the volume fractal dimension to be approximated from two dimensional geometries of aggregates that are generally easy to obtain. However, this method is derived from abiotic aggregates, and thus excludes the effects/alterations of microbial colonization and aggregation. The processes of microbial cell colonization, and production of organic matter to adhere and bridge inorganic particles into aggregates are complex. Maggi and Tang (2015) analysed 52 datasets of microbial sediment aggregates with different organic fractions from 0 to 1 and found non-linearity of fractal dimension with the changes of organic fraction. Chu and Lee (2004) found that the internal structures of microbial sediment aggregates present multiscale features. Nguyen, et al. (2017) found distinct patterns of microbial colonization due to cell colonization of sediment particles at different development stage, which in turn would mediate their settling velocities by affecting the surface roughness, internal flow infiltration and drag. The structural complexities caused by the presence of microbiology needs to be better characterized for settling

velocity estimates. Direct characterization of microbiologically-mediated 3D structures, e.g. a direct characterization of volume fractal dimension, is needed, and may be achieved through the imaging and quantification of the 3D BSA matrices.

1.4.4 The effects of shear velocities on aggregate deposition behaviours

Aggregation processes are dominated by three primary mechanisms: Brownian motion, differential settling and turbulence. In dynamic environments of estuaries and coastal areas, aggregation is mainly driven by turbulence (Mietta et al., 2009). Turbulent shear can cause collisions between particles and promote aggregate formation, and on the other hand can also break aggregates into smaller ones (Winterwerp, 1998). At low shear stresses, the aggregate size increases with shear velocities, but shows an opposite trend at high shear velocities (Winterwerp et al., 2006). It is generally believed that turbulence affects the processes of aggregation and breakup in two ways. Turbulent diffusion at the scale of aggregate sizes promotes aggregation, while the turbulence-induced shear when exceeding the strength of aggregates breaks aggregates (Mietta et al., 2009; Winterwerp and van Kesteren, 2004). In general, for dispersed (non-flocculated) particle suspensions, the dominant effect of shear velocities at the initial stage is to enhance aggregation. As time increases, the generated aggregate population reaches a dynamic equilibrium when the aggregation and breakup processes are balanced. At high shear stresses, breakup is expected to be dominant over the aggregation processes according to the model proposed by Winterwerp (1998). By contrast, at low shear stresses, the residence time of aggregates become an important parameter. When the residence time for aggregation among particles/aggregates is smaller than the equilibrium time for the aggregate populations to reach a dynamic balance of aggregation verse breakup, the mean aggregate size is expected to be smaller than the equilibrium size. When the residence time is longer than the equilibrium time, the aggregate size should have reached the equilibrium size, and theoretically decreases as shear velocity increases (Winterwerp, 1998). Previous prediction and observation of mud flocs showed that, under a constant shear velocity, aggregate size grows slowly for

the initial few minutes but can rapidly grow to their equilibrium size as time increases, which can occur in less than 5 minutes (Winterwerp, 1998).

Winterwerp (1998) also investigated the effects of turbulence on aggregate settling velocity, where the aggregates were considered as having self-similarity and the structures were characterized through fractal dimensions. The settling velocities of the aggregates developed under turbulence were found to correlate with the equivalent diameter of the aggregates *(L)* as L^{Dv-1}, instead of L^2 as suggested by Stokes law. Similar results were also found from the in situ measurements of aggregate settling velocities along New Jersey coast, where the settling velocities correlated with $L^{1.2}$ (1.2 is within the range of D_v-1) (Agrawal and Pottsmith, 2000). Similar trends occur where the settling velocities of aggregates developed under shear velocities show strong dependence on structural features (fractal dimension), which implies the importance of structural features in the settling velocities for those turbulence-induced aggregates, and should be properly accounted for.

1.4.5 Measurement of settling velocities

To achieve in situ sampling of aggregates and measurement of their settling velocities with minimal disruption of aggregate structure and size, an IN Situ SEttling Velocity instrument (INSSEV) was developed by Fennessy et al. (1994). The main feature of this instrument is the ability to simultaneously capture the size (down to 20 μm) and settling velocity of SPM in turbid environments up to 200 mg l^{-1} (Fennessy et al., 1994). INSSEV is comprised of two chambers, a top chamber to collect samples and deliver samples to the underneath settling column. The settling column is equipped with an underwater camera and video used to measure the size and velocities (Manning and Dyer, 2002).

Optical measurements obtained through videoing settling aggregates are widely applied to both laboratories and fields to obtain the settling velocities. One typical instrument is the Laboratory Spectral FLOcculation Characteristics (LabSFLOC) (Manning, 2006).

LabSFLOC is comprised of a high resolution video camera at the bottom and outside a Perspex settling column. This measurement technique requires the tested suspended aggregates to be immediately transferred to the settling column through a wide-mouth pipette, after the extraction of the samples. To minimize disruption to the size and structure of the samples, the pipette mouth is gently placed right underneath the water surface and the pipette body should be held vertically to allow the settling of aggregates through gravitational forces. This technique has been examined as one of those creating minimal disruptions to the tested aggregates (Manning et al., 2007). Videos of settling aggregates will be recorded with time-referencing information to allow image processing and settling velocity estimates.

As suggested by Manning et al. (2011), natural aggregates have multiple components, such as inorganic particles from different sources, various microbe species and different contents of organic matter, which appears to result in complex structural arrangement and heterogeneous distributions of the components. As a result, a systematic and quantitative understanding regarding the settling behaviours of aggregates appear to be lacking, and direct measurements of aggregate size and velocity become a key step.

1.5 Aims and objectives

Microbial influences on aquatic sediment transport processes are commonly presented in natural environments, which are complex and our present understanding remain incomplete. This thesis seeks to present a clearer and more comprehensive understanding of microbial sediment interactions and the mechanisms and properties of microbial influences on the resuspension and deposition processes of sediment transport.

BSA comprises a high-water content, either within internal pores and channels, or absorbed around particles or bound by EPS forming a highly hydrated microbial matrix (EPS are comprised of more than 90% of water (Schmitt and Flemming, 1999)). Desiccation of BSA alters the morphology of the microbial substances and thus the

physical characteristics of porous media, such as binding mechanisms within BSA and internal pore geometries for flows. Observing BSA in their naturally hydrated form is essential but historically hampered due to the lack of techniques for imaging and discerning hydrated materials. The first objective of this thesis is to develop an appropriate BSA specimen preparation method with no need to desiccate BSA and allow for the high-resolution imaging and quantification of the 3D matrices of BSA. To achieve this goal, a new approach using a micro-CT technique is developed in Chapter 2, which allows the 3D matrices of BSA to be imaged and quantified in their hydrated states. This method was then combined with some well-established techniques for studying sediment transport, including the use of annular flumes (Amos et al., 2004; Amos et al., 1992; Thompson et al., 2013), settling columns and camera-video systems (Manning, 2006; Manning et al., 2007), to investigate the 'cycle' of sediment transport through settling, deposition and resuspension in the presence of microbiology. The protocols of the new approach and the general methodology are outlined in Chapter 2.

The summary of existing work implies the effects of microbial influences on sediment stability might not just enhance sediment stabilities as generally expected but also reduce sediment erosion thresholds. Whilst the majority of current studies acknowledge the presence of biofilm as biostabilizing sediment stability, the results of some experimental and field observations show that a moderate destabilization effect can occur at the initial stages of microbiology development in sediments. Therefore, the second objective of this thesis is to experimentally investigate whether BSA at different states behave in the same way as a mature microbial mat, and whether microbial mediation can destabilize sediments. The results of flume resuspension tests and micro-CT experiments will be presented in Chapter 3, presenting the resuspension resistance of two distinct BSA matrices that are established at different development states. The BSA geometries, mediations of sediment stability and the significance of the study findings will be detailed in Chapter 3.

Present efforts, either from qualitative or quantitative aspects, are paid to study the

microbial mediations on slow-settling aggregates that are generally comprised of fine-grained clay and silty particles. The microbial influences on the fast-settling aggregates, e.g. with sand grains being attached, appears to be less investigated. The third objective of this thesis is thus to study the effects of bio-sediment association on the settling velocities and drag of aggregates. The results of both settling tests and micro-CT experiments will be presented. The characteristics of BSA internal structures, settling velocities and drag will be analysed and discussed in detail in Chapter 4.

The fourth objective of this thesis is to pursue an integrated view of microbial influences on the resuspension and deposition processes of sediment transport, from both qualitative and quantitative aspects. To achieve this goal, the phenomena observed in Chapter 3 and 4 from the laboratory created BSA will be tested using the BSA sampled from the field, to help a better understanding of real-world applicability. Both the resuspension and deposition properties of field-sampled BSA will be experimentally studied and analysed in Chapter 5. After this, based on the experimental data of both laboratory-created and field-sampled BSA, the microbial influences on the resuspension and deposition processes of sediment transport will be quantitatively analysed. Predictive relationships for estimating BSA resuspension thresholds, drag and settling velocities will also be presented in Chapter 5. A summary of the major study findings and the future research requirements of this thesis is outlined in Chapter 6.

Chapter 2 Method development and general methodology

The contents of section 2.1 have been published as Zhang et al.[1] during the PhD candidature of this author. Naiyu Zhang designed the study, prepared the samples, developed the methods, collected and analysed the data, and led the writing of the manuscript. Charlotte E. L. Thompson assisted with the study design and the manuscript editing. Kathryn E. Rankin assisted with the development of micro-CT machine operation protocols. Ian H. Townend, David M. Paterson, and Andrew J. Manning assisted with the manuscript editing.

This chapter is comprised of two major sections. Section 2.1 develops a new approach using micro-CT to imaging and quantifying the 3D geometry and internal structure of BSA in a hydrated status (section 2.1). This method is then combined with some of the mostly well-established techniques for studying sediment resuspension and deposition process, e.g. annular flume, camera-video system for recording fine particle settling velocity, and dedicated settling column with mass balancing and time recording systems, to study the microbial influences on sediment transport. Section 2.2 then summarises the general methodology of utilizing these sediment transport techniques.

2.1 Non-destructive 3D imaging and quantification of hydrated BSA using X-ray microcomputed tomography

BSA are highly hydrated, with the biological components binding sometimes more than 90% of water (Flemming and Wingender, 2010). To more fully represent the 3D

[1] Nondestructive 3D Imaging and Quantification of Hydrated Biofilm-Sediment Aggregates Using X-ray Microcomputed Tomography, Naiyu Zhang, Charlotte E. L. Thompson, Ian H. Townend, Kathryn E. Rankin, David M. Paterson, and Andrew J. Manning, Environmental Science & Technology 2018 52 (22), 13306-13313

geometry and internal structure, and to avoid the significant geometry distortion caused by the complete desiccation steps that have been generally applied in the current available methods, there is a need to capture the 3D matrices of BSA in a hydrated state. Generally applied imagery techniques, such as scanning electron microscopy (SEM), transmission electron microscopy (TEM), and focused ion beam nano-tomography (FIB-nt)), involve the complete desiccation of BSA or prevent differentiation between BSA components such as inorganic particles and pore water (confocal laser scanning microscopic (CLSM)). To address the above difficulties, a number of trials for different specimen preparation methods were carried out. Different preparation methods were cross compared to investigate the best preparation methods for imaging BSA. Quantitative analysis based on the three-dimensional models of the BSA obtained using this newly-developed method is subsequently discussed in section 2.1.6. Section 2.1.7 describes an adjusted preparation method for seabed sediments using an alternative micro-CT machine, which allows to scan seabed sediment cores that may contain coarser sand grains and enables a larger field of view.

2.1.1 BSA specimen preparation methods

Different BSA specimen preparation methods for micro-CT were chosen and compared, to assess the suitability for imaging. The ultimate purpose of each preparation method was to enable the 3D matrices of aggregates to be imaged at high resolution and in hydrated states.

Liquid nitrogen freezing BSA

Liquid nitrogen (LN_2) was used as a high-speed freezing treatment to minimize the freezing artefacts that can result from freezing process (Parker and Collins, 1999). Fresh aggregate samples were placed in a 20ml plastic syringe (radius 2 cm and depth 3 cm), and immediately immersed into an LN_2 pool at -196℃ for 2 min, which ensured that the aggregates were sufficiently frozen (Chen et al., 2001). The frozen aggregates were freeze dried, as while drying preserves the fibril bundles of biofilms, it does not sustain

the hydrated polymers in BSA (Perkins et al., 2006). As thawing of the frozen samples can cause significant displacement of features inside the specimen, the specimen vial was held in dry ice (-79 ºC) during scanning.

Embedding BSA in resin

A 3 mm-diameter hole (3 mm depth) in a pre-prepared pure resin block was created in advance to hold aggregates that were carefully transferred into the hole immediately after creation. As epoxy resin is hydrophobic, the aggregates were repeatedly soaked in anhydrous acetone to replace the internal water. This is followed by resin filtration and addition, after which the sample was cured at 60℃. A 5x5x5 mm resin sub-block containing the target aggregates was sectioned for whole-volume scanning to avoid artefacts during alignment of the sectioned image series to a 3D dataset. This also allows a higher scanning resolution to be obtained.

Wet staining BSA

A sealed 200 μl pipette was used as the specimen container for wet aggregates. The pipettes are composed of polypropylene. The thin walls (200-300 microns) (Metscher, 2009) of the container allows the minimisation of the amount of media between the aggregate target and the detecting probe, reducing extra X-ray absorption (Hubbell and Seltzer, 1995). One of the most challenging problems for wet aggregate scanning is to stabilize aggregates in the liquid media during the entire scanning process which can last several to dozens of hours. To address this from a specimen preparation approach, initial attempts were made to stabilize the samples in an absolute alcohol treatment. The alcohol treatment aims to immobilize the algae, which can cause irreparable failure in image reconstruction. Following the alcohol treatment, Alcian blue dye solution was added in specimen for a 7 min staining period following (Bar-Zeev et al., 2012). Alcian Blue has been used in several studies investigating the size, form and abundance of acidic polymeric substances (APS) which contribute significantly to biofilm adhesion (Passow et al., 2014; Thornton and Visser, 2009). The Alcian blue treatment (Sigma;

0.4% wt/wt at pH 2.5) (Bar-Zeev et al., 2012) was sonicated for 15 min to disaggregate the particles and then passed through a 0.45 micron filter twice to remove stacked particles and ensure a homogeneous solution before use.

2.1.2 BSA scans by micro-CT

The LN_2 frozen aggregates packed with dry ice were imaged with X-ray micro-CT using a modified 225 kVp Nikon HMX ST, while the 3D imaging of BSA embedded in resin and in liquid (stained and unstained) were conducted using a Zeiss 160kVp Versa 510 X-ray microscope, both located at the μ-VIS X-ray Imaging Centre, University of Southampton. The latter scanner uses a two-stage magnification approach, combining the geometric magnification of the X-ray cone beam and source-to-detector/object distances, with optical magnification through a microscope lens system to further magnify the image ahead of the detector (Figure 2.1). In the reconstructed stack images, voxel intensity (greyscale value, Hounsfield unit, a dimensionless unit used in CT scanning) reflects the variation in X-ray absorption, which is a function of the material's physical and radio-density throughout the volume (Amos, et al., 2003; Kamaruddin et al., 2016). In summary, it can be inferred that brighter pixels represent denser materials (e.g. sediment in this case), while darker pixels represent less dense materials (biofilm and pore water) (Hale et al., 2015) (Figure 2.1). Details of the density calibration and estimation protocols are explained in section 2.1.7. Scan protocols optimised to suit each type of BSA specimen were applied and listed as follows.

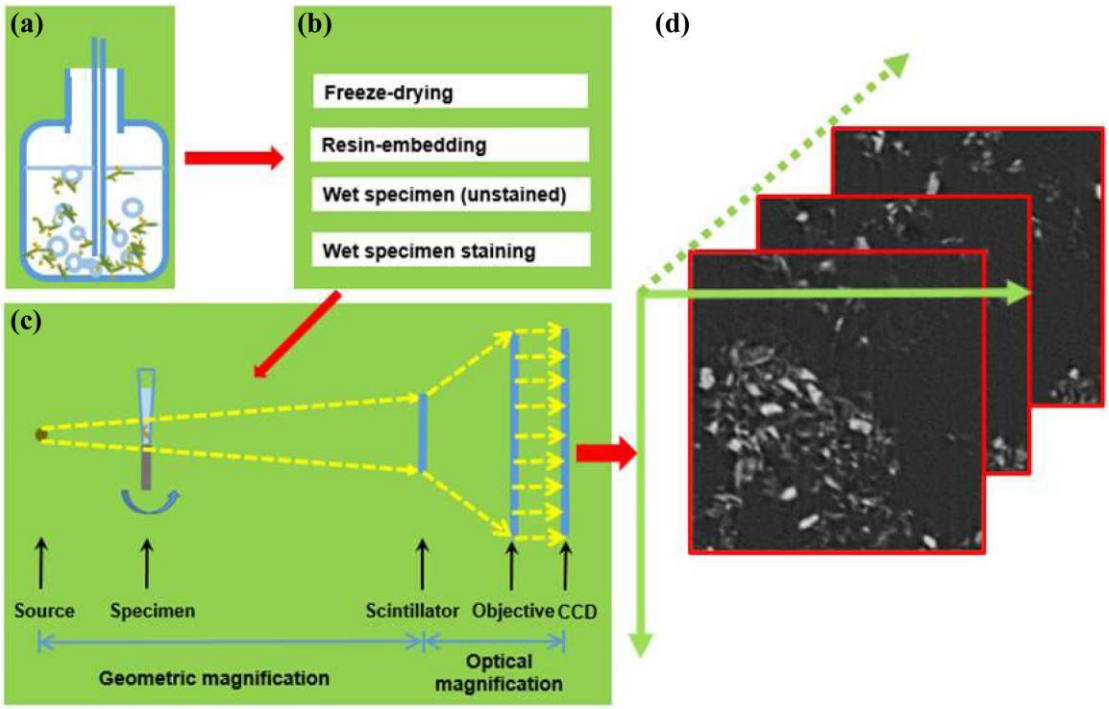

Figure 2.1 Schematic illustrations of workflow from BSAs creation (a), sampling and BSA specimen prepared using a full range of available protocols (b), to X-ray micro-CT setup (c). Illustrates the dual-magnification imaging system including both the geometric magnification and optical magnification. The resulting reconstructed volumetric slice images composed of different voxel greyscale values representing the X-ray absorption map throughout the volume which is closely relevant to the material density variations (d).

LN_2 BSA imaging

Each CT scan was performed at 160 kVp (peak voltage) and 140 μA, using an exposure time of 250 ms, and acquiring 3142 projection images with 2 frames averaged per projection, 1x binning and 24 dB analogue gain. The projection images were reconstructed into 3D volumetric data using the filtered back-projection algorithm embedded within X-TEK CT Pro 3D and CT Agent software (Nikon Metrology, UK). The resulting voxel (3D pixel) resolution was 10.1 x 10.1 x 10.1 μm.

Resin-embedded BSA imaging

The resin embedded specimen was scanned at 80 kVp and 7 W, with the beam pre-

filtered through 0.34 mm of SiO_2 to reduce beam hardening artefacts. Using the 20X objective with 2X binning (a way of combining signals reflected from adjacent elemental detectors, to increase contrast resolution) (Abdelnour et al., 2007) and an exposure time of 20 s, the voxel resolution achieved was 0.683 μm, and the resulting scan time was around 14 hours with 2401 projection images acquired.

Unstained wet BSA imaging

The unstained wet specimen was scanned at 80 kVp and 7 W, with the beam pre-filtered through 0.15 mm of SiO_2 to reduce beam hardening artefacts. Using the 20X objective with 2X binning and an exposure time of 20 s, the voxel resolution achieved was 0.683 μm, and the resulting scan time was around 14 hours with 2401 projection images acquired.

Stained wet BSA imaging

The scan of the wet stained specimen was conducted at 80 kVp and 7 W, with no pre-filtration of the beam due to the improved X-ray penetration and the reduced exposure time. The increase in image intensity allowed a reduction in exposure time to 5 s, and the scanning time was reduced to 3 hours with 1601 projection images acquired. The imaging time was kept as short as possible to reduce the likelihood of the stained BSA drifting in the liquid during the scan. Using the 20X objective with 2X binning, the resulting voxel resolution was 0.777 μm.

2.1.3 Image processing

Multi-purpose image processing was conducted using Avizo™ 9.3.0 software (FEI Hillsboro, OR, USA) in cooperation with Fiji/ImageJ (National Institutes for Health, USA), including image filtration and image segmentation (Schindelin et al., 2012; Zhou et al., 2016). The ultimate purpose was to distinguish different material components (organic matter, pore water and sediment particles in this circumstance) within a BSA. In order to increase the accuracy and efficiency of image segmentation, image filtration

was conducted using the Avizo^{TM} 9.3.0 Median Filter to average out image noise. Segmentation relied on a Trainable Weka Segmentation 3D plugin within Fiji/Image J, using a collection of visualization tools and machine-learning algorithms based on the user input, and then performing the same task in the untested data (https://imagej.net/Trainable_Weka_Segmentation) (Carreras et al., 2017). By identifying and recognizing targeted objects manually in a subset of images, and annotating them to train the classifier, the machine-learning algorithms apply multiple filters to perform particle separation and segmentation (Schindelin et al., 2012; Wheatland et al., 2017). Thereafter, successfully segmented organic matter (biofilms), pore water and sediment particles could be imported together into Avizo 9.3.0. A 'Separate objects' module, developed in Avizo 9.3.0 using a combination of watershed, distance transform and numerical reconstruction algorithms, is applied to distinguish individual aggregates (Callow et al., 2018; Sharma et al., 2017). This method enables the voxels connected by a common face to be assigned as belonging to the same aggregates (Callow et al., 2018). This method has been widely applied to distinguish connected pores from the disconnected ones in rocks and has recently been successfully applied for separating and identifying individual polymer-induced kaolinite aggregates (Sharma et al., 2017). Subsequent volume rendering, quantitative label analysis can then be conducted in Avizo 9.3.0.for each aggregate (Avizo, 2016; Callow et al., 2018).

With the identification of individual aggregates and segmentation of aggregate components, volume-equivalent diameter, 3D volume and surface area of each individual aggregate and each aggregate component can be estimated, through the Label Analysis module provided in Avizo 9.3.0^{TM} (Avizo, 2016; Callow et al., 2018). The volume fractal dimension of the 3D matrices of each individual BSA can be estimated by using the Bone J plugin provided in Fiji/Image J (https://bonej.org/). Bone J utilises the widely-applied box counting method to obtain volume fractal dimension of 3D structures. The box-counting method enables the volume fractal dimension to be directly calculated by covering the 3D fractal structures by N_r elements (voxels) of size

r (Fazzalari and Parkinson, 1996; Vahedi and Gorczyca, 2011):

$$D_v = \lim_{r \to 0} \frac{\log(N_r)}{\log(1/r)} \quad \text{Eq. 2.1}$$

2.1.4 Comparisons of different specimen preparation methods

LN_2-freezing specimens

Keeping aggregate specimens frozen during the several-hour scanning period was challenging due to the room-temperature scanning environment. Covering the aggregate specimen in dry ice effectively mitigates the temperature difference, but increases the distance between the specimen and the X-ray source. As a result, the best achievable resolution is sacrificed. This effect may be minimised by reducing the amount of dry ice used, but then insufficient cooling can lead to the sample defrosting and therefore scanning failure. Given an average scan time of several hours, it was challenging keeping specimens sufficiently frozen, even without reducing the amount of dry ice used. The best scan provided a 10-micron resolution. No aggregates were captured in the image (may be due to the low contrast of aggregates), which instead indicated a considerable amount of ice crystal formation and air bubbles within the sample (Figure 2.2). The results indicate that high-speed freezing by LN_2 can still result in the formation of ice crystals, and the authors advise caution when using freezing methods to interpret microbial sediment binding due to potentially significant freezing artefacts (Parker and Collins, 1999; Perkins et al., 2006). As such, freezing aggregates by LN_2 was not deemed a suitable specimen preparation method for Micro-CT.

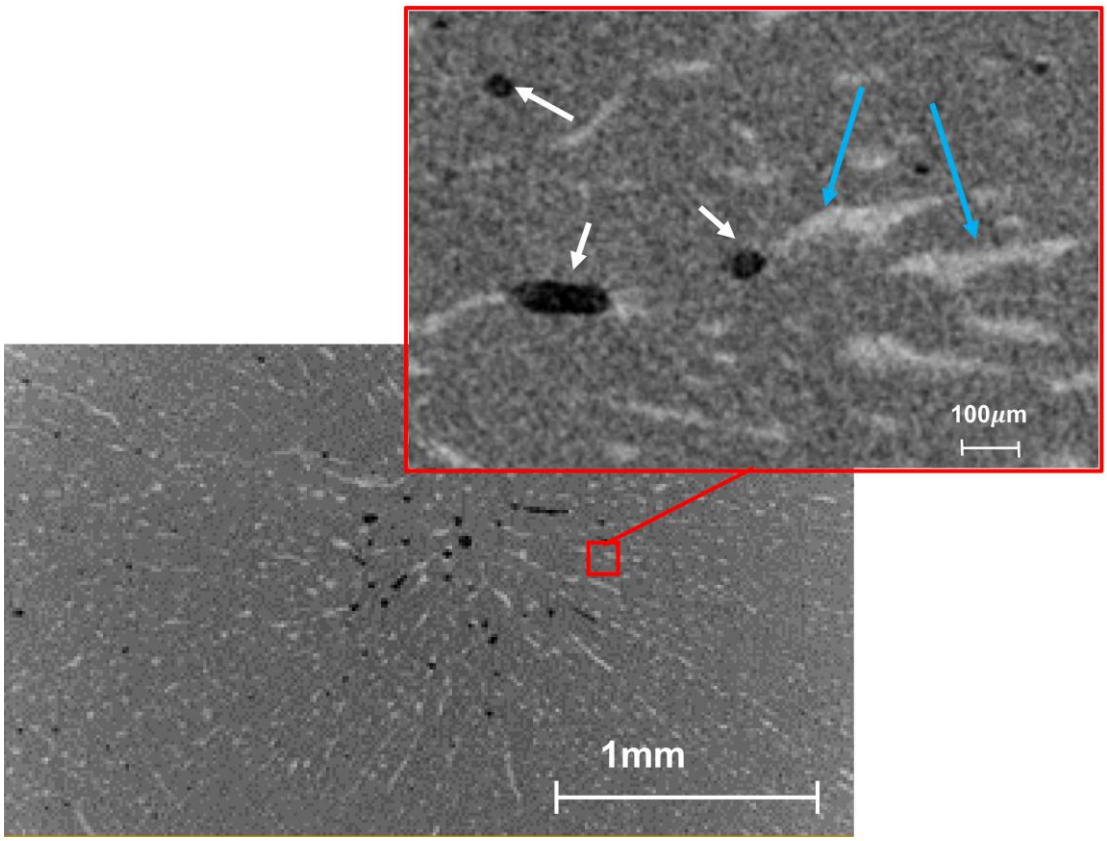

Figure 2.2 Resulting scans of the LN_2-frozen BSA. White arrows indicate the air bubbles, and crystals with blue arrows. Aggregates were not captured, but crystals and air bubbles formed during LN_2-freezing are considerable.

Resin-embedded aggregates scanning

As the aggregates were well stabilized in the resin block, a 20 h long scan was possible, which secured a high-resolution of 0.683 microns (Figure 2.3). Although primary particles and sufficient aggregates were detectable, a considerable number of aggregates showed blurred boundaries of the organic matter (BSAs 4, 5, 6 in Figure 2.3 (a)). This may be due to the high X-ray absorption properties of resin materials. This prevents a precise discrimination of aggregate morphology, biofilm matrix, or the internal pore geometry against the background resin during subsequent image processing for some samples. Meanwhile, some aggregates show distinct, regular, sharp and spherical edges (BSAs 1, 2, 3 in Figure 2.3 (a)), as well as an easily detectable biofilm network, which was common in the scans. As widely acknowledged by prior

investigations (Stone et al., 2008) and optical microscopy observation of untreated aggregates, the shape of aggregates is generally irregular and amorphous, and a regular sphere was not expected. This architecture may result from the preparation procedure during embedding BSA in resin. The resin should theoretically penetrate into the pores within aggregates to replace the bulk liquid without any perturbation by compression or dehydration (Leppard et al., 1996). However, the regular and circle-like aggregates observed may indicate that, instead of penetrating these pores, the resin wraps around the aggregate body, possibly due to the complex and non-trivial internal micro-/nano-pore geometry. Some compression effects on aggregates structure seem unavoidable. Thus, although a dense network of organic matter (biofilms) can sometimes be observed, caution should be taken to interpret the structure and biofilm matrixes of resin-embedded aggregates.

It should also be noted that not all resin penetration into the aggregates failed (blue arrows in Figure 2.3 (b)). In these areas, aggregates have irregular morphology, but this is associated with a low contrast between the biofilm matrix and the surrounding resin. A high noise and low contrast were typical of resulting images. This may be partially caused by the high X-ray absorption of resin materials. However, sufficient contrast can be obtained when the hydrophobic epoxy resin fails to completely penetrate into the pores of aggregates but instead forms around the aggregate body (BSAs1, 2, 3 in Figure 2.3 (a)). It is thus clear that the contrast between the saturated biofilm and the resin itself is enough to be detected, and so the low contrast highlighted in the blue-arrowed aggregates may result from the resin-penetrated biofilm. As explained in the introduction, biofilms are predominantly comprised of water, the majority of which is bound by EPS forming the hydrated matrix of organic matter. Such water is easily removed through dehydration and replacement (Schmitt and Flemming, 1999), which are always accompanied with resin penetration, and always associated with artefacts (e.g. shrinkage) (Paterson, 1995). Therefore, the resin-penetrated biofilm and BSA were unavoidably altered. In conclusion, embedding hydrated biofilm-sediment aggregates

in resin might not be optimal to allow interpretation of the hydrated matrix characteristics, due to the resulting low-contrast, possible compression by resin and partial dehydration.

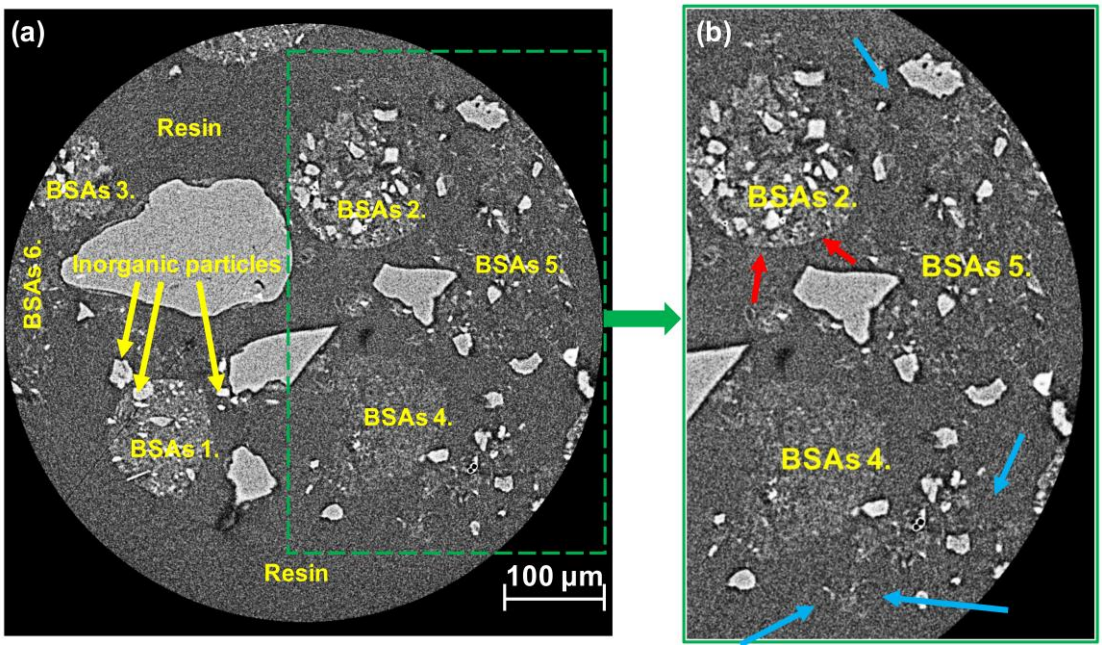

Figure 2.3 An example image slice of resin embedded BSA. The inorganic fine particles and a sufficient amount of aggregates were detected (a): BSAs1, 2, 3 showed a sufficient contrast with surrounding resin, BSAs 4, 5, 6 showed poor discrimination against surrounding resin and poor discrimination of components. Aggregates with a sufficient contrast present sharp, regular and curved edges (e.g. BSAs2 red-arrow in (b)), while the aggregates with an amorphous shape suffer from a lower contrast with surrounding resin (blue-arrow in (b)).

Wet specimen scanning: stained and unstained

Stabilizing aggregates in a liquid media remains a problem during the long scanning process. To achieve the best spatial resolutions of 0.683 µm, a 14 h plus scanning period is typically required. However, initial results indicate that such scanning period results in considerable movement of the untreated wet aggregates, causing a complete failure of image reconstruction. The consolidation of materials, movement of the algae cells, and the production of bubbles by live algae during scans lasting > 14 h can cause considerable movement. The problem of acquiring acceptable scans thus remains:

how can the scanning period be reduced without sacrificing image resolution, contrast and signal to noise ratio (SNR). The micro-CT machine parameters were adjusted for conducting a shorter 3-hour scan. However, tests of untreated samples showed significant sample movements even within 3 hours.

To address the above difficulties, absolute alcohol treatment was applied to immobilize algae cells. Alcian blue treatment was then applied to help discern hydrated microbial matrices from surrounding pore water. This procedure led to successful images of the wet aggregates. The resulting scanning time was 3h, with a high-resolution of 0.777 μm, and allowed to the discrimination of hydrated biofilm from surrounding water and sediment particles. As such, the following analysis and results are all based on the wet scanning of stained specimens.

2.1.5 Three dimensional models of BSA

In the cross-sectional greyscale raw images (Figure 2.4 (a)), an image was segmented into different regions (Figure 2.4 (b)), based on the greyscale values (at a resolution of 0.777 μm) and architectures of each voxel using semi-automatic trainable segmentation tool in Fiji/Image J (Carreras et al., 2017; Schindelin et al., 2012). Greyscale levels reflect the X-ray attenuation degrees which are determined by the densities of different materials (Hale et al., 2015). Each component of an aggregate, such as sediment particles, biofilm and water, produces their own specific greyscale ranges (details in section 2.17) reflecting their different geometries, which enables partition of an aggregate into three component materials. The raw image stacks (2D image slices) of an aggregate were divided into three image stacks: sediment particles, biofilms, and water. Each 2D image stack is then reconstructed to 3D dataset/model by the volume rendering algorithm in Avizo^{TM} 9.3.0 (Figure 2.4 (c), operation manual (Avizo, 2016)). The 3D models of each of the components can then be overlaid to reconstruct the intact aggregate (Figure 2.4 (d) and 2.4 (e)). This method avoids complete desiccation of BSA, and allows discrimination of internal pores from comparable matrices of hydrated

organic matter.

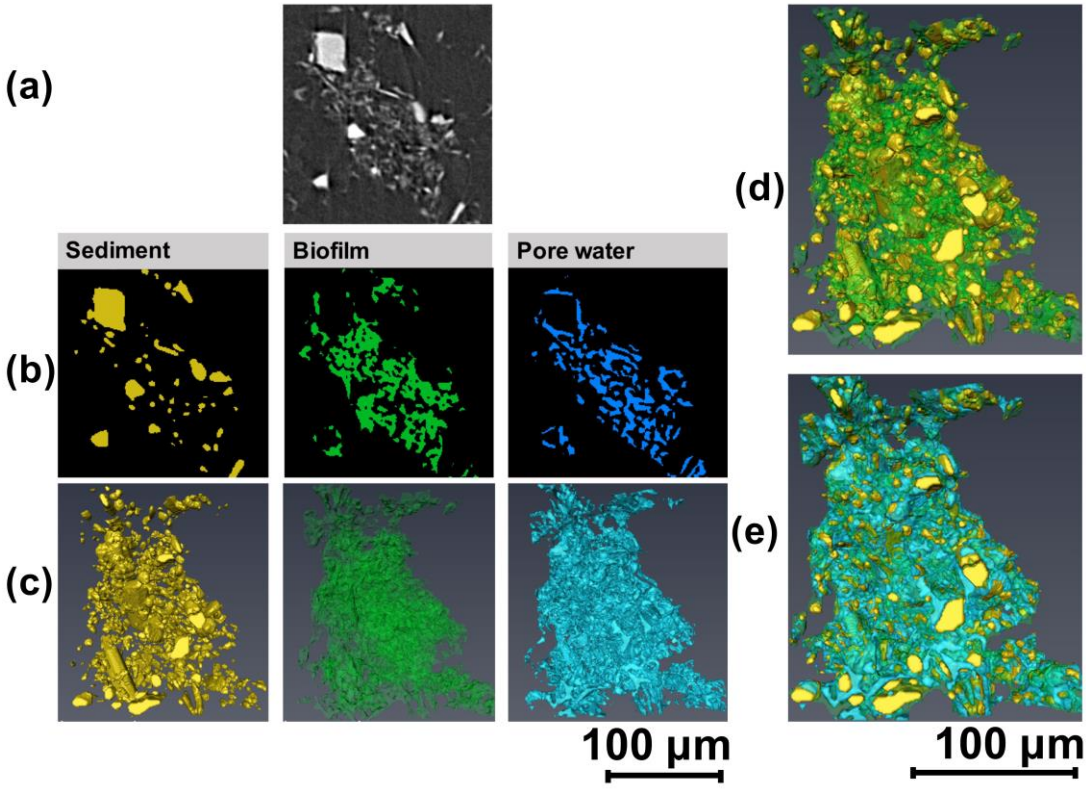

Figure 2.4 Greyscale raw images (a) processed by image demonising and segmentation to separate aggregate components into: organic matter (biofilms), pores, and sediment particles channels (b). (c) shows 3D reconstructed model of each constitute by volume. (d) is the 3D view of the distribution of microbial sediment binding matrices in an individual BSA, giving an insight into the microbial sediment interactions at hydrated states. (e) 3D model of one intact aggregate comprising of each single component, including internal pore water.

2.1.6 BSA analysis

Particle size distribution (PSD) analysis

PSD was measured by labelling sediment particles and conducting label analysis using Avizo^{TM} 9.3.0. This was compared to more conventional laser sizing data. These two methods are both based on using a spherical volume equivalent diameter to measure the sediment particle size. The CT-based PSD showed a distribution with a median grain size d_{50} = 4.72 microns (Figure 2.5 (a)), validated against the Coulter-measured PSD

d_{50} (d_{50} = 5.11 microns), both of which exceed the size range of the primary particles (1-1.8 microns). Considering that a voxel resolution of 0.777 microns allows the detection of particles within this primary particle size range, this suggests aggregation of the primary clay particles. A comparison of the two datasets shows that d_{10}, d_{25}, d_{50} all exhibit similar results, while d_{75} and d_{90} showed some differences (Figure 2.5 (b)). The coulter-measured PSD showed that particles ranging from 15 to 77 µm account for 12% of the distribution, while less than 1% was observed in CT-based PSD (Figure 2.5 (a)). This significant difference may be due to potential electrochemical interactions among the kaolinite clays enhanced by moderate turbulence (Winterwerp, 1998), which is a typical step of stirring the samples during the Coulter-measurement procedure. CT-based PSD also has the added benefit of direct visualization of 3D architecture of individual sediment particles, enabling further shape geometry analysis of each single particle, such as by image-based programming (Zhao and Wang, 2016).

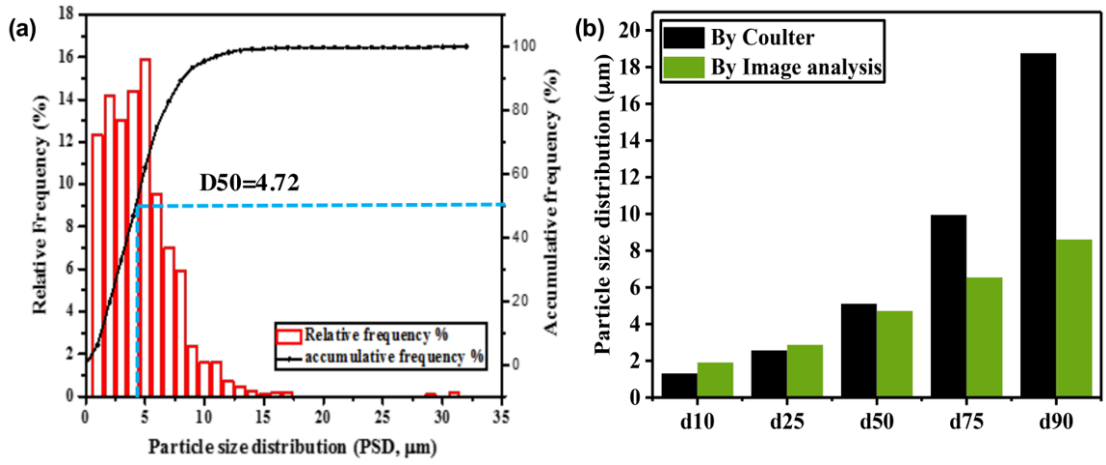

Figure 2.5 (a) CT image-based distribution of sediment particles embedded in biofilm aggregates (PSD, microns). (b) Comparisons between measured PSD by Coulter and by CT image analysis.

Microbial sediment binding matrices

As discussed above, water bound by an EPS hydrogel is easily lost. The distortion of the microbial matrices of organic matter, and the internal geometries of BSA by dehydration seems largely unavoidable in the majority of previous imaging

methodologies. Since no desiccation or freezing is involved in the proposed methodology, direct 3D imaging of the wet matrices of organic matter is possible (Figure 2.6). The detailed matrix of organic matter (biofilms), including the fabric-like stands and plates, gel-like materials, as well as the matrix voids, as defined by Flemming (Flemming and Wingender, 2010) as *'a pore or channel in the biofilm matrix that contains liquid water and is not filled with hydrated EPS molecules'*. These voids are important for the uptake and accumulation of nutrients, heavy metals, organic substances, and particles (Flemming, 2011), and are especially well represented using this methodology.

This method succeeded in capturing different microbial sediment binding matrices within an individual BSA at a 3D, sub-micron voxel resolution, and in their hydrated form. We note that the majority of sediment particles are bound/bridged in the microbial matrices of aggregates (Liss et al., 1996) (Figure 2.4 (c) and (d)). This might be due to the presence of microbial cells, influencing the shape and surface properties of the inorganic particles compared with purely abiotic conditions (Gerbersdorf and Wieprecht, 2015). Natural aggregates are significantly microbiologically-mediated, indicating the importance of appropriately considering the microbial processes in aggregation, e.g. for large-scale morphodynamic modelling (D'Alpaos et al., 2007).

This result illustrates the successful capture of tiny biofilm patches attached to sediment particles (green arrow in Figure 2.6 (b)). This may arise as an initial attachment with single cell colonizing the sediment particle surfaces (Rusconi et al., 2014), which is followed by copious EPS secretion, forming a localized biofilm patches (Alldredge et al., 1993; Decho, 2000; Gerbersdorf and Wieprecht, 2015). Alternatively, this might be caused by the breakup of the biofilm bridge with another aggregate. Further investigations applying this method as a straightforward tool are needed to test these hypotheses. Some relatively developed biofilm patches with different geometries have also been observed. Some appear 'loosely-connected' with a few particles (yellow arrows in Figure 2.6 (a) and (b)), while others appear to be 'well packed' with more

particles embedding (red arrows in Figure 2.6 (a) and (b)). This is consistent with the hypothesized cell colonization patterns of 'poorly-touched' and 'well-touched' defined in the studies of biomineral aggregates (Nguyen et al., 2017). Clearly, the mechanisms of these various microbial sediment binding matrixes are still unclear, and the described methodology provides a visual tool for informing and testing, and producing further understanding of these mechanisms.

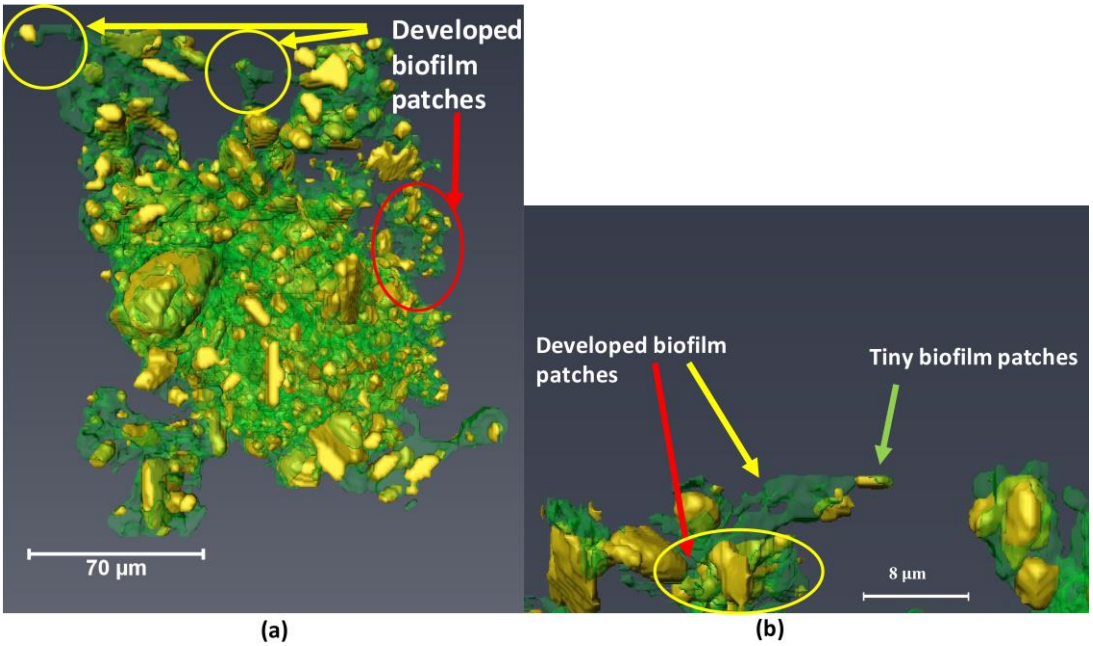

Figure 2.6 An illustration of microbial sediment binding matrices in BSA. inorganic sediment particles are yellow, while green is assigned to the organic matter.

Quantification of BSA component density

Grey scale values for each pixel in raw images reflect the variations in the densities of the component materials (Hale et al., 2015). Beer's law can be used to relate pixel intensity (greyscale value) to the corresponding density of the organic matter, sediment particles, and pore water (Kamaruddin et al., 2016). This takes the form of a linear relationship between the Hounsfield unit (HU, which reflects a spectrum of X-ray attenuation (Kamaruddin et al., 2016)) and the bulk density of sediment, and has been evaluated and successfully applied to approximate sediment density (Amos et al., 2004; Amos, et al., 2003). The linear relationship (the slope ratio and intercept) is not constant, but varies with spatial variations of the components and structures due to the

photoelectric effect (Orsi, 1995). In prior work, the entire specimen was usually assigned a single linear relationship between density and pixel intensity, here the linear relationship was re-calibrated within every 10 image slices for the entire 180 slices of the single aggregate. The aim is to reduce the potential photoelectric effects caused by spatial disunity of components and structure distribution within one specimen. For each 10 image slice, 10-15 regions of interest (ROI) were selected. The selection of each ROI was strictly specified: only the areas containing all three materials were chosen (Figure 2.7). This is because we assume the densities and pixel intensities of sediment, biofilm and pore water within this small area obey the same linear relationship. Comparison of the values of pixel intensity along the transect with material type at the corresponding position allows the average pixel intensity of the sediment, pore water and organic matter to be estimated, and a specific linear relationship calculated for each region. The densities of sediment particles and water were measured in advance and the pixel intensities of all sediment particles, organic matter and pore water were measured from the raw greyscale images. Based on the densities and intensities of sediment particles and pore water, the linear relationship (intercept and the slope) between pixel intensity and density in the area was calibrated, by which the density of organic matter (biofilms) can then be calculated (Figure 2.7). Interestingly, results illustrate that the value of organic matter density in the aggregate is very variable. For example, the organic matter density in the three ROI lines varies from 1155 to 1503 kg/m^3. This is not surprising, given that the polymers that form microbial matrices are themselves very variable depending not only on their source and age, but also on local physico-chemical conditions as hydration state, molecular bonding, and composition. The microbial matrices within the aggregate may form initially from microbe clusters. As the growth of these residential microorganisms and the amount of EPS they secrete increases, more particles and microbes are adhered, forming a microbial sediment patch of higher maturity.

To estimate the density of an aggregate rather than the detailed aggregate development

mechanisms, the densities of organic matter along each ROI line were then averaged and the heterogeneous characteristics were simplified. As a result, each material component has one averaged density value, ρ_{ci}. Accordingly, the average density of aggregates can be calculated as:

$$\rho = (\sum_{i=1}^{n} \rho_{ci} v_{ci}) / (\sum_{i=1}^{n} v_{ci}) \qquad \text{Eq. 2.2}$$

where ρ is aggregate density, ρ_{ci} and v_{ci} are the averaged density and volume of hydrated organic matter, sediment particles and pore water, respectively. The volume of each target component is calculated by counting the voxel number included in this component, each voxel volume is 0.777^3 μm^3.

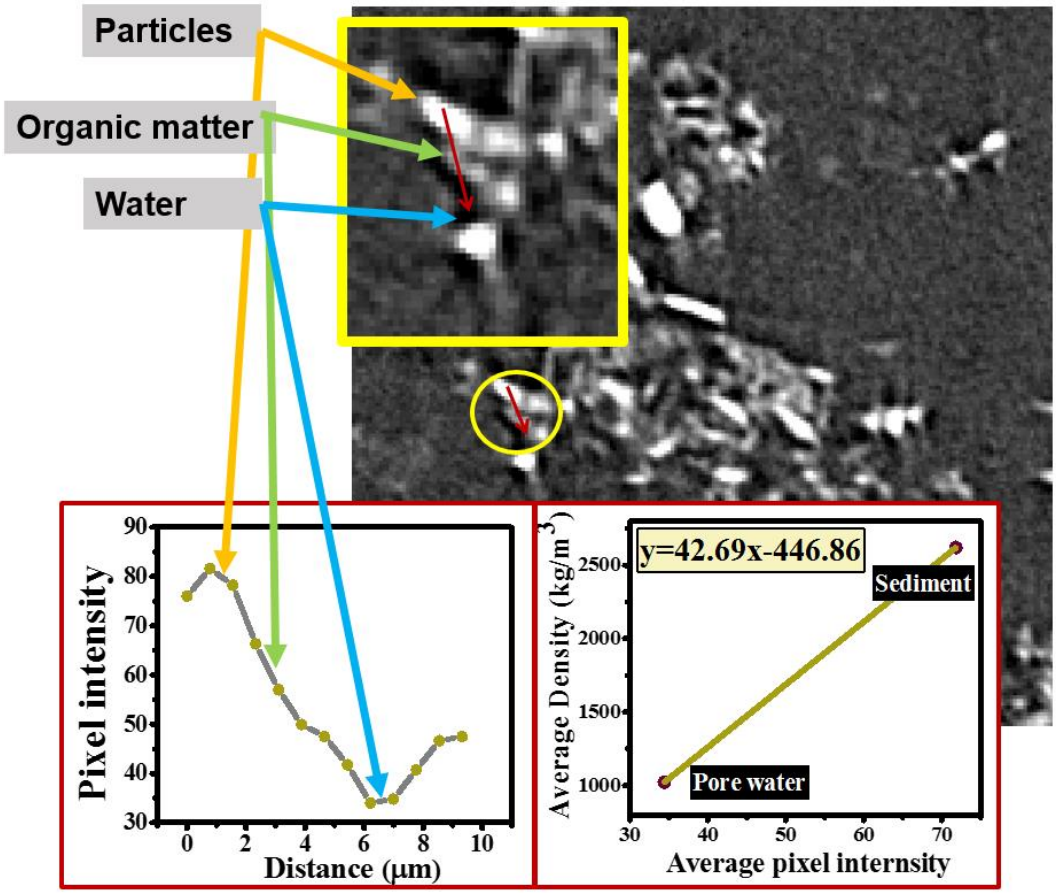

Figure 2.7 Example ROI which containing all three different materials on the left-hand side. Each material shows a specific range of grey values: Inorganic sediment particles (orange arrows)

represent the highest grey value range, while the intensity of pore water (blue arrows) shows a slightly lower intensity than organic matter (green arrows). The calibration of the linear relationship between intensity and density is illustrated in this selected ROI line.

2.1.7 Applications to sand BSA

The above methodology applies to the laboratory-created BSA comprised of fine-grained particles, which generally have a diameter less than 10 microns. However, natural BSA can also contain much coarser sediment particles, such as sand grains. To ensure the applicability of the method to a broader type of BSA that may contain coarse sand grains, the application of this wet staining method and micro-CT technique are adjusted.

To sample the seabed sediments, a 50 ml plastic syringe corer was initially used to sample sediments. After this, the syringe sediment core was placed in a sealed glass vessel which was topped up with absolute alcohol and Alcian Blue dye solution (Sigma; 0.4 wt%/wt at pH 2.5). After an overnight treatment, the sediments of the top ~ 3 cm in the syringe core was sectioned using a steel knife. Before each sectioning, the knife was carefully washed and rinsed using distilled water and ethanol in succession. The sectioned layer of the sediments were subsampled using borosilicate Nuclear Magnetic Resonance (NMR) tubes (Norell™ Standard Series™; outer diameter 4.9mm, inner diameter 4.2 mm, depth 20 mm), by inserting the tube into the sectioned sediment layer. After the sub-sampling, wet staining liquid (absolute alcohol and Alcian Blue dye solution) was gently added into the tube to ensure the sampled BSA in hydrated states and the NMR tubes were then sealed using NMR caps and sealing parafilm, in order to avoid potential evaporation and desiccation during the scanning process.

Sand grains in BSA can exceed the diameter of the clay minerals to a magnitude of two orders, which thus needs considerably larger field of view. The Zeiss 160kVp Versa 510 X-ray microscope can no longer be applied in this case. Instead, the modified 225 kVp Nikon HMX ST, located at the μ-VIS X-ray Imaging Centre, University of

Southampton, was applied for a larger field of view. Scanning was performed at 100 kV and 66 uA, using an exposure time of 708 ms, acquiring 1201 projection images with 4 frames averaged per projection, 1x binning and 24 dB analogue gain. The projection images were reconstructed into 3D volumetric data using no pre-filtration of the beam. In the HMX, the detector is a Perkin Elmer XRD 1621 CN14HS. Each scan took approximately 1 hour, and the resulting voxel (3D pixel) resolution was 4.5 x 4.5 x 4.5 microns. Image processing and analysis follow the same protocols as the clay BSA (section 2.1.3, 2.1.5-2.1.6).

2.2 General methodology

General methodology applied in this thesis includes three main sections: BSA incubation and creation, flume resuspension tests, and settling velocity tests. This is then followed by a summary of experimental workflow at the end of this section.

2.2.1 BSA creation and sampling

Clay BSA

Simplified, replicable laboratory-cultivated aggregates formed of algae cells, algae-produced organic matter and clay minerals were cultivated and used to ensure reproducibility. A commercially available kaolinite powder (ACROS Organics^{TM}) was fully saturated in distilled water before use and placed under vacuum to eliminate potential hydrophobic effects caused by air bubbles on particle surfaces (Mietta et al., 2009). Primary particle size distribution (PSD) was measured using a LS300 Coulter laser (Thompson et al., 2017), for later comparison with primary particle size of the created aggregates using imaging analysing. The algae, *Phaeodactylum tricornutum*, was used as a single species for aggregation (cultured in the Research Aquarium Laboratory, National Oceanography Centre, Southampton (NOCS)). The algae was cultured in artificial seawater (Sigma sea salts, salinity 35 ppt) with added nutrients (sodium metasilicate) and added sodium hypochlorite, to inhibit bacterial growth in

order to simplify the whole system. The culture solution was left illuminated for 24 h at 18℃, after which, 1.25ml sodium thiosulphate was added to neutralize the pH. After this, 100 ml kaolinite and 100 ml algal suspension was added and were gently mixed. After a 6-day incubation period, aggregates were found suspended in the water column and formed a fluff layer at the bottom of the incubation vessel. Aggregates at the surficial fluff layer were easily suspended through gentle agitation.

Fluff BSA

Fluff BSA were created in the laboratory Core Mini Flume (CMF) during a 6-day incubation period of daily resuspension and deposition. The CMF, designed by Thompson et al. (2013), is a small worktop flume based on the design of widely used annular flumes. It has two acrylic tubes. The outer diameter is 200 mm and the inner diameter is 110 mm, which leaves a 40 mm-wide working channel in which a sediment bed can be formed (Figure 2.8). Abiotic sediment substratum that is comprised of fine-grained sand sieved to the range of 125-250 microns with a d_{50}=195 microns was hand-prepared as a 6 cm depth of flat sediment seabed. It was overlaid with 15 cm depth of artificial seawater (Sigma sea salts, salinity 35ppt). The prepared clay BSA following the protocols listed above were then added into the CMF and settled overnight. During the following 6-day incubation period, daily resuspension (6 hours) and deposition (18 hours) of hydrodynamic cycles are applied at a constant applied shear stress that exceeds the resuspension threshold of the sand grains (τ_b= 1.0 Pa). The CMFs were kept illuminated for 24 h at 18 ℃ during the 6-day incubation. To keep the microbes alive, the CMFs were also kept oxygenated through air stones for 24 hrs per day during the incubation period.

Mat BSA

Mat BSA were created in the CMF during a 6-day incubation period, with the addition of the same clay BSA, using the same sand grains as substratum, experimental apparatus and being cultivated under the same 6-day cultivation period as fluff BSA

(salinity 35ppt, temperature 18 ℃, illuminated and oxygenated for 24 hrs per day). Different hydrodynamic conditions were however applied during the same 6-day cultivation period. These BSA, instead of being daily suspended, were grown under quiescent flow conditions with no hydrodynamic disturbances (i.e. no bed shear stresses were applied to suspend the seabed materials).

Field sampled BSA

Field sediment samples with the presence of microbes and organic matter used for experiments were taken at the end of October in 2019, from two close sampling sites of tidal flats at the Tay estuary, Scotland (56º26'42" N, 2º52'11" W is the location for site 1 while the location recording for site 2 is lost). The Tay estuary is a macrotidal, 50-km long coastal embayment eastern coast of Scotland, UK. Sediments from site 1 are silty while the other site is sandy. At each site, the top ~10mm sediments were sampled to optimally contain the microphytobenthos and their organic matter products. The collected samples were preserved in plastic boxes with ice bags under dark conditions. The transport duration was ~12-hour and the samples were kept in the fridge at 4 ºC under dark conditions for one week at National Oceanography Centre, Southampton, UK. These field sediments from each site were mixed to homogenize the sediment and organic matter and remoulded into a plane bed surface in each of the two laboratory CMFs (Thompson et al., 2013). One CMF was for the resuspension experiment, and the other was for micro-CT coring and scanning. The field sediments were then overlaid with 15 cm depth of artificial seawater (Sigma sea salts, salinity 35ppt) and settled overnight before experiments. The CMFs were kept at 18 ℃, illuminated and oxygenated, to create consistent environmental conditions with the laboratory incubation experiments.

According to Folk's sediment classification system (Folk, 1954), field BSA taken from site 1 belong to sandy silt sediments (sand fraction of 43.3%, median particle size of sand fraction (>63 microns) =76.7 microns, median particle size of sediments =12.4

microns), thus is referenced to field silty BSA. BSA taken from site 2 comprise sandier sediments (sand fraction of 87.1%, median particle size of sand fraction =169.5 microns, median particle size of sediments =27.9 microns) and is referenced to field sandy BSA.

2.2.2 Flume resuspension experiments

Resuspension experiments were performed in laboratory CMF (Thompson et al., 2013) (Figure 2.8), under illuminated conditions at 18 ºC, with the salinity of 35 ppt. An Optical backscatter sensor (OBS) is placed 4cm above the bed at the same height as a suspension sampling port, and a Nortek Vectrino Acoustic Doppler Velocimeter (ADV) is used to measure flow velocity at 6 cm above the sediments. Steady currents are generated by 4 equidistant motor-controlled paddles, the speed of which can be computer programmed (Thompson et al., 2013). In the resuspension tests, 19 stepwise increases in motor speed were programmed. As a result, 19 stepped current velocities were applied to suspend the microbial sediments after the incubation periods for each type of BSA. Time steps of 10-minute were used and the experimental procedure followed the well-established and widely-applied annular flume experiment protocols (Amos et al., 1992; Chen, et al., 2017; Thompson et al., 2013, 2017).

OBS data were calibrated against the measured concentration of suspended materials (g/L) sampled from the same height as the OBS every 2-3 velocity steps (Thompson et al., 2013). Suspension samples for OBS calibration were taken using 50 ml plastic syringe and filtered by 47 mm GF/F Whatman filter. The filters were than dried in 60 ºC oven and weighed to calibrate the OBS data. Suspension samples for settling velocity tests were taken during the last 5 minutes of a resuspension step, to allow a stable state for the aggregates to be developed. The suspension samples were taken by opening the valve of the rubber tube that is connected to the sampling port on CMF. A syringe was not used to sample the suspension for settling velocity test. This was to avoid the aggregate structures being broken by the pressure effects with the usage of syringes. The suspension was collected using a 50 ml centrifuge tube and stored in the fridge at

4 ºC under dark conditions. Time-series of suspension concentration profile during the entire resuspension processes can then be obtained. Bed shear stress was estimated using the Turbulent kinetic energy method (TKE) (Thompson et al., 2004; Thompson et al., 2003). TKE measures the intensity of turbulent motions within a shearing fluid and calculates the turbulent kinetic energy density, *E*, from the spectrum of a velocity time series: $E = 1/2\,\rho_w(\overline{u_t^2} + \overline{v_t^2} + \overline{w_t^2})$ (in which, ρ_w is water density, u_t, v_t and w_t are flow velocity fluctuations in stream-wise, cross-stream and vertical directions) (Thompson et al., 2004; Yao et al., 2018). The mean bed shear stress can be calculated according to $\overline{\tau_b} = 0.19E$ (Soulsby, 1997). The resuspension threshold was then derived by plotting the applied bed shear stresses estimated using the above TKE method against the suspended sediment concentration (Amos, et al., 2003).

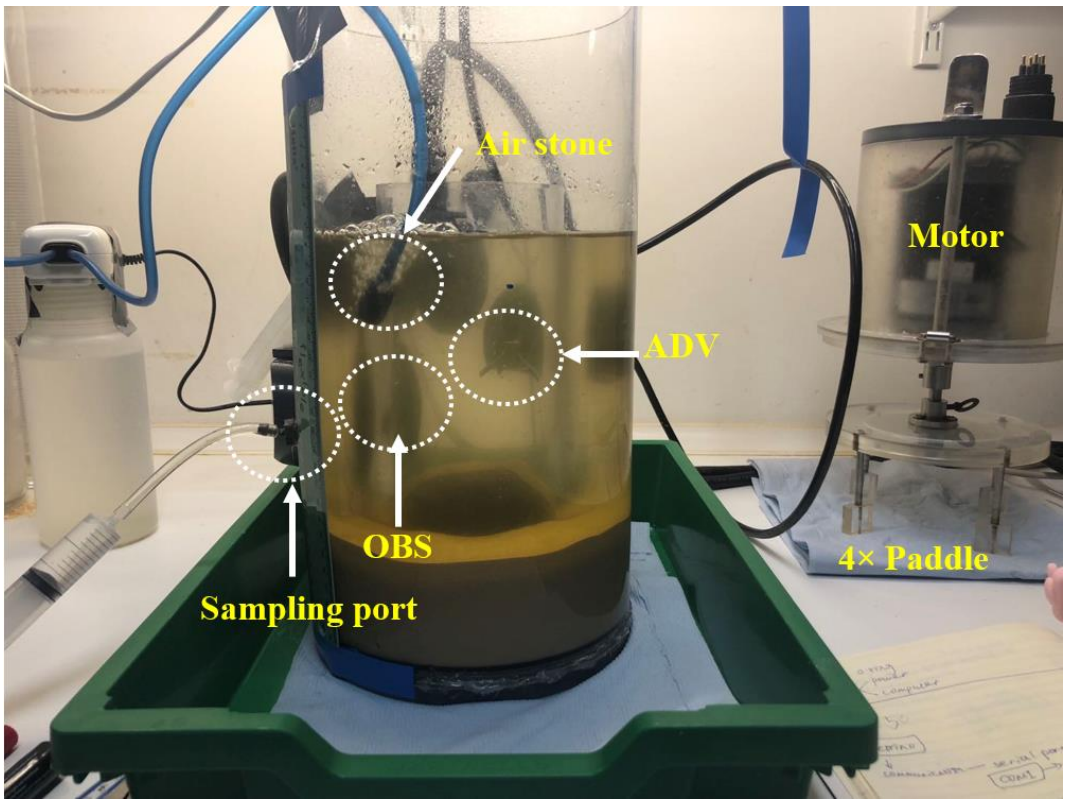

Figure 2.8 The laboratory CMF with the prepared microbial sediments sitting inside.

2.2.3 Settling velocity tests

Settling velocity tests were conducted in two types of apparatus. For slowly-settling materials, such as the aggregates made of fined-grained sediment particles, a camera-video system was used (Figure 2.9 (a)). The camera-video camera system comprises a 19 cm high x 10 cm square Perspex settling column, magnified camera lens, charge-coupled device (CCD) camera and particle tracking image processing system, and was developed by A. Manning and K. Dyer (Dyer and Manning, 1999; Manning et al., 2007; Manning and Dyer, 2002). This camera video system has been widely applied to tracking the settling velocity of slowly-settled particles, such as mud flocs, both in situ and in the laboratory. However, the coarser sand grains used in the work were found to settle quickly and this was difficult to be precisely captured in the camera system. This is mainly due to the limited imaging area and the image capture interval. Therefore, for the fast-settling particles, the 177 cm high laboratory settling column equipped with a mass balance tracking system, a dedicated system for recording the settling velocities and particle sizes of fast-settling particles, e.g. sand grains (Villatoro, 2010), was used (Figure 2.9 (b)).

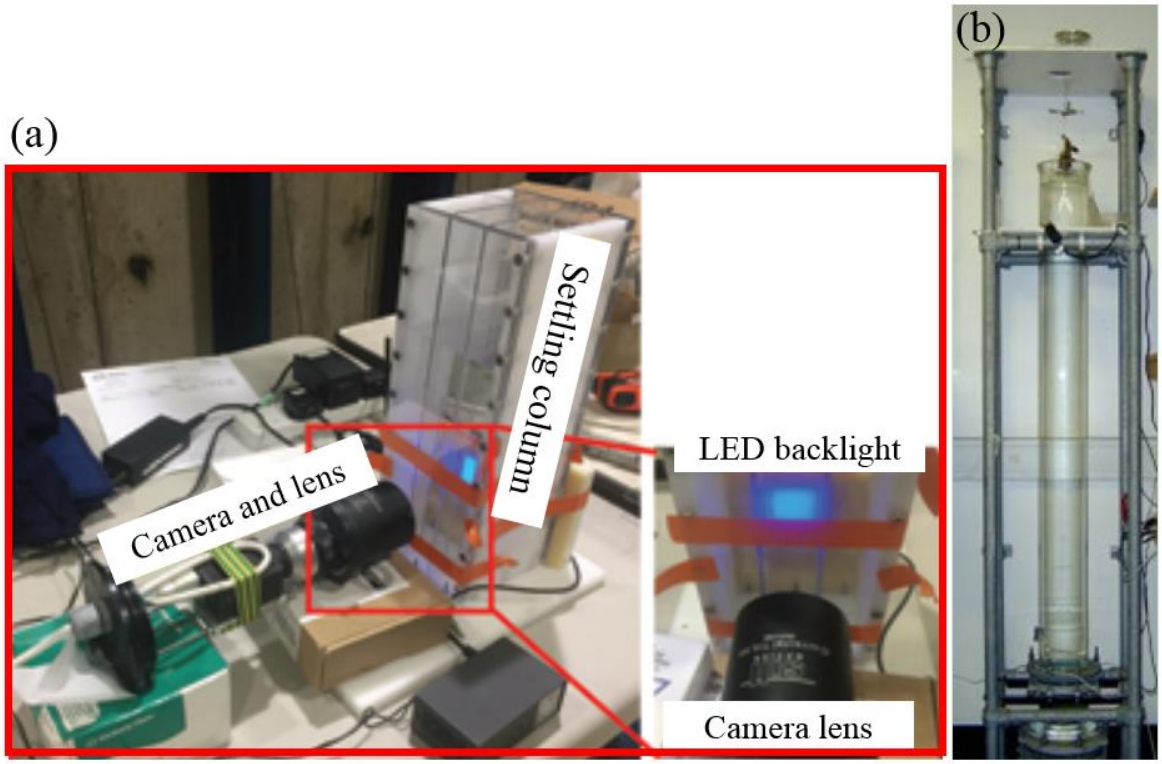

Figure 2.9 (a) Images illustrating the main components of the camera-video system (image sources from Ye et al., 2018), (b) image of the settling column for measuring the mass settling velocities of fast-settling particles (image sources from Villatoro, 2010).

2.2.4 Summary of experimental workflow

Micro-CT experiments, flume resuspension experiments and settling velocity tests were conducted for both laboratory-created and field-sampled BSA. The experimental procedures are schematically set out in Figure 2.10.

For each type of BSA, during the BSA preparation procedure, two identical flumes from the same sediment and biological sources were prepared. One flume is prepared for the subsequent resuspension tests to measure the critical shear stress for sediment resuspension (Flume 1, Figure 2.10). The other flume is prepared to provide identical but non-destructive sediments (as no resuspension tests were taken, the damage of BSA structures were avoided) for sediment coring, specimen preparation and micro-CT scan experiments (Flume 2, Figure 2.10). Suspended BSA samples were taken during the resuspension tests of flume 1 for the subsequent OBS calibration and settling velocity

tests. In the meantime, the identical BSA prepared in flume 2 were collected using syringe sediment cores, sectioned, sub-cored and wet-stained following the protocols developed in section 2.1. The obtained BSA specimens then underwent micro-CT experiments using the protocols listed in section 2.1.

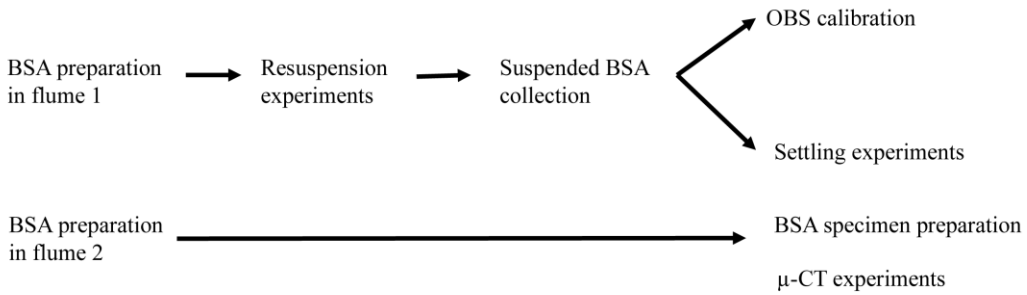

Figure 2.10 Schematic illustrations of the experimental workflows of the work in this thesis.

Chapter 3 Microbial influences on the resuspension behaviours of sediment transport

3.1 Introduction

The dynamic nature of coastal oceans creates sediment fluxes, in response to the variations of hydrodynamic forces, and is largely dependent on the stability of coastal sediments. These sediment fluxes in turn influence a variety of coastal processes at a range of scales, including the evolution of coastal wetlands (D'Alpaos et al., 2005; Mariotti and Fagherazzi, 2010, 2013), the fate of coastal habitats (Duarte et al., 2013; Joensuu et al., 2018), variations of sedimentary carbon sequestration (Alongi, 2012; Fourqurean et al., 2012; Macreadie et al., 2019), and coastal environmental stability (Milligan and Law, 2013). Most aquatic sediments are to some extent microbiologically-mediated (Flemming, 2019; Probandt et al., 2018). Due to the ubiquitous presence of microorganisms (bacteria, algae, diatoms, fungi, and archaea) and the copious amount of organic matter (e.g. extracellular polymeric substances, EPS) secreted by these microorganisms, aggregation among sediment particles, microbial cells and organic matter promotes the establishment of various matrices of BSA extensively present as part of upper aggregated seafloor sediment layers (Malarkey et al., 2015). The establishment of BSA alters the physical transport of sediments, and an improved precision of sediment budgets and transport rates requires that microbial mediations of sediment stability are suitably characterised (Fang et al., 2020).

Previous studies have acknowledged that the development of BSA can suppress sediment resuspension (de Boer, 1981; Paterson, 1989) However, some recent studies demonstrated that BSA at early development stages (within several hours) can accelerate the motion of sediment particles (De Brouwer et al., 2005; Mariotti et al., 2014). Little is known of the mechanisms leading to this contradictory phenomenon. Whether microbial mediation of sediment stability can always be summarised as biostabilization is therefore questionable.

Biostabilizing BSA were observed to present as a mat-like matrix, where sediment particles are tightly adhered, embedded and covered to resist hydrodynamic resuspension (Malarkey et al., 2015; Vignaga et al., 2013). However, the production of organic matter by microorganisms is a progressive process, and the establishment of a mat matrix takes several days (Chen et al., 2019; Chen, et al., 2017). Quiescent or moderate energy periods of this duration are rare in many coastal and oceanic locations in nature. The dynamic nature of coastal environments dictates that BSA at intermediate stages of development, such as those formed under frequent resuspension-deposition cycles, and developed within several hours, may be of more relevance. Whether the BSA at such intermediate stages of development also enhance sediment stability through the same modes as the mat BSA matrix, or destabilizes sediments, remains unclear.

This present work was therefore designed to determine:

Do BSA always enhance sediment stability, or do they have a range of effects, including destabilization?

3.2 Materials and Methods

To investigate the above question, we conducted a series of laboratory flume and micro-CT experiments. Instead of only investigating mat BSA grown under quiescent or moderate flow conditions, two types of BSA developed in different states subject to distinct flow conditions during the same growth period were studied.

(i) BSA grown as a mat-like sediment-water interface, where the microbial sediment interactions were allowed to occur over a 6-day period in quiescent flow conditions with no hydrodynamic disturbance.

(ii) BSA grown as a fluffy sediment-water interface, where the microbial sediment interactions developed over the same 6-day period but were subject to daily resuspension-deposition cycles with 6-hours of hydrodynamic erosion each day.

Experimental conditions for (i) were selected to allow the mat matrices of biofilm to develop and to test the resuspension and structural properties of the mat. Experimental conditions for (ii) were selected to create the bio-sediment associations established under frequent disturbances, and test the resuspension and structural behaviours.

The experimental workflow comprises three main parts:

(1) BSA preparation, which includes the creation of both BSA (i) and (ii) (For detailed BSA creation protocols see section 2.2.1);

(2) resuspension tests for each type of BSA, through application of 19 stepwise increasing bed shear stresses to the microbial sediments using the CMF (For detailed flume erosion protocols see section 2.2.2);

(3) the preparation of BSA specimens for subsequent micro-CT scans, following the protocols of the newly developed imaging techniques detailed in section 2.1.

3.3 Results

3.3.1 3D imaging: mat and fluff BSA

Micro-CT scans show two distinct BSA matrices from the mat-like sediment water interface (the mat, Figure 3.1 (a)) and the fluff sediment-water interface (the fluff, Figure 3.1 (b)). BSA from the mat were developed under no hydrodynamic disturbances, which allows the development of copious amount of organic matter, aggregated into multilayer structures, and adhering large amounts of sand grains in a mat matrix (referred to as mat BSA, Figure 3.1 (a), (c), (d)). Sand grains were tightly covered, adhered and embedded in the organic mat, which minimizes the exposure of sand grains to flow forces. In contrast, 3D imaging illustrates a distinctly different appearance for the BSA grown from the fluff, where the BSA are loosely-structured, with scattered microbial patches attaching to relatively few sand grains, referred to as fluff BSA herein (Figure 3.1 (e), (f)). In general, the organic matter appears to be more fully developed in mat BSA compared to the fluff BSA. This is because the growth of microbial life and

the production of organic matter during the development processes of mat BSA was not subject to hydrodynamic disturbances and were allowed to be more fully developed. As a result, the mat sediments contain the relatively well-developed organic matter with a higher content of organic matter (organic fraction = 0.65 - 0.74), 2-6 times higher than that of the fluff BSA (organic fraction = 0.12 - 0.37). This in turn enables the adherence of an order of magnitude larger number of sand grains into larger aggregates, and a more well packed internal structure to be developed.

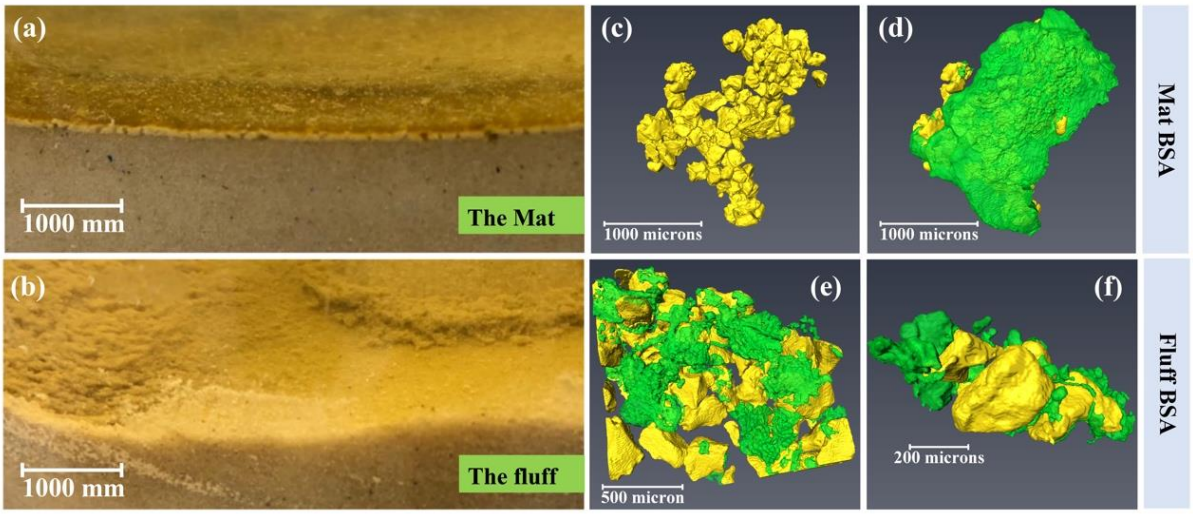

Figure 3.1 Distinct appearances of the sediment-water interfaces are established and illustrated using images taken through the wall of the flumes during the experiments: the mat (a) the fluff (b). Micro-CT scans show distinct matrices of BSA across the mat and the fluff, mat BSA ((c), (d)), and fluff BSA ((e), (f)). In (c) –(f), inorganic sediment particles are yellow, while green is assigned to the organic matter.

3.3.2 Resuspension thresholds: stability enhancement vs. destabilization

Resuspension tests were conducted on both mat and fluff BSA, and compared against abiotic control sediments, to examine the influences of BSA presence on sediment stability. The threshold for suspending abiotic sand grains into the water column was τ_{crit} = 0.84 Pa (Figure 3.2(a)).

The theoretical threshold is calculated using the following empirical equations proposed in previous studies with the usage of the same flume apparatus (Roe, 2007; Villatoro, 2010):

$$\theta_{crit} = \frac{\tau_{crit}}{(\rho_s - \rho_w) g d_{50}} = 0.043 D_*^{1.152}, \quad D_* < 10 \qquad \text{Eq. 3.1}$$

$$D_* = [\frac{(\rho_s / \rho_w - 1) g}{\upsilon^2}]^{1/3} d_{50}$$

In which the dimensionless critical Shields parameter, θ_{crit}, is a function of non-dimensional grain diameter, D_*. τ_{crit} is the critical bed shear stress for initiating the sediment resuspension, ρ_s and ρ_w are densities of sediment and water respectively, $\rho_s / \rho_w - 1 = 1.65$, υ is kinematic viscosity of water. The calculated threshold of the applied shear stress for suspending the bare sand grains (d_{50}=195 microns, D_*= 4.93) is 0.85 Pa. Mat and fluff BSA presented a two-stage resuspension process with each stage initiated at a different threshold (Figure 3.2 (b-d)). An examination of the suspended material during the first stage showed no sand grains were present, while a large proportion of organic matter were suspended (stage 1, where the dried filters taken from the suspension contained no sand grains). Suspension of sand grains occurred at the second stage (in stage 2 a considerable number of sand particles were accumulated on the filters). We therefore consider stage 1 as the removal of surface organic matter, and stage 2 as sediment entrainment. For mat BSA, only a small proportion of surface organic matter (up to 0.2g/L) was lifted into suspension in stage 1, at a bed shear stress of 0.43 Pa (Figure 3.2 (b), (d)). In contrast, 3 times more surface organic matter was suspended from the fluff, at a lower threshold of 0.31Pa (Figure 3.2 (c), (d)). In stage 2, mat BSA resuspension was initiated at 0.94 Pa, indicating BSA were retained on the bed to a higher flow intensity than bare sands (Figure 3.2 (b), (d)), while fluff BSA were suspended at the lower applied shear stress of 0.74 Pa (Figure 3.2 (c), (d)). The

mediation of resuspension is therefore quite different for fluff and mat BSA. Fluff BSA did not increase resuspension resistance as previously assumed, but instead acted as a destabilizer. Clearly, BSA matrices can act as either a stabilizer or destabilizer, depending on their constituent make-up, geometry and stage of development, and a suitable characterisation of these differing behaviours is needed before quantitative modelling can be meaningfully attempted.

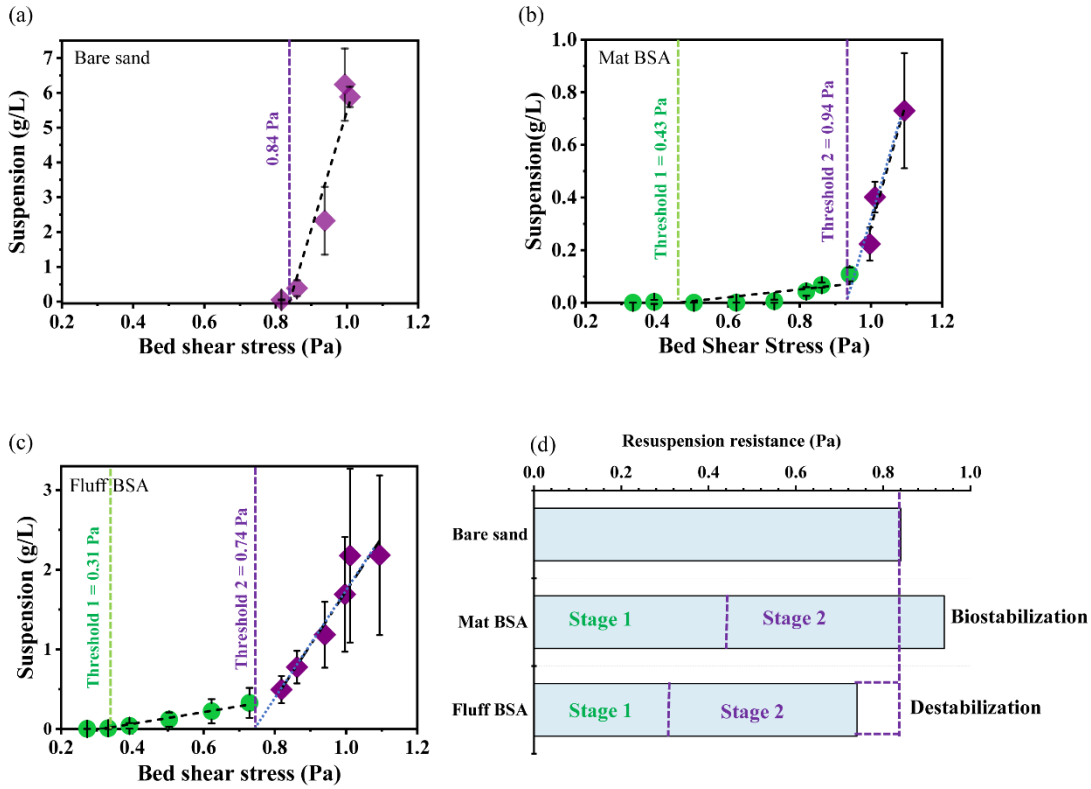

Figure 3.2 Time-series of suspension concentration (g/L) are plotted against the applied shear stress (Pa) from three cases: abiotic control sediments (a), mat BSA (b) and fluff BSA (c). Suspension thresholds of both Stage 1 and 2 for each case are compared in (d).

3.3.3 Suspension processes of fluff and mat BSA

Abiotic sand grains, mat BSA and fluff BSA present distinct resuspension processes.

Bare sand grains usually move as bed-load transport, e.g. sliding, and rolling, when the local flow-induced drag force overcome the friction resistance, referred to as initiation

of motion. With the increase of flow velocity, once the flow lift force exceeds the stabilizing forces provided by submerged gravity, the sand grains will be lifted into the water and transported as suspended-load, referred to as initiation of suspension (Amos et al., 2004; Dey, 2014; Soulsby, 1997). Microbial development in sediments mediate this process, making it more complicated.

Biostabilization

Mat BSA act to armour sediment-water interfaces, inhibiting horizontal and vertical transport (Figure3.3 (1a)). During stage 1, mat BSA allow a small proportion of surface organic matter to be removed at a moderate applied shear stress. The detached organic matter may be relatively young, randomly-developed branches of organic matter that protrude into the flow when on the bed and, therefore, experience a stronger bed shear stress than the planar areas (Flemming and Wingender, 2010). The loss of these protrusions does not eliminate the overall mat BSA stability. The armour matrix in stage 1 retains its integrity and so continues to provide effective protection to the underlying materials (Figure 3.3 (1b)). If this were not the case, the underlying sand grains should enter the water column at their threshold shear stress (in our experiment this was at an applied stress of 0.84 Pa), which did not occur. The immobilised sand grains also mean no bed-load transport. Once the applied flow shear stress exceeds the adhesion between the mat BSA and the underlying sediment bed, the local integrity of the mat matrix is lost. The torn mat BSA fragments are quickly suspended, exposing the underlying materials to the flow at a higher shear stress than the thresholds for the bare sand entrainment (Figure 3.3 (1c)), hence causing immediate resuspension of the bed sediments (Figure 3.3 (1d)). Therefore, the entrainment of mat BSA is largely determined by the adhesion with the bed sediments, or to be more precise, both the adhesion and gravity forces. This is because if the torn mat BSA have enough mass for the gravity force to resist the exerted flow-induced drag and lift forces, BSA entrainment will not occur and the torn BSA will remain on the seabed.

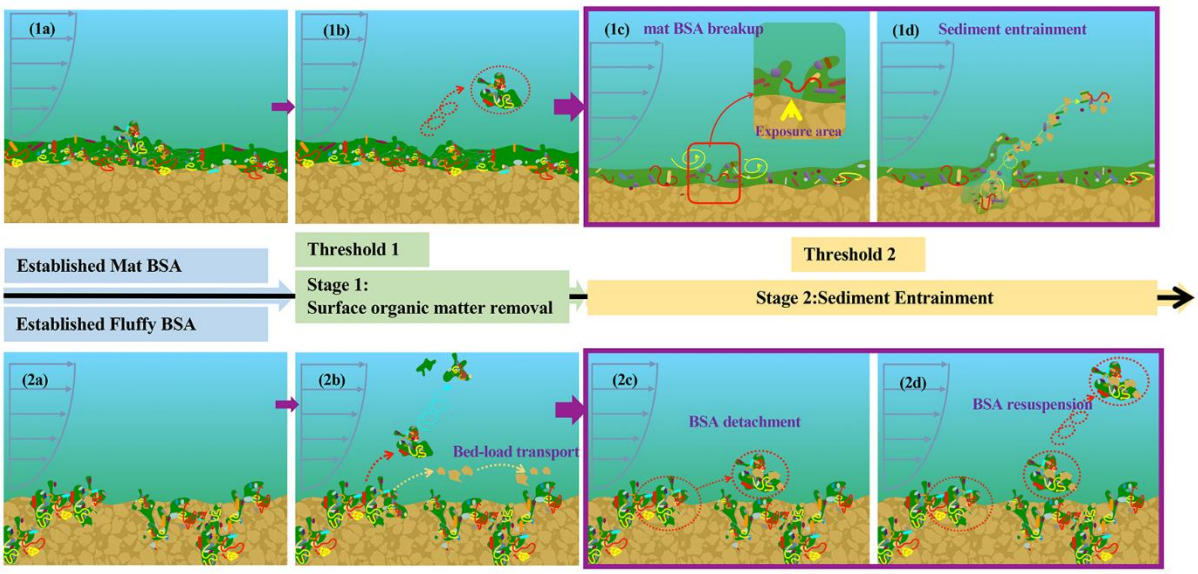

Figure 3.3 Conceptual framework for the resuspension processes of mat BSA (1a) -(1d) and fluff BSA (2a) -(2d) under a stepwise increasing shear erosion test, summarized as a two-stage process of surface organic matter removal and BSA resuspension. The purple boxes illustrate the critical moment for the mat BSA ((1c) and (1d)) and fluff BSA (2d) to be suspended. At the same moment of local breakup of mat BSA in (1c), the resuspension of mat BSA fragments occurs (1d).

Destabilisation

For fluff BSA (Figure 3.3 (2a)), surface organic matter removal occurs at a lower flow intensity (at 0.31 Pa < 0.43 Pa of mat BSA), indicating less maturity and inherent strength are developed under daily cycles of resuspension and deposition. Weaker connections with sand grains, individual organic patches not fully aggregated into BSA, or some relatively new, and hence poorly integrated organic branches may all lead to relatively easy breakup of these structures. They undergo some temporary sliding or rolling on top of the sediments and then were quickly suspended into the water (Figure 3.3 (2b)). In the meantime, some bare sand grains that have either separated during a breakup of the BSA, or were not aggregated into a BSA, may slide or roll on the bed sediments, as the local shear stress is higher than the theoretical threshold for horizontal bed-load transport of individual sand grains (0.16 Pa)(Soulsby, 1997). While organic matter introduces adhesion to sediments and should in theory stabilize sand grains, our

results show that fluff BSA entered the water column at a lower flow velocity than the threshold for the bare sand, where sediment stability is reduced. This is because the adhesion between organic matter and sand grains leads to the aggregation of the two, thereby reducing the overall density of the fluff BSA (from 2650 to the range of 1540-2270 kg/m^3), and lowering the effective stabilizing gravity force. Therefore, at a threshold below that of bare sand, fluff BSA can overcome the adhesion with the bed sediments (Figure 3.3 (2c)) and enter the water column (Figure 3.3 (2d)).

3.3.4 Application of Shields diagram

To date, multiple well-established criteria have been established to characterize the thresholds of sediments into different transport conditions. This includes the standard Shields curve for the initiation of motion of sand on the seabed (Figure 3.4 (a))(Shields, 1936). By establishing the relationships between the dimensionless Shields parameter, θ_{crit}, and the dimensionless diameter of sediment particles, D_*, the Shields diagram enables the transport thresholds and transport statuses of non-cohesive sand grains to be approximated (Buffington, 1999). After the initiation of motion, sand grains start bed-load transport, e.g. sliding and rolling on the seabed. With a continued increase of applied bed shear stresses, the motion of sand grains as suspension is initiated. Van Rijn (1984) characterized the threshold shear stresses for the initiation of suspension (solid brown lines, Figure 3.4 (a)), defined as *'at which locally turbulent bursts with sediment particles are lifted from the bed into suspension'* (Van Rijn, 1993). In contrast, Bagnold (1966) defined an upper limit threshold for suspension, where stable concentration profile of suspension develops (Bagnold, 1966; Van Rijn, 1993). In order to define more precisely in terms of Bagnold's suspension criterion for sand of small sizes ($2 < D_* < 8$) and investigate the transport mechanisms at the area where Bagnold's criterion intersects with Shields' curve, Roe, (2007) conducted a series of resuspension experiments, and proposed a revised Bagnold's suspension criterion (dashed brown lines in Figure 3.4 (a)) (Roe, 2007; M. Villatoro *et al.*, 2010). Nino et al. (2003)

conduced both experimental and analytical analysis to investigate van Rijn's suspension criterion, and they found a higher bed shear stress is needed for small particles to enter water. This is considered as a consequence of an abrupt drop in turbulent intensities within the viscous sublayer for sediment entrainment. A revised criterion for the initiation of suspension for small sand grains was thus proposed (brown dash dot line, Figure 3.4 (a)). The above four criteria intersect and establish a threshold envelope for suspension (green hatched area in Figure 3.4 (a)). In general, for values of bed shear stress greater than those show in the envelope, particles are suspended into the water column and stable suspended concentration profiles develop. For the values of bed shear stresses falling within the envelope, suspension of particles is initiated, through the lifting of local turbulent bursts, but with no stable suspended concentration profile developed. For the bed shear stresses lower than the threshold range of the envelope, particles are not suspended. If the shear stress is above Shields curve, they would be expected to travel as bedload. The entrainment processes for sediment particles and the threshold definition criteria vary among different resuspension test apparatus and measurement techniques, which may result in the development of a wide envelope.

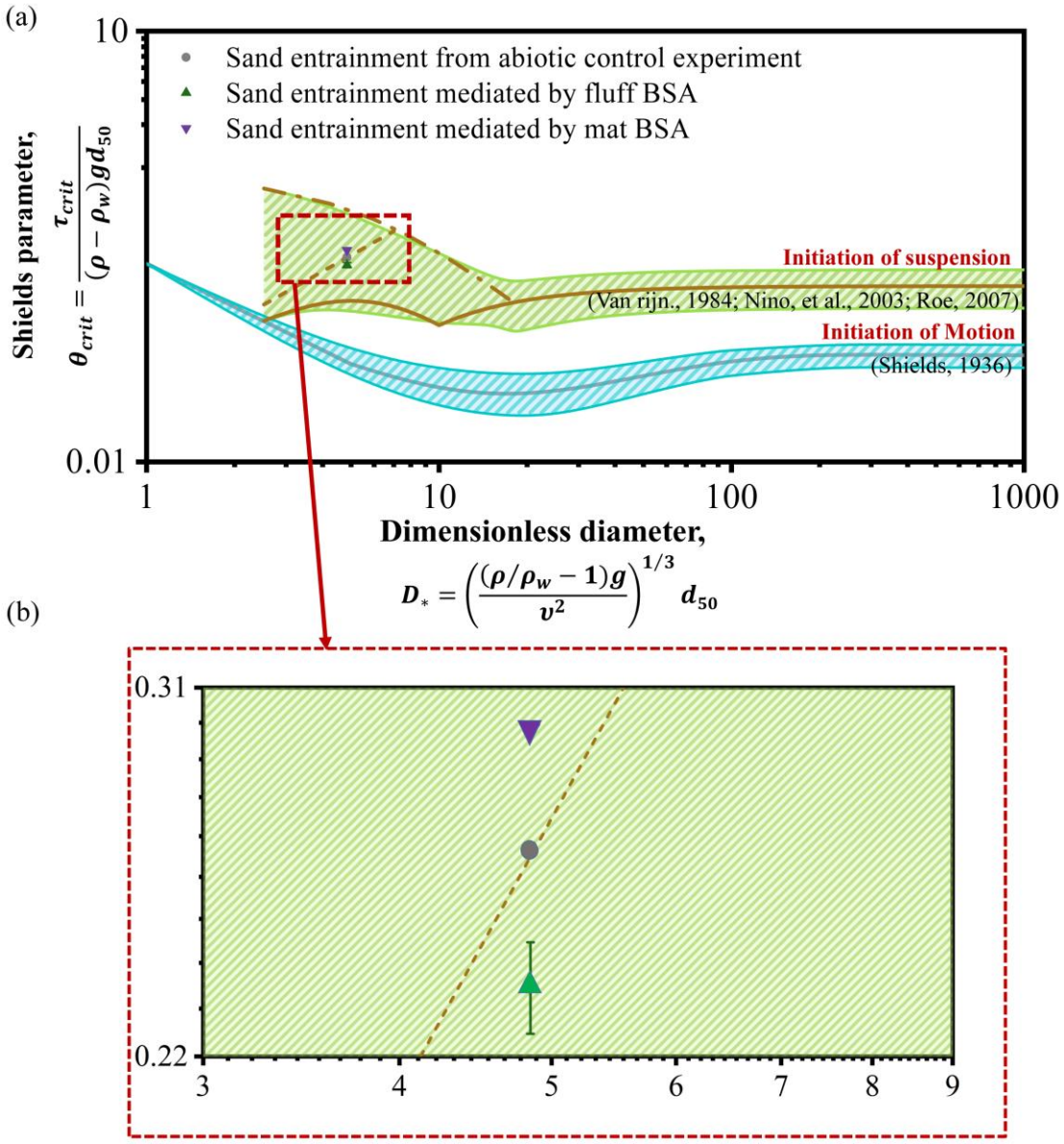

Figure 3.4 (a) Plots of Shields parameter against dimensionless diameter of sand, when sand entrainment occurs at 0.84 Pa from the abiotic control experiments, at 0.94 Pa from the sediments with microbial mat established, and at 0.74 Pa from the sediments with fluff BSA established. To obtain a clearer view, the area where the three datasets locate is magnified (b). Error bars are the standard errors of the Shields parameter.

The critical Shields parameter for bare sand agrees with the suspension criterion established by Roe (2007) (Figure 3.4 (b)), indicating the suspension of bare sand grains occur at τ_{crit} =0.84 Pa for the abiotic control experiments. The point for sand

entrainment from the mat (purple triangle, Figure 3.4 (b)) sits above the bare sand within the suspension threshold envelop, indicating a biostabilization effect on the suspension of sand grains (i.e. threshold occurs at a higher shear stress). The point for sand entrainment from the fluff sits below the bare sand (green triangle, Figure 3.4 (b)), indicating a destabilization effect on the suspension of sand grains. Whilst the differences between the critical Shields parameters for abiotic sand and the biotic sand held within fluff and mat BSA are only moderate after scaling the critical shear stress by particle gravity, the relative states of biostabilization and destabilization are clearly indicated (Figure 3.4 (b)). In the abiotic Shields diagram of Figure 3.4 (a), the critical Shields parameter at the threshold condition is regarded as a function of abiotic sediment particle size and density. As such, the mat and fluff BSA prepared from identical abiotic sediment particles should have the same resuspension threshold as the abiotic control experiments, which is not the case. This is largely caused by the development of microbial sediment associations, which hold the sand grains within the aggregates of differentiated sizes and densities from the single abiotic sand grains. The abiotic Shields diagram in Figure 4.3 (a) only provides an approximate indication of such microbial mediations. Hence, a more robust interpretation of the Shields parameter for microbial mediated sediments likely requires more explicit account of the changes in size, density, porosity and adhesion due to microbial mediation.

3.4 Discussion

Natural bio-sediment combinations are extremely complex, and present large diversity (e.g. due to diversity in microbe species) (Watermann et al., 1999). In this chapter, the microbial mediations from a single diatom species, *Phaeodactylum tricornutum,* were investigated. The behaviours of the mat BSA established by this diatom species agree with the generally-reported biostabilization effects from previous studies of both laboratory and field experiments. Over the 6-day incubation, the mat BSA were found to increase the sediment resuspension threshold by ~ 10%. This value is similar to the results from laboratory incubations using other single diatom species (Chen, et al.,

2017), but generally lower than that for mixed microbial species, and those using field sediments that have microorganisms already developed within sediment matrices (Lubarsky et al., 2010; Lundkvist et al., 2007). An increasing body of recent studies have found mixed diatoms and bacteria can enhance sediment stability to a larger extent than that of single microbial species, possibly due to the production of proteins and/or nutrient cycling between diatoms and bacteria. Chen et al. (2019) found, after disturbances/reworking, sediments that have microbial mat previously established could regain their stabilities much quicker than the bare sediments. Over the same incubation period, the regained stabilities can be higher than that before disturbances. As such, laboratory experiments incubating single diatom species within bare sediments might have limited representation for the microbial processes in natural environments. However, as a very preliminary exploration to reveal the effects of bio-destabilization, variable-control experiments, such as using single microbial species, are necessary, as they can help to understand whether the bio-destabilization is an artefact of species competition, and/or diatom-bacteria interactions. There is no doubt that testing the representability of the bio-destabilization and considering the effects of a range of environmental conditions in natural environments are important. There is thus a need for future studies to consider the extent to which the bio-destabilization is affected in natural environments when a large variety of environmental factors are accounted for.

A reduced sediment stability has been observed previously in fine-grained, non-cohesive substratum after the interactions of diverse microbial species (bacteria, cyanobacteria, and benthic diatoms), but there has been no evidence of similar bio-destabilization in muddy environments. Does such a bio-destabilization effect also occur in cohesive sediments? The saltation of large, dense particles, such as shells, (which impart a physical force, usually termed as the ‘ballistic momentum flux’), on the bed, and the activities of macro-fauna, may have additional effects especially for muddy sediments (Amos et al., 1998). The stability of bio-sediments is affected by

depositional history, nutrient levels, and temperature. For example, beds that developed under quiescent and sheared conditions exhibit significant differences (Lau and Droppo, 2000). Nutrient levels can mediate biofilm structures and the bio-sediment combinations (Droppo, 2009). Temperature determines the microbe species that prevail in sediment substratum and the development state of bio-sediment associations, contributing to strong seasonal and spatial variations in microbial sediment stability. Additionally, biofilm age may alter the organic matter content, and the adhesive strength of BSA internal structures to affect BSA density and size, which in turn affects sediment stability (Stone et al., 2008). Hence the limited parameter space investigated in the experiments presented, whilst providing new insights into the role of microbial mediation, may be only a partial represention of natural environments. To explore the effects of all the relevant variables in providing relationships for modelers to better predict such natural processes, future research work in the present subject should include the results of data from field sediments.

What is the importance of ‘fluff BSA’ to transport thresholds?

This chapter shows that microbial sediment interactions can lead to the establishment of a distinctly different state from the widely-acknowledged microbial mat, referred to as fluff BSA in this work. This occurs during the development processes of microbial sediment interactions, but before a microbial mat can be established, presenting an intermediate state of microbial sediment interaction /aggregation. The microbial mediations at such intermediate states, e.g. fluff BSA, behave distinctly from the relatively well-developed microbial mat, with respect to both transport thresholds and processes.

Current understanding of microbial sediment transport appears to be limited to the biostabilization effects of microbial mats, where it tends to assign all microbial sediments an enhanced sediment stability to model the microbiologically-mediated sediment transport and related processes (Marani et al., 2007), but with little

acknowledgement of the destabilization effects presented by the intermediate mediations. However, observations show a microbial mat from the winter sediments with little active microbiology can take several months to establish (De Brouwer et al., 2005). Overlooking microbial mediation at intermediate states, e.g. regarding destabilized sediments as biostabilized sediments, for such a long period may lead to considerable misunderstandings of natural processes. One significant example is the evolution of tidal flats. According to the conceptual model developed by Fagherazzi et al. (2006), there are two equilibrium states indicated, where the rates of erosion and deposition are equal (Fagherazzi et al., 2006) (Figure 3.5 (1)). For elevations between these two states, the erosion rate is higher than the deposition rate, tidal flats deepen and develop towards the stable equilibrium point. Elevations that are too shallow (to the left of the plot) are unstable and accrete to become emergent saltmarsh. Whereas elevations that are too deep (to the right of the plot) also accrete but to the stable tidal flat equilibrium point (Fagherazzi et al., 2006).

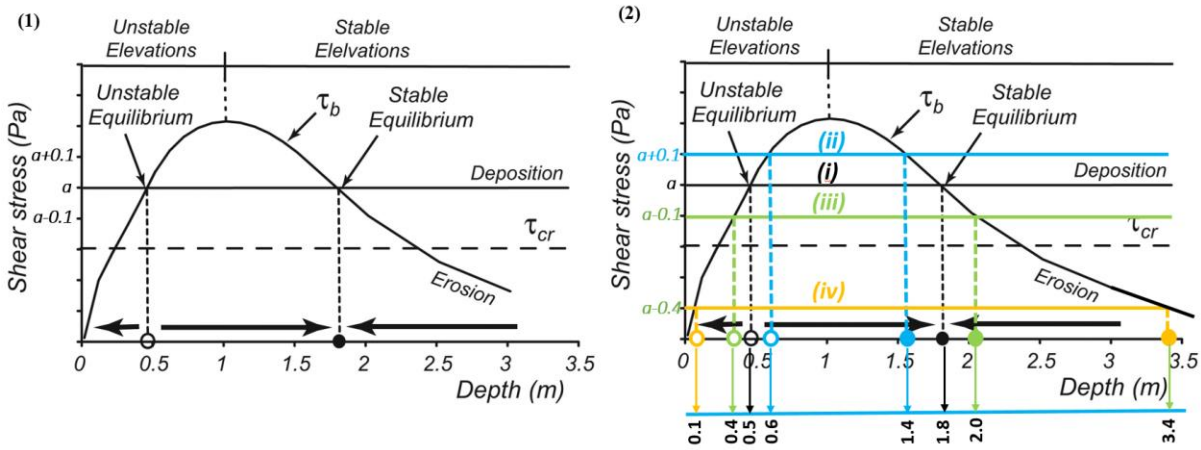

Figure 3.5 (1) Conceptual model developed by Fagherazzi et al. (Figure 4A)(Fagherazzi et al., 2006), which shows the bed shear stress distribution with bed elevation. The intersections between the bed shear stress curve and the coupling effects of deposition and resuspension, determine the possible equilibrium states of a tidal flat. In (2), black lines are considered as biotic cases, while blue, green and yellow dashed lines are added by this work, to schematically illustrate variations of the equilibrium state caused by the presence of microbial life and their organic products. Blue dashed

lines show the mediations of biostabilization with an increased bed shear stress by 10%, while green and yellow dashed lines show the variations of microbiologically-destabilised sediments, with the resuspension resistance being decreased by 10% and 40%, respectively (these values being indicative of the difference between fluff and matt BSA based on the reported laboratory and field results).

Such variations of bed elevation are senstive to microbial mediations of sediment stability. For example, a 10% increase in sediment stability, case (ii), (blue dashed lines in Figure 3.5 (2)), causes the range of water depths over which the bed deepens to narrow by ~ 40%. Compared to the abiotic case (i), (black lines in Figure 3.5 (2)), the bed elevations become easier to accrete, either towards marshes or stable tidal flats.

If the tidal flats are bio-destabilized by 10%, as in case (iii), (green dashed lines in Figure 3.5 (2)), bed elevations tend to have a reduced chance of accretion, as the likely range of water depths for bed deepening is expanded by ~30%. The larger the bio-destabilization the greater the effect. If the stability is reduced by 40%, the tidal flats will be deepened in most cases (case (iv), yellow dashed line). Clearly, the mediations of bio-stabilization and destabilization on the evolutionary trend of tidal flats are considerably different. Hence, both effects need to be considered. It must be noted that Figure 3.5 can only be regarded as an illustrative comparison to show the potential effects of biofilms and BSA on tidal flat morphology. The exact degrees of changes in bed elevations in the presence of biofilms/BSA need to be tested in the field, through accounting for a variety of environment conditions., which is beyond the scope of current work.

Our findings of the microbial mediations at intermediate states also leads to a better understanding of some poorly understood phenomena. For example, *in situ* observations by De Brouwer et al. (2005) show that, before the establishment of a mature mat, associated with the increase in chlorophyll *a*, there is a notable reduction in sediment stability. Recent studies by Hope et al. (2020) in the Dee Estuary also found

that microbial biomass and organic matter production played a negative role in the stability of sandy sediments in a very energetic system when subject to frequent processes of hydrodynamic reworking. This is contradictory to the generally-expected positive relationships between sediment stability and biological parameters of microbial biomass and EPS production, but can be explained by the destabilization effects of intermediate state BSA. Under the conditions of frequent disturbances (by rainfall, hydrodynamics, and biological activities), the well-developed mat matrices of biofilm cannot be established but BSA at intermediate states, such as the fluff BSA created and observed in this work, might form and present as a fluff layer across the sediment-water interfaces (Hope et al., 2020; Orvain et al., 2014). The fluff BSA from the fluff layer follow different ways of mediating sediment stabilities from the mat BSA, leading to a reduction of sediment stability. The microbial mediations at such intermediate states before a microbial mat is formed should not be neglected in understanding sediment transport and sediment-transport related processes in the presence of microbial development and bio-sediment association.

Chapter 4 Microbial influences on the deposition behaviours of sediment transport

4.1 Introduction

Suspended particulate matter (SPM), either from the suspension of sediments or the advection from neighbouring ecosystems, is commonly mediated by the extensive presence of microorganisms and their produced organic matter (Maggi, 2013; Maggi and Tang, 2015). SPM usually transports in the form of aggregates due to the complex interactions among the living cells, organic matter and inorganic particles, such as mineral sediment particles and contaminants (Droppo, 2001). The vertical transport and the settling rate of SPM determines the vertical fluxes of both the inorganic and organic matter, which plays an important role in a range of earth processes (Kwon et al., 2009; Voulgaris and Meyers, 2004), including the evolution trend of coastal habitats, the global biogeochemical cycling and air-sea CO_2 balance. As organic matter in the oceans usually transport as aggregates, an adequate understanding of the depositional behaviours of the aggregates serve an important role in budgeting the vertical fluxes of organic matter, and better understanding the variations of atmospheric carbon dioxide.

With the secretion of abundant organic substances, e.g. EPS, microorganisms, attaching to sediment particles, growing microbial patches on the sediment particle interfaces, coating the particles and bridging neighbouring particles into aggregates. Such processes shape the roughness of particle morphologies (Liss et al., 1996; Zhao, et al., 2011), alter internal pore structures (Chu and Lee, 2004), and affect internal pore water pathways (Perujo et al., 2017). In turn, the transport dynamics are affected. For example, microbial colonization and the formation of microbial patches coatings and bridges could increase the surface roughness of particles, which increase the drag exerted on the settling particles leading the settling velocities to be reduced (Andalib, et al., 2010; Shang et al., 2014). The changes of porosity due to microbial colonization and aggregation also mediate the internal flow permeation, leading to the reduction of drag

and increase of settling velocities(Masliyah and Polikar, 1980; Li and Yuan, 2002; Mu, et al., 2008). Soft surfaces due to the microbial colonization and coatings may behave largely different from the solid particles with rigid surfaces, such as causing deformation, which can also lead to the mediations of drag and settling velocity (Greene et al., 1993; Saravanan and Sreekrishnan, 2005).

Recent efforts have sought to relate the transport dynamics of BSA with their compositional features (Armstrong et al., 2009; Maggi, 2013; Maggi and Tang, 2015; Passow et al., 2014; Tang, 2017.). Fractal dimension has been shown to be an effective indicator to quantify the internal structure complexity and heterogeneity (Droppo, 2001; Maggi and Tang, 2015). BSA taken from upper/mid- water (e.g. pelagic) depths show distinct patterns from those in the benthic nepheloid layer, in terms of both textual and compositional features (Ransom et al., 1998). Aggregates from pelagic waters appear to be more loosely-connected and more rich in organic matter, while the aggregates close to seabed have more packed structures and comprise more inorganic sediment particles (Ransom et al., 1998). However, recent studies found some non-linearity of fractal dimension with the changes of organic fraction (Maggi and Tang, 2015). In addition to architecture, Passow et al.(2014) found that the settling velocities are largely correlated with the content and compositions of clay minerals. High illite content tends to form aggregates of small sizes and slow settling velocities (Passow et al., 2014). Similarly, strong quantitative relationships between organic matter fluxes and the content of minerals are proposed (Armstrong et al., 2002, 2009). However, recent quantitative work shows that the average settling velocities of aggregates are nearly invariant against the changes of componential fractions (with the organic matter fraction in the analysed aggregates changing in the range of 0%-100%) (Maggi and Tang, 2015).The above work clearly shows the microbial sediment interactions and the subsequent influences on architectures and settling velocities of BSA are complex and heterogeneous. Whilst a quantitative map has been recently established to approximate the architecture and the settling velocities of BSA (Maggi and Tang, 2015), the

applicability is restricted to slow-settling aggregates of fine particles (e.g. clay and silts). The aggregates that have sand grains attached, which have been found in both high-and low-energetic tidal environments (Virolle, et al., 2019; Duteil et al., 2020), may not apply.

This chapter aims to study the architecture, settling velocity and drag of both slow-settling and fast-settling aggregates though conducting experiments under laboratory-controlled conditions, to pursue a clearer understanding of the microbial sediment interactions and the influences on BSA deposition.

4.2 Materials and Methods

4.2.1 Experiments

To achieve this investigation objective, two types of suspended material, sampled in the resuspension stage 1 (surface organic matter removal) and 2 (sediment entrainment) from the fluff sediments (for the description of stage 1 and stage 2 see Chapter 3), are tested and analysed. To enable the aggregate development at a steady state under the effects of shear stresses, the BSA were sampled during the 6-10 minutes after the shear stresses were applied.

The BSA from resuspension stage 1 predominantly comprise organic matter and fine-grained clay particles, and have no aggregated sand grains (median particle size of the clay particles = 5.5 μm, the fraction of sand grains is zero), referred to as clay BSA. Clay BSA are suspended during the Stage 1 of surface removal processes from the fluff sediments, at a critical shear stress of 0.27-0.33 Pa. 36 clay BSA samples were captured in micro-CT experiments. The clay BSA are slow-settling aggregates and the settling velocities are tested using camera-video systems (section 2.2). The micro-CT scan experiments of clay BSA follows the protocols developed in section 2.1, with an image resolution of 0.777 μm.

The fluff BSA from resuspension stage 2 are aggregated with considerable sand grains

(median particle size of the sand particles = 195 μm, the fraction of sand grains is 94.3%; for more details of the BSA characteristics see Appendix A). Fluff BSA entered the water column during the resuspension stage 2 from the fluff sediments, at a critical shear stress of 0.72-0.82 Pa. 12 fluff BSA samples were captured in micro-CT experiments. The fluff BSA are fast-settling aggregates and could not be tested using the camera-video system. The settling velocities are thus tested in a laboratory settling column, equipped with a dedicated mass balancing and time tracking system, following the protocols set-out in section 2.2. The micro-CT scan experiments of fluff BSA follows the protocols in section 2.1 with an image resolution of 4.5 μm.

4.2.2 Theory and comparative equations

General theory: force balance and terminal settling velocity

Theories that will be applied in this chapter to investigate the settling velocities of BSA are clarified in this section.

Falling particles in quiescent water achieve terminal settling velocity when the gravitational forces, $F_g = \rho g V$, are balanced by buoyant forces, $F_b = \rho_w g V$, and drag forces, $F_d = \frac{1}{2} C_D \rho_w A w_s^2$ as:

$$F_g - F_b = F_d \qquad \text{Eq. 4.1}$$

In which V and A are the body volume and projected area of falling particles, ρ and ρ_w are the densities of falling particles and water, respectively. w_s is the terminal still water settling velocity and C_D is the drag coefficient.

Eq. 4.1 can be solved to obtain the settling velocity (for spheres), if the particle size, L, density, ρ, and drag coefficient, C_D, are known:

$$w_s = \sqrt{\frac{4}{3}\frac{(\rho - \rho_w)gL}{C_D\rho}} \quad \text{Eq. 4.2}$$

Comparative equations

BSA comprises three fractions: inorganic sediment particles, organic matrices formed by microbial cells and the produced organic matter, and pore water. These three phases of matter determine the mass and volume of BSA, which in turn affect the settling velocities of BSA. To test the relative contribution/significance of sediment particles, organic matter and pore water to the settling velocities, four settling velocities are calculated:

(i) a settling velocity estimated by simply considering the content of sediment particles (for creeping flow regime, Re<1);

(ii) a settling velocity estimated by considering the contents of both sediment particles and organic matter (for creeping flow regime, Re<1);

(iii) a settling velocity estimated by considering all the three fractions of components: sediment particles, organic matter, as well as pore water (for creeping flow regime, Re<1);

(iv) a settling velocity estimated by considering all the three fractions, but for fast-settling particles of higher Reynolds number, Re>1;

(i) Settling velocity considering sediment fractions (creeping flow regime, Re < 1)

This method is proposed to see whether the settling velocities of BSA can be calculated by simply considering the sediment fraction, or in other words, whether the attachment of microbiology, the production of organic matter and the arrangement of microbial influenced pore space can be overlooked. For this estimate, only the contents of sediment particles held by BSA are considered. Therefore, the BSA is simplified as a solid sphere made of sediment particles, the volume of which is the same as the sum

volume of all sediment particles held within the BSA. The size L, and density ρ in Eq. 4.2 can be expressed as:

$$L = d_s = (V_S \frac{6}{\pi})^{1/3} \quad \text{Eq. 4.3}$$

$$\rho = \rho_s$$

In which, d_s is the spherical equivalent diameter of the sum volume of all sediment particles, and V_S is the sum volume of all sediment particles aggregated within BSA. ρ_s is the density of sediment particles and is considered as 2650 kg/m^3 herein. Considering Stokes' drag, $C_D = \frac{24}{\mathrm{Re}}$, we can then obtain the following equation for settling velocity:

$$w_{s-S} = \frac{(\rho_s - \rho_w)\mathrm{g}}{18\mu} d_s^{\,2} \quad \text{Eq. 4.4}$$

(ii) Settling velocity considering the components of sediment and organic fractions (creeping flow regime, Re < 1)

This method is proposed to see if taking account of the organic matter will improve the accuracy of the velocity estimate. The results may indicate the extent to which the organic fraction can affect settling velocity.

Each BSA is simplified as a solid sphere, the volume of which is the same as the sum volume of all the matter of sediment particles and organic matter enveloped per BSA. The size *L* and ρ in Eq. 4.2 can be expressed as:

$$L = d_M = (V_M \frac{6}{\pi})^{1/3} \quad \text{Eq. 4.5}$$

$$\rho = \rho_M = \rho_s \varphi_s + \varphi_b \rho_b$$

In which V_M is the sum volume of all the sediment particles and organic matter aggregated per BSA. d_M is the spherical volume equivalent diameter of V_M. φ_s and φ_b are the fractions of inorganic sediments and organic matter, respectively. ρ_b is the average density of organic matter. Sediment fraction φ_s =1- φ_b , and ρ_b can be estimated from CT-scanned BSA images. Considering Stokes' drag, $C_D = \frac{24}{\mathrm{Re}}$, we can then obtain the following equation for settling velocity:

$$w_{s-M} = \frac{(\rho_M - \rho_w)\mathrm{g}}{18\mu} d_M{}^2 \qquad \text{Eq. 4.6}$$

(iii) Settling velocity considering sediment, organic fractions and pore water (creeping flow regime, Re < 1)

This method enables the effects of pore water to be incorporated into settling velocity estimates. The results may indicate the extent to which pore water can affect settling velocity.

Each BSA is simplified as a solid sphere, the volume of which is the same as the sum volume of sediment particles, organic matter, and pore water, held per BSA. The size *L* and ρ in Eq. 4.2 can be expressed as:

$$L = d_A = (V_A \frac{6}{\pi})^{1/3} \qquad \text{Eq. 4.7}$$

$$\rho = \rho_A = \rho_w + (\rho_M - \rho_w)(1-\varepsilon)$$

In Eq. 4.7, d_A is the spherical volume equivalent diameter of V_A. V_A is obtained by assuming aggregates as ellipsoids. The volume of aggregates, V_A , can then be determined by three diameter variables as $V_A = \frac{\pi}{6} d_x d_y d_z$. By considering d_x , d_y and d_z as the maximum projected diameter of BSA on x-, y-, and z- axes, V_A can then be

obtained.

For clarification, details regarding the derivation of ρ_A are listed as follows:

The three components of each aggregate (sediment particle, organic matter and pore water) can be classified into two types: pore water held per aggregate and matter enveloped per aggregate (matter includes sediment particle + organic matter). As such, the total volume of aggregate, V_A, is equal to the sum volume of pore water, V_w, and matter, V_M:

$$V_A = V_M + V_w \quad \text{Eq. 4.7.1}$$

Similarly, the total mass of aggregate, M_A, is the summation of the mass of pore water, M_w, and the mass of matter, M_M. The total mass balance of aggregate is:

$$M_A = M_w + M_M \quad \text{Eq. 4.7.2}$$

Considering $M_A = \rho_A V_A$ (ρ_A and V_A are the density and volume of aggregate), $M_w = \rho_w V_w$ (ρ_w and V_w are the density and volume of water), and $V_M = \rho_M V_M$ (ρ_M and V_M are the density and volume of matter), Eq. 4.7.2 can be expressed as:

$$M_A = \rho_A V_A = \rho_w V_w + \rho_M V_M \quad \text{Eq. 4.7.3}$$

Based on Eq. 4.7.3, we can obtain:

$$\rho_A V_A = \rho_w V_w + \rho_M V_M \quad \text{Eq. 4.7.4}$$

Aggregate density, ρ_A, can be expressed as:

$$\rho_A = \rho_w \frac{V_w}{V_A} + \rho_M \frac{V_M}{V_A} \quad \text{Eq. 4.7.5}$$

Considering aggregate porosity $\varepsilon = \frac{V_w}{V_A} = 1 - \frac{V_M}{V_A}$, the expressions of aggregate density, ρ_A in Eq. 4.7.5, can be converted to:

$$\rho_A = \rho_w \varepsilon + \rho_M (1-\varepsilon) \quad \text{Eq. 4.7.6}$$

According to Eq. 4.7.6, we can obtain:

$$\rho_A - \rho_w = \rho_w \varepsilon + \rho_M (1-\varepsilon) - \rho_w = \rho_w (\varepsilon - 1) + \rho_M (1-\varepsilon) \quad \text{Eq. 4.7.7}$$

Thus, we have

$$\rho_A = \rho_w + \rho_w (\varepsilon - 1) + \rho_M (1-\varepsilon) = \rho_w + (\rho_M - \rho_w)(1-\varepsilon) \quad \text{Eq. 4.7.8}$$

Based on the above derivation from Eq. 4.7.1-4.7.8, the expressions of aggregate density, ρ_A, in Eq. 4.7 can be obtained.

Considering Stokes' drag, $C_D = \frac{24}{\mathrm{Re}}$, we can obtain the following equations for settling velocity:

$$w_{s-A} = \frac{(\rho_A - \rho_w)\mathrm{g}}{18\mu} d_A^{\,2} \quad \text{Eq. 4.8}$$

(iv) Settling velocity considering the effects of form drag (1< Re < 200)

As flow velocity increases, the effects of inertial forces increase and become no longer negligible. To obtain the transport of particles in different systems from low to medium Reynolds number, considerable efforts have been paid to simulate the drag coefficient exerted on falling particles in different Reynolds number regimes (details can be found

in review (Clift and Gauvin, 1971; Pang and Wei, 2011)). Among these different expressions for C_D, Schiller and Naumann's expression for Re < 200 are widely used for estimating the falling of sediment aggregates and found good agreement (Winterwerp, 2002):

$$C_D = \frac{24}{\mathrm{Re}}(1+0.15\mathrm{Re}^{0.687}) \qquad \text{Eq. 4.9}$$

With the combination of method (iii), we can obtain the following equation for settling velocity:

$$w_{s-AD} = \frac{(\rho_A-\rho_w)\mathrm{g}}{18\mu} d_A{}^2(1+0.15\mathrm{Re}^{0.687}) \qquad \text{Eq. 4.10}$$

This settling velocity takes account of each fraction of BSA components, including sediment particles, organic fraction and pore water, as well as the form drag which results from the increased inertial forces for higher Reynolds number (1<Re<200). Table 4.1 summarises the above four comparative settling equations. For a clearer view and easier reference.

Table 4.1 A summary of comparative equations for settling velocity estimates.

Methods	**Equations**	**Explanations**
Method (i)	$w_{s-S} = \frac{(\rho_s-\rho_w)\mathrm{g}}{18\mu} d_s{}^2$	The effects of sediment fraction are considered in settling velocity estimates, with Stokes drag (Re<1)
Method (ii)	$w_{s-M} = \frac{(\rho_M-\rho_w)\mathrm{g}}{18\mu} d_M{}^2$	Sediment and organic matter are considered in settling velocity estimates, with Stokes drag (Re<1)
Method (iii)	$w_{s-A} = \frac{(\rho_A-\rho_w)\mathrm{g}}{18\mu} d_A{}^2$	Sediment, organic matter and pore water are considered in settling velocity estimates, with

		Stokes drag (Re<1)
Method (iv)	$w_{s-AD}=\frac{(\rho_A-\rho_w)g}{18\mu}d_A^{\,2}\times(1+0.15\,\mathrm{Re}^{0.687})$	Sediment, organic matter and pore water are considered in settling velocity estimates, with both viscous (Stokes) and form drag (1<Re<200)

4.3 Results

4.3.1 Fractal dimensions of clay and fluff BSA

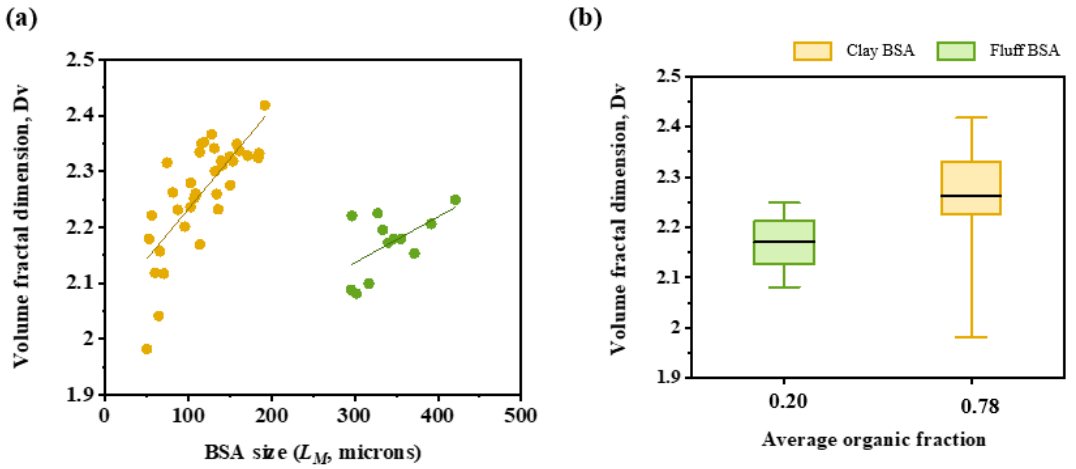

Figure 4.1 Relationships between the volume fractal dimension and the size, L_M, of BSA in (a) (yellow dots for clay BSA and green dots for fluff BSA). The mean, min and max values of BSA fractal dimension for clay (with an average organic fraction of 0.78) and fluff BSA (with an average organic fraction of 0.20) are presented as box plots in Figure 4.1 (b). The bars indicate the maximum and minimum values of volume fractal dimension and the extent of the box indicates the values account for 25%-75% of overall accumulate distribution. Middle solid black lines in each box represent the mean fractal dimension.

Table 4. 2 Bivariate correlation between BSA size, L_M, and volume fractal dimension, D_v for clay and fluff BSA.

Bivariate correlation between L_M and Dv		
Clay BSA	Pearson Correlation	0.758**

	Spearman Correlation	0.740**
	Sig. (2-tailed)	$p < 0.05$
	N	36
Fluff BSA	Pearson Correlation	0.573
	Spearman Correlation	0.431
	Sig. (2-tailed)	0.052
	N	12

Table 4. 3Statistical results of Nonparametric Mann-Whitney test and independent T test of organic fraction differences between clay and fluff BSA.

	Clay BSA	Fluff BSA	Nonparametric Mann-Whitney U test	Independent-samples T test*
	$\tilde{X}; \bar{X} \pm SD(n)$ **		p value ***	p value ***
Organic fraction	0.79; 0.78 ± 0.09 (36)	0.20; 0.20 ± 0.07 (12)	< 0.05	< 0.05
Volume fractal dimension	2.28; 2.26 ± 0.09 (36)	2.18; 2.17 ± 0.06 (12)	N/A	< 0.05

* The organic fraction of clay BSA does not apply to normal distribution and Mann-Whitney U test were applied to the comparison tests. After normal transformation (the normality was tested again), independent-samples T test were also performed. The volume fractal dimension of both clay and fluff BSA apply to normal distribution, thus only independent-samples T test were performed.

** $\tilde{X}$:median; $\bar{X}$:mean; SD: standard deviation to the mean; n: number of observations/estimations.

*** Only p values larger than 0.05 are indicated.

Figure 4.1 (a) plots the volume fractal dimension against the size of BSA, L_M, which shows a clear positive trend: the volume fractal dimension increases as BSA size increases. This implies that as BSA size increases, the internal structure of BSA becomes increasingly compacted. Bivariate correlation analysis confirms significant correlations between volume fractal dimension and BSA size for clay BSA. In the case of fluff BSA, the volume fractal dimension in general positively relates to BSA size but the correlation is not statistically significant (Table 4.2). Figure 4.1 (b) presents that the clay BSA with a high organic fraction has, on average, a more compact internal structure ($p < 0.05$, Table 4.3).

Both clay and fluff BSA show generally positive relationships with size, though the correlation for fluff BSA is not statistically significant. It is clear that neither of the two BSA presents negative correlations with aggregate size. This finding is contrary to the majority of previous work, where the aggregates develop towards more loosely-connected structures (Maggi, 2013; Nguyen et al., 2017; Vahedi and Gorczyca, 2011). The negative relationships between BSA structure and size agree with the cluster-cluster kinetic and diffusion-limited aggregation model, which hypothesizes that aggregation is caused by collision and the clusters and/or particles are randomly brought together due to diffusion and form loose and porous aggregates (Meakin, 1991; Nguyen et al., 2017). Maggi and Tang (2015) analysed 52 datasets of aggregate architecture collected from various ecosystems, in which some aggregates present positive correlations between volume fractal dimension and aggregate size. The authors in that work discussed possible mechanisms and suggested microbial development, such as cell colonization and organic matter production, might lead the structures to be better filled, resulting in a more compact structure (Maggi and Tang, 2015). Maggi and Tang (2015) found the positive correlations occurred in organic-rich BSA (referred to as biomineral aggregates in their work) at a higher probability, as compared with sediment-rich aggregates (referred to as mineral aggregates in their work), indicating the important role of cell colonization and organic matter production in the processes of aggregate structure compaction. The results of this chapter provide supportive evidence for Maggi and Tang (2015) results, where the positive correlation between volume fractal dimension is at a higher significant level for the organic-rich clay BSA (of high organic fraction = 0.78), than sediment-rich fluff BSA (low organic fraction = 0.20).

An alternative explanation could also be made that the positive relationships between size and volume fractal dimension might be a characteristic of seabed BSA development. Similar positive relationships to those shown in Figure 4.1, that BSA become increasingly well-packed as the BSA size develops, also occurred in field

observations of SPM from seabed sediments, as listed in Table 4.4 (Lick, et al., 1993; Sternberg, et al., 1999; Voulgaris and Meyers, 2004; Curran et al., 2007). The processes for aggregate growth within seabed sediments might be different from those in a water column (Bar-Zeev et al., 2012; He et al., 2012; Maggi, 2005; Perujo et al., 2017). Aggregate growth during the flocculation processes in water is associated with collisions among clusters, e.g. described as cluster-cluster aggregation (CCA, in which clusters are randomly brought together through diffusion), resulting in poorly-connected structures with reduced compactness. Such a collision process, however, is unlikely to occur in seabed sediment substratum where there is already close contact between clusters. When sitting at seabed, the growth of BSA might be dominated by microbial development such as covering exposed surfaces of sediment particles and filling the internal pores, leading to a more compact internal structure to develop. To test this explanation, the extent to which clay and fluff BSA, as well as the field BSA listed in Table 4.4, were developed at the seabed or within the water column might need to be better understood. Whilst no robust explanation could be made for the positive and uncertain correlations between volume fractal dimension and BSA size could be made, it is clear that the results of this study alongside with Maggi and Tang's (2015) work suggest that microbial mediations influence the development patterns of aggregate structures in a complex manner. Further tests are needed to provide a more robust and mechanistic explanation of these observations.

Table 4. 4 A summary of field observations of SPM close to seabed that showed similar increasing trend to the present work.

Reference	**Measurement summary**
Lick et, al. (1993)	Laboratory measurements of SPM generated from natural bottom sediments, Detroit River, USA.
Sternberg et al. (1999)	*In situ* measurements of SPM at 2m above seabed, on a tripod

	located in 62-m water depth, Eureka, USA.
Curran et al. (2007)	*In situ* measurements of SPM at 1.7m above seabed, by INSSECT, to study the suspended sediment in coastal bottom boundary layer, Gulf of Lions, France.
Voulgaris and Meyers. (2004)	*In situ* measurements of SPM at 0.42 and 0.15 m above a creek bed of intertidal saltmarshes, South Carolina, USA.

4.3.2 Settling velocities of clay and fluff BSA

Four different estimated settling velocities were obtained and compared with the experimentally-tested velocities, with the aim of investigating the relative significance/contributions of different BSA components, sediment particles, organic matter and pore water, to settling velocity. Box A in Figure 4.2 plots the experimentally-tested settling velocities, while boxes B-E are the estimated velocities by using the methods (i)- (iv) listed in Table 4.1, respectively. Statistical analysis was performed to examine the mean differences between the experimentally-tested and theoretically-estimated velocities (Table 4.5). The full details of the statistical analysis can be found in Appendix C.

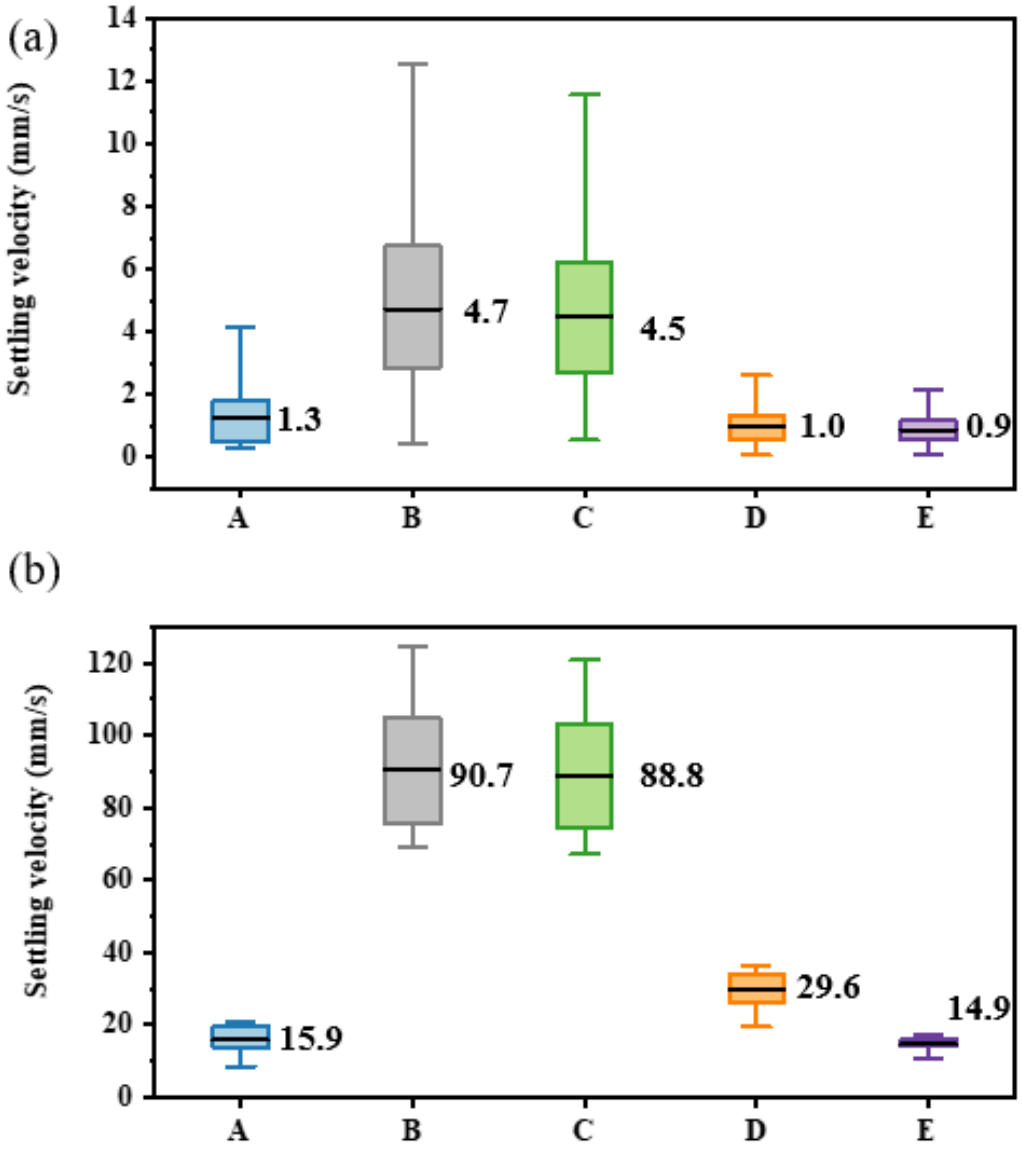

Figure 4.2 Comparisons between experimental settling velocity and estimated settling velocity for clay BSA (a) and fluff sand BSA (b). A is the experimentally-tested settling velocity; B is the estimated velocity which only accounts the mass of sediment fraction but exclude the organic fraction; C is the estimated velocity which includes the organic fractions in mass; D is the estimated velocity which takes account of volumetric characteristics; E is the estimated velocity which considers the form drag effects by using Schiller-Naumann's empirical drag (while B-D simply considers the skin friction drag by using Stokes drag). The bars indicate the maximum and minimum values of settling velocities and the extent of the box indicates the velocities account for 25%-75% of overall accumulate distribution. Middle solid black lines in each box represent the mean settling velocities, with the average settling velocity being labelled on the right hand side.

Table 4.5 Comparisons of statistical differences between the experimentally-tested and theoretically-estimated velocities for clay and fluff BSA.

BSA type	**Experimentally-tested velocities**	**Estimated velocities**		**Statistical comparisons***		**Statistical difference**
		$\tilde{X}; \bar{X} \pm SD(n)$		**Method**	***p* value**	
Clay BSA	Box A 0.77; 1.27 ± 1.37 (129)	Box B	4.69; 4.74 ± 2.68 (36)	Mann-Whitney U test	< 0.05	Significant difference
		Box C	4.69 4.47 ± 2.54 (36)	Mann-Whitney U test	< 0.05	Significant difference
		Box D	1.02 1.00 ± 0.55 (36)	Mann-Whitney U test	0.67	**No significant difference**
		Box E	0.92 0.89 ± 0.46 (36)	Mann-Whitney U test	0.87	**No significant difference**
Fluff BSA	Box A 15.81; 15.88 ± 3.85 (13)	Box B	88.40; 90.68 ± 17.86 (12)	Bonferroni test	< 0.05	Significant difference
		Box C	86.72; 88.79 ± 17.27 (12)	Bonferroni test	< 0.05	Significant difference
		Box D	30.43; 29.56 ± 5.37 (12)	Bonferroni test	< 0.05	Significant difference
		Box E	15.19; 14.86 ± 1.85 (12)	Bonferroni test	0.99	**No significant difference**

*Nonparametric tests were conducted for clay BSA as the tested velocities of clay BSA do not apply to normal distribution and failed to be converted to normal distribution. Non-parametric Mann-Whitney U test was performed. By contrast, all the five velocity datasets of fluff BSA apply to normal distribution, and ANOVA tests were performed for multiple comparison.

The settling velocities in Box B are estimated considering only the content of abiotic sediment particles, and exclude organic matter and pore water. Comparisons with the experimentally-tested velocities show a significant discrepancy, overestimating by about more than 3 times for clay BSA and more than 5 times for fluff BSA. The differences are statistically significant as confirmed by $p < 0.05$. This is perhaps not surprising, as ignoring the organic matter and pore water components can lead to significant overestimation of density and underestimation of flow resistance acting on the settling BSA.

The velocity estimates in Box C take consideration of the organic matter, but still exclude the pore water. Whilst the velocity overestimation is reduced compared to the estimates from Box B, the reduction appears to be moderate but a significant overestimation remains ($p < 0.05$). This trend occurs for both the clay (of a high organic fraction of 0.78) and fluff BSA (of a lower organic fraction of 0.20), indicating the content of organic matter may affect BSA's settling velocity, to some degree.

Velocity estimates in Box D, where the volume of pore water is taken into account, in addition to the sediment particles and organic matter content, exhibit better agreement with the experimental data, compared to the estimates from Box B and C. This suggests that pore water makes an important contribution to BSA settling velocity. This is especially true for clay BSA, as the estimates in Box D present very close estimates to the experimental data, with the overestimates being reduced from more than 3 times to only ~20%, and confirmed by the statistically insignificant differences between Box A and D ($p > 0.05$) in Table 4.5. By contrast, whilst a more than 3 times improvement is presented for fluff BSA, the estimates in Box D remain a significant overestimate from 15.9 mm/s to 29.6 mm/s ($p < 0.05$). A possible reason is that the fluff BSA settle at a rate that is about 10 times higher than the clay BSA settling velocity. Under these conditions, the surrounding flow can no longer be characterized as creeping flow. In theory, the flow should be separated behind the shoulders of the falling fluff BSA, and the inertial forces lead to non-negligible form drag on the fluff BSA (Clift and Gauvin,

1971; Kelbaliyev, 2011). The improved agreement by the estimates in Box E, after the consideration of form drag, agrees with this hypothesized explanation. The statistical results in Table 4.5 confirms no significant differences between the velocities in Box A and E ($p > 0.05$). Therefore, in addition to pore water, for fast-settling aggregates, such as fluff BSA, the form drag should also be included.

Summarizing, the volume of pore water is found to play a significant role on the settling velocities of BSA, while the contributions of organic matter are much small. For the fast-settling aggregates with Re >1 (e.g. fluff BSA), the effects of form drag are also important and should not be overlooked.

4.3.3 Drag of clay and fluff BSA

This section aims to pursue a preliminary exploration of microbial influences on drag.

As shown in Figure 4.3 (a) for clay BSA and (b) for fluff BSA, C_{Db} is the drag exerting on microbial aggregates. C_{Db} is obtained by applying the experimental settling velocities from Eq.4.2. C_{Ds} represents the drag exerting on solid spheres in the absence of microbiology, and can be obtained using existing equations, such as the Stokes or Schiller and Naumann drag equations. Considering the latter accounts for the inertial effects and can be applied to a wider flow regime (1< Re < 200), it is applied herein and has the following form: $C_{Ds} = \frac{24}{\mathrm{Re}}(1+0.15\mathrm{Re}^{0.687})$.

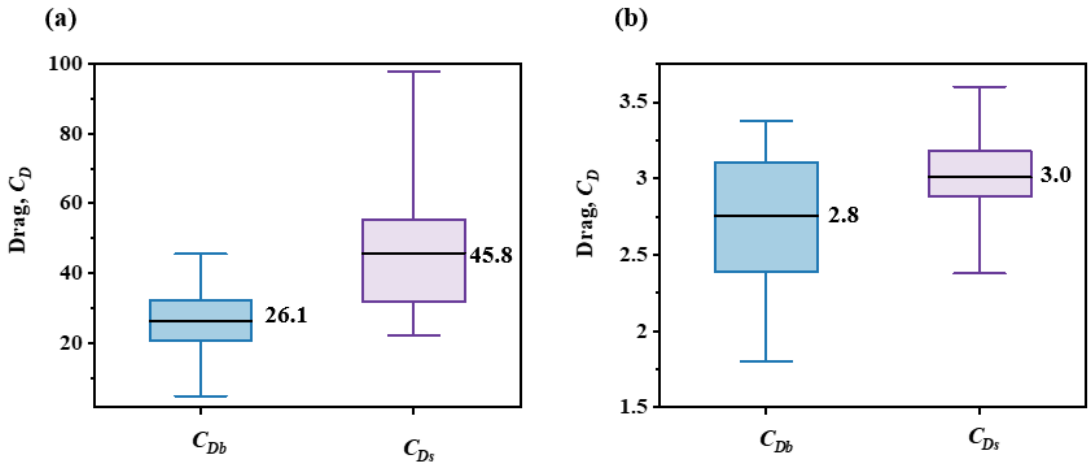

Figure 4.3 Comparisons between biotic (C_{Db} , blue box) and abiotic drag (C_{Ds} , purple box ~~abiotic drag~~), for clay BSA (a) and fluff BSA (b). The bars indicate the maximum and minimum values of drag and the extent of the box indicates the drag accounts for 25%-75% of overall accumulate distribution. Black solid lines in the middle of each box represents the mean value of drag and the value is labelled on the right hand side.

Table 4. 6 Statistical differences between the means of biotic and abiotic drag for clay and fluff BSA.

	Biotic drag C_{Db}	Abiotic drag C_{Ds}	Statistical comparison
	$\tilde{X}; \bar{X} \pm SD(n)$		p value *
Clay SBA	27.73; 26.14 ± 9.77(36)	42.17; 45.78 ± 19.29(36)	< 0.05
Fluff BSA	2.76; 2.84 ±0.48(12)	3.00; 3.00 ± 0.30(12)	0.079

* As the abiotic drag of clay BSA do not apply to normal distribution and cannot be converted to normal distribution, nonparametric Wilcoxon tests for paired comparisons were applied. As both the biotic and abiotic drag of fluff BSA apply to normal distributions, paired T tests were performed to compare the statistical differences between the drags of the fluff BSA.

Abiotic drag closely approximates the biotic drag of fluff BSA (Figure 4.4 (b)) but overestimate the drag for clay BSA by some 175% (Figure 4.4 (a)). Statistical comparisons confirm there is no significant difference between the abiotic and biotic

drag of fluff BSA ($p > 0.05$, Table 4.6)), while the exclusion of microbial influences on drag causes significant differences for clay BSA ($p < 0.05$, Table 4.6). Hence, the microbial influences on the drag of clay and fluff BSA appear to be clearly differentiated.

Drag can be affected by multiple factors. For example, the permeable flow passing through the internal pore structures are found to reduce drag, for both abiotic and biotic spheres (Emadzadeh and Chiew, 2020; Mu et al., 2008). Microbial coatings increase surface roughness which has been found have a substantial effect on enhancing drag (Nicolella et al., 1999; Saravanan and Sreekrishnan, 2005; Shang et al., 2014). In addition to the surface roughness, it is also suggested that due to soft surfaces of organic matter coatings on particle surfaces, deformation may occur during the falling process (Andalib et al., 2010; Saravanan and Sreekrishnan, 2005). It is believed for flow regimes with small Reynolds number (e.g. $Re<1$), there is no/negligible deformation and the falling particles retain their shape stability. With an increase of Reynolds number to an intermediate regime, deformation occurs and the measured drag coefficient becomes larger than that exerted on solid spheres, which also results in an increased drag. Differences between the biotic drag and abiotic drag may be caused by the combined effects of the above factors (e.g. permeable flow, surface roughness, bio-coating, shapes in internal pore structures and deformation).

Although the effects of permeable flow, bio-coating induced surface roughness, and potential microbial aggregate deformation are investigated and quantified in previous research, the combined effect of microbial influences on drag appears to be lacking. To explore this further, a parameter referred to as the biotic drag ratio is introduced. This biotic drag ratio, η, is supposed to represent such combined influences:

$$\eta = \frac{C_{Db}}{C_{Ds}} \qquad \text{Eq. 4.11}$$

In which, C_{Db} is obtained through applying the laboratory-measured settling velocities into Eq. 4.2, and C_{Ds} is obtained according to $C_{Ds}=\frac{24}{\mathrm{Re}}(1+0.15\mathrm{Re}^{0.687})$. Figure 4.4 (a) plots the bio-drag ratio, η, for both clay and fluff BSA, against the dimensionless aggregate diameter $D_{*A}=(\frac{(\rho_A/\rho_w-1)\mathrm{g}}{\upsilon^2})^{1/3}d_A$. Clay and fluff BSA present distinct patterns, which may be caused by distinct features of geometry and architecture, such as porosity, and organic /sediment fraction.

To consider the effects of these characteristics, an adjusted biotic drag ratio is proposed as $\eta\cdot(1-\varphi_b)(1-\varepsilon)$. The derivation of this adjusted biotic drag ratio and physical meaning of the variables are explained as follows.

For clarification, each aggregate is considered to be comprised of three component types: organic matter, sediment particles and pore water, in which organic matter and sediment particles are the matter enveloped per aggregate. As such, the total volume of matter, V_M, refers to the summation of total volume of organic matter, V_B, and sediment particles, V_S:

$$V_M=V_B+V_S \qquad \text{Eq. 4.12}$$

Total volume of aggregates, V_A, refers to the summation of volume of both matter and pore water, or in other words, the sum volume of organic matter, sediment particles and pore water. As such, V_A can be expressed as:

$$V_A=V_M+V_w=V_B+V_S+V_w \qquad \text{Eq. 4.13}$$

φ_b is defined as organic fraction of matter (please note, φ_b is not organic fraction of aggregate). Organic fraction of matter, φ_b, represents the volumetric fraction of organic matter within the total volume of matter enveloped per aggregate, and can be

expressed as:

$$\varphi_b = \frac{V_b}{V_M} = \frac{V_b}{V_B + V_S} \quad \text{Eq. 4.14}$$

Similarly, sediment fraction of matter, φ_s, can be expressed as:

$$\varphi_s = \frac{V_s}{V_M} = \frac{V_s}{V_B + V_S} \quad \text{Eq. 4.15}$$

As the matter enveloped per aggregate are comprised of only sediment particles and organic matter, we can obtain:

$$\varphi_b + \varphi_s = \frac{V_b}{V_B + V_S} + \frac{V_s}{V_B + V_S} = 1 \quad \text{Eq. 4.16}$$

ε defines aggregate porosity, which is the volumetric fraction of pore water in the total volume of aggregates. ε can be expressed as:

$$\varepsilon = \frac{V_w}{V_A} = \frac{V_w}{V_B + V_S + V_w} \quad \text{Eq. 4.17}$$

By applying equation (4.14-4.17) into the expression of $(1-\varphi_b)(1-\varepsilon)$, we can obtain Eq. 4.18 as:

$$(1-\varphi_b)(1-\varepsilon)=\varphi_s(1-\varepsilon)=\frac{V_s}{V_B+V_S}\cdot(1-\frac{V_w}{V_B+V_S+V_w})$$
$$=\frac{V_s}{V_B+V_S}\cdot\frac{V_B+V_S}{V_B+V_S+V_w}$$
$$=\frac{V_s}{V_B+V_S+V_w}$$
$$=\frac{V_s}{V_A} \qquad \text{Eq. 4.18}$$

V_S is the total volume of sediment particles per aggregate. V_A is the total volume of aggregate. $\frac{V_S}{V_A}$ thus refers to the volumetric fraction of sediment particles in the total volume of the aggregate (note: the sediment fraction of matter is $\varphi_b=\frac{V_S}{V_M}$, which refers to the volumetric fraction of sediment particles in the total volume of matter). Thus, the physical meaning of $(1-\varphi_b)(1-\varepsilon)$ is the sediment fraction of the aggregate.

Figure 4.4 (b) plots the adjusted biotic drag ratio of clay and fluff BSA against D_{*A}. It shows that the scatters of clay and fluff BSA are reduced and unifies the data to a single underlying trend (Figure 4.4(b)). The adjusted biotic drag ratio and the dimensionless aggregate size present the following power law relationship:

$$\eta\cdot(1-\varphi_b)(1-\varepsilon)=0.0003D_{*A}^{\ 2},\ R^2=0.81,\ p<0.05 \qquad \text{Eq. 4.19}$$

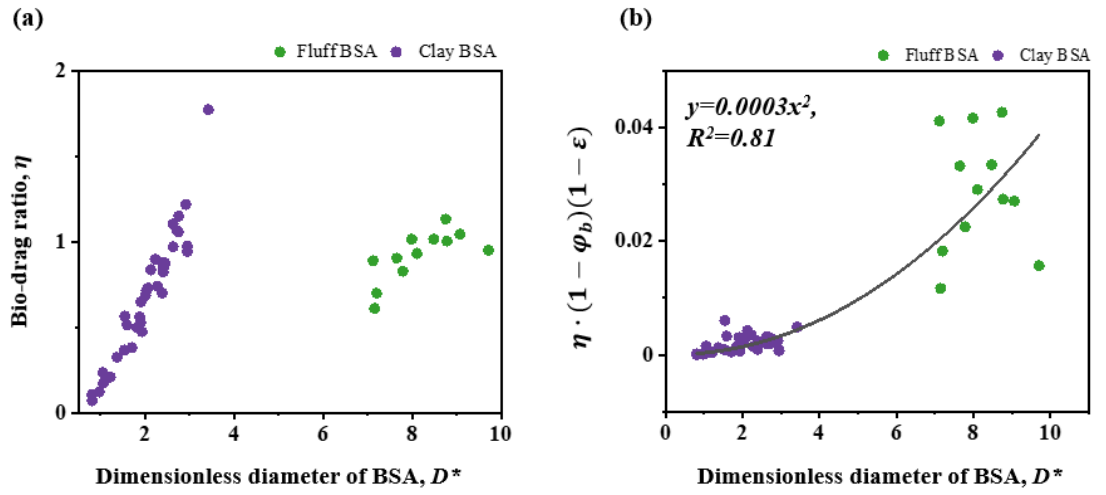

Figure 4.4 Plots of biotic drag ratio against dimensionless diameter of clay and fluff BSA (a); plots of the adjusted biotic drag ratio against dimensionless diameter of clay and fluff BSA (b).

Regression analysis confirms the power law relationship between the dimensionless diameter of BSA and the adjusted biotic drag ratio is statistically significant ($p < 0.05$, Table 4.7). This relationship provides a quantitative description of the microbial influences on drag. The differentiated patterns presented by clay and fluff BSA in Figure 4.4 (a) appear to be diminished after taking account of the compositional features of BSA (sediment/organic fraction) and the structural characteristics (e.g. porosity). This result implies a close relationship between BSA's compositional and structural features and drag. Some possible reasons are discussed in more detail in section 4.4.

4.4 Discussion

Clay BSA were developed under frequent disturbances (under 6 hours of resuspension at an applied shear stresses of 1.0 Pa each day). The extraction was done from the applied bed shear stress of 0.27-0.34 Pa during the erosion of clay BSA. The relevance of the applied shear stresses to natural environments is discussed as follows. For example, Anderson et al. (2007) found bed shear stresses in the range of 0.1-0.6 Pa are common at the Kongsmark mudflat, Danish Wadden Sea. Cohesive sediments can be eroded by bed shear stress of 0.2-0.6 Pa (Andersen et al., 2007; Widdows et al., 1998). Amos et al. (2017) analysed 15 deployments of in situ annular flume (Sea Carousel) to

two estuaries in Canada, and found 14 sites were eroded at shear stresses of less than 0.3 Pa. Some freshly-deposited materials at mudflats can enter water at a much lower level of bed shear stresses of <0.2 Pa, which has been reported for the Skeffling mudflat in the Humber Estuary, UK (Houwing, 1999), and the mudflat of the Eastern Chongming Island, Yangtze River (Shi et al., 2012). However, when a biofilm mat can be established, much higher bed shear stresses are needed for erosion, such as 0.86 - 3.06 Pa in Amos et al.'s (2010) work on cohesive sediments in Venice Lagoon. As such, the depositional behaviours of clay BSA observed in this work might be more related to SPM from the cohesive sediments that underwent frequent disturbances or that are freshly deposited, rather than the mudflat with microbial mat established. Fluff BSA were also developed under frequent disturbances (under 6 hours of resuspension at an applied shear stress of 1.0 Pa each day). The extraction was done at shear stress level of 0.73-0.82 Pa during the resuspension processes. According to literature, the bed shear stress level of 0.73 -0.82 Pa often occurs under energetic hydrodynamics. In situ measurements of current-induced bed shear stresses over the sites with similar grain sizes were within the range of 0.2-0.6 Pa (Ward et al., 2015), while, as a combined result of waves and currents, the shear stresses can exceed 1.0 Pa, such as those found in the Dee estuary (D_{50} of sand = 227 μm) (Lichtman et al., 2018). The depositional behaviours of fluff BSA observed herein seems to be relevant to SPM that can be eroded from sandy sediments within wave-tide combined, energetic conditions. As the fluff BSA were established during frequent disturbances, no mat matrices of biofilm were able to develop. Thus, the results from the depositional behaviours of fluff BSA might not apply to the SPM eroded from mat-armoured sandy sediments.

The results of this chapter provide strong evidence for the importance of pore water in determining the settling velocities of the BSA. The estimated velocities, by simply including the effects of organic matter, remain significantly overestimated, as compared with the experimentally-tested velocities. By contrast, with the consideration of pore water, the discrepancies with the experimental velocities became largely diminished.

This result may require some contrasting observations from previous work to be better explained. For example, aggregates of high inorganic fraction were found to associate with accelerated settling velocities, possibly due to the increase of aggregate densities. However, some work found aggregates of higher inorganic fraction do not always settle faster. For example, Maggi and Tang's (2015) work shows that the average velocities poorly correlate with the change of organic fraction (Maggi and Tang, 2015). As discussed in their work, the non-linearity may be due to the attachment of large living cells. In these large cell attached aggregates, despite similar organic fraction to the aggregates of without large living cells attached, they may have very different porosities/pore spaces (cells are non-porous). The results from this chapter confirm the importance of pore water and suggest a need to consider such effects, especially when interpreting the relationships between aggregate composition (organic/inorganic ratio) and settling velocities.

A second important finding of these experiments is that the biotic drag ratio appears to depend on the sediment/organic fraction and porosity. The fraction of sediment particles/organic matter can reflect microbial colonization activities, such as the production of EPS (Bar-Zeev et al., 2012), or the establishment of biofilm matrices to provide a protective shell from surrounding predators (Flemming and Wingender, 2010), and the degradation by living cells/microorganisms attaching to the aggregates (Arndt et al., 2013). Such microbial activities at different development stages and/or under different mechanisms may have different effects on shaping roughness. For example, the BSA developed under a longer rest time in calm water conditions from seabed sediments are found to be less convoluted, compared to those that have only a short rest period, thus having different surface roughness (Stone, et al., 2008). Previous work has found that surface roughness is a significant factor to influence drag (Fang et al., 2020; Shang et al., 2014), which may then give an explanation regarding why the microbial mediation of drag is related to organic fraction. Porosity is another well-known factor to affect drag, due to the close relationships with the flow infiltration (Masliyah and

Polikar, 1980). The increasing porosity is found to decrease drag and increase settling velocity increment (when Re<~100) (Emadzadeh and Chiew, 2020; Mu et al., 2008). For microbiologically mediated porous and permeable aggregates, the colonization of microbiology, in addition to shaping the surface roughness of particles, can also mediate the arrangement of internal pore structures and pore spaces (porosity) (Martinsson et al., 2007; Perujo et al., 2017), which in turn affects flow infiltration. The above mechanisms may together contribute to the distinct drag patterns exhibited by fluff and clay BSA, and the relevance of the biotic drag ratio and the proposed adjustment to account for the sediment fraction of aggregate: $(1-\varphi_b)(1-\varepsilon)$. However, it is the author's belief that there is insufficient data at this stage to draw firm conclusions and further investigation is needed.

4.5 Conclusion

This chapter presents the internal structure (through volume fractal dimension), settling velocities and drag of two types of BSA created from laboratory settlings, slow-settling clay BSA and fast-settling fluff BSA. This work shows a positive trend that the growth of BSA size form more packed internal structures. The positive trend is statistically significant for clay BSA with better developed organic matter, while the positive trend is statistically insignificant for fluff BSA when organic matter fractions are low. Neither of the two BSA types present the generally-expected negative correlations as reported in previous work. As suggested by Maggi and Tang (2015), the differentiated development patterns of BSA structures might be due to the attachment of microbial cells and the production of organic matter. Whilst no robust explanation could be made, microbial development plays an import role in mediating the developing patterns of aggregate structures and needs further investigations to confirm.

Taking account of organic components may better estimate settling velocity to some degree. Accounting for pore water leads to a notable improvement, indicating that the volume of pore water plays a significant role in moderating settling velocities. For fast-

settling fluff BSA with Re = ~ 10-20, the form drag is another important consideration for settling velocity estimates.

Microbial influences on drag are found to be distinct for clay and fluff BSA. The discrepancies appear to be diminished after taking account of the differences in their sediment/organic fraction and porosity. This suggests that the microbial influences on drag may be associated with both the constituent components and structure of the BSA.

Chapter 5 An integrated view of microbial influences on sediment resuspension and deposition

5.1 Introduction

To pursue a clearer understanding of the effect of microbial influences on sediment suspension and settling processes, chapters 3 and 4 investigate laboratory-created BSA, including mat, fluff and clay BSA. In natural ecosystems, field sediments are more complex and heterogeneous. It is therefore necessary to test whether the phenomena observed in laboratory-created sediments will also occur for field sediments. This chapter is therefore conducted with the following objectives:

(i) to test whether microbial mediation of sediment suspension-deposition observed in chapter 3 and 4 also occur in field sediments;

(ii) to test whether the microbial influences on sediment suspension and deposition, e.g. sediment stability and settling velocity, can be quantitatively characterized.

5.2 Materials and Methods

To achieve the above objectives, two types of field BSA from the tidal flats of the Tay estuary, field sandy BSA and field silty BSA, are studied. Details of sediment sampling and seabed sediment preparation can be found in section 2.2.1. Field sandy BSA aggregates consist predominantly of sand grains (the median particle size of sand (>63 μm) = 169.5 μm, and the sand fraction = 87.1%) and have a relatively low organic fraction, with the average organic fraction = 15% (for more details of the BSA characteristics see Appendix A). Field silty BSA have a smaller proportion of sand grains and are of smaller size (the median particle size of sand (> 63 μm) = 76.7 μm, the sand fraction = 43.3 %). The field silty BSA are rich in organic matter, with the average organic fraction = 79% (for more details of the BSA characteristics see Appendix A). Both field sandy and silty BSA underwent flume resuspension

experiments, settling velocity tests and micro-CT experiments. The experimental workflows follow those presented in section 2.2, and are briefly summarised herein.

Each type of field BSA was placed in plastic boxes with ice bags during the ~10 hrs of transport duration. After transporting back to NOCS, the samples were stored in the fridge at 4 ºC before experiments. Each type of BSA were prepared following the methods listed in section 2.2. and placed in two identical Core Mini Flumes (CMF), with one CMF for resuspension tests and the other for coring and subsequent micro-CT scanning. In each flume, a total depth of 15 cm laboratory-prepared artificial seawater (Sigma sea salts, 35 ppt) was gently added to keep the sediment-water interfaces undisturbed, and the flumes were left illuminated and at 18 ºC. After 24 hours of settling, the sediments in the resuspension flume underwent standard laboratory resuspension tests with motor-controlled, stepwise-increased flow velocity, following the protocols of section 2.2.2. Due to the limited number of field samples, no further replicates of the resuspension tests were possible. During the resuspension tests, samples of the suspended material were taken from the sampling port located at the same height of OBS sensors. The samples were then used for OBS calibration and settling speed tests using the laboratory settling column equipped with mass balancing and time tracking systems. Protocols of settling speed tests can be found in more detail in section 2.2.3. In the meantime, sediments in the other CMF were cored, sectioned and sub-cored following the protocols provided in section 2.1.7. The top 10 mm sediment specimen that had been successfully wet-stained then underwent micro-CT scan experiments (section 2.1). The experimental workflows are schematically illustrated in Figure 2.10.

5.3 Results

Results of this chapter comprise two main parts: (i) section 5.3.1 presents the experimental results of field sandy and silty BSA, with respect to the suspension threshold, internal structure, settling velocity and drag; (ii) section 5.3.2 summarises

the resuspension and deposition data from both laboratory and field BSA, and presents predictive/quantitative characterization of microbial influences on sediment resuspension threshold and drag.

5.3.2 Resuspension and deposition characteristics

Resuspension threshold of BSA

The suspension concentration during the resuspension processes of the field-sampled sediments against the local bed shear stresses applied at each resuspension step are shown in Figure 5.1 (a). Regression lines enable the resuspension threshold to be estimated. The critical bed shear stress for suspension is estimated to 0.44 Pa for the field silty BSA, and 1.05 Pa for the field sandy BSA. According to van Rijn's formulas for sand-mud mixed sediments under abiotic conditions (van Rijn, 2007; Yao et al., 2018), the critical shear stress, $\tau_{m,crit}$, can be calculated as follows:

$$\tau_{m,crit} = (\frac{c_{gel}}{c_{gel,s}})(\frac{d_{sand}}{d_{50}})^{\gamma}\tau_{crit}, \text{ for } d_{50} < 62\ \mu m \qquad \text{Eq. 5.1}$$

in which $\tau_{m,crit}$ is the critical shear stress for sand-mud mixed sediments under abiotic conditions. c_{gel} is the gelling mass concentration of the fine particles, $c_{gel,s}$ is the dry bulk density of sand bed by mass, and $c_{gel} = (d_{50}/d_{sand})c_{gel,s}$. γ is an empirical coefficient, in the range of 1-2 (1.5 is generally adopted and also selected in this work (Yao et al., 2018)). Critical shear stress for initiating abiotic sand grains, τ_{crit}, is calculated using empirical equations previously developed using the same flume apparatus:

$$\theta_{crit} = \frac{\tau_{crit}}{(\rho_s - \rho_w)gd_{50}} = 0.043D_*^{1.152},\ D_* < 10 \qquad \text{Eq. 5.2}$$

$$D_* = [\frac{(\rho_s/\rho_w - 1)g}{\upsilon^2}]^{1/3} d_{50}$$

The calculated empirical resuspension threshold is 0.28 Pa for Field silty BSA (d_{50}=14.2μm, d_{sand} = 76.7 μm), and 1.55 Pa for field sandy BSA (d_{50}=27.9 μm, d_{sand} = 169.5 μm). Compared to the tested resuspension threshold from the experiments (0.44 Pa for the field silty BSA, and 1.05 Pa for the field sandy BSA), the presence of microbial life and organic matter enhances sediment stability against resuspension in the case of field silty BSA, while reduces the sediment resuspension resistance for field sandy BSA (Figure 5.1 (b)).

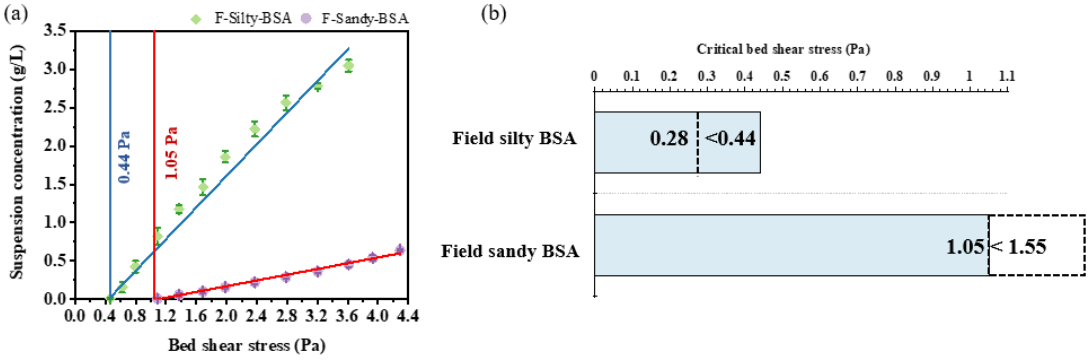

Figure 5.1 Suspension features of field sandy and silty BSA. (a) plots the step-varying suspension concentration against the bed shear stress applied at each step, for field sandy BSA (blue) and field silty BSA (red). (b) Comparisons between the resuspension threshold of field sandy and silty BSA, and the theoretical resuspension threshold of abiotic conditions.

Fractal structure of BSA

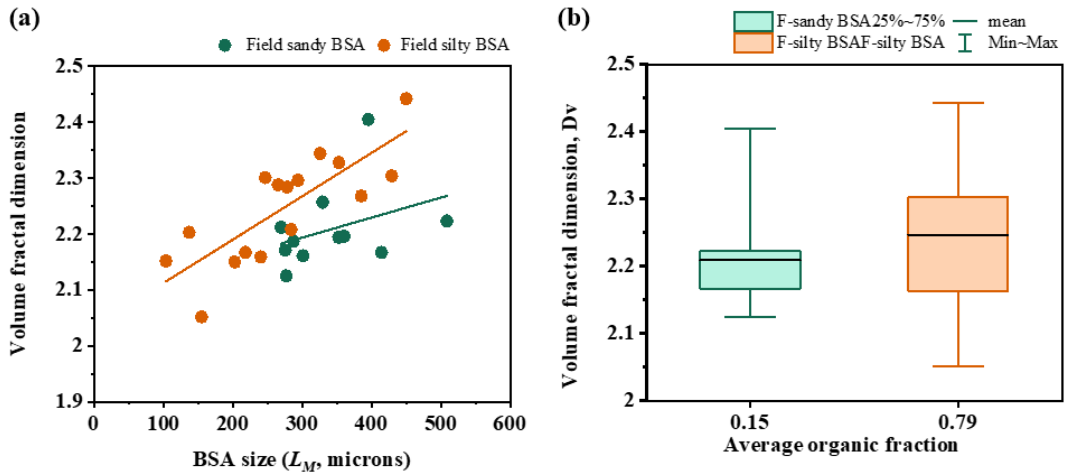

Figure 5.2 Variations of volume fractal dimension as BSA size increases for field sandy BSA (green dots) and field silty BSA (orange dots) (a); volume fractal dimension distributions (min- max, 25%-75%, and mean values as solid black lines of each box) for field sandy BSA of 15% organic fraction and for field silty BSA of 79% organic fraction.

Table 5. 1 Bivariate correlation between BSA size, L_M, and volume fractal dimension, Dv for field silty and sandy BSA.

Bivariate correlation between L_M and Dv		
Field silty BSA	Pearson Correlation	0.803**
	Spearman Correlation	0.819**
	Sig. (2-tailed)	$p < 0.05$
	N	16
Field sandy BSA	Pearson Correlation	0.351
	Spearman Correlation	0.379
	Sig. (2-tailed)	0.29
	N	11

Table 5. 2 Statistical results of nonparametric Mann-Whitney U test for organic fraction differences between clay and fluff BSA

	Field silty BSA	Field sandy BSA	Nonparametric Mann-Whitney U test	Independent-samples T test*
	$\tilde{X}; \bar{X} \pm SD(n)$		p value	p value
Organic fraction	0.80; 0.79 ± 0.58 (16)	0.16; 0.15 ± 0.50 (11)	N/A	< 0.05
Volume fractal dimension	2.28; 2.24 ± 0.10 (16)	2.19; 2.21 ± 0.07 (11)	0.245	N/A

*The organic fraction of both field silty and sandy BSA apply to normal distribution, and thus independent-samples T test were performed. Volume fractal dimension of field sandy BSA do not apply to normal distribution, nonparametric Mann-Whitney U test was performed.

A consistent pattern of the positive trend between BSA size and volume fractal

dimension is presented in the two field BSA, which agrees with the laboratory clay and fluff BSA (Figure 4.1, Chapter 4). Neither of the two field BSA present the generally-expected negative trend that BSA should develop towards loosely-connected structures. As discussed in Chapter 4, such increasing trends might result from a compaction process caused by microbial cell colonization and organic matter production, and might also be caused by a distinct BSA development pattern at the seabed. The BSA of a higher organic matter is associated with, on average, a more packed internal structure (Figure 5.2(b)). The differences in average volume fractal dimension between field silty and sandy BSA are however insignificant, as indicated in Table 5.2. This implies that the processes of BSA structure development are complex, and some other processes, in addition to organic matter production, might also be involved to influence the structure development.

Settling velocities of BSA

Similar to the settling velocity analysis in Chapter 4, the experimentally-tested settling velocities are compared with the four estimated velocities using the same four principles applied in Chapter 4 (listed in Table 4.1), for both field sandy (Figure 5.3 (a)) and silty BSA (Figure 5.3 (b)). Box A in Figure 5.3 plots the experimentally-tested settling velocities, while box B-E plot the estimated velocities from using the methods (i)-(iv) of Table 4.1. Statistical results of the differences between the experimentally-tested and the theoretically-estimated velocities are listed in Table 5.3.

The estimated settling velocity in Box B is calculated by simply considering the contents of sediment particles, and exclude the organic matter and pore water. Box C plots the velocity estimates by taking account of both sediment particles and organic matter. The velocity estimates in Box B and C show significant discrepancies with the experimental velocities (p <0.05, Table 5.3). This result indicates consistent trends to those of clay and fluff BSA, that only considering the solid matter component of organic

matter and sediment particles does not provide reliable estimates of the settling velocity. Box D plots the estimated settling velocity after taking account of the pore water, and improves the level of agreement with the experimental data. This result presents is consistent with the laboratory clay and fluff BSA results, that the pore water appears to be significantly correlated with settling velocity. As the Reynolds number of both field sandy and silty BSA exceeds 1, some overestimation remains because form drag is not accounted for. This is confirmed by the significant differences between the velocities in Box A and D (p <0.05). After taking account of the form drag by using Schiller and Naumann's empirical equation, the estimated velocities show further improved agreement with the experimental data (plotted as Box E) for both field sandy and silty BSA.

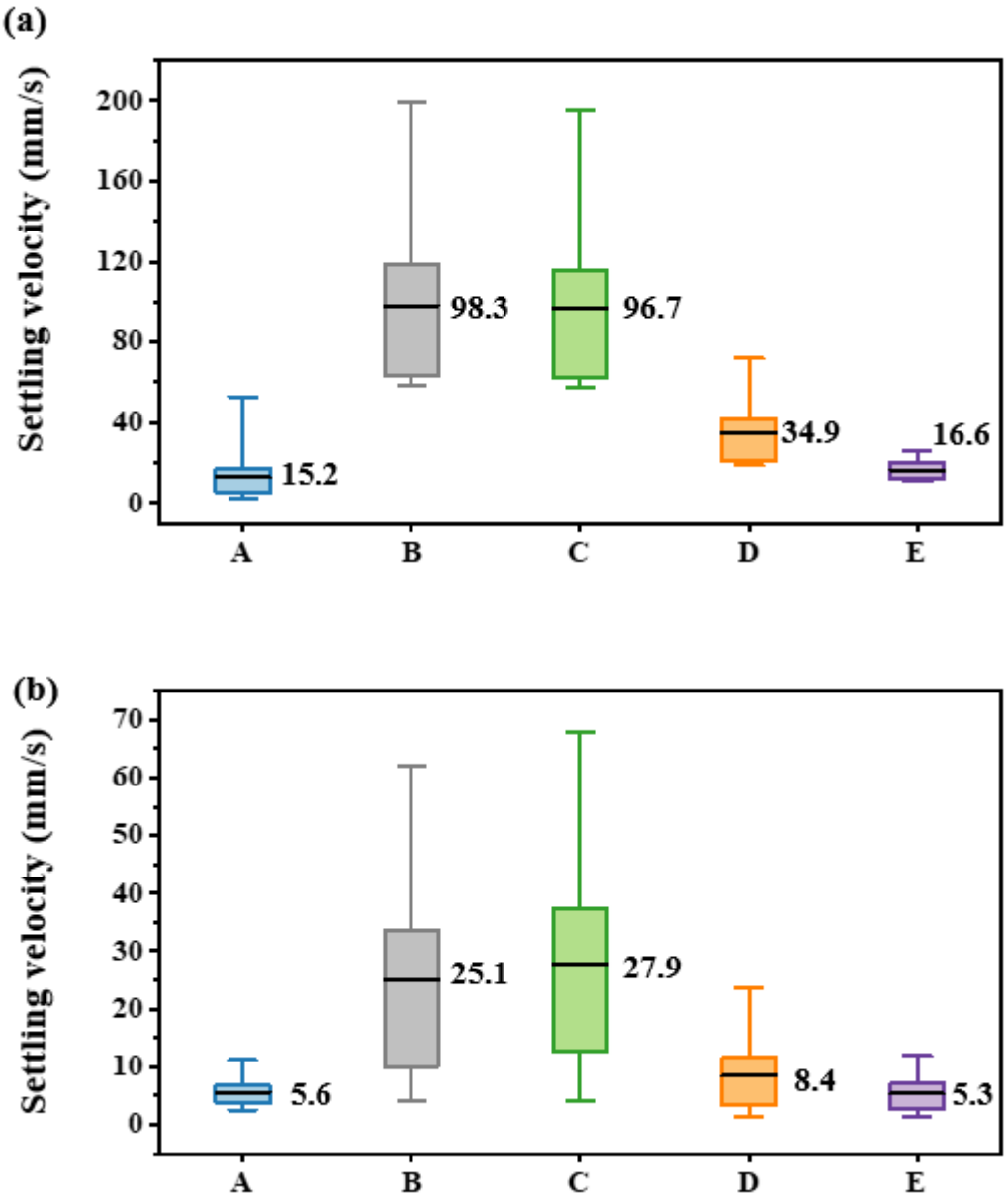

Figure 5.3 **C**omparisons between experimental settling velocity and estimated settling velocity for field sandy BSA (a) and field silty BSA (b). Box A is the experimentally-tested settling velocity, B-D are estimated settling velocities using the methods (i)-(iii) as listed in Table 4.1. In particular, B is the estimated velocity which only accounts the mass of sediment fraction but exclude the organic fraction; C is the estimated velocity which includes the organic fractions in mass; D is the estimated velocity which takes account of volumetric characteristics; E is the estimated velocity which considers the form drag effects by using Schiller-Naumann's empirical drag (while B-D simply considers the skin friction drag by using Stokes drag). The bars indicate the maximum and minimum

values of settling velocities and the extent of the box indicates the velocities account for 25%-75% of overall accumulate distribution. Middle solid black lines in each box represent the mean settling velocities, with the values being labelled on the right hand side.

Table 5. 3 Statistical results of the differences between the experimentally-tested and theoretically-estimated velocities for field silty and sandy BSA.

BSA type	**Experimentally-tested velocities**	**Estimated velocities**		**ANOVA (Bonferroni) *p* value**	**Statistical difference**
		$\tilde{X}; \bar{X} \pm SD(n)$			
Field silty BSA	Box A 5.55; 5.60 ± 2.34 (41)	Box B	23.83; 25.07 ± 15.97 (16)	< 0.05	Significant difference
		Box C	25.33; 27.87 ± 17.93 (16)	< 0.05	Significant difference
		Box D	7.63 8.40 ±5.80 (16)	1.00	**No significant difference**
		Box E	5.37 5.29 ± 2.82 (16)	1.00	**No significant difference**
Field sandy BSA	Box A 15.0; 15.2 ± 8.38 (91)	Box B	90.30; 98.34 ± 44.08 (11	< 0.05	Significant difference
		Box C	89.21; 96.74 ± 43.28 (11)	< 0.05	Significant difference
		Box D	28.32; 34.86 ± 17.51 (11)	< 0.05	Significant difference
		Box E	15.57; 16.56 ± 5.37 (11)	1.00	**No significant difference**

Drag of BSA

The estimates of biotic drag show a close agreement with abiotic drag

($C_{Ds} = \frac{24}{\mathrm{Re}}(1+0.15\mathrm{Re}^{0.687})$ for both the field sandy and silty BSA (Figure 5.4 (a) and (b)). The statistical results in Table 5.4 confirm that there is no significant difference between the biotic and abiotic drag for both field sandy and silty BSA. The drag of field sandy BSA appears to be underestimated while the drag of field silty BSA seems to be overestimated, however the differences are almost negligible. Instead of rushing to conclude that the microbial influences on the drag of the field sandy and silty BSA can be overlooked, it may be worth taking a look at the potential reasons/mechanisms from existing literature. Mu e al. (2008) studied the drag of microbial granules which have relatively smooth surfaces but high porosities and found the drag of microbial granules show reduced drag compared to that for abiotic solid spheres with rigid surfaces. Their work demonstrates such reduction effects are caused by the permeable flow through the internal pore space of the granules (Mu et al., 2008). Nicolella et al. (1999), Saravanan and Sreekrishnan (2005), and Andalib et al. (2010), studied the drag of biofilm-coated particles and found increased drag due to microbial mediations, which they explained was due to the increase of surface roughness by biofilm-coating as well as the potential deformation processes due to the colonization of soft organic matter (Nicolella et al., 1999; Saravanan and Sreekrishnan, 2005; Andalib, et al., 2010). The effects of microbial colonization/coating/aggregation therefore seem to have a range of effects, including both increasing drag, and decreasing drag. If this is true, a transitional zone should exist between the increasing effects of drag and the decreasing effect of drag for microbial influences. For the aggregates in this transition zone, the increasing and decreasing effects tend to be neutralized, resulting in a drag that is similar to the abiotic case of impermeable, solid spheres with rigid surfaces. It may therefore be the case that the moderate drag differences from abiotic drag, C_{Ds}, that occurred in field sandy and silty BSA, as well as the fluff BSA investigated in Chapter 4 may result from such neutralization of drag reduction and enhancement. However, such transitional zone has, to the best of the author's knowledge, not been recorded in literature, and can only be

regarded as a hypothesis at this stage.

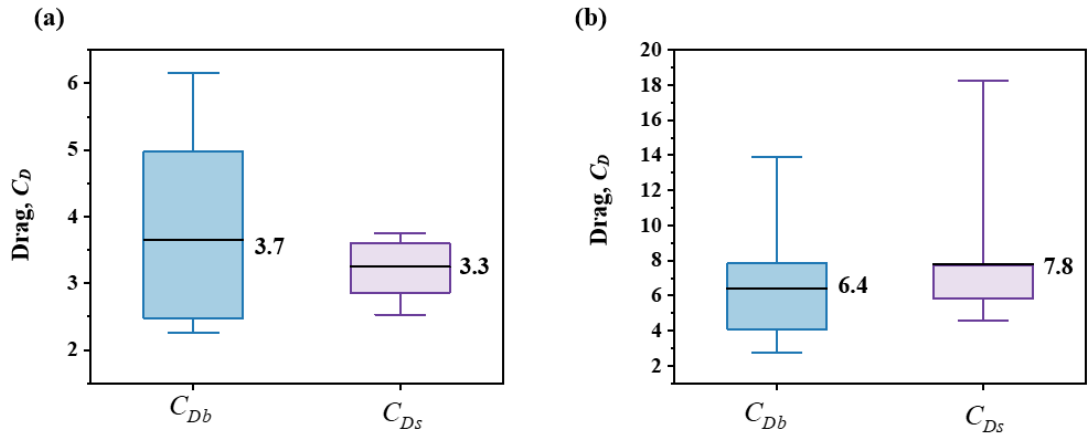

Figure 5.4 Comparisons between biotic (C_{Db}, blue box) and abiotic drag (C_{Ds}, purple box), for field sandy BSA (a) and field silty BSA (b). The bars indicate the maximum and minimum values of drag and the extent of the box indicates the drag accounts for 25%-75% of overall accumulate distribution. Black solid lines in the middle of each box represents the mean value of drag and is also labelled on the right hand side.

Table 5. 4 Statistical results of the differences between biotic and abiotic drag for field sandy and silty BSA.

	Biotic drag C_{Db}	Abiotic drag C_{Ds}	Pairwise comparison	
	$\tilde{X}$; $\bar{X} \pm SD(n)$		p value *	Statistical difference
Field sandy BSA	2.98; 3.65 ± 1.37(11)	3.43; 3.25 ± 0.41(11)	0.41	No significant difference
Field silty BSA	6.84; 6.41 ±2.82 (16)	7.21; 7.80 ± 3.43 (16)	0.35	No significant difference

5.3.3 Quantitative analysis of microbial influences on sediment resuspension and deposition

This section summarizes the resuspension and deposition features of field sandy and silty BSA together with laboratory clay, fluff and mat BSA, to pursue a systematic and

quantitative understanding of microbial mediations.

Analysis of microbial influences on sediment resuspension

The dimensionless critical Shields parameter, $\theta_{crit,A} = \frac{\tau_{crit}}{(\rho_A - \rho_w)gd_A}$, and dimensionless diameter, $D_{*,A} = (\frac{(\rho_A / \rho_w - 1)g}{\nu^2})^{1/3} d_A$, are calculated using ρ_A and d_A, for field sandy and silty BSA and laboratory mat, fluff and clay BSA. The plots of $\theta_{crit,A}$ against $D_{*,A}$ in Figure 5.5 (a) (linear axis) and (b) (log-log axis) show the dimensionless critical Shields parameter appear to present the following power law relationship as a function of dimensionless diameter:

$$\theta_{crit,A} = 16.7 D_{*A}^{-1.2},\ \mathrm{R}^2 = 0.90,\ p < 0.05 \qquad \text{Eq. 5.3}$$

In Figure 5.6 the dimensionless critical Shields parameter, $\theta_{crit,A}$, is plotted against the flow Reynolds number, $\mathrm{Re}_A = \frac{u_* d_A \rho_w}{\nu^2}$, and present a similar power law relationship as a function of flow Reynolds number:

$$\theta_{crit,A} = 75.1 \mathrm{Re}_A^{-1.2},\ \mathrm{R}^2 = 0.75,\ p < 0.05 \qquad \text{Eq. 5.4}$$

These relationships indicate a predictive way for characterizing microbial mediations. The relationships appear not to be differentiated between the biostabilization and destabilization BSA, for both the relationships of $\theta_{crit,A} \sim D_{*,A}$, and $\theta_{crit,A} \sim \mathrm{Re}_A$. The only exception may be the mat BSA in the relationship of $\theta_{crit,A} \sim D_{*,A}$, which exhibit more scattered compared to the other BSA but show better agreement with the power law relationship between $\theta_{crit,A} \sim \mathrm{Re}_A$. Potential reasons may be the limited number of mat BSA that were analysed in this work, or missing mechanisms, such as different

resuspension responses between the BSA developed under calm water (mat BSA) and the BSA developed under cyclic resuspension-deposition (laboratory clay and fluff BSA, field sandy and silty BSA).

Experimentally-tested suspension thresholds are plotted against the estimated suspension thresholds in Figure 5.7, using the empirical relationships between $\theta_{crit,A} \sim D_{*,A}$ in (a), and $\theta_{crit,A} \sim \mathrm{Re}_A$ in (b) respectively. The results show a good level of agreement, with results falling on or close to the 1:1 agreement line. Mat BSA is the one exception, for which the resuspension threshold is largely underestimated using both relationships. The mat BSA is established after a 6-day incubation period sitting in flume under quiescent flow conditions, while the other four types of BSA are grown under cyclic conditions. Such differentiated hydrodynamic forcing may lead to different responses of BSA to the local flow erosion during the resuspension tests. Previous work shows that the resuspension of microbial sediments that established under calm flow conditions show different resuspension patterns with those grown under cyclic resuspension conditions, in terms of resuspension process, erosion rate and ripple structures (Chen et al., 2019). It has also been found that different rest times for BSA sitting in seabed sediments under calm flow conditions leads to different architectures of the BSA to be developed, e.g. as the rest time increases, the internal structure of the BSA appears to be less prevalent (Stone, et al., 2008). Besides the internal structure, according to the findings of Fang et al., (2020), the adhesion strength may also vary, which in turn affects the responses of BSA to local flow resuspension forcing. Further work regarding the above effects may thus be needed to improve the accuracy of the empirical relationships proposed in this work.

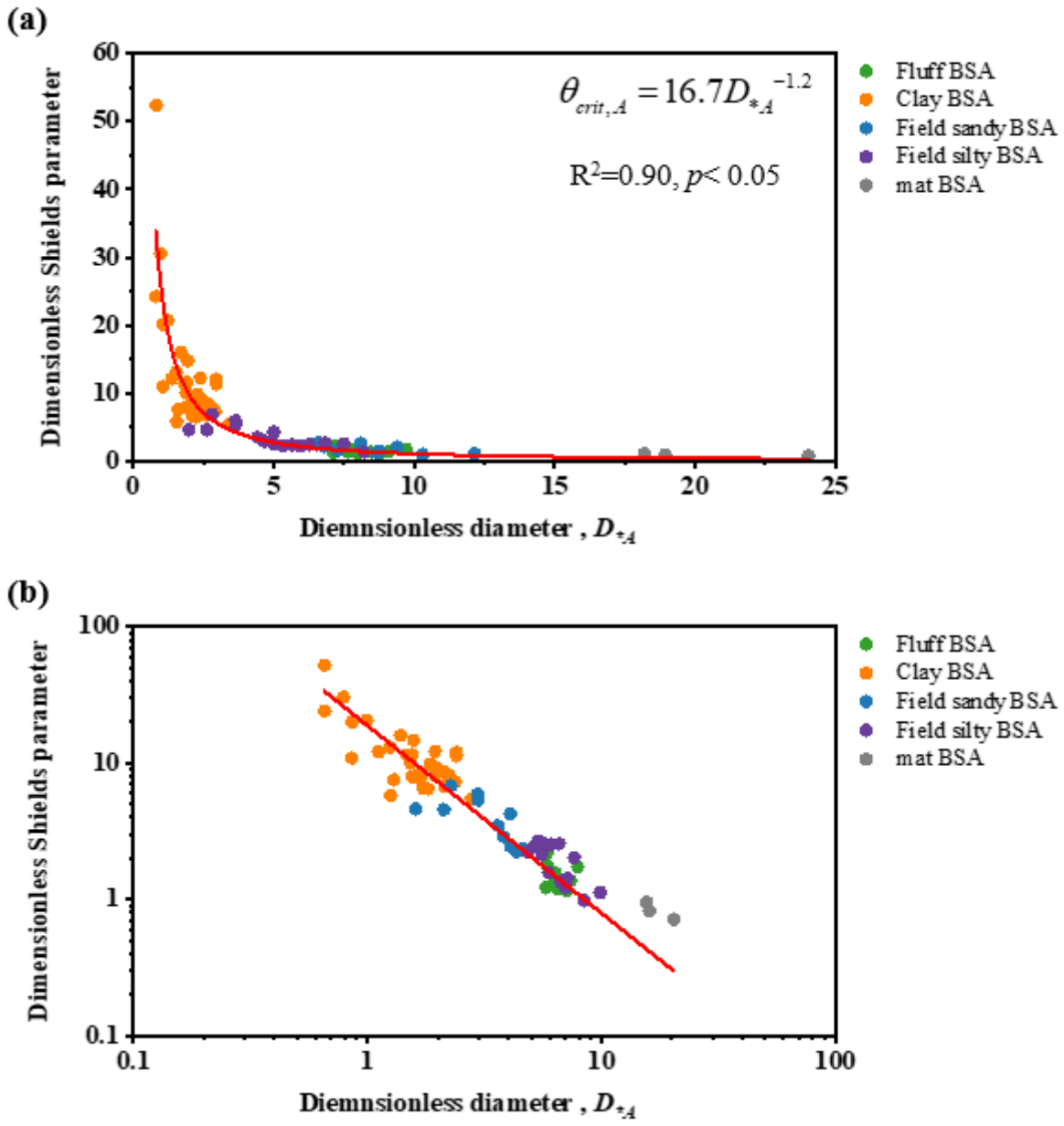

Figure 5.5 Plots of the relationships between dimensionless Shields diameter, $\theta_{crit,A}$, and dimensionless diameter, $D_{*,A}$, for laboratory mat, fluff, clay BSA, and field sandy and silty BSA. (a) using a linear axis and (b) using a log-log axis.

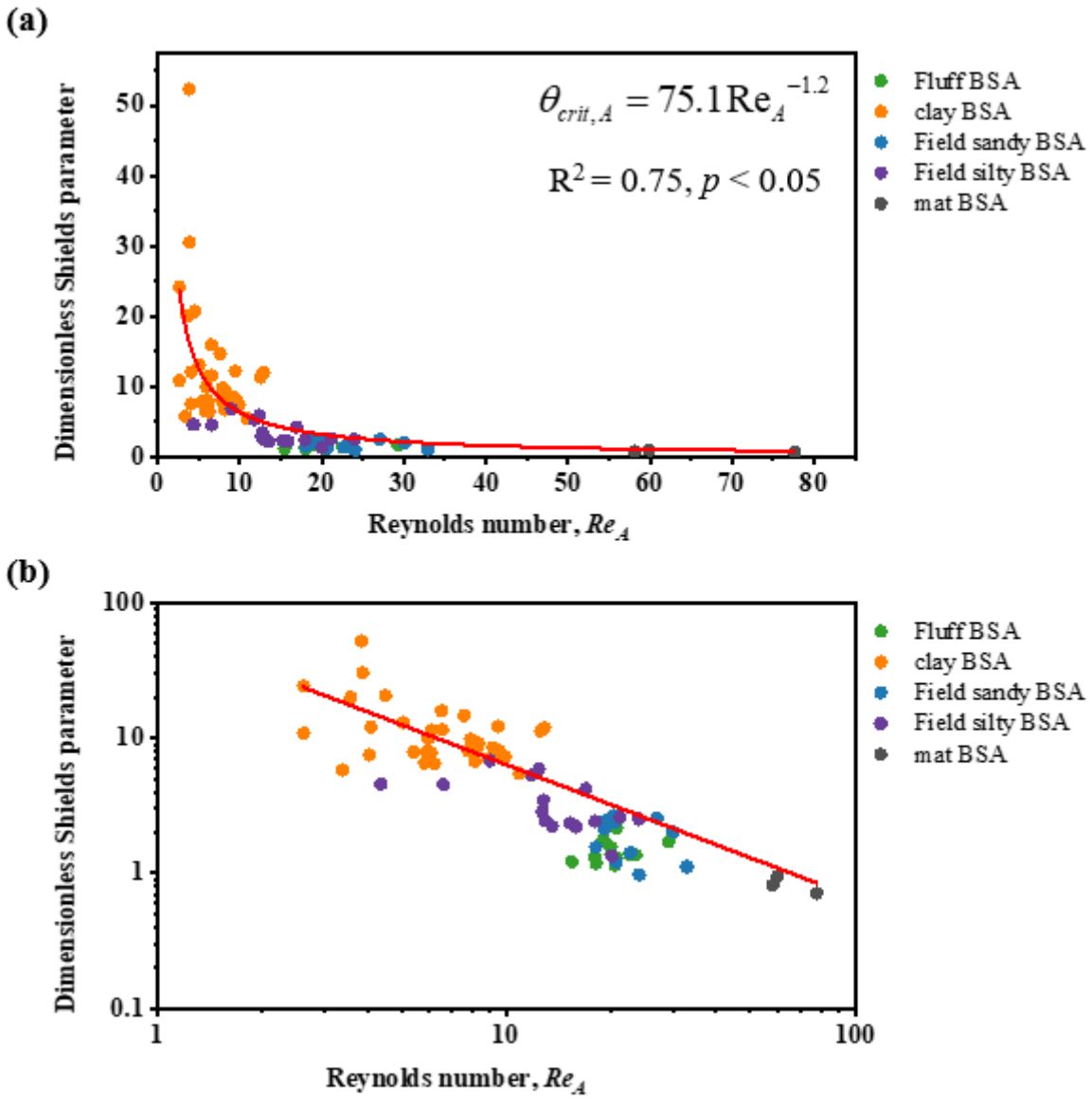

Figure 5.6 Plots of lots of the relationships between dimensionless Shields diameter, $\theta_{crit,A}$, and Reynolds number, Re_A, for laboratory mat, fluff, clay BSA, and field sandy and silty BSA. (a) using a linear axis and (b) using a log-log axis.

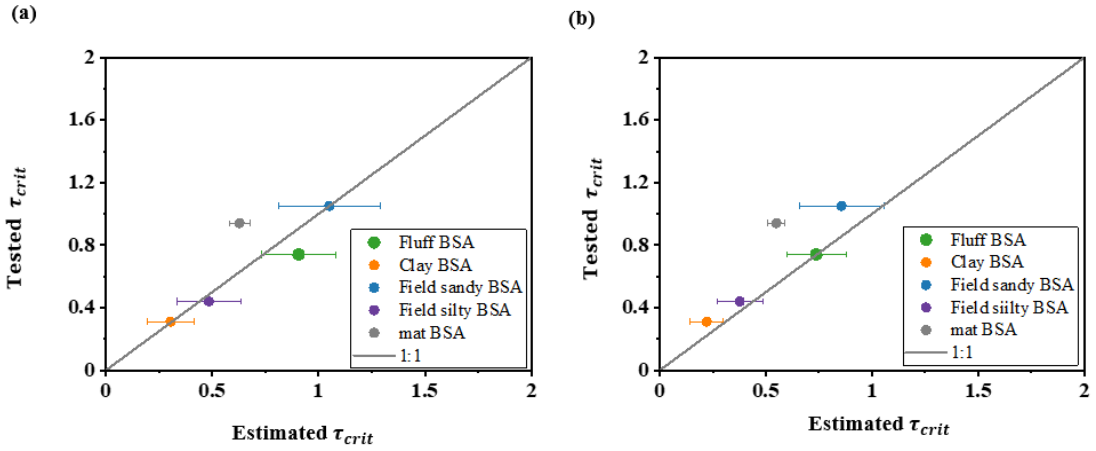

Figure 5.7 Plots of the experimentally-tested resuspension threshold, τ_{crit}, against the estimated resuspension threshold using the empirical relationships of $\theta_{crit,A} \sim D_{*,A}$ (a), and $\theta_{crit,A} \sim \mathrm{Re}_A$ (b), respectively.

Analysis of microbial influences on sediment deposition

To understand the microbial influences on drag, the biotic drag ratio which is proposed in Chapter 4 to characterize the combined microbial mediations of drag is calculated for field BSA and summarized together with laboratory BSA. Figure 5.8 (a) plots the biotic drag ratio against BSA dimensionless diameter and Figure 5.9 (a) plots the biotic drag ratio against the BSA Reynolds number. Whilst the microbial influences on drag are small, distinct patterns of such microbial influences are discernible in both Figure 5.8 (a) and Figure 5.8 (b), for clay, field silty, field sandy and fluff BSA. By multiplying the biotic drag ratio, η, with $(1-\varphi_b)(1-\varepsilon)$ (where $\varphi_s+\varphi_b=1$), the differentiated patterns appear to be diminished and start to align to one line. By plotting the adjusted biotic drag ratio, $\eta(1-\varphi_b)(1-\varepsilon)$, against both dimensionless diameter, $D_{*,A}$ (Figure 5.9 (a) and (b)), and Reynolds number, Re_A (Figure 5.10 (a) and (b)), the trend becomes clearer and can be described by the following relationships:

$$\eta(1-\varphi_b)(1-\varepsilon) = 0.0004\,\mathrm{D}_{*,A}^{\,2.1},\ \mathrm{R}^2 = 0.80,\ p < 0.05 \qquad \text{Eq. 5.5}$$

$$\eta(1-\varphi_b)(1-\varepsilon) = 0.0025\,\mathrm{Re}_A,\ \mathrm{R}^2 = 0.48,\ p < 0.05 \qquad \text{Eq. 5.6}$$

From which, we can obtain the two following expressions of biotic drag in terms of either dimensionless diameter and Reynolds number, respectively:

$$C_{Db} = 0.0004\,\mathrm{D}_{*,A}^{\,2.1} \cdot \frac{C_{Ds}}{(1-\varphi_b)(1-\varepsilon)} \qquad \text{Eq. 5.7}$$

$$C_{Db} = 0.0025\,\mathrm{Re}_A \cdot \frac{C_{Ds}}{(1-\varphi_b)(1-\varepsilon)} \qquad \text{Eq. 5.8}$$

The above relationships present a quantitative characterization of the microbial influences on drag for different types of BSA, representing the combined microbial influences from permeable flow, surface roughness, internal pore architecture and potential deformation. The settling velocities estimated by taking microbial influences on drag into account are plotted against the average settling velocity of the experimental tested results in Figure 5.11, by using the relationships with $\mathrm{D}_{*,A}$ in (a) and the relationship with Re_A in (b). The quality of fitting is generally acceptable with an average root mean square error of 1.5-10.4 for using $\mathrm{D}_{*,A}$ and 0.6-8 using Re_A, suggesting the relationship of Re_A provides a slightly better representation for the tested BSA.

It may be worth noting the quantitative relationships obtained from the above analysis, e.g. the resuspension thresholds of microbial sediments and microbial influences on drag, should be regarded as a preliminary start and more tests of microbial sediments, to characterise a larger spatial and temporal range, are needed for a more robust

predictive/modelling capability.

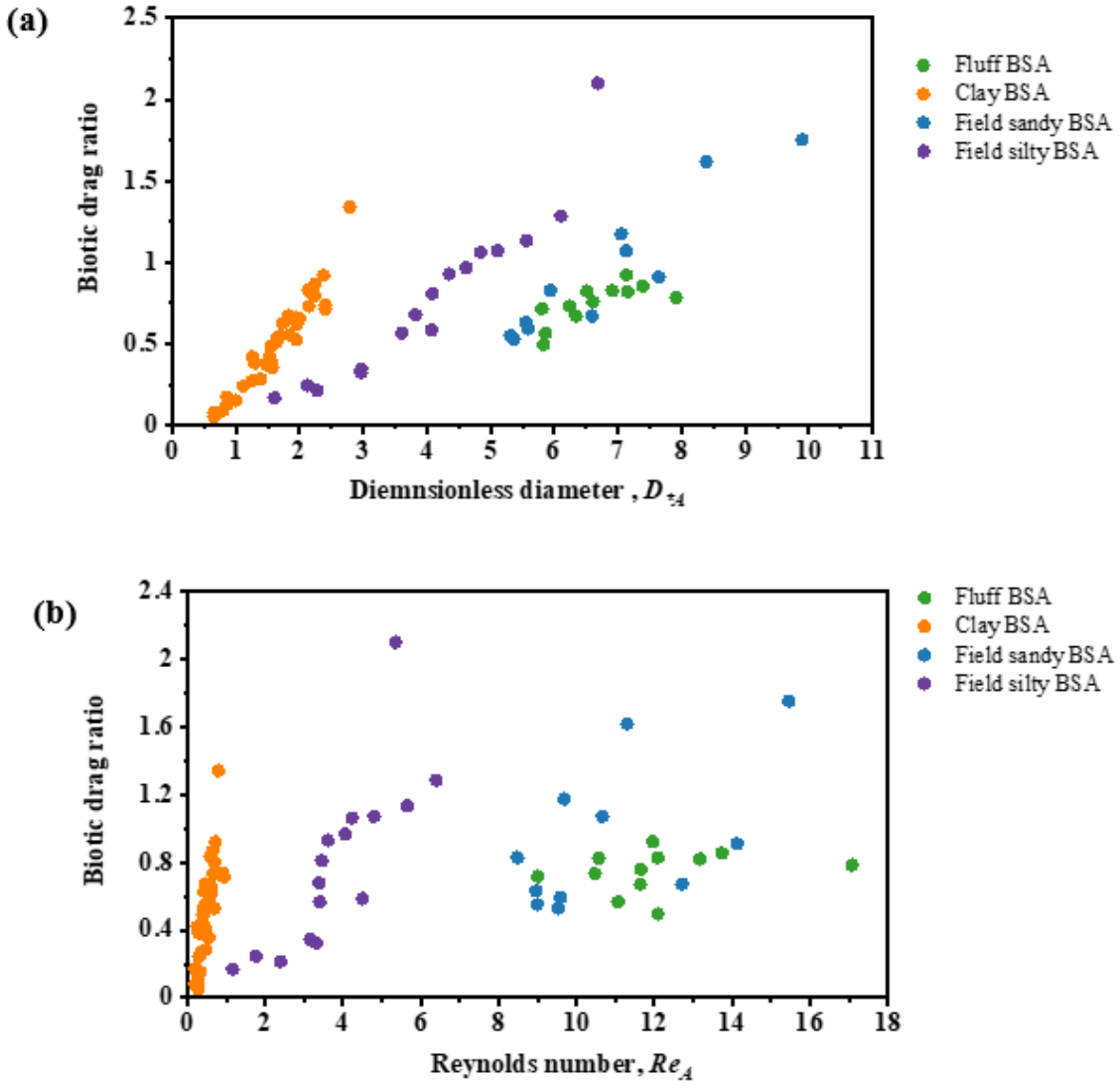

Figure 5.8 Plots of biotic drag against dimensionless diameter of BSA (a) and against BSA Reynolds number in (b).

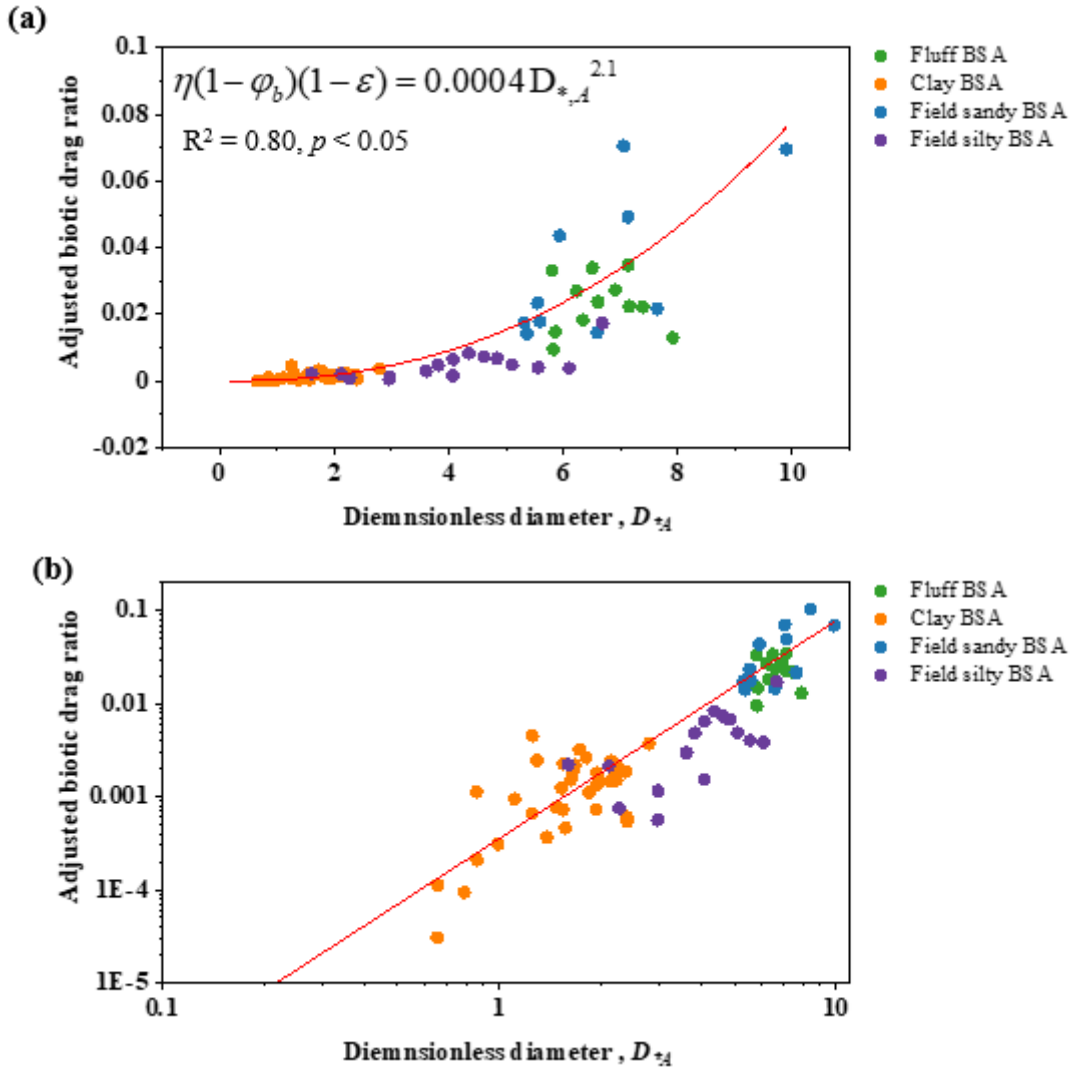

Figure 5.9 Plots of the relationships between adjusted biotic drag ratio, $\eta(1-\varphi_b)(1-\varepsilon)$, and dimensionless diameter, $D_{*,A}$, for laboratory mat, fluff, clay BSA, and field sandy and silty BSA. (a) using a linear axis and (b) using a log-log axis.

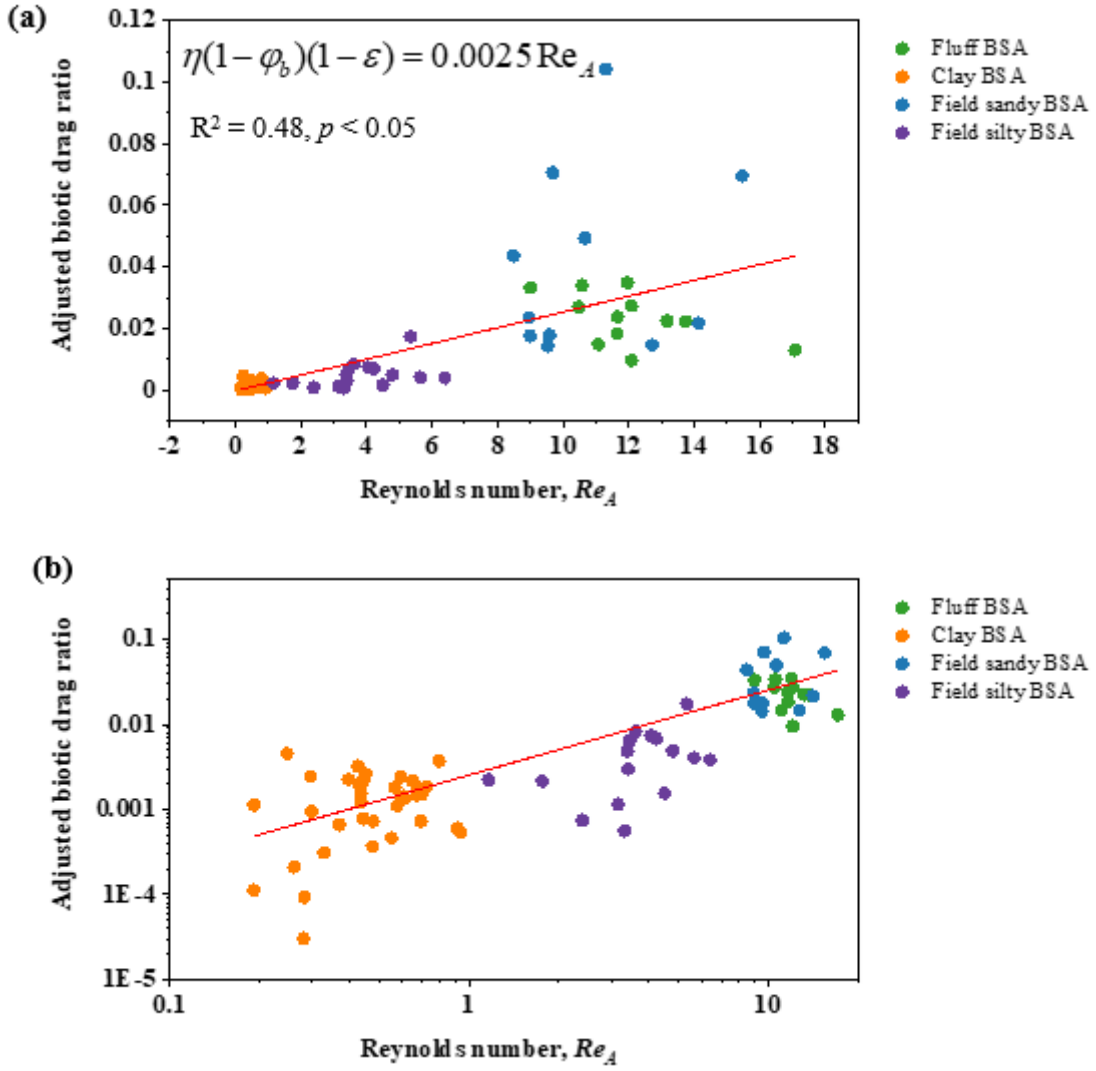

Figure 5.10 Plots of the relationships between adjusted biotic drag ratio, $\eta(1-\varphi_b)(1-\varepsilon)$, and Reynolds number, Re_A, for laboratory mat, fluff, clay BSA, and field sandy and silty BSA. (a) using a linear axis and (b) using a log-log axis.

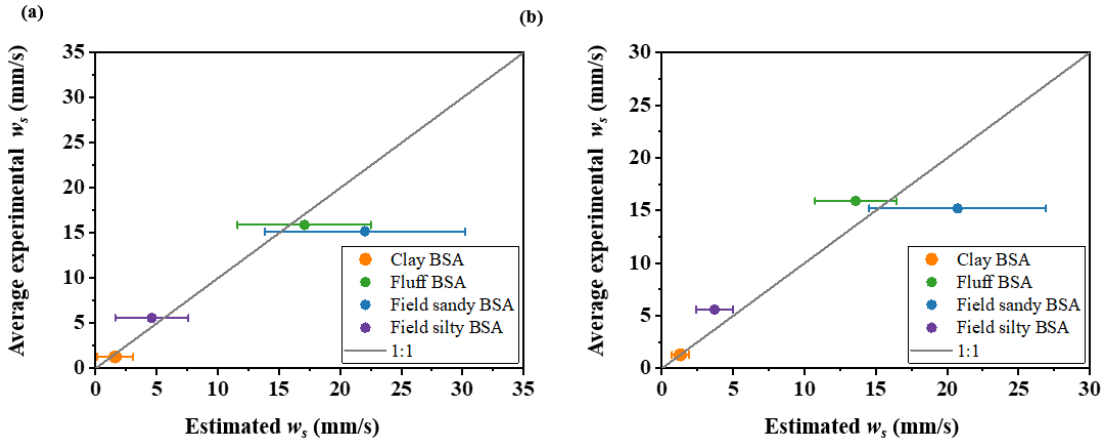

Figure 5.11 Plots of the average settling velocity obtained from experimental tests against the estimated settling velocity by taking account of microbial influences on drag. Velocity estimated according to Eq. 5.7 is plotted in (a) and the velocity estimated according to Eq. 5.8 is plotted in (b).

5.4 Discussion

Microbial colonization of sediment particles and the copious secretion of mucilaginous EPS bridge sediment particles into aggregates, forming complex matrices (Decho, 2000; Flemming, 2019). When the microbial sediment interactions are well developed and a mat matrix is established, the sediment particles are densely populated and adhered, where mat-like matrices up to a centimetre thick can be established (Cuadrado et al., 2014; Gerbersdorf and Wieprecht, 2015). Vignaga et al.(2013) found that sediment particles are tightly adhered into mature microbial mat matrices over a ten-week incubation and behaved as an elastic membrane in the face of hydrodynamic forcing. The strong adherence strength provided by the microbial mat is thought to provide important support for the sediment particles to be retained on the seabed, and the adhesive force provided by the gluing effects of mucilaginous microbial substances is generally considered as an important stabilizing force for sediments to resist flow erosion (Fang et al., 2014; Fang et al., 2017). Such adhesion forces are found to be determined by the development period of microbial cells within sediment matrices. Fang et al. (2014) experimentally investigated the changes of adhesion forces and found

during the beginning 2-3 works the adhesion force increases with time to a peak value, after which it starts to decrease slowly with time. This could explain why the 4-week old microbial sediments have a higher stability than the 8-week old microbial sediments (Fang et al., 2014). The above knowledge of microbial mediations of sediments explains the biostabilization of mat BSA observed in this work, as the incubation in calm water during a six-day period leads the microbial adhesion with sediment particles to be more fully developed compared, to the fluff BSA and thus exhibit an enhanced stabilizing force. However, the destabilization observed in this work cannot be fully explained by the above knowledge of microbial sediment stability. This is because, according to the above theory, even a short rest time (less than 24 hours) should enable the development of microbial adhesion, which should aid the microbial sediments to resist low flow forcing, rather than advance the motion of sediment particles. One possible explanation may be that microbial colonization modifies aggregate density. In particular, the mucilaginous EPS forming microbial matrices are highly hydrated, sometimes binding more than 90% of water (Schmitt and Flemming, 1999) and have much lower density compared to the sediment particles (Andalib et al., 2010; Flemming and Wingender, 2010). The colonization of such microbial substances reduces the gross density of the sediments compared to the abiotic conditions (ρ_M of BSA analysed in this work show an average value of ~1845 kg/m^3, much lower than the density of abiotic sediments, ~ 2650 kg/m^3), which in turn has a negative effect of sediment stabilization. However, the densities of both the mat and fluff BSA are reduced. The mechanism that leads the sediment stabilities to be reduced seems difficult to be determined simply by the densities, and might be attributed to a range of factors. For example, as the development time for microbial substances increases, aggregates became less convoluted (Stone, et al., 2008). Microbial matrices with fewer irregularities can decrease flow drag, and have the erosion thresholds increased (De Brouwer et al., 2005; Friend et al., 2008). The microbial attachment on sediment particles, the coating of

particle surfaces and the penetration of EPS to the internal pore spaces may also induce differentiated flow infiltration and thus drag exerted on sediment particles, which in turn affects the sediment stability (Mohr et al., 2018).

Natural ecosystems, in which bio-sediment combinations develop, vary across different spatial and temporal scales, and are affected by a range of environmental conditions (Friend, et al., 2003; Le Hir et al., 2007; Lundkvist et al., 2007). This includes the migration and restoration of coastal vegetation (Feagin et al., 2009), the bioturbations of macro-fauna (Orvain et al., 2004), the frequency and intensity of rainfalls and the diverse distribution of microorganisms (Gerbersdorf and Wieprecht, 2015; Paterson et al., 2000; Paterson, 1989). These factors perform combined effects to determine the responses of natural microbial sediments against flow resuspension. To which extent the destabilization effects are of relevance in natural ecosystems and should be accounted in modelling remains a question and is worth further study through more extensive investigation of field sediments.

5.5 Conclusions

This chapter comprises two major components. The first part is the experimental studies of the resuspension threshold, volume fractal dimension, settling velocity and drag of field BSA, and the second part pursues a quantitative understanding of microbial mediations to sediment resuspension and deposition.

Resuspension tests find the field sandy BSA present a decreased resuspension threshold compared to the theoretical thresholds of abiotic conditions, while the field silty BSA present an increased threshold. This suggests the existence of microbial destabilization effects in the field, though as discussed in section 5.4, understanding the extent and relevance of destabilised BSA needs more extensive testing.

The field silty BSA with high organic fraction show consistent results with the highly-organic laboratory-created clay BSA, in which the volume fractal dimension

significantly increases as BSA size develops. The field sandy BSA, with much lower organic fraction of 15% present, shows a generally positive relationship with volume fractal dimension but the relationship is not statistically significant. Whilst the majority of previous studies suggest that aggregates develop towards loosely-connected structures, none of the laboratory-created and field-collected BSA shows such negative trend. The different development trends of BSA structures were hypothesized to occur as a result of microbial influences on aggregate structures, which cannot be characterized by existing aggregation models (e.g. CCA) and suggest a need to better account for microbial mediation in future work.

Comparisons between the estimated and experimental settling velocities suggest that simply considering the effects of sediment and/or organic matter components does not provide good velocity estimates, leading to significant overestimation. Both the laboratory-created and field-collected samples agree that considering the effects of pore water is necessary for velocity estimates, which provides strong evidence for the importance of pore water in determining aggregate deposition behaviours. In addition, form drag should also be considered when $Re > 1$ and including Schiller and Naumann's drag correction further improves the overall goodness of fit.

A quantitative analysis of these two types of field BSA as well as the laboratory mat, fluff and clay BSA investigated in Chapter 3 and 4 is conducted to pursue a quantitative understanding of microbial influences on sediment stability. The dimensionless Shields parameter for these five types of BSA can be described by a power law relationship with both the BSA dimensionless diameter and Reynolds number. This, as a preliminary start, provides a quantitative characterization of the microbial influences on sediment stability.

The biotic drag ratio of field BSA also show consistent patterns with the laboratory data, whereby the organic/sediment fraction and porosity can help to explain the distinct

patterns of microbial influence on drag. A quantitative characterization of microbial mediations on drag is presented, with a need for more extensive testing to further develop the ideas tentatively explored here.

Chapter 6 Conclusions and perspectives

The findings of this thesis provide a clearer and more comprehensive understanding of the mechanisms and properties of microbial sediment interactions and their influences on sediment transport. A new approach successfully characterizes BSA compositions and structures by utilising the novel technique of micro-CT scanning, and is used alongside more well-established techniques for studying sediment transport. The combination allows the microbial influences on the resuspension and deposition processes of sediment transport to be investigated down to the microscale. The volume, size and density of all components in each aggregate (e.g. sediment particles, organic matter and pore water), and the aggregate architectures (e.g. 3D volume fractal dimension) can be directly obtained from the 3D CT-scanned BSA matrices. Shields parameter estimates and force analysis for the critical processes of resuspension and deposition were analysed and used to account for the microbial mediations. A clearer understanding of microbiologically-mediated sediment transport becomes possible, providing an improved qualitative understanding and a framework for quantitative estimates.

6.1 Conclusions

The findings of this work progress our understanding of the mechanisms and properties of microbial sediment interactions and transport, and advances our current knowledge. A summary of the key findings is outlined as follows.

- The microbial growth, the production of organic matter, and the interaction/aggregation with sediment particles are found to play a fundamentally important role in shaping BSA architecture. In contrast to the established trend that aggregates always develop towards loosely-connected structures, due to the complexities of microbial development and interactions with sediment particles, BSA structures observed in this work generally develop towards more compact structures. The positive trend between BSA structure and size is significant for the

BSA with high organic fraction (clay and field silty BSA), but is much less significant for the BSA with low organic fraction (fluff and field sandy BSA). At different stages of development, the BSA also present distinct geometries. For example, the fluff BSA at initial growth states of microbial development with low organic fractions (10-31%), appear to be more loosely-structured and adhere with relatively few sediment particles (< 10), forming smaller-sized aggregates. By contrast, the mat BSA, at a more fully developed state of microbial growth with a higher organic content (53-60%), tightly adhere and embed a larger number of sand grains (40-100) into the well-established mat-like matrices and form the BSA of 3-4 times larger sizes than the fluff ones.

- The BSA at different development states are also found to mediate the resuspension process in distinct ways. Where the microbial growth is at a more fully developed state with higher organic fractions, e.g. the mat BSA and the field silty BSA (organic fraction = 53-91%), the BSA are found to biostabilize sediments, resulting in enhanced resuspension thresholds. By contrast, the BSA that are less well developed, with lower organic fractions, e.g. the fluff BSA and the field sandy BSA (organic fraction = 7-31%), destabilize sediments, reducing the resuspension threshold. To date, the biostabilization effects of the microbial mat are widely acknowledged, while the BSA at younger states of development have been less well studied. This work clearly shows that the microbial sediment interactions at different development stages can have a range of effects on sediment stability.

- For depositional processes, the results of both the laboratory-created and field-collected aggregates in this work provides strong evidence to support the importance of pore water in settling velocity estimates. In contrast to the resuspension processes, the content of organic matter, as a sign of microbial growth state, is found to correlate with the drag of settling BSA but play a much less significant role on the settling velocities.

- The results highlight how the microbial influences on resuspension and deposition processes exhibit distinct patterns. The mediations of resuspension processes are sensitive to the development states of BSA, while the deposition processes are significantly determined by the volume of pore water and are less influenced by the organic matter content. To the best of the author's knowledge, the differentiated patterns of microbial influences on sediment resuspension and deposition processes are revealed for the first time, and clarify the needs for future investigations of the governing mechanisms.

- This work also undertook comprehensive quantitative analysis of the complex and variable microbial influences described. The predictive relationships proposed allow the key parameters for characterizing the dynamic processes of sediment transport in the presence of microbiology to be estimated, including the resuspension thresholds, drag and settling velocities. The advances presented provide a new understanding of the key mechanisms and help identify further work needed to better understand the sediment transport in the presence of microbiology.

6.2 Future research needs

The methods and findings of this work are likely to be of interest to a number of different research disciplines. Potential research needs are listed as follows for future research work to be meaningfully attempted.

- Some improvements to the methods presented may be needed for future work to achieve wider applicability. Three aspects of potential improvements are suggested: (1) the method established could be improved by programming dedicated scripts for analysing CT-images. This will allow the users to processes a larger number of scanned samples at a better efficiency, avoid the long period of image processing and analysis, and enable many more investigations of this kind; (2) future work may want to combine the micro-CT approach with other novel imaging techniques, such as FIB-nt, which has recently been used to make advanced progress in

detecting and characterising the individual microbial cells attached to aggregates; (3) testing whether the parameters obtained by micro-CT techniques could be obtained by more common and more budget-friendly techniques, to allow future investigations at a larger scale.

- Future research work may want to test natural BSA of larger temporal and spatial heterogeneity. Microbial sediment interactions and microbial sediment transport are complex and the exploration in this thesis is at preliminary stage. To progress further, future work is needed to test the theories and relationships presented in this thesis, such as through the investigation of field sediments to account for greater spatial and temporal variability.

- The growth of microbial cells, the production of organic matter and the interactions with sediment particles are consecutive processes that occur at different growth phases. The fluff and mat BSA, established at different development stages, play contrasting roles in mediating sediment stability, which includes both enhancing and reducing sediment stability. This result might highlight a need for future work to account for the effects of the microbial development stages on sediment stability, before modelling and prediction work can be meaningfully attempted.

- Microbial development in sediment matrices are sensitive to a range of environmental conditions, including disturbances by e.g. rainfall, bioturbation, storm events and hydrodynamic cycles, and nutrient conditions by e.g. local nitrogen depletion. Future work might want to conduct both laboratory and field experiments to take a more systematic consideration of such environmental influences on the establishment of BSA and the subsequent influences on resuspension and deposition behaviours.

- Microbial development with sediment particles can both increase and reduce the drag exerted on sediment particles, through increasing the particle surface roughness, and forming porous structures to allow internal flow filtration. As such,

this work hypothesized a transition zone in which microbial mediations of increasing and reducing drag co-occur and become neutralised. It is suggested that future research examines the transition zone and tests the potential threshold conditions for such a transition zone to occur.

Appendix A BSA geometrical characteristics summary

Table A is a summary of BSA geometrical characteristics. The volume of matter enveloped per aggregate (V_M), the maximum projected diameter of BSA on x-, y-, and z- axes (d_x, d_y and d_z, respectively) were measured based on the CT-scanned 3D BSA structures using "Label Analysis" module in Avizo 9.3.0. Aggregate volume (including both matter and pore water, V_A) were calculated according to $V_A = \frac{\pi}{6} d_x d_y d_z$.The sphere volume equivalent diameter of matter and aggregate (d_M), and aggregate (d_A), were calculated according to Eq. 4.5 and Eq.4.7. Aggregate porosity (ε) was calculated according to Eq. 4.17, sediment fraction (φ_s) and organic fraction (φ_b) of the matter enveloped per aggregate were calculated according to Eq. 4.15 and 4.14, respectively. The volume fractal dimension of BSA (D_v) was measured using Box-counting method provided by Bone-J plugin from Fiji/Image J software. Density of matter (ρ_M) and aggregate (ρ_A) were calculated according to Eq. 4.5 and 4.7.

BSA type	V_M (μm^3)	d_x (μm)	d_y (μm)	d_z (μm)	V_A (μm^3)	d_M (μm)	d_A (μm)	ε	φ_s	φ_b	D_v	ρ_M (kg/m^3)	ρ_A (kg/m^3)
Clay BSA	6.70E+04	144.21	143.43	157.68	1.37E+07	50.38	296.60	1.00	0.12	0.88	1.98	1415.29	1002.04
Clay BSA	7.73E+04	84.07	115.46	106.61	4.33E+06	52.86	202.30	0.98	0.08	0.92	2.18	1362.06	1006.46
Clay BSA	9.22E+04	132.56	126.03	62.11	4.35E+06	56.06	202.48	0.98	0.30	0.70	2.22	1675.33	1014.33
Clay BSA	1.13E+05	185.39	141.57	127.38	1.40E+07	60.04	299.06	0.99	0.13	0.87	2.12	1427.78	1003.46
Clay BSA	1.40E+05	219.27	155.09	154.78	2.20E+07	64.37	347.90	0.99	0.32	0.68	2.04	1692.22	1004.38
Clay BSA	1.50E+05	162.55	138.00	117.28	1.10E+07	65.94	276.09	0.99	0.12	0.88	2.16	1418.99	1005.71
Clay BSA	1.84E+05	197.51	127.58	156.33	1.65E+07	70.58	315.87	0.99	0.35	0.65	2.12	1740.43	1008.26
Clay BSA	2.18E+05	120.59	121.37	152.82	9.37E+06	74.67	261.55	0.98	0.46	0.54	2.32	1896.77	1020.87

BSA type	V_M (μm^3)	d_x (μm)	d_y (μm)	d_z (μm)	V_A (μm^3)	d_M (μm)	d_A (μm)	ε	φ_s	φ_b	D_v	ρ_M (kg/m^3)	ρ_A (kg/m^3)
Clay BSA	2.82E+05	134.89	215.23	132.04	1.61E+07	81.40	313.01	0.98	0.36	0.64	2.26	1760.68	1013.38
Clay BSA	3.51E+05	192.85	229.37	168.36	3.12E+07	87.53	390.57	0.99	0.21	0.79	2.23	1549.57	1006.18
Clay BSA	4.65E+05	281.27	183.73	178.71	3.87E+07	96.12	419.61	0.99	0.39	0.61	2.20	1792.90	1009.53
Clay BSA	5.69E+05	283.49	282.20	199.69	6.69E+07	102.81	503.71	0.99	0.15	0.85	2.24	1461.95	1003.93
Clay BSA	5.70E+05	249.57	273.97	178.87	5.12E+07	102.90	460.79	0.99	0.26	0.74	2.28	1619.14	1006.89
Clay BSA	6.45E+05	296.39	218.80	200.47	5.45E+07	107.18	470.27	0.99	0.18	0.82	2.25	1495.78	1005.87
Clay BSA	6.66E+05	252.21	280.19	183.37	5.43E+07	108.37	469.76	0.99	0.32	0.68	2.26	1703.56	1008.64
Clay BSA	6.78E+05	159.44	248.33	288.42	4.78E+07	109.00	450.38	0.99	0.36	0.64	2.26	1757.33	1010.74
Clay BSA	7.70E+05	264.73	288.73	212.59	6.81E+07	113.74	506.58	0.99	0.16	0.84	2.33	1476.19	1005.39
Clay BSA	7.77E+05	402.63	338.35	183.37	1.05E+08	114.08	584.66	0.99	0.17	0.83	2.17	1494.30	1003.67
Clay BSA	8.17E+05	324.36	139.55	262.31	4.97E+07	115.98	456.27	0.98	0.21	0.79	2.35	1545.02	1008.95
Clay BSA	8.77E+05	294.06	240.45	172.96	5.12E+07	118.77	460.78	0.98	0.17	0.83	2.35	1491.79	1008.42
Clay BSA	1.10E+06	221.91	319.81	194.72	5.79E+07	127.88	479.94	0.98	0.21	0.79	2.37	1538.62	1010.19
Clay BSA	1.19E+06	326.75	396.42	218.80	1.19E+08	131.39	609.77	0.99	0.20	0.80	2.34	1528.34	1005.29
Clay BSA	1.21E+06	319.81	406.92	207.15	1.13E+08	132.18	599.69	0.99	0.25	0.75	2.30	1606.49	1006.50
Clay BSA	1.26E+06	496.66	216.16	309.20	1.39E+08	134.12	642.77	0.99	0.24	0.76	2.26	1586.02	1005.32
Clay BSA	1.32E+06	395.18	285.71	433.57	2.05E+08	135.97	731.63	0.99	0.21	0.79	2.23	1550.63	1003.53
Clay BSA	1.43E+06	259.67	335.35	358.15	1.31E+08	139.72	629.55	0.99	0.19	0.81	2.32	1520.57	1005.69
Clay BSA	1.46E+06	443.36	259.99	282.58	1.36E+08	140.76	638.72	0.99	0.20	0.80	2.31	1535.56	1005.73
Clay BSA	1.76E+06	377.00	198.29	412.54	1.29E+08	149.83	627.19	0.99	0.21	0.79	2.33	1549.06	1007.49
Clay BSA	1.79E+06	525.41	273.66	308.42	1.86E+08	150.54	707.91	0.99	0.21	0.79	2.28	1542.86	1005.22

BSA type	V_M (μm^3)	d_x (μm)	d_y (μm)	d_z (μm)	V_A (μm^3)	d_M (μm)	d_A (μm)	ε	φ_s	φ_b	D_v	ρ_M (kg/m^3)	ρ_A (kg/m^3)
Clay BSA	1.90E+06	465.89	216.16	443.62	1.87E+08	153.54	709.67	0.99	0.22	0.78	2.32	1563.62	1005.71
Clay BSA	2.08E+06	263.56	402.64	381.46	1.70E+08	158.31	686.72	0.99	0.20	0.80	2.35	1535.27	1006.56
Clay BSA	2.21E+06	325.72	411.19	372.14	2.09E+08	161.56	736.02	0.99	0.18	0.82	2.34	1499.13	1005.28
Clay BSA	2.65E+06	341.57	308.62	529.87	2.34E+08	171.59	764.52	0.99	0.18	0.82	2.33	1499.91	1005.65
Clay BSA	3.26E+06	347.47	648.48	545.41	5.15E+08	184.03	994.36	0.99	0.12	0.88	2.32	1417.95	1002.65
Clay BSA	3.32E+06	388.66	601.55	485.58	4.76E+08	185.01	968.42	0.99	0.12	0.88	2.33	1413.24	1002.88
Clay BSA	3.71E+06	587.10	597.20	212.85	3.13E+08	192.13	842.04	0.99	0.23	0.77	2.42	1576.06	1006.84
Fluff BSA	1.35E+07	517.44	552.62	372.24	4.46E+08	295.76	947.84	0.97	0.86	0.14	2.09	2466.46	1044.55
Fluff BSA	1.37E+07	308.84	418.00	444.40	2.40E+08	296.61	771.36	0.94	0.81	0.19	2.22	2410.73	1080.21
Fluff BSA	1.44E+07	615.37	440.00	511.89	5.81E+08	301.91	1035.03	0.98	0.77	0.23	2.08	2355.96	1033.65
Fluff BSA	1.67E+07	369.60	616.00	396.00	3.78E+08	317.08	896.81	0.96	0.83	0.17	2.10	2434.05	1063.38
Fluff BSA	1.84E+07	513.04	439.37	411.84	3.89E+08	327.37	905.59	0.95	0.87	0.13	2.23	2483.42	1070.07
Fluff BSA	1.94E+07	587.84	552.64	381.04	5.19E+08	333.63	996.75	0.96	0.72	0.28	2.20	2294.72	1048.55
Fluff BSA	2.06E+07	545.60	444.40	513.04	5.21E+08	339.96	998.38	0.96	0.79	0.21	2.17	2383.95	1054.64
Fluff BSA	2.18E+07	447.04	574.64	539.44	5.80E+08	346.51	1034.96	0.96	0.88	0.12	2.18	2495.05	1056.11
Fluff BSA	2.35E+07	526.24	559.66	455.84	5.62E+08	355.53	1024.09	0.96	0.90	0.10	2.18	2522.03	1063.68
Fluff BSA	2.69E+07	838.64	455.84	469.04	7.51E+08	371.65	1127.79	0.96	0.76	0.24	2.15	2344.26	1048.11
Fluff BSA	3.15E+07	619.77	394.24	832.48	8.52E+08	391.66	1176.21	0.96	0.70	0.30	2.21	2265.95	1046.74
Fluff BSA	3.90E+07	838.64	821.04	567.33	1.64E+09	420.74	1462.03	0.98	0.69	0.31	2.25	2253.54	1029.88
Mat BSA	8.16E+08	1998.48	2378.64	1073.33	2.14E+10	1159.46	3443.11	0.96	0.47	0.53	2.27	2019.74	1038.94
Mat BSA	3.95E+08	1613.04	1466.08	906.13	8.98E+09	909.99	2578.46	0.96	0.48	0.52	2.29	2028.57	1045.21

BSA type	V_M (μm^3)	d_x (μm)	d_y (μm)	d_z (μm)	V_A (μm^3)	d_M (μm)	d_A (μm)	ε	φ_s	φ_b	D_v	ρ_M (kg/m^3)	ρ_A (kg/m^3)
Mat BSA	3.95E+08	1672.86	1679.04	835.73	9.83E+09	910.01	2658.02	0.96	0.40	0.60	2.22	1940.98	1037.76
Field silty BSA	4.77E+07	842.40	513.90	634.23	1.15E+09	449.94	1299.90	0.96	0.20	0.80	2.44	1617.03	1025.59
Field silty BSA	4.13E+07	1125.90	936.90	445.23	1.97E+09	428.94	1554.61	0.98	0.14	0.86	2.30	1543.12	1011.41
Field silty BSA	2.99E+07	828.90	986.40	395.73	1.36E+09	385.15	1373.03	0.98	0.16	0.84	2.27	1568.30	1012.54
Field silty BSA	2.30E+07	533.70	902.70	410.40	8.28E+08	353.04	1165.14	0.97	0.16	0.84	2.33	1570.72	1015.88
Field silty BSA	1.81E+07	601.20	479.70	472.23	5.70E+08	325.72	1028.99	0.97	0.20	0.80	2.34	1620.25	1019.67
Field silty BSA	1.33E+07	509.40	533.70	440.73	5.02E+08	293.77	985.99	0.97	0.29	0.71	2.30	1731.51	1019.35
Field silty BSA	1.20E+07	684.90	502.20	477.90	6.89E+08	284.12	1095.58	0.98	0.15	0.85	2.21	1555.45	1009.69
Field silty BSA	1.13E+07	506.70	500.40	332.73	3.53E+08	278.05	877.17	0.97	0.28	0.72	2.28	1721.79	1022.99
Field silty BSA	9.78E+06	484.20	488.70	311.40	3.09E+08	265.35	838.48	0.97	0.25	0.75	2.29	1684.89	1021.71
Field silty BSA	7.85E+06	434.70	466.20	341.73	2.90E+08	246.58	821.32	0.97	0.26	0.74	2.30	1699.63	1018.93
Field silty BSA	7.26E+06	538.20	477.90	275.40	2.97E+08	240.26	827.52	0.98	0.21	0.79	2.16	1636.94	1015.59
Field silty BSA	4.36E+06	518.40	371.70	292.23	2.36E+08	202.72	766.58	0.98	0.18	0.82	2.15	1592.25	1010.95
Field silty BSA	1.94E+06	484.20	297.90	170.73	1.03E+08	154.87	581.87	0.98	0.18	0.82	2.05	1598.51	1011.28
Field silty BSA	5.43E+06	585.90	405.90	274.23	2.73E+08	218.11	805.03	0.98	0.09	0.91	2.17	1472.28	1009.39
Field silty BSA	1.35E+06	234.90	209.70	197.73	4.08E+07	136.97	427.12	0.97	0.26	0.74	2.20	1699.53	1023.07
Field silty BSA	5.81E+05	180.90	108.90	143.73	1.19E+07	103.54	282.94	0.95	0.27	0.73	2.15	1704.70	1034.53
Field sandy BSA	6.88E+07	995.40	599.40	553.23	1.38E+09	508.40	1382.19	0.95	0.80	0.20	2.22	2388.96	1069.12
Field sandy BSA	3.73E+07	459.90	698.40	401.40	5.40E+08	414.42	1010.37	0.93	0.93	0.07	2.17	2564.51	1107.96
Field sandy BSA	3.23E+07	585.90	758.70	566.73	1.06E+09	395.18	1263.14	0.97	0.78	0.22	2.41	2362.23	1041.71
Field sandy BSA	2.45E+07	461.70	486.90	482.40	4.54E+08	360.29	953.75	0.95	0.85	0.15	2.20	2461.42	1078.78

BSA type	V_M (μm^3)	d_x (μm)	d_y (μm)	d_z (μm)	V_A (μm^3)	d_M (μm)	d_A (μm)	ε	φ_s	φ_b	D_v	ρ_M (kg/m^3)	ρ_A (kg/m^3)
Field sandy BSA	2.29E+07	452.70	504.90	355.23	3.40E+08	352.51	866.04	0.93	0.89	0.11	2.19	2509.61	1101.81
Field sandy BSA	1.87E+07	653.40	686.70	409.23	7.69E+08	329.50	1136.75	0.98	0.89	0.11	2.26	2509.18	1036.75
Field sandy BSA	1.43E+07	403.20	367.20	368.73	2.29E+08	301.21	758.70	0.94	0.84	0.16	2.16	2443.91	1090.35
Field sandy BSA	1.24E+07	473.40	385.20	431.73	3.30E+08	287.15	857.18	0.96	0.80	0.20	2.19	2391.66	1052.32
Field sandy BSA	1.11E+07	344.70	518.40	359.73	2.69E+08	277.03	801.17	0.96	0.90	0.10	2.13	2515.91	1062.68
Field sandy BSA	1.09E+07	441.90	486.90	359.73	3.24E+08	275.47	852.33	0.97	0.80	0.20	2.17	2393.39	1047.04
Field sandy BSA	1.02E+07	389.70	405.90	410.40	2.72E+08	269.47	803.80	0.96	0.84	0.16	2.21	2445.79	1054.47

Appendix B Data summary for the results of resuspension and settling experiments

Table B-1 Resuspension data summary

	Stage No.	Applied bed shear stresses (Pa)	Suspension concentration (Mean ± Standard deviation) (g/L)		
			Replicate 1	Replicate 2	Replicate 3
Abiotic sand	N/A	0.82	0.02 ± 0.01	NO DATA	NO DATA
		0.86	0.36 ± 0.23	NO DATA	NO DATA
		0.94	2.30 ± 0.98	NO DATA	NO DATA
		1.00	6.23 ± 1.04	NO DATA	NO DATA
		1.01	5.87 ± 0.29	NO DATA	NO DATA
mat BSA	Stage 1	0.33	0.00 ± 0.00	NO DATA	NO DATA
		0.39	0.00 ± 0.00	NO DATA	NO DATA
		0.50	0.00 ± 0.00	NO DATA	NO DATA
		0.62	0.00 ± 0.00	NO DATA	NO DATA

		0.73	0.01 ± 0.01	NO DATA	NO DATA
		0.82	0.04 ± 0.02	NO DATA	NO DATA
		0.86	0.07 ± 0.01	NO DATA	NO DATA
		0.94	0.11 ± 0.03	NO DATA	NO DATA
	Stage 2	1.00	0.22 ± 0.06	NO DATA	NO DATA
		1.01	0.40 ± 0.06	NO DATA	NO DATA
		1.09	0.73 ± 0.22	NO DATA	NO DATA
Fluff BSA	Stage 1	0.27	0.00 ± 0.00	0.00 ± 0.00	0.00 ± 0.00
		0.33	0.01 ± 0.00	0.01 ± 0.01	0.01 ± 0.00
		0.39	0.05 ± 0.02	0.07 ± 0.01	0.01 ± 0.01
		0.50	0.16 ± 0.04	0.17 ± 0.05	0.02 ± 0.01
		0.62	0.28 ± 0.02	0.34 ± 0.04	0.05 ± 0.03
		0.73	0.36 ± 0.02	0.50 ± 0.05	0.13 ± 0.05
	Stage 2	0.82	0.45 ± 0.03	0.68 ± 0.06	0.35 ± 0.09

		0.86	0.56 ± 0.04	0.93 ± 0.08	0.84 ± 0.20
		0.94	0.73 ± 0.04	1.29 ± 0.12	1.53 ± 0.26
		1.00	0.93 ± 0.06	1.78 ± 0.14	2.36 ± 0.31
		1.01	1.14 ± 0.06	2.07 ± 0.03	3.32 ± 0.21
		1.09	1.46 ± 0.10	2.47 ± 0.17	3.32 ± 0.36
Field silty BSA	N/A	0.46	0.02 ± 0.01	NO DATA	NO DATA
		0.62	0.16 ± 0.07	NO DATA	NO DATA
		0.80	0.42 ± 0.08	NO DATA	NO DATA
		1.09	0.82 ± 0.11	NO DATA	NO DATA
		1.37	1.18 ± 0.05	NO DATA	NO DATA
		1.69	1.46 ± 0.10	NO DATA	NO DATA
		1.98	1.86 ± 0.07	NO DATA	NO DATA
		2.37	2.22 ± 0.10	NO DATA	NO DATA
		2.78	2.56 ± 0.10	NO DATA	NO DATA

		3.20	2.78 ± 0.04	NO DATA	NO DATA
Field sandy BSA	N/A	1.09	0.01 ± 0.01	NO DATA	NO DATA
		1.37	0.06 ± 0.02	NO DATA	NO DATA
		1.69	0.10 ± 0.03	NO DATA	NO DATA
		1.98	0.16 ± 0.02	NO DATA	NO DATA
		2.37	0.22 ± 0.02	NO DATA	NO DATA
		2.78	0.29 ± 0.02	NO DATA	NO DATA
		3.20	0.36 ± 0.02	NO DATA	NO DATA
		3.61	0.45 ± 0.03	NO DATA	NO DATA
		3.93	0.54 ± 0.03	NO DATA	NO DATA
		4.29	0.64 ± 0.02	NO DATA	NO DATA

Table B-2 Summary of settling velocity statistics for tested and estimated velocities (mm/s) for both laboratory-created and field-collected BSA.

	N	Median	Mean		Std. Deviation	Variance	Skewness		Kurtosis	
	Statistic	Statistic	Statistic	Std. Error	Statistic	Statistic	Statistic	Std. Error	Statistic	Std. Error
wso_boxA_clayBSA	129	0.77	1.27	0.12	1.37	1.86	2.27	0.21	4.92	0.42
ws_s_boxB_clayBSA	36	4.69	4.74	0.45	2.68	7.19	0.46	0.39	0.50	0.77
ws_m_boxC_clayBSA	36	4.24	4.47	0.42	2.54	6.44	0.46	0.39	0.18	0.77
ws_a_boxD_clayBSA	36	1.02	1.00	0.09	0.55	0.31	0.50	0.39	0.76	0.77
ws_ad_boxE_clayBSA	36	0.92	0.89	0.08	0.46	0.21	0.25	0.39	0.23	0.77
wso_boxA_fluff BSA	13	15.81	15.88	1.07	3.85	14.82	-0.31	0.62	-0.56	1.19

ws_s_boxB_fluff BSA	12	88.40	90.68	5.15	17.86	318.83	0.39	0.64	-0.74	1.23
ws_m_boxC_fluff BSA	12	86.72	88.79	4.98	17.27	298.20	0.34	0.64	-0.86	1.23
ws_a_boxD_fluff BSA	12	30.43	29.56	1.55	5.37	28.80	-0.56	0.64	-0.66	1.23
ws_ad_boxE_fluff BSA	12	15.19	14.86	0.53	1.85	3.41	-0.99	0.64	0.73	1.23
wso_field sandy BSA	91	15.02	15.18	0.88	8.38	70.25	1.83	0.25	5.47	0.50
ws_s_field sandy BSA	11	90.30	98.34	13.29	44.08	1943.14	1.35	0.66	1.65	1.28
ws_m_field sandy BSA	11	89.21	96.74	13.05	43.28	1873.16	1.32	0.66	1.53	1.28
ws_a_field sandy BSA	11	28.32	34.86	5.28	17.51	306.44	1.21	0.66	0.69	1.28
ws_ad_field sandy BSA	11	15.57	16.56	1.62	5.37	28.83	0.82	0.66	-0.57	1.28

wso_boxA_field silty BSA	41	5.55	5.60	0.37	2.34	5.47	0.73	0.37	-0.07	0.72
ws_s_boxB_field silty BSA	16	23.83	25.08	3.99	15.97	254.95	0.65	0.56	0.29	1.09
ws_m_boxC_field silty BSA	16	25.33	27.87	4.48	17.93	321.52	0.70	0.56	0.14	1.09
ws_a_boxD_field silty BSA	16	7.63	8.40	1.45	5.80	33.69	1.10	0.56	1.70	1.09
ws_ad_boxE_field silty BSA	16	5.37	5.29	0.70	2.82	7.94	0.54	0.56	0.35	1.09

Appendix C Statistical analysis

C1. Statistical analysis in Chapter 4

C1.1 Statistical analysis for Figure 4.1

C1.1.1 Normality test

Organic fraction of clay BSA does not apply to normal distribution ($p < 0.05$, Table C4.1), but can be converted to normal distribution by computing Log_{10} (max+1-x) transform. To be comparable, the organic fraction of both clay and fluff BSA were converted and normality test was performed again to check the normality after the transform (Table C4.2). The results of normality tests before and after the transform are listed in Table C4.1 and C4.2, which confirms the successful normal transformation ($p > 0.05$).

Volume fractal dimension of both clay and fluff BSA apply to normal distribution ($p > 0.05$).

Table C4.1 Normality tests of the organic fraction and volume fractal dimension distribution of clay and fluff BSA.

Tests of Normality for raw data						
	Kolmogorov-Smirnov			Shapiro-Wilk*		
	Statistic	df	Sig.	Statistic	df	Sig.
Organic fraction _clay BSA	0.194	36	0.001	0.927	36	0.021
Organic fraction _fluff BSA	0.138	12	0.200	0.945	12	0.568
D_v_0.78_clay	0.122	12	0.200	0.961	12	0.801
D_v_0.20_sand	0.177	12	0.200	0.921	12	0.290

* Kolmogorov-Smirnov needs the sample number to exceed 2000-5000, while Shapiro-Wilk test is applicable to small samples. Therefore, results from the latter are considered herein.

Table C4.2 Normality tests of the organic fraction and volume fractal dimension distribution of clay and fluff BSA after normal transformation.

Tests of Normality for converted data						
	Kolmogorov-Smirnov			Shapiro-Wilk		
	Statistic	df	Sig.	Statistic	df	Sig.
Organic fraction _clay BSA	0.181	36	0.004	0.943	36	0.064

Organic fraction _fluff BSA	0.138	12	0.200	0.942	12	0.531

C1.1.2 Mean comparison

Two methods were applied to compare the mean organic matter between clay and fluff BSA. After the successful normal transformation, independent samples T test were applied to the converted data. Meanwhile, nonparametric independent samples comparison (Mann-Whitney U test) were also applied to the unconverted data. These two methods show consistent results that significant differences were presented between the clay and fluff BSA in terms of their organic fraction ($p<0.05$, Table C4.3, Table C4.4).

D_v of fluff and clay BSA apply to normal distribution, and thus independent-samples T test was performed to compare the mean differences. Significant differences are present ($p<0.05$, Table C4.3).

Table C4.3 Independent T tests for mean organic fraction and volume fractal dimension comparisons between clay and fluff BSA (after transformation).

Independent-Samples T test							
	Levene's Test for Equality of Variances		T test for Equality of Means				
	F	Sig.	t	df	Sig. (2-tailed)	Mean Difference	Std. Error Difference
Organic fraction_ clay vs. fluff BSA	2.185	0.146	18.258	46	0.000	-0.178	0.010
D_v_ clay vs. fluff BSA	2.392	0.129	3.189	46	0.003	0.092	0.029

Table C4.4 Mann-Whitney U tests for organic fraction comparisons between clay and fluff BSA (unconverted data).

Test Statistics	
Mann-Whitney U	
Asymp. Sig. (2-tailed)	0.000

C1.1.3 Bivariate correlation between BSA size and volume fractal dimension

Bivariate correlation tests show that there is significant correlation between BSA size and volume fractal dimension for clay BSA (correlation is significant at the 0.01 level

in Table C4.5. The Pearson coefficient of 0.758 suggest the two variables are significantly correlated. By contrast, the correlation between BSA size and volume fractal dimension for fluff BSA is insignificant ($p > 0.05$, Table C4.6).

Table C4.5 Bivariate correlations between BSA size and volume fractal dimension for clay BSA.

Bivariate correlations		
		Dv_clay BSA
L_M_clay BSA	Pearson Correlation	0.758**
	Sig. (2-tailed)	0.000
	Spearman Correlation	0.740**
	Sig. (2-tailed)	0.000
	N	36
**. Correlation is significant at the 0.01 level (2-tailed).		

Table C4.6 Bivariate correlations between BSA size and volume fractal dimension for fluff BSA.

Correlations		
		L_M_fluff BSA
D_v_fluff BSA	Pearson Correlation	0.573
	Sig. (2-tailed)	0.052
	Spearman Correlation	0.431
	Sig. (2-tailed)	0.162
	N	12

C1.2 Statistical results of Figure 4.2_ settling velocity comparisons

C1.2.1 Normality test

Normality tests for the settling velocities of clay and fluff BSA are listed in Table C4.7. The experimentally-tested settling velocities of clay BSA do not apply to normal distribution, while the four estimated velocities apply to normal distribution. Three different methods were tried to convert the settling velocities of clay BSA to normal distribution, which include to take logarithm, square root, and reciprocal value of the settling velocities. After each conversion, the normality tests were performed again for each of the converted datasets. The p value of the normality tests for each converted datasets remain smaller than 0.05. The experimentally-tested velocities of clay BSA cannot be converted to normal distribution.

For fluff BSA, each of the five settling velocity datasets of fluff BSA applies to normal distribution (Table C4.7).

Table C4.7 Normality tests of the settling velocity distribution.

Tests of Normality						
	Kolmogorov-Smirnova			Shapiro-Wilk		
	Statistic	df	Sig.	Statistic	df	Sig.
Clay BSA						
BoxA_clay BSA	0.183	129	0.000	0.804	129	0.000
BoxB_clay BSA	0.070	36	0.200	0.961	36	0.234
BoxC_clay BSA	0.075	36	0.200	0.965	36	0.303
BoxD_clay BSA	0.057	36	0.200	0.964	36	0.284
BoxE_clay BSA	0.072	36	0.200	0.971	36	0.452
Fluff BSA						
BoxA_fluffBSA	0.138	13	0.200	0.951	13	0.621
BoxB_fluff BSA	0.129	12	0.200	.940	12	0.496
BoxC _fluff BSA	0.139	12	0.200	.939	12	0.483
BoxD _fluff BSA	0.138	12	0.200	.943	12	0.535
BoxE_fluff BSA	0.177	12	0.200	.922	12	0.301

C1.2.2 Mean comparison

As the settling velocities of clay BSA do not apply to normal distribution and cannot be simultaneously converted to normal distribution for comparison purposes. Non-parametric Kruskal-Wallis tests were applied to compare whether there are significant differences among the five settling velocity groups (Table C4.8). To further compare the differences between the tested and estimated results, non-parametric Mann-Whitney U test was applied (Table C4.9). Significant differences remain between the velocities in Box A and Box B-C ($p < 0.05$), but the differences are diminished when the effects of pore water are considered in Box D and E ($p > 0.05$).

Each of the settling velocity datasets of fluff BSA apply to normal distribution. ANOVA and independent-samples T tests can be applied to compare the mean differences. The results of ANOVA tests are listed in Table C4.8, which shows that there is significant difference among the five settling velocities. The results in Table C4.9 further compare the differences between the experimentally-tested and the theoretically-estimated results. For fluff BSA, velocity estimates in Box B-D remain significant differentiated from the teste velocities (Box A) with p <0.05, while the differences become diminished when both the effects of pore water and form drag are

accounted for in Box E ($p > 0.05$).

Table C4.8 Kruskal-Wallis and ANOVA tests for the multiple comparisons among the five settling velocity datasets.

Kruskal-Wallis tests for clay BSA					
Kruskal-Wallis H	98.215				
Asymp. Sig.	0.000				
ANOVA tests for fluff BSA					
	Sum of Squares	df	Mean Square	F	Sig.
Between Groups	71863.986	4	17965.996	136.212	0.000
Within Groups	7254.338	55	131.897		
Total	79118.323	59			

Table C4.9 ANOVA tests of the mean velocity comparisons among the five velocity groups for fluff BSA.

BSA type	**Experimentally-tested velocities**	**Estimated velocities**		**Statistical comparisons***		**Statistical difference**
	$\tilde{X}; \bar{X} \pm SD(n)$			**Method**	***p* value**	
Clay BSA	Box A 0.77; 1.27 ± 1.37 (129)	Box B	4.69; 4.74 ± 2.68 (36)	Mann-Whitney U test	< 0.05	Significant difference
		Box C	4.69 4.47 ± 2.54 (36)	Mann-Whitney U test	< 0.05	Significant difference
		Box D	1.02 1.00 ± 0.55 (36)	Mann-Whitney U test	0.67	**No significant difference**
		Box E	0.92 0.89 ± 0.46 (36)	Mann-Whitney U test	0.87	**No significant difference**
Fluff BSA	Box A 15.81; 15.88 ± 3.85 (13)	Box B	88.40; 90.68 ± 17.86 (12)	Bonferroni test	< 0.05	Significant difference
		Box C	86.72;	Bonferroni	< 0.05	Significant

	88.79 ± 17.27 (12)	test		difference
Box D	30.43; 29.56 ± 5.37 (12)	Bonferroni test	< 0.05	Significant difference
Box E	15.19; 14.86 ± 1.85 (12)	Bonferroni test	0.99	**No significant difference**

*****Nonparametric tests were conducted for clay BSA as the tested velocities of clay BSA do not apply to normal distribution and failed to be converted to normal distribution. Non-parametric Mann-Whitney U test was performed. By contrast, all the five velocity datasets of fluff BSA apply to normal distribution, and ANOVA tests were performed for multiple comparison.

C1.3 Statistical results of Figure 4.3 (a) and (b)_ differences between the biotic and abiotic drag

C1.3.1 Normality test

Normality test results of biotic and abiotic drag of clay and fluff BSA are summarized in Table C4.10. The abiotic drag of clay BSA does not apply to normal distribution. Normal transformation by taking square root, e-base and 10-base logarithms and reciprocal value of the variables failed to convert the abiotic drag of clay BSA to normal distribution.

Both biotic and abiotic drag of fluff BSA apply to normal distribution.

Table C4.10 Normality tests of the abiotic and biotic drag of clay and fluff BSA.

Tests of Normality						
	Kolmogorov-Smirnova			Shapiro-Wilk		
	Statistic	df	Sig.	Statistic	df	Sig.
C_{Db} _ clay BSA	0.097	36	0.200	0.983	36	0.850
C_{Ds}_ clay BSA	0.195	36	0.001	0.876	36	0.001
C_{Db} _ fluff BSA	0.212	12	0.142	0.942	12	0.531
C_{Ds} _ fluff BSA	0.187	12	0.200	0.961	12	0.799

C1.3.2 Mean comparison

For clay BSA, instead of paired T test, non-parametric Wilcoxon tests were applied to

test the significance of the differences between the biotic and abiotic drag (Table C 4.11). As both the abiotic and biotic drag of fluff BSA apply to normal distribution, paired T tests were applied to fluff BSA (Table C4.12). The results show that the difference between the biotic and abiotic drag of clay BSA is significant, while there is no significant difference between the biotic and abiotic drag of fluff BSA.

Table C4.11 Wilcoxon tests of the statistical differences between biotic and abiotic drag for clay and paired T tests for fluff BSA.

Wilcoxon tests for C_{Db} _clay BSA & C_{Ds} _clay BSA	
Z	-4.258
Asymp. Sig. (2-tailed)	0.000
Paired-Samples T test for C_{Db} _fluff BSA & C_{Ds} _fluff BSA	
N	12
Correlation	0.406
Sig.	0.191

C1.4 Correlations between the adjusted biotic drag ratio and the dimensionless aggregate size.

Bivariate correlation analysis shows that the adjusted biotic drag ratios are significantly correlated with the aggregate dimensionless diameter, D_{*A}.(Table C4.12). Regression analysis in Table C4.13 shows that the aggregate dimensionless diameter, D_{*A}, has a significant relationship with the adjusted biotic drag ratio, $\eta\cdot(1-\varphi_b)(1-\varepsilon)$

Table C4.12 Bivariate correlations between the adjusted biotic drag ratio and the dimensionless diameter of BSA.

		Adjusted biotic drag ratio $\eta\cdot(1-\varphi_b)(1-\varepsilon)$
Dimensionless aggregate diameter, D_{*A}	Pearson Correlation	0.893**
	Spearmen correlation	0.754**
	Sig. (2-tailed)	0.000
	N	48
**. Correlation is significant at the 0.01 level (2-tailed).		

Table C4.13 Regression analysis of the adjusted biotic drag ratio and aggregate dimensionless diameter.

Model Summary and Parameter Estimates

Equation	Model Summary					Parameter Estimates	
	R Square	F	df1	df2	Sig.	Constant	b1
Power	0.811	198.031	1	46	0.000	0.000	2.069
The independent variable is D_{*A}, and the dependent variable is $\eta\cdot(1-\varphi_b)(1-\varepsilon)$							

C2. Statistical analysis in Chapter 5

C2.1 Statistical analysis for Figure 5.2

C2.1.1 Normality test

The organic fraction of field silty and sandy BSA apply to normal distribution. Independent-samples T test was applied, in which significant differences of organic fraction present.

Volume fractal dimension of field sandy BSA does not apply to normal distribution and failed to be converted to normal distribution (.

Table C2.1 Normality tests for the organic matter distribution of field silty and sandy BSA.

Tests of Normality						
	Kolmogorov-Smirnova			Shapiro-Wilk		
	Statistic	df	Sig.	Statistic	df	Sig.
Organic fraction _field silty BSA	0.155	16	0.200*	0.950	16	0.490
Organic fraction _field sandy BSA	0.193	11	0.200*	0.927	11	0.384
Dv _field silty BSA	0.193	11	0.200*	0.931	11	0.416
Dv _field sandy BSA	0.265	11	0.030	0.776	11	0.005

C2.2.2 Mean comparison

Independent-samples T tests were performed to compare the mean differences between field silty and sandy BSA, in terms of organic fraction. Significant differences of organic fraction present between the field silty and sandy BSA ($p<0.05$, Table C2.2). Non-parametric Mann-Whitney U test was applied to compare the volume fractal dimensions between the two field BSA, which shows the differences of the volume fractal dimension are insignificant ($p>0.05$, Table C2.2).

Table C2.2 Independent-samples T tests for mean organic fraction and volume fractal dimension comparisons between field silty and sandy BSA.

Independent Samples T Test							
	Levene's Test for Equality of Variances		t-test for Equality of Means				
	F	Sig.	t	df	Sig. (2-tailed)	Mean Difference	Std. Error Difference
Organic fraction _field silty BSA vs. field sandy BSA	0.446	0.511	29.816	25	0.000	0.64227	0.02154
Mann-Whitney U test							
Dv _ field silty BSA vs. field sandy BSA	Asymp Sig (2-tailed)						
	0.245						

C2.1.3 Bivariate correlations between volume fractal dimension and BSA size

Bivariate correlations between volume fractal dimension and BSA size were analyzed (Table C2.3). Pearson and Spearman tests provide consistent results for field silty and sandy BSA, in which the volume fractal dimension of field silty BSA significantly correlates with BSA size (Table C2.3), while no significant correlations present for field sandy BSA (Table C2.4).

Table C2.3 Bivariate correlations between BSA size and volume fractal dimension for field silty BSA.

Bivariate correlations		
		D_v_field silty BSA
L_M_field silty BSA	Pearson Correlation	0.803**
	Sig. (2-tailed)	0.000
	Spearman Correlation	0.819**
	Sig. (2-tailed)	0.000
	N	16

**. Correlation is significant at the 0.01 level (2-tailed).

Table C2.4 Bivariate correlations between BSA size and volume fractal dimension for field sandy BSA.

Bivariate correlations		
		D*v*_field sandy BSA
L_M_field sandy BSA	Pearson Correlation	0.351
	Sig. (2-tailed)	0.290
	Spearman Correlation	0.379
	Sig. (2-tailed)	0.250
	N	11
**. Correlation is significant at the 0.01 level (2-tailed).		

C2.2 Statistical analysis of Figure 5.3_ settling velocity comparisons

C2.2.1 Normality test

The tested velocities of field sandy and silty BSA do not apply to normal distribution. while the other datasets of settling velocities apply to normal distribution (Table C2.5). To be comparable, each of the settling velocity datasets of field silty and sandy BSA were simultaneously converted to normal distribution by computing the e-base logarithm value of the velocities. Normality tests confirm that the velocities after the transformation apply to normal distribution (Table C2.6).

Table C2.5 Normality tests of the settling velocities of field sandy and silty BSA.

Tests of Normality						
	Kolmogorov-Smirnova			Shapiro-Wilk		
	Statistic	df	Sig.	Statistic	df	Sig.
Field sandy BSA						
BoxA_field sandy BSA	0.140	91	0.000	0.855	91	0.000
BoxB_ field sandy BSA	0.181	11	0.200*	0.857	11	0.052
BoxC_ field sandy BSA	0.180	11	0.200*	0.858	11	0.055
BoxD_ field sandy BSA	0.191	11	0.200*	0.856	11	0.051
BoxE_ field sandy BSA	0.191	11	0.200*	0.883	11	0.113
Field silty BSA						
BoxA_field silty BSA	0.163	41	0.008	0.924	41	0.009

BoxB_ field silty BSA	0.181	11	0.200*	0.857	11	0.052
BoxC_ field silty BSA	0.180	11	0.200*	0.858	11	0.055
BoxD_ field silty BSA	0.191	11	0.200*	0.856	11	0.051
BoxE_ field silty BSA	0.191	11	0.200*	0.883	11	0.113

Table C2.6 Normality tests for the velocities of field sandy and silty BSA after normal transformation.

Tests of Normality after normal transformation						
	Kolmogorov-Smirnova			Shapiro-Wilk		
	Statistic	df	Sig.	Statistic	df	Sig.
Field sandy BSA						
BoxA_field sandy BSA	0.248	91	0.056	0.877	11	0.096
BoxB_ field sandy BSA	0.169	11	0.200	0.919	11	0.313
BoxC_ field sandy BSA	0.165	11	0.200	0.919	11	0.313
BoxD_ field sandy BSA	0.149	11	0.200	0.924	11	0.349
BoxE_ field sandy BSA	0.179	11	0.200	0.917	11	0.298
Field silty BSA						
BoxA_field silty BSA	0.147	41	0.025	0.956	41	0.111
BoxB_ field silty BSA	0.159	16	0.200	0.933	16	0.272
BoxC_ field silty BSA	0.154	16	0.200	0.950	16	0.489
BoxD_ field silty BSA	00.130	16	0.200	0.954	16	0.559
BoxE_ field silty BSA	.155	16	0.200	0.934	16	0.285

C2.2.2 Mean comparisons

Nonparametric Kruskal-Wallis tests were performed to compare the mean velocity differences for both field sandy and silty BSA, when the data were not converted (Table C2.7). After normal transformation, ANOVA testes were also conducted for the mean velocity comparison (Table C2.8). Nonparametric Kruskal-Wallis and ANOVA tests present consistent results that there are significant differences among the five velocity datasets for both field sandy and silty BSA.

Table C2.7 Nonparametric tests for mean velocity differences among the five velocity datasets (for unconverted data).

Kruskal-Wallis test	
Field sandy BSA	
Kruskal-Wallis H	69.121
Asymp. Sig.	0.000
Field silty BSA	
Kruskal-Wallis H	47.177

Asymp. Sig.	0.000

Table C2.8 ANOVA tests for mean velocity comparisons among the five velocity datasets (after normal transformation).

ANOVA					
Field sandy BSA					
	Sum of Squares	df	Mean Square	F	Sig.
Between Groups	68.035	4	17.009	70.288	0.000
Within Groups	31.458	130	0.242		
Total	99.493	134			
Field silty BSA					
	Sum of Squares	df	Mean Square	F	Sig.
Between Groups	42.996	4	10.749	26.541	0.000
Within Groups	40.499	100	0.405		
Total	83.495	104			

To further compare between the experimentally-tested and theoretically-estimated velocities, similar to Table C2.7 and C2.8, two methods, non-parametric Mann-Whitney for the raw velocities of non-normal distribution (Table C2.9) and Bonferroni method of ANOVA tests for the converted velocities of normal distribution (after normal transformation, Table C2.9), were conducted. These two methods derived consistent results. In particular, the velocities of field silty BSA in Box B-C are significantly different from the tested velocities in Box A ($p < 0.05$), while the differences become diminished after the consideration of the effects of pore water for the velocities in Box D and E ($p > 0.05$). Field sandy BSA, only when both the effects of pore water and form drag are accounted for in Box E, the differences from the tested velocities become diminished ($p > 0.05$).

Table C2.9 Statistical comparisons between the experimentally-tested and theoretically-estimated velocities for field silty and sandy BSA.

Experimentally-tested velocities	Estimated velocities	Statistical comparisons		
$\tilde{X}; \bar{X} \pm SD(n)$		Mann-Whitney U test	ANOVA (Bonferr-oni test)	Statistical difference
		p value	p value	
Field silty BSA				

Box A 5.55; 5.60±2.34 (41)	Box B	23.83; 25.07 ± 15.97 (16)	< 0.05	< 0.05	Significant difference
	Box C	25.33; 27.87 ± 17.93 (16)	< 0.05	< 0.05	Significant difference
	Box D	7.63 8.40 ±5.80 (16)	0.12	1.00	**No significant difference**
	Box E	5.37 5.29 ± 2.82 (16)	0.67	1.00	**No significant difference**
Field sandy BSA					
Box A 15.0; 15.2 ±8.38 (91)	Box B	90.30; 98.34 ± 44.08 (11	< 0.05	< 0.05	Significant difference
	Box C	89.21; 96.74 ± 43.28 (11)	< 0.05	< 0.05	Significant difference
	Box D	28.32; 34.86 ± 17.51 (11)	< 0.05	< 0.05	Significant difference
	Box E	15.57; 16.56 ± 5.37 (11)	0.35	1.00	**No significant difference**

C2.3 Drag comparisons between field sandy and silty BSA

C2.3.1 Normality test

Normality tests of the biotic and abiotic drag of field silty and sandy BSA are listed in Table C2.10. Both biotic and abiotic drag of field sandy BSA apply to normal distribution, while the abiotic drag of field silty BSA does not apply to normal distribution. Normal transformation was applied to biotic and abiotic drag of field silty BSA, by computing the e-base logarithm value of the variables. Normality tests in Table C2.11 confirmed the normal transformation is successful.

Table C2.10 Normality tests for the distribution of abiotic and biotic drag for field silty and sandy BSA (raw data).

Tests of Normality (raw data)						
	Kolmogorov-Smirnov			Shapiro-Wilk		
	Statistic	df	Sig.	Statistic	df	Sig.
C_{Db}_Field silty BSA	0.172	16	0.200	0.896	16	0.069
C_{Ds}_Field silty BSA	0.304	16	0.000	0.747	16	0.001
C_{Db}_Field sandy BSA	0.232	11	0.100	0.880	11	0.103
C_{Ds} _Field sandy BSA	0.219	11	0.147	0.920	11	0.322

Table C2.11 Normality tests for the distribution of abiotic and biotic drag for field silty and sandy BSA (converted data after normal transformation).

Tests of Normality (converted data)						
	Kolmogorov-Smirnov			Shapiro-Wilk		
	Statistic	df	Sig.	Statistic	df	Sig.
C_{Db}_Field silty BSA	0.179	16	0.183	0.945	16	0.414
C_{Ds}_Field silty BSA	0.227	16	0.027	0.893	16	0.063

C2.3.2 Mean comparison

As field sandy BSA apply to normal distribution, paired-samples T tests are applied to compare between the biotic and abiotic drag for field sandy BSA.

For field silty BSA, two methods were applied for comparisons, nonparametric Wilcoxon for the unconverted velocities and paired-samples T test for the converted velocities. The statistical results are listed in Table C2.12. There are no significant differences between the biotic and abiotic drag for both field silty and sandy BSA.

Table C2.12 Statistical results of the comparisons between abiotic and biotic drag for field silty and sandy BSA.

Paired Samples Test for the field sandy BSA and converted field silty BSA						
	Paired Differences					
	Mean	Std. Deviation	Std. Error Mean	t	df	Sig. (2-tailed)
C_{Db}_field sandy BSA - C_{Ds}_field sandy BSA	0.400	1.545	0.466	0.858	10	0.411
C_{Db}_field silty BSA (converted) - C_{Ds}_field silty BSA (converted)	-0.220	0.712	0.178		15	0.235
Wilcoxon test for unconverted field silty BSA						
	Z			Asymp. Sig. (2-tailed)		
C_{Db}_silty-C_{Ds}_silty BSA	-0.621			0.35		

C2.4 Regression analysis of the predictive relationships in Chapter 5.

C2.4.1 Critical Shields parameter, $\theta_{crit,A}$, and aggregate dimensionless diameter, $D_{*,A}$.

Table C2.13 Regression analysis for the relationship between Critical Shields parameter, $\theta_{crit,A}$, and aggregate dimensionless diameter, $D_{*,A}$.

Coefficients

	Unstandardized Coefficients			
	B	Std. Error	t	Sig.
$\ln(D_{*A})$	-1.191	0.044	-26.876	0.000
Constant	16.741	1.029	16.276	0.000

Model Summary			
R	R Square	Adjusted R Square	Std. Error of the Estimate
0.951	0.905	0.904	0.305

ANOVA					
	Sum of Squares	df	Mean Square	F	Sig.
Regression	67.237	1	67.237	722.307	0.000
Residual	7.075	76	0.093		
Total	74.312	77			
Equation	$\theta_{cirt,A} = 16.7 D_{*A}^{-1.2}$, $R^2 = 0.90$, $p < 0.05$				

C2.4.2 Critical Shields parameter, $\theta_{crit,A}$, and aggregate Reynolds number, Re_A

Table C2.14 Regression analysis for the relationship between Critical Shields parameter, $\theta_{crit,A}$, and aggregate Reynolds number, Re_A.

Coefficients				
	Unstandardized Coefficients			
	B	Std. Error	t	Sig.
$\ln(\mathrm{Re}_A)$	-1.172	0.078	-15.082	0.000
Constant	75.149	14.894	5.046	0.000

Model Summary			
R	R Square	Adjusted R Square	Std. Error of the Estimate
0.866	0.750	0.746	0.495

ANOVA					
	Sum of Squares	df	Mean Square	F	Sig.
Regression	55.701	1	55.701	227.455	0.000
Residual	18.611	76	0.245		
Total	74.312	77			
Equation	$\theta_{cirt,A} = 75.1 \mathrm{Re}_A^{-1.2}$, $R^2 = 0.75$, $p < 0.05$				

C2.4.3 Adjusted biotic drag ratio, $\eta(1-\varphi_s)(1-\varepsilon)$, and aggregate dimensionless diameter, $D_{*,A}$

Table C2.15 Regression analysis for the relationship between adjusted biotic drag ratio, $\eta(1-\varphi_s)(1-\varepsilon)$, and aggregate Reynolds number, $D_{*,A}$.

Coefficients				
	Unstandardized Coefficients		t	Sig.
	B	Std. Error		
$\ln(D_{*,A})$	2.114	0.123	-15.082	0.000
Constant	0.0004	0.000	5.046	0.000

Model Summary			
R	R Square	Adjusted R Square	Std. Error of the Estimate
.895	0.801	0.798	0.763

ANOVA					
	Sum of Squares	df	Mean Square	F	Sig.
Regression	171.393	1	171.393	294.099	0.000
Residual	42.542	73	0.583		
Total	213.935	74			
Equation	$\eta(1-\varphi_s)(1-\varepsilon) = 0.0004 D_{*A}^{2.1}$, $R^2 = 0.80$, $p < 0.05$				

C2.4.4 Adjusted biotic drag ratio, $\eta(1-\varphi_s)(1-\varepsilon)$, and aggregate Reynolds number, Re_A

Table C2.15 Regression analysis for the relationship between adjusted biotic drag ratio, $\eta(1-\varphi_s)(1-\varepsilon)$, and aggregate Reynolds number, Re_A.

Coefficients				
	Unstandardized Coefficients		t	Sig.
	B	Std. Error		
Re_A	0.0025	0.000	-15.082	0.000
Constant	0.000	0.002	5.046	0.000

Model Summary			
R	R Square	Adjusted R Square	Std. Error of the Estimate
0.895	0.691	0.477	0.470

ANOVA					
	Sum of Squares	df	Mean Square	F	Sig.
Regression	0.012	1	0.012	66.668	0.000
Residual	0.013	73	0.000		
Total	0.025	74			

Equation	$\eta(1-\varphi_s)(1-\varepsilon) = 0.0025\,\mathrm{Re}_A$, $R^2 = 0.69$, $p < 0.05$

Appendix D Micro-CT images of 3D BSA matrices

3-4 BSA samples from each type are selected as examples to illustrate the 3D matrices.

Clay BSA

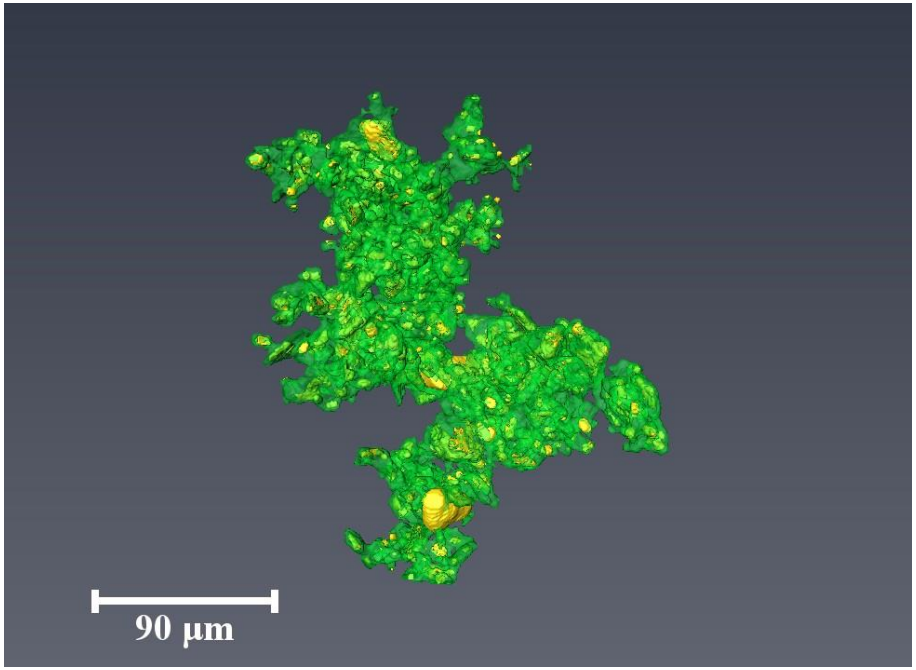

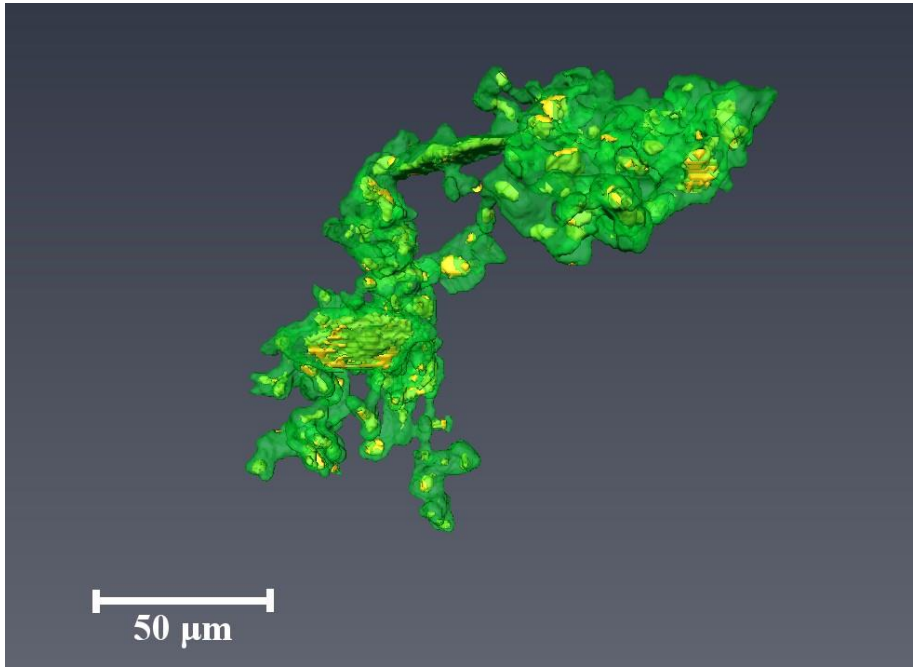

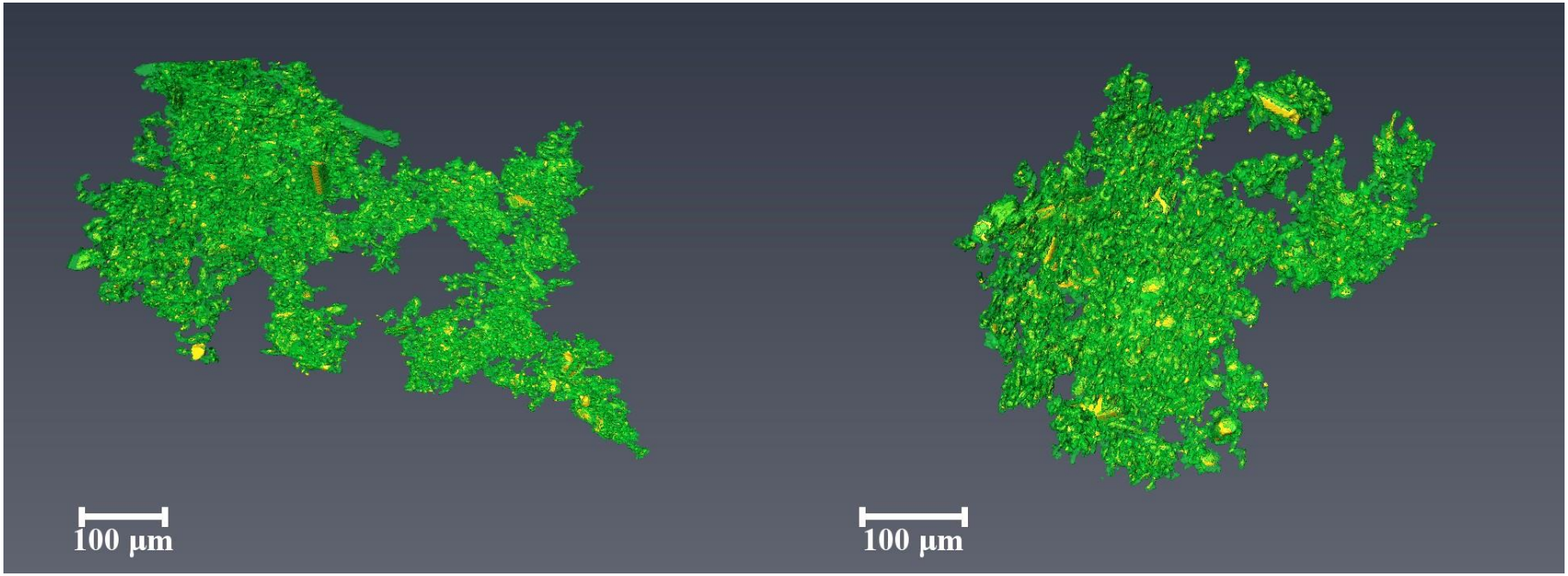
100 µm
100 µm

Fluff BSA

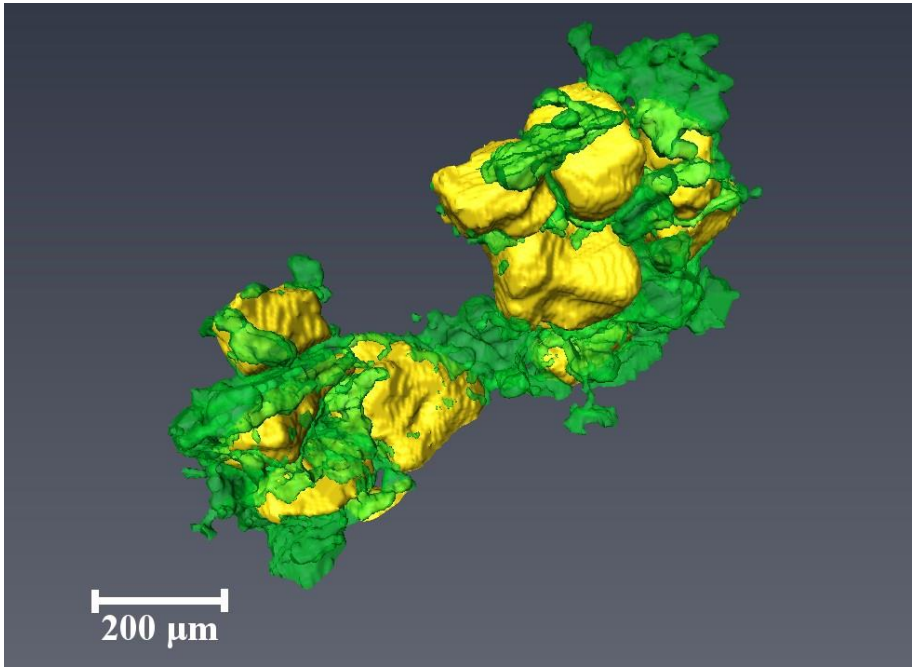

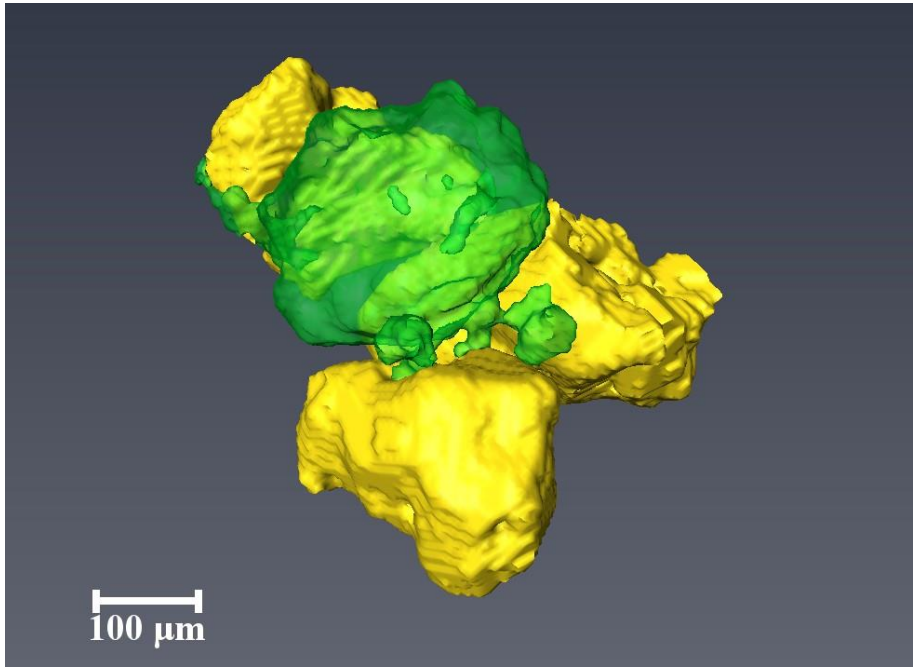

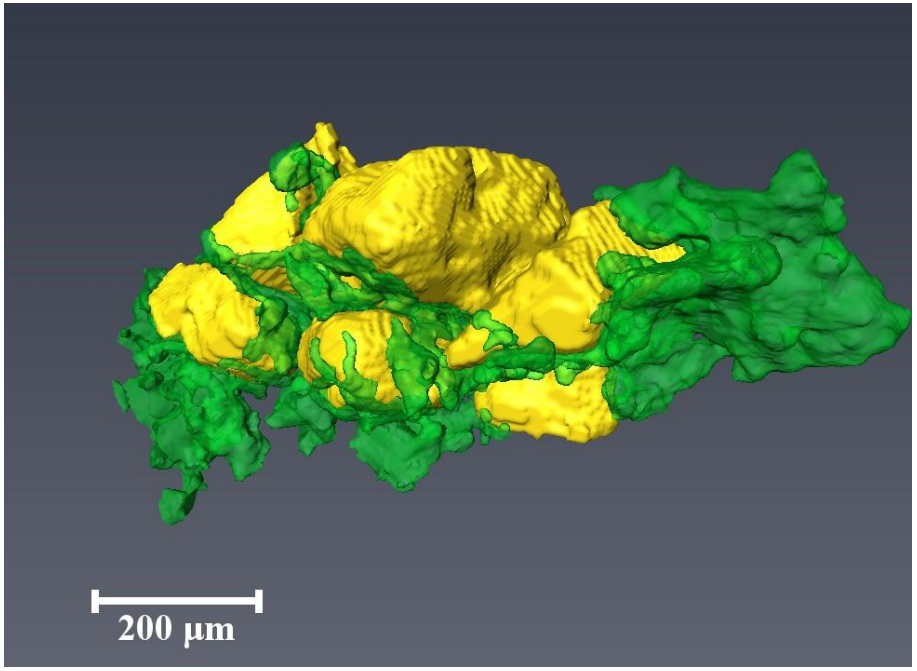
200 µm

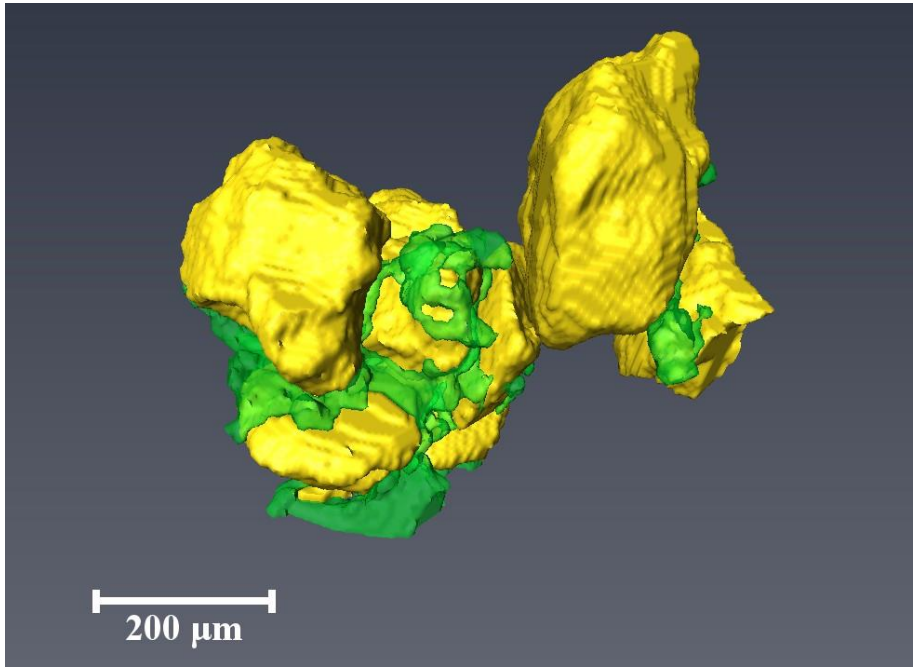
200 µm

Mat BSA

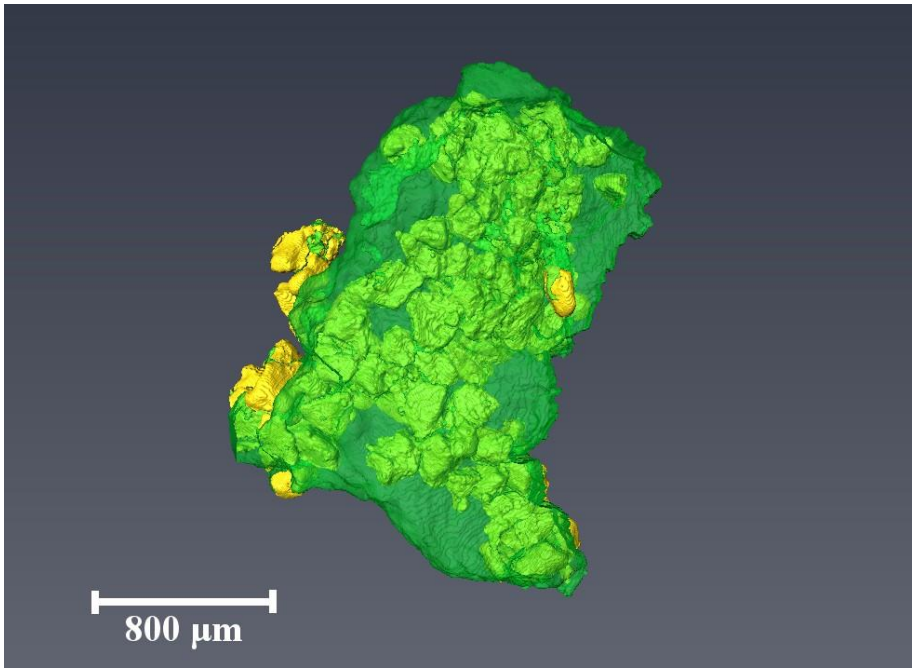

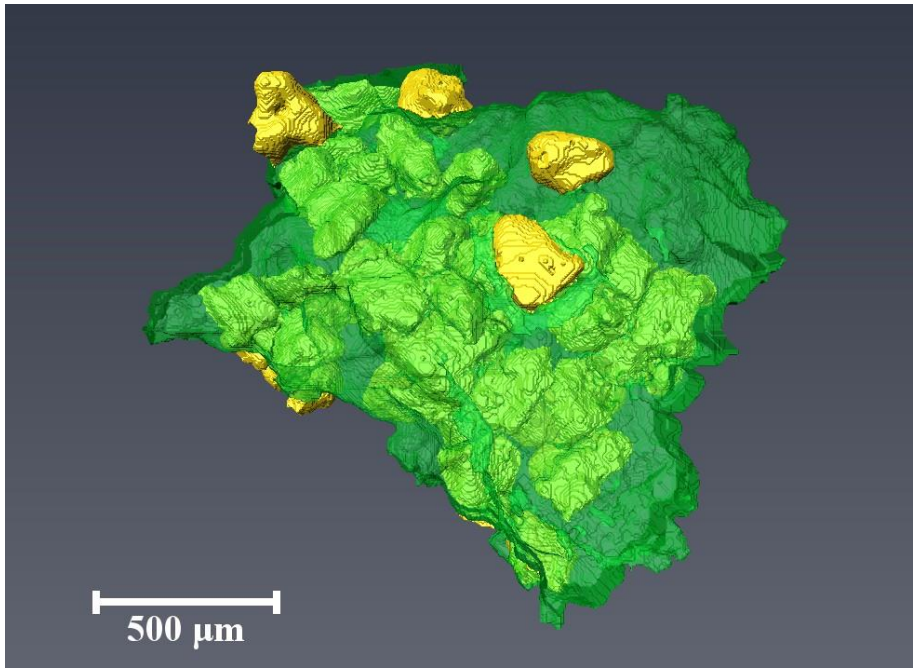

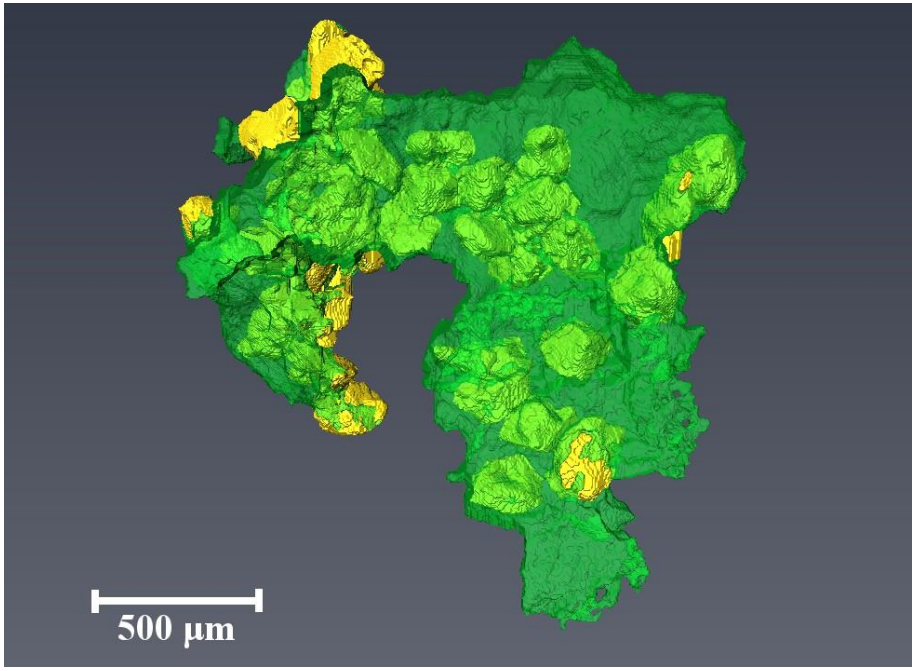
500 µm

Field silty BSA

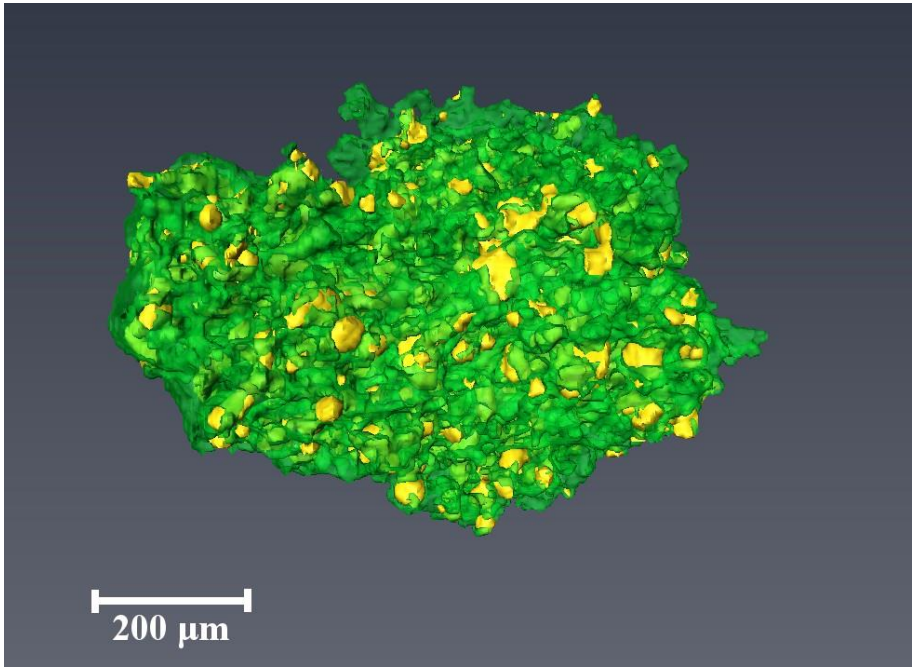

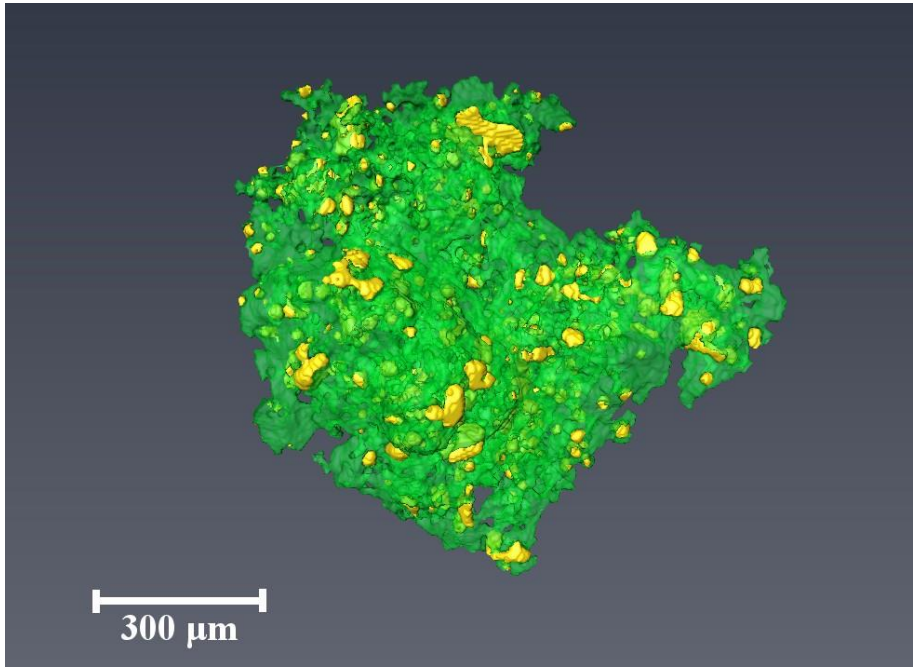

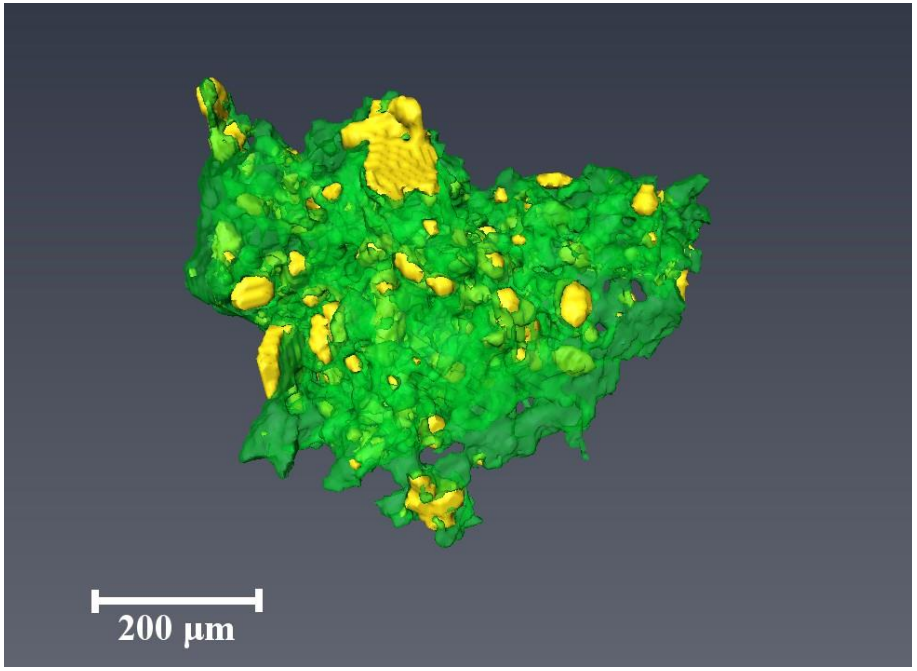
200 µm

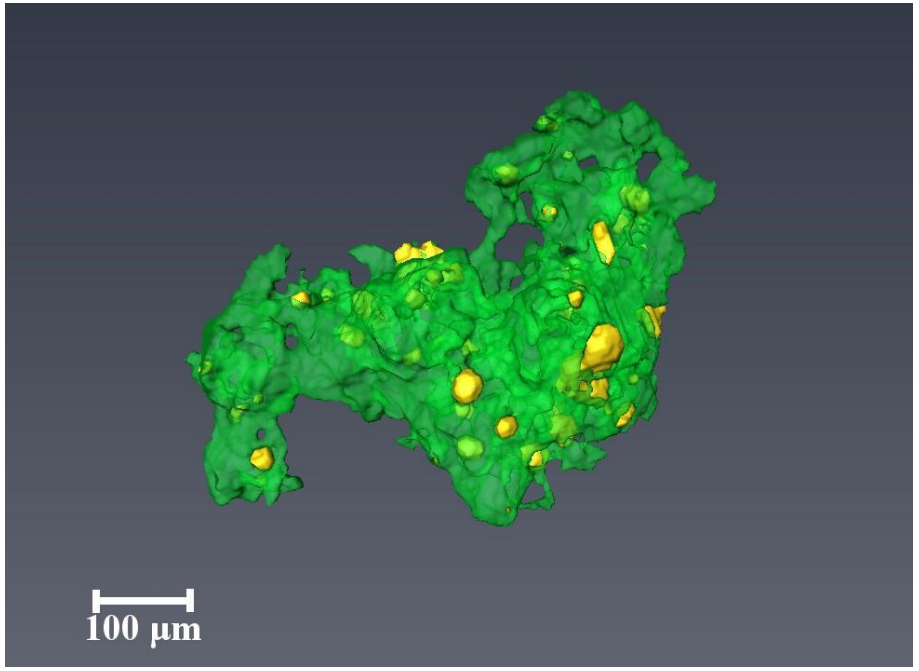
100 µm

Field sandy BSA

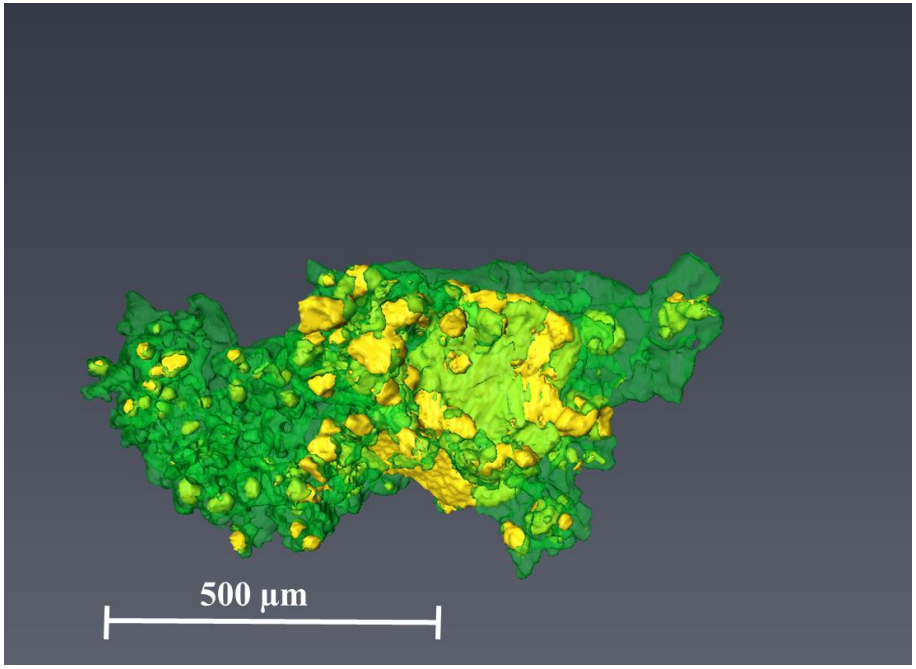

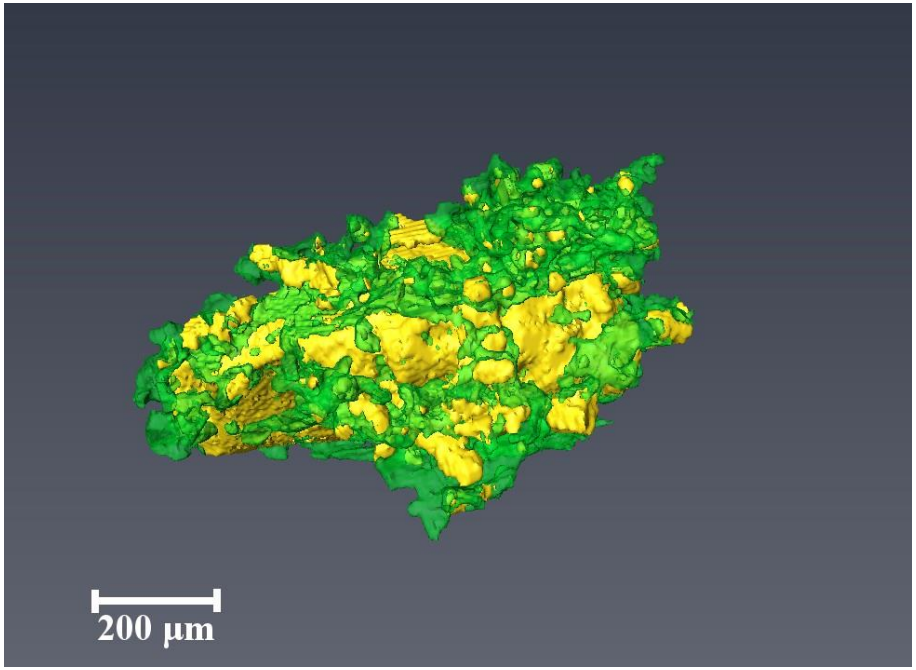

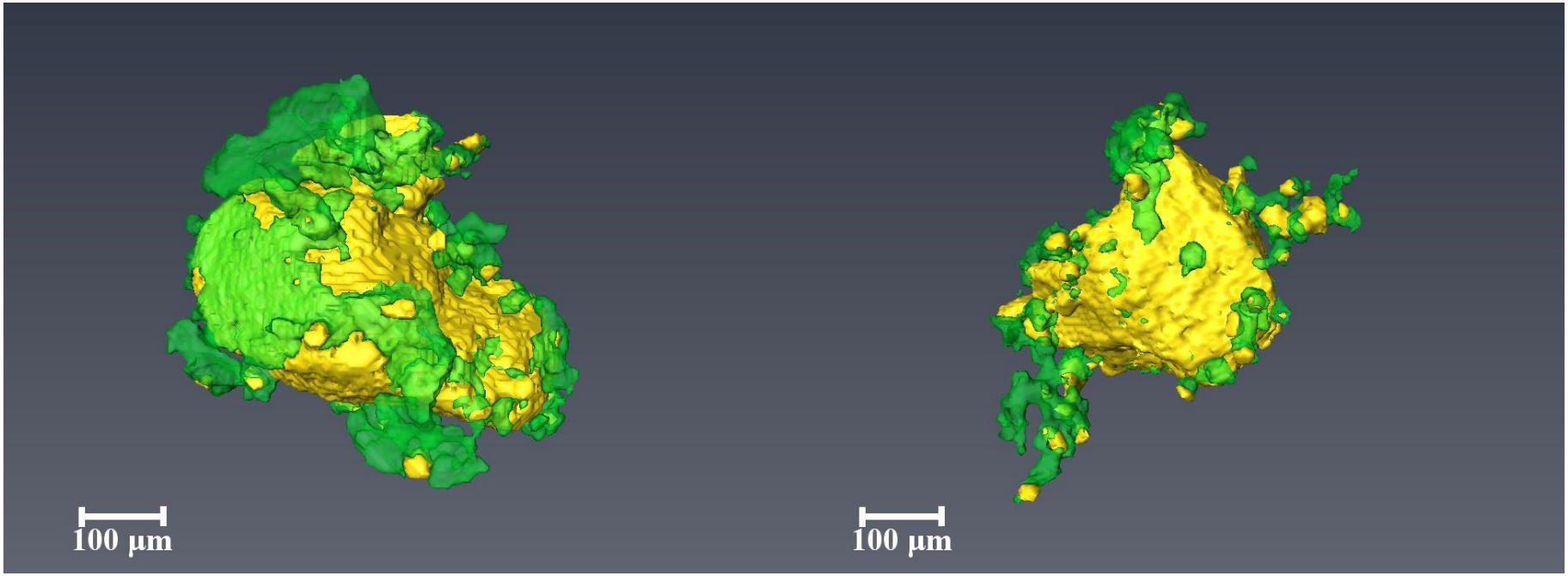
100 µm
100 µm

References

Abdelnour, A. F., Nehmeh, S. A., Pan, T., Humm, J. L., Vernon, P., Schöder, H., et al. (2007). Phase and amplitude binning for 4D-CT imaging. *Physics in Medicine and Biology*. https://doi.org/10.1088/0031-9155/52/12/012

Agrawal, Y. C., & Pottsmith, H. C. (2000). Instruments for particle size and settling velocity observations in sediment transport. *Marine Geology*. https://doi.org/10.1016/S0025-3227(00)00044-X

Alldredge, A. L., Passow, U., & Logan, B. E. (1993). The abundance and significance of a class of large, transparent organic particles in the ocean. *Deep-Sea Research Part I*, *40*(6), 1131–1140. https://doi.org/10.1016/0967-0637(93)90129-Q

Alongi, D. M. (2012). Carbon sequestration in mangrove forests. *Carbon Management*, *3*(3), 313–322. https://doi.org/10.4155/cmt.12.20

Amos. (2017). Stability of Seabed Sediments in the Embayments of North Rustico, Prince Edward Island, Canada. *Journal of Coastal Research*. https://doi.org/10.2112/JCOASTRES-D-16-00192.1

Amos, C. L., Li, M. Z., & Sutherland, T. F. (1998). The contribution of ballistic momentum flux to the erosion of cohesive beds by flowing water. *Journal of Coastal Research*.

Amos, C. L., Bergamasco, A., Umgiesser, G., Cappucci, S., Cloutier, D., Denat, L., et al. (2004). The stability of tidal flats in Venice Lagoon - The results of in-situ measurements using two benthic, annular flumes. *Journal of Marine Systems*, *51*(1-4 SPEC. ISS.), 211–241. https://doi.org/10.1016/j.jmarsys.2004.05.013

Amos, Carl L., Daborn, G. R., Christian, H. A., Atkinson, A., & Robertson, A. (1992). In situ erosion measurements on fine-grained sediments from the Bay of Fundy. *Marine Geology*, *108*(2), 175–196. https://doi.org/10.1016/0025-3227(92)90171-D

Amos, Carl L., Sutherland, T. F., Radzijewski, B., & Doucette, M. (2003). A rapid technique to

determine bulk density of fine-grained sediments by X-ray computed tomography. *Journal of Sedimentary Research*, *66*(5), 1023–1024. https://doi.org/10.1306/d4268144-2b26-11d7-8648000102c1865d

Amos, Carl L., Droppo, I. G., Gomez, E. A., & Murphy, T. P. (2003). The stability of a remediated bed in Hamilton Harbour, Lake Ontario, Canada. *Sedimentology*, *50*(1), 149–168. https://doi.org/10.1046/j.1365-3091.2003.00542.x

Amos, Carl L., Umgiesser, G., Ferrarin, C., Thompson, C. E. L., Whitehouse, R. J. S., Sutherland, T. F., & Bergamasco, A. (2010). The erosion rates of cohesive sediments in Venice lagoon, Italy. *Continental Shelf Research*, *30*(8), 859–870. https://doi.org/10.1016/j.csr.2009.12.001

Andalib, M., Zhu, J., & Nakhla, G. (2010). Terminal settling velocity and drag coefficient of biofilm-coated particles at high Reynolds numbers. *AIChE Journal*. https://doi.org/10.1002/aic.12184

Andersen, T. J. (2001). Seasonal variation in erodibility of two temperate, microtidal mudflats. *Estuarine, Coastal and Shelf Science*. https://doi.org/10.1006/ecss.2001.0790

Andersen, T. J., Lund-Hansen, L. C., Pejrup, M., Jensen, K. T., & Mouritsen, K. N. (2005). Biologically induced differences in erodibility and aggregation of subtidal and intertidal sediments: A possible cause for seasonal changes in sediment deposition. *Journal of Marine Systems*, *55*(3–4), 123–138. https://doi.org/10.1016/j.jmarsys.2004.09.004

Andersen, T. J., Fredsoe, J., & Pejrup, M. (2007). In situ estimation of erosion and deposition thresholds by Acoustic Doppler Velocimeter (ADV). *Estuarine, Coastal and Shelf Science*, *75*(3), 327–336. https://doi.org/10.1016/j.ecss.2007.04.039

Arganda-Carreras, I., Kaynig, V., Rueden, C., Eliceiri, K. W., Schindelin, J., Cardona, A., & Seung, H. S. (2017). Trainable Weka Segmentation: A machine learning tool for microscopy pixel classification. *Bioinformatics*, *33*(15), 2424–2426. https://doi.org/10.1093/bioinformatics/btx180

Armstrong, R. A., Lee, C., Hedges, J. I., Honjo, S., & Wakeham, S. G. (2002). A new, mechanistic model for organic carbon fluxes in the ocean based on the quantitative association of POC with ballast minerals. *Deep-Sea Research Part II: Topical Studies in Oceanography*.

https://doi.org/10.1016/S0967-0645(01)00101-1

Armstrong, R. A., Peterson, M. L., Lee, C., & Wakeham, S. G. (2009). Settling velocity spectra and the ballast ratio hypothesis. *Deep-Sea Research Part II: Topical Studies in Oceanography*, *56*(18), 1470–1478. https://doi.org/10.1016/j.dsr2.2008.11.032

Arndt, S., Jørgensen, B. B., LaRowe, D. E., Middelburg, J. J., Pancost, R. D., & Regnier, P. (2013). Quantifying the degradation of organic matter in marine sediments: A review and synthesis. *Earth-Science Reviews*, *123*, 53–86. https://doi.org/10.1016/j.earscirev.2013.02.008

Avizo. (2016). Avizo 3D Software User's Guide. Retrieved July 7, 2017, from https://www.fei.com/software/avizo- user-guide/

Bagnold, R. A. (1966). An Approach to the Sediment Transport Problem from General Physics. *USGS Professional Paper*.

Bar-Zeev, E., Berman-Frank, I., Girshevitz, O., & Berman, T. (2012). Revised paradigm of aquatic biofilm formation facilitated by microgel transparent exopolymer particles. *Proceedings of the National Academy of Sciences of the United States of America*, *109*(23), 9119–24. https://doi.org/10.1073/pnas.1203708109

Bauer, J. E., Cai, W. J., Raymond, P. A., Bianchi, T. S., Hopkinson, C. S., & Regnier, P. A. G. (2013). The changing carbon cycle of the coastal ocean. *Nature*. https://doi.org/10.1038/nature12857

Black, K. S., Tolhurst, T. J., Paterson, D. M., & Hagerthey, S. E. (2002). Working with natural cohesive sediments. *Journal of Hydraulic Engineering*, *128*(1), 2–8. https://doi.org/10.1061/(ASCE)0733-9429(2002)128:1(2)

Blanchard, G. F., Guarini, J. M., Orvain, F., & Sauriau, P. G. (2001). Dynamic behaviour of benthic microalgal biomass in intertidal mudflats. *Journal of Experimental Marine Biology and Ecology*. https://doi.org/10.1016/S0022-0981(01)00312-4

de BOER, P. L. (1981). Mechanical effects of micro-organisms on intertidal bedform migration. *Sedimentology*. https://doi.org/10.1111/j.1365-3091.1981.tb01670.x

Boyd, P. W., & Trull, T. W. (2007). Understanding the export of biogenic particles in oceanic waters: Is there consensus? *Progress in Oceanography*, *72*(4), 276–312. https://doi.org/10.1016/j.pocean.2006.10.007

De Brouwer, J. F. C., & Stal, L. J. (2001). Short-term dynamics in microphytobenthos distribution and associated extracellular carbohydrates in surface sediments of an intertidal mudflat. *Marine Ecology Progress Series*. https://doi.org/10.3354/meps218033

De Brouwer, J. F. C., Wolfstein, K., Ruddy, G. K., Jones, T. E. R., & Stal, L. J. (2005). Biogenic stabilization of intertidal sediments: The importance of extracellular polymeric substances produced by benthic diatoms. *Microbial Ecology*, *49*(4), 501–512. https://doi.org/10.1007/s00248-004-0020-z

Buffington, J. M. (1999). The Legend of A. F. Shields. *Journal of Hydraulic Engineering*. https://doi.org/10.1061/(asce)0733-9429(1999)125:4(376)

Butcher, S. S., Charlson, R. J., Orians, G. H., & Wolfe, G. V. (1992). Global biogeochemical cycles. *Global Biogeochemical Cycles*, 175–193. https://doi.org/10.1111/1462-2920.13280

Cabrita, M. T., & Brotas, V. (2000). Seasonal variation in denitrification and dissolved nitrogen fluxes in intertidal sediments of the Tagus estuary, Portugal. *Marine Ecology Progress Series*. https://doi.org/10.3354/meps202051

Callow, B., Falcon-Suarez, I., Ahmed, S., & Matter, J. (2018). Assessing the carbon sequestration potential of basalt using X-ray micro-CT and rock mechanics. *International Journal of Greenhouse Gas Control*, *70*(August), 146–156. https://doi.org/10.1016/j.ijggc.2017.12.008

Carniello, V., Peterson, B. W., van der Mei, H. C., & Busscher, H. J. (2018). Physico-chemistry from initial bacterial adhesion to surface-programmed biofilm growth. *Advances in Colloid and Interface Science*. https://doi.org/10.1016/j.cis.2018.10.005

Chen, D., Li, M., Zhang, Y., Zhang, L., Tang, J., Wu, H., & Wang, Y. P. (2020). Effects of diatoms on erosion and accretion processes in saltmarsh inferred from field observations of hydrodynamic and sedimentary processes. *Ecohydrology*. https://doi.org/10.1002/eco.2246

Chen, L. C., Chian, C. Y., Yen, P. S., Chu, C. P., & Lee, D. J. (2001). High-speed sludge freezing. *Water Research*, *35*(14), 3502–3507. https://doi.org/10.1016/S0043-1354(01)00048-3

Chen, X., Zhang, C., Paterson, D. M., Townend, I. H., Jin, C., Zhou, Z., et al. (2019). The effect of cyclic variation of shear stress on non-cohesive sediment stabilization by microbial biofilms: the role of 'biofilm precursors.' *Earth Surface Processes and Landforms*. https://doi.org/10.1002/esp.4573

Chen, X. D., Zhang, C. K., Paterson, D. M., Thompson, C. E. L., Townend, I. H., Gong, Z., et al. (2017). Hindered erosion: The biological mediation of noncohesive sediment behavior. *Water Resources Research*, *53*(6), 4787–4801. https://doi.org/10.1002/2016WR020105

Chen, X. D., Gong, Z., Zhou, Z., Tao, J. F., Feng, Q., Paterson, D. M., et al. (2017). Stabilizing Effects of Bacterial Biofilms: EPS Penetration and Redistribution of Bed Stability Down the Sediment Profile. *Journal of Geophysical Research: Biogeosciences*, *122*(12), 3113–3125. https://doi.org/10.1002/2017jg004050

Chu, C. P., & Lee, D. J. (2004). Multiscale structures of biological flocs. *Chemical Engineering Science*, *59*(8–9), 1875–1883. https://doi.org/10.1016/j.ces.2004.01.040

Clift, R., & Gauvin, W. H. (1971). Motion of entrained particles in gas streams. *The Canadian Journal of Chemical Engineering*, *49*(4), 439–448. https://doi.org/10.1002/cjce.5450490403

Cram, J. A., Weber, T., Leung, S. W., McDonnell, A. M. P., Liang, J. H., & Deutsch, C. (2018). The Role of Particle Size, Ballast, Temperature, and Oxygen in the Sinking Flux to the Deep Sea. *Global Biogeochemical Cycles*. https://doi.org/10.1029/2017GB005710

Cuadrado, D. G., Perillo, G. M. E., & Vitale, A. J. (2014). Modern microbial mats in siliciclastic tidal flats: Evolution, structure and the role of hydrodynamics. *Marine Geology*, *352*(June), 367–380. https://doi.org/10.1016/j.margeo.2013.10.002

Curran, K. J., Hill, P. S., Milligan, T. G., Mikkelsen, O. A., Law, B. A., Durrieu de Madron, X., & Bourrin, F. (2007). Settling velocity, effective density, and mass composition of suspended sediment in a coastal bottom boundary layer, Gulf of Lions, France. *Continental Shelf Research*,

27(10–11), 1408–1421. https://doi.org/10.1016/j.csr.2007.01.014

D'Alpaos, A., Lanzoni, S., Marani, M., Fagherazzi, S., & Rinaldo, A. (2005). Tidal network ontogeny: Channel initiation and early development. *Journal of Geophysical Research: Earth Surface*, *110*(2), 1–14. https://doi.org/10.1029/2004JF000182

D'Alpaos, A., Lanzoni, S., Marani, M., & Rinaldo, A. (2007). Landscape evolution in tidal embayments: Modeling the interplay of erosion, sedimentation, and vegetation dynamics. *Journal of Geophysical Research: Earth Surface*, *112*(1), 1–17. https://doi.org/10.1029/2006JF000537

Dade, W. B., Self, R. L., Pellerin, N. B., Moffet, A., Jumars, P. A., & Nowell, A. R. M. (1996). The effects of bacteria on the flow behavior of clay-seawater suspensions. *Journal of Sedimentary Research*. https://doi.org/10.1306/D42682A7-2B26-11D7-8648000102C1865D

Dade, W. Brian, Davis, J. D., Nichols, P. D., Nowell, A. R. M., Thistle, D., Trexler, M. B., et al. (1990). Effects of bacterial exopolymer adhesion on the entrainment of sand. *Geomicrobiology Journal*. https://doi.org/10.1080/01490459009377874

Daggers, T. D., Herman, P. M. J., & van der Wal, D. (2020). Seasonal and Spatial Variability in Patchiness of Microphytobenthos on Intertidal Flats From Sentinel-2 Satellite Imagery. *Frontiers in Marine Science*, *7*. https://doi.org/10.3389/fmars.2020.00392

Decho, A. W. (2000). Microbial biofilms in intertidal systems: An overview. *Continental Shelf Research*, *20*(10–11), 1257–1273. https://doi.org/10.1016/S0278-4343(00)00022-4

De Deckere, E. M. G. T., Tolhurst, T. J., & De Brouwer, J. F. C. (2001). Destabilization of cohesive intertidal sediments by infauna. *Estuarine, Coastal and Shelf Science*. https://doi.org/10.1006/ecss.2001.0811

Dey, S. (2014). *Fluvial Hydrodynamics*. https://doi.org/10.1007/978-3-642-19062-9

Droppo, I G, Ross, N., Skafel, M., & Liss, S. N. (2007). Biostabilization of cohesive sediment beds in a freshwater wave-dominated environment. *Limnology and Oceanography*, *52*(2), 577–589.

https://doi.org/10.4319/lo.2007.52.2.0577

Droppo, Ian G. (2001). Rethinking what constitutes suspended sediment. *Hydrological Processes*, *15*(9), 1551–1564. https://doi.org/10.1002/hyp.228

Droppo, Ian G. (2009). Biofilm structure and bed stability of five contrasting freshwater sediments. *Marine and Freshwater Research*, *60*(7), 690–699. https://doi.org/10.1071/MF08019

Droppo, Ian G., Flannigan, D. T., Leppard, G. G., Jaskot, C., & Liss, S. N. (1996). Floc stabilization for multiple microscopic techniques. *Applied and Environmental Microbiology*, *62*(9), 3508–3515.

Duarte, C. M., Losada, I. J., Hendriks, I. E., Mazarrasa, I., & Marbà, N. (2013). The role of coastal plant communities for climate change mitigation and adaptation. *Nature Climate Change*, *3*(11), 961–968. https://doi.org/10.1038/nclimate1970

Duteil, T., Bourillot, R., Grégoire, B., Virolle, M., Brigaud, B., Nouet, J., et al. (2020). Experimental formation of clay-coated sand grains using diatom biofilm exopolymers. *Geology*, *48*(10), 1012–1017. https://doi.org/10.1130/G47418.1

Dyer, K. R., & Manning, A. J. (1999). Observation of the size, settling velocity and effective density of flocs, and their fractal dimensions. *Journal of Sea Research*, *41*(1–2), 87–95. https://doi.org/10.1016/S1385-1101(98)00036-7

Emadzadeh, A., & Chiew, Y.-M. (2020). Settling Velocity of Porous Spherical Particles. *Journal of Hydraulic Engineering*, *146*(1), 04019046. https://doi.org/10.1061/(asce)hy.1943-7900.0001655

Fagherazzi, S., Carniello, L., D'Alpaos, L., & Defina, A. (2006). Critical bifurcation of shallow microtidal landforms in tidal flats and salt marshes. *Proceedings of the National Academy of Sciences of the United States of America*, *103*(22), 8337–8341. https://doi.org/10.1073/pnas.0508379103

Fang, H., Shang, Q., Chen, M., & He, G. (2014). Changes in the critical erosion velocity for sediment colonized by biofilm. *Sedimentology*, *61*(3), 648–659. https://doi.org/10.1111/sed.12065

Fang, H., Fazeli, M., Cheng, W., Huang, L., & Hu, H. (2015). Biostabilization and transport of cohesive sediment deposits in the Three Gorges Reservoir. *PLoS ONE*, *10*(11), 1–15. https://doi.org/10.1371/journal.pone.0142673

Fang, H., Huang, L., Zhano, H., Cheng, W., Chen, Y., Fazeli, M., & Shang, Q. (2020). *Mechanics of Bio-Sediment Transport*. Springer, Berlin, Heidelberg. https://doi.org/https://doi.org/10.1007/978-3-662-61158-6

Fang, H. W., Lai, H. J., Cheng, W., Huang, L., & He, G. J. (2017). Modeling sediment transport with an integrated view of the biofilm effects. *Water Resources Research*, *53*(9), 7536–7557. https://doi.org/10.1002/2017WR020628

Fazzalari, N. L., & Parkinson, I. H. (1996). Fractal dimension and architecture of trabecular bone. *Journal of Pathology*. https://doi.org/10.1002/(SICI)1096-9896(199601)178:1<100::AID-PATH429>3.0.CO;2-K

Feagin, R. A., Lozada-Bernard, S. M., Ravens, T. M., Möller, I., Yeager, K. M., & Baird, A. H. (2009). Does vegetation prevent wave erosion of salt marsh edges? *Proceedings of the National Academy of Sciences of the United States of America*, *106*(25), 10109–10113. https://doi.org/10.1073/pnas.0901297106

Feats, N. G., & Michener, H. J. (1999). *SedErode measurements in Venice Lagoon*. *Hydraulics Research Report TR90*.

Fennessy, M. J., Dyer, K. R., & Huntley, D. A. (1994). inssev: An instrument to measure the size and settling velocity of flocs in situ. *Marine Geology*, *117*(1–4), 107–117. https://doi.org/10.1016/0025-3227(94)90009-4

Flemming, H.-C. (2019). Bacteria and archaea on Earth and. *Nature Reviews Microbiology*, *17*, 247–260. https://doi.org/10.1038/s41579-019-0158-9

Flemming, H C, & Wingender, J. (2002). What biofilms contain - Proteins, polysaccharides, etc. *Chemie in Unserer Zeit*.

Flemming, Hans Curt. (2011). The perfect slime. *Colloids and Surfaces B: Biointerfaces*, *86*(2), 251–259. https://doi.org/10.1016/j.colsurfb.2011.04.025

Flemming, Hans Curt, & Wingender, J. (2010). The biofilm matrix. *Nature Reviews Microbiology*, *8*(9), 623–633. https://doi.org/10.1038/nrmicro2415

Folk, R. L. (1954). The Distinction between Grain Size and Mineral Composition in Sedimentary-Rock Nomenclature. *The Journal of Geology*. https://doi.org/10.1086/626171

Fourqurean, J. W., Duarte, C. M., Kennedy, H., Marbà, N., Holmer, M., Mateo, M. A., et al. (2012). Seagrass ecosystems as a globally significant carbon stock. *Nature Geoscience*, *5*(7), 505–509. https://doi.org/10.1038/ngeo1477

Friend, P. L., Ciavola, P., Cappucci, S., & Santos, R. (2003). Bio-dependent bed parameters as a proxy tool for sediment stability in mixed habitat intertidal areas. *Continental Shelf Research*. https://doi.org/10.1016/j.csr.2002.12.001

Friend, P. L., Collins, M. B., & Holligan, P. M. (2003). Day-night variation of intertidal flat sediment properties in relation to sediment stability. *Estuarine, Coastal and Shelf Science*, *58*(3), 663–675. https://doi.org/10.1016/S0272-7714(03)00178-1

Friend, P. L., Lucas, C. H., & Rossington, S. K. (2005). Day-night variation of cohesive sediment stability. *Estuarine, Coastal and Shelf Science*, *64*(2–3), 407–418. https://doi.org/10.1016/j.ecss.2005.03.006

Friend, P. L., Lucas, C. H., Holligan, P. M., & Collins, M. B. (2008). Microalgal mediation of ripple mobility. *Geobiology*, *6*(1), 70–82. https://doi.org/10.1111/j.1472-4669.2007.00108.x

Ganju, N. K., Schoellhamer, D. H., & Bergamaschi, B. A. (2005). Suspended sediment fluxes in a tidal wetland: Measurement, controlling factors, and error analysis. *Estuaries*, *28*(6), 812–822. https://doi.org/10.1007/BF02696011

Gerbersdorf, S. U., & Wieprecht, S. (2015). Biostabilization of cohesive sediments: Revisiting the role of abiotic conditions, physiology and diversity of microbes, polymeric secretion, and biofilm

architecture. *Geobiology*, *13*(1), 68–97. https://doi.org/10.1111/gbi.12115

Gerbersdorf, Sabine Ulrike, Jancke, T., & Westrich, B. (2005). Physico-chemical and biological sediment properties determining erosion resistance of contaminated riverine sediments - Temporal and vertical pattern at the Lauffen reservoir/River Neckar, Germany. *Limnologica*, *35*(3), 132–144. https://doi.org/10.1016/j.limno.2005.05.001

Gerbersdorf, Sabine Ulrike, Manz, W., & Paterson, D. M. (2008). The engineering potential of natural benthic bacterial assemblages in terms of the erosion resistance of sediments. *FEMS Microbiology Ecology*, *66*(2), 282–294. https://doi.org/10.1111/j.1574-6941.2008.00586.x

Gerbersdorf, Sabine Ulrike, Bittner, R., Lubarsky, H., Manz, W., & Paterson, D. M. (2009). Microbial assemblages as ecosystem engineers of sediment stability. *Journal of Soils and Sediments*. https://doi.org/10.1007/s11368-009-0142-5

Grabowski, R. C., Droppo, I. G., & Wharton, G. (2011). Erodibility of cohesive sediment: The importance of sediment properties. *Earth-Science Reviews*, *105*(3–4), 101–120. https://doi.org/10.1016/j.earscirev.2011.01.008

Greene, G. A., Irvine, T. F., Gyves, T., & Smith, T. (1993). Drag relationships for liquid droplets settling in a continuous liquid. *AIChE Journal*, *39*(1), 37–41. https://doi.org/10.1002/aic.690390106

Gust, G., & Müller, V. (1997). Interfacial hydrodynamics and entrainment functions of currently used erosion devices. *Wiley*, 149–174.

Hale, R., Boardman, R., Mavrogordato, M. N., Sinclair, I., Tolhurst, T. J., & Solan, M. (2015). High-resolution computed tomography reconstructions of invertebrate burrow systems. *Scientific Data*, *2*, 1–5. https://doi.org/10.1038/sdata.2015.52

Hamm, C. E. (2002). Interactive aggregation and sedimentation of diatoms and clay-sized lithogenic material, *47*(6), 1790–1795.

He, W., Nan, J., Li, H., & Li, S. (2012). Characteristic analysis on temporal evolution of floc size and

structure in low-shear flow. *Water Research*. https://doi.org/10.1016/j.watres.2011.11.040

Le Hir, P., Monbet, Y., & Orvain, F. (2007). Sediment erodability in sediment transport modelling: Can we account for biota effects? *Continental Shelf Research*, *27*(8), 1116–1142. https://doi.org/10.1016/j.csr.2005.11.016

Hope, J. A., Malarkey, J., Baas, J. H., Peakall, J., Parsons, D. R., Manning, A. J., et al. (2020). Interactions between sediment microbial ecology and physical dynamics drive heterogeneity in contextually similar depositional systems. *Limnology and Oceanography*, *65*(10), 2403–2419. https://doi.org/10.1002/lno.11461

Houwing, E. J. (1999). Determination of the critical erosion threshold of cohesive sediments on intertidal mudflats along the Dutch Wadden Sea coast. *Estuarine, Coastal and Shelf Science*. https://doi.org/10.1006/ecss.1999.0518

Houwing, E. J., & van Rijn, L. C. (1997). In Situ Erosion Flume (ISEF): determination of bed-shear stress and erosion of a kaolinite bed. *Journal of Sea Research*, *39*, 243–253.

Hubbell, J. H., & Seltzer, S. M. (1995). *Tables of X-Ray mass attenuation coefficients and mass energy-absorption coefficients 1 keV to 20 MeV for Elements Z=1 to 92 and 48 Additional substances of Dosimetric Interest. http://physics.nist.gov/xaamdi*. https://doi.org/http://physics.nist.gov/xaamdi

Ibrahim, E., Adam, S., De Wever, A., Govaerts, A., Vervoort, A., & Monbaliu, J. (2014). Investigating spatial resolutions of imagery for intertidal sediment characterization using geostatistics. *Continental Shelf Research*. https://doi.org/10.1016/j.csr.2014.05.012

Iversen, M. H., & Ploug, H. (2010). Ballast minerals and the sinking carbon flux in the ocean: Carbon-specific respiration rates and sinking velocity of marine snow aggregates. *Biogeosciences*, *7*(9), 2613–2624. https://doi.org/10.5194/bg-7-2613-2010

Iversen, Morten H., & Lampitt, R. S. (2020). Size does not matter after all: No evidence for a size-sinking relationship for marine snow. *Progress in Oceanography*, *189*(September), 102445. https://doi.org/10.1016/j.pocean.2020.102445

Jacobs, W., Le Hir, P., Van Kesteren, W., & Cann, P. (2011). Erosion threshold of sand-mud mixtures. *Continental Shelf Research*, *31*(10 SUPPL.), S14–S25. https://doi.org/10.1016/j.csr.2010.05.012

Jesus, B., Brotas, V., Ribeiro, L., Mendes, C. R., Cartaxana, P., & Paterson, D. M. (2009). Adaptations of microphytobenthos assemblages to sediment type and tidal position. *Continental Shelf Research*, *29*(13), 1624–1634. https://doi.org/10.1016/j.csr.2009.05.006

Joensuu, M., Pilditch, C. A., Harris, R., Hietanen, S., Pettersson, H., & Norkko, A. (2018). Sediment properties, biota, and local habitat structure explain variation in the erodibility of coastal sediments. *Limnology and Oceanography*, *63*(1), 173–186. https://doi.org/10.1002/lno.10622

Kamaruddin, N., Rajion, Z. A., Yusof, A., & Aziz, M. E. (2016). Relationship between Hounsfield unit in CT scan and gray scale in CBCT. *AIP Conference Proceedings*, *1791*. https://doi.org/10.1063/1.4968860

Keevil, C. W., & Walker, J. T. (1992). Nomarski DIC microscopy and image analysis of biofilm. *Binary Comput.Microbiol*, *4*, 93–95.

Kelbaliyev, G. I. (2011). Drag coefficients of variously shaped solid particles, drops, and bubbles. *Theoretical Foundations of Chemical Engineering*, *45*(3), 248–266. https://doi.org/10.1134/S0040579511020084

Keyes, S. D., Daly, K. R., Gostling, N. J., Jones, D. L., Talboys, P., Pinzer, B. R., et al. (2013). High resolution synchrotron imaging of wheat root hairs growing in soil and image based modelling of phosphate uptake. *New Phytologist*, *198*(4), 1023–1029. Retrieved from http://eprints.soton.ac.uk/350444/1/Manuscript_25-3-13.pdf

Khelifa, A., & Hill, P. S. (2006). Models for effective density and settling velocity of flocs. *Journal of Hydraulic Research*, *44*(3), 390–401. https://doi.org/10.1080/00221686.2006.9521690

Klaas, C., & Archer, D. E. (2002). Association of sinking organic matter with various types of mineral ballast in the deep sea: Implications for the rain ratio. *Global Biogeochemical Cycles*, *16*(4), 63-1-63–14. https://doi.org/10.1029/2001gb001765

Kornman, B. A., & De Deckere, E. M. G. T. (1998). Temporal variation in sediment erodibility and suspended sediment dynamics in the Dollard estuary. *Geological Society Special Publication*. https://doi.org/10.1144/GSL.SP.1998.139.01.19

Kranenburg, C. (1994). The fractal structure of cohesive sediment aggregates. *Estuarine, Coastal and Shelf Science*, *39*(6), 451–460. https://doi.org/10.1016/S0272-7714(06)80002-8

Kwon, E. Y., Primeau, F., & Sarmiento, J. L. (2009). The impact of remineralization depth on the air-sea carbon balance. *Nature Geoscience*, *2*(9), 630–635. https://doi.org/10.1038/ngeo612

Lau, Y. L., & Droppo, I. G. (2000). Influence of antecedent conditions on critical shear stress of bed sediments. *Water Research*, *34*(2), 663–667. https://doi.org/10.1016/S0043-1354(99)00164-5

Laurenceau-Cornec, E. C., Le Moigne, F. A. C., Gallinari, M., Moriceau, B., Toullec, J., Iversen, M. H., et al. (2020). New guidelines for the application of Stokes' models to the sinking velocity of marine aggregates. *Limnology and Oceanography*, *65*(6), 1264–1285. https://doi.org/10.1002/lno.11388

Van Ledden, M., Van Kesteren, W. G. M., & Winterwerp, J. C. (2004). A conceptual framework for the erosion behaviour of sand-mud mixtures. *Continental Shelf Research*, *24*(1), 1–11. https://doi.org/10.1016/j.csr.2003.09.002

Leppard, G. G., Heissenberger, A., & Herndl, G. J. (1996). Ultrastructure of marine snow. I. Transmission electron microscopy methodology. *Marine Ecology Progress Series*, *135*(1–3), 289–298. https://doi.org/10.3354/meps135289

Li, X. Y., & Yuan, Y. (2002). Settling velocities and permeabilities of microbial aggregates. *Water Research*, *36*(12), 3110–3120. https://doi.org/10.1016/S0043-1354(01)00541-3

Lichtman, I. D., Baas, J. H., Amoudry, L. O., Thorne, P. D., Malarkey, J., Hope, J. A., et al. (2018). Bedform migration in a mixed sand and cohesive clay intertidal environment and implications for bed material transport predictions. *Geomorphology*. https://doi.org/10.1016/j.geomorph.2018.04.016

Lick, W., Hening Huang, & Jepsen, R. (1993). Flocculation of fine-grained sediments due to differential settling. *Journal of Geophysical Research*, *98*(C6), 279–288. https://doi.org/10.1029/93jc00519

Liss, S. N., Droppo, I. G., Flannigan, D. T., & Leppard, G. G. (1996). Floc architecture in wastewater and natural riverine systems. *Environmental Science and Technology*, *30*(2), 680–686. https://doi.org/10.1021/es950426r

Lubarsky, H. V., Hubas, C., Chocholek, M., Larson, F., Manz, W., Paterson, D. M., & Gerbersdorf, S. U. (2010). The Stabilisation Potential of Individual and Mixed Assemblages of Natural Bacteria and Microalgae. *PLoS ONE*, *5*(11). https://doi.org/10.1371/journal.pone.0013794

Lundkvist, M., Grue, M., Friend, P. L., & Flindt, M. R. (2007). The relative contributions of physical and microbiological factors to cohesive sediment stability. *Continental Shelf Research*, *27*(8), 1143–1152. https://doi.org/10.1016/j.csr.2006.01.021

Macreadie, P. I., Anton, A., Raven, J. A., Beaumont, N., Connolly, R. M., Friess, D. A., et al. (2019). The future of Blue Carbon science. *Nature Communications*, *10*(1), 1–13. https://doi.org/10.1038/s41467-019-11693-w

Maggi, F., & Winterwerp, J. C. (2004). Method for computing the three-dimensional capacity dimension from two-dimensional projections of fractal aggregates. *Physical Review E - Statistical Physics, Plasmas, Fluids, and Related Interdisciplinary Topics*, *69*(1), 8. https://doi.org/10.1103/PhysRevE.69.011405

Maggi, F., Mietta, F., & Winterwerp, J. C. (2007). Effect of variable fractal dimension on the floc size distribution of suspended cohesive sediment. *Journal of Hydrology*, *343*(1–2), 43–55. https://doi.org/10.1016/j.jhydrol.2007.05.035

Maggi, Federico. (2005). Flocculation dynamics of cohesive sediment. *Communications on Hydraulic and Geotechnical Engineering*, *5*(1), 1–139.

Maggi, Federico. (2007). Variable fractal dimension: A major control for floc structure and flocculation kinematics of suspended cohesive sediment. *Journal of Geophysical Research:*

Oceans, *112*(7), 1–12. https://doi.org/10.1029/2006JC003951

Maggi, Federico. (2013). The settling velocity of mineral, biomineral, and biological particles and aggregates in water. *Journal of Geophysical Research: Oceans*, *118*(4), 2118–2132. https://doi.org/10.1002/jgrc.20086

Maggi, Federico, & Tang, F. H. M. (2015). Analysis of the effect of organic matter content on the architecture and sinking of sediment aggregates. *Marine Geology*, *363*, 102–111. https://doi.org/10.1016/j.margeo.2015.01.017

Malarkey, J., Baas, J. H., Hope, J. A., Aspden, R. J., Parsons, D. R., Peakall, J., et al. (2015). The pervasive role of biological cohesion in bedform development. *Nature Communications*, *6*, 2–7. https://doi.org/10.1038/ncomms7257

Manning， A., Baugh, J., Soulsby, R., Spearman, J., & Whitehouse, R. (2011). Cohesive Sediment Flocculation and the Application to Settling Flux Modelling. In *Sediment Transport*. https://doi.org/10.5772/16055

Manning, A. J. (2006). *LabSFLOC—a laboratory system to determine the spectral characteristics of flocculating cohesive sediments*. HR Wallingford Technical Report No.156.

Manning, A. J., Friend, P. L., Prowse, N., & Amos, C. L. (2007). Estuarine mud flocculation properties determined using an annular mini-flume and the LabSFLOC system. *Continental Shelf Research*, *27*(8), 1080–1095. https://doi.org/10.1016/j.csr.2006.04.011

Manning, Andrew James, & Dyer, K. R. (2002). The use of optics for the in situ determination of flocculated mud characteristics. *Journal of Optics A: Pure and Applied Optics*, *4*(4), S71–S81. https://doi.org/10.1088/1464-4258/4/4/366

Marani, M., D'Alpaos, A., Lanzoni, S., Carniello, L., & Rinaldo, A. (2007). Biologically-controlled multiple equilibria of tidal landforms and the fate of the Venice lagoon. *Geophysical Research Letters*. https://doi.org/10.1029/2007GL030178

Mariotti, G., Pruss, S. B., Perron, J. T., & Bosak, T. (2014). Microbial shaping of sedimentary wrinkle

structures. *Nature Geoscience*, *7*(10), 736–740. https://doi.org/10.1038/NGEO2229

Mariotti, Giulio, & Fagherazzi, S. (2010). A numerical model for the coupled long-term evolution of salt marshes and tidal flats. *Journal of Geophysical Research: Earth Surface*. https://doi.org/10.1029/2009JF001326

Mariotti, Giulio, & Fagherazzi, S. (2013). Critical width of tidal flats triggers marsh collapse in the absence of sea-level rise. *Proceedings of the National Academy of Sciences of the United States of America*, *110*(14), 5353–5356. https://doi.org/10.1073/pnas.1219600110

Martinsson, P.-G., Rokhlin, V., Liberty, E., Tygert, M., & Woolfe, F. (2007). Randomized algorithms for the low-rank approximation of matrices. *Proceedings of the National Academy of Sciences*, *104*(51), 20167–20172. https://doi.org/10.1073/pnas.0709640104

Masliyah, J. H., & Polikar, M. (1980). Terminal velocity of porous spheres. *The Canadian Journal of Chemical Engineering*. https://doi.org/10.1002/cjce.5450580303

Meakin, P. (1991). Fractal aggregates in geophysics. *Reviews of Geophysics*. https://doi.org/10.1029/91RG00688

Metscher, B. D. (2009). Micro CT for comparative morphology: Simple staining methods allow high-contrast 3D imaging of diverse non-mineralized animal tissues. *BMC Physiology*, 9:11. https://doi.org/10.1186/1472-6793-9-11

Mietta, F., Chassagne, C., & Winterwerp, J. C. (2009). Shear-induced flocculation of a suspension of kaolinite as function of pH and salt concentration. *Journal of Colloid and Interface Science*, *336*(1), 134–141. https://doi.org/10.1016/j.jcis.2009.03.044

Milligan, T. G., & Law, B. A. (2013). Contaminants at the Sediment–Water Interface: Implications for Environmental Impact Assessment and Effects Monitoring. *Environmental Science & Technology*, *47*(11), 5828–5834. https://doi.org/10.1021/es3031352

Mitchener, H. J., Whitehouse, R. J. S., Souslby, R. L., & Lawford, V. A. (1996). *Development of SedErode - Instrument for In-Situ Mud Erosion Measurement*.

Mohr, H., Draper, S., White, D. J., & Cheng, L. (2018). The influence of permeability on the erosion rate of fine-grained marine sediments. *Coastal Engineering*. https://doi.org/10.1016/j.coastaleng.2018.04.013

Molins, S. (2015). Reactive Interfaces in Direct Numerical Simulation of Pore-Scale Processes. *Reviews in Mineralogy and Geochemistry*, *80*, 461–481. https://doi.org/10.2138/rmg.2015.80.14

Mu, Y., Ren, T. T., & Yu, H. Q. (2008). Drag coefficient of porous and permeable microbial granules. *Environmental Science and Technology*, *42*(5), 1718–1723. https://doi.org/10.1021/es702708p

Nguyen, T. H., Tang, F. H. M., & Maggi, F. (2017). Optical Measurement of Cell Colonization Patterns on Individual Suspended Sediment Aggregates. *Journal of Geophysical Research: Earth Surface*, 1794–1807. https://doi.org/10.1002/2017JF004263

Nichols, P. D., & Mancuso Nichols, C. A. (2008). Microbial signature lipid profiling and exopolysaccharides: Experiences initiated with Professor David C White and transported to Tasmania, Australia. *Journal of Microbiological Methods*, *74*(1), 33–46. https://doi.org/10.1016/j.mimet.2007.06.017

Nicolella, C., Van Loosdrecht, M. M. C., Di Felice, R., & Rovatti, M. (1999). Terminal settling velocity and bed-expansion characteristics of biofilm- coated particles. *Biotechnology and Bioengineering*. https://doi.org/10.1002/(SICI)1097-0290(19990105)62:1<62::AID-BIT8>3.0.CO;2-U

Nino, Y., Lopez, F., & Garcia, M. (2003). Threshold for particle entrainment into suspension. *Sedimentology*, *50*(2), 247–263. https://doi.org/10.1046/j.1365-3091.2003.00551.x

Orsi, T. H. (1995). Computed Tomography of Macrostructure and Physical Property Variability of Seafloor Sediments. *Oceanography*, *8*, 61–64.

Orvain, F., Lefebvre, S., Montepini, J., Sébire, M., Gangnery, A., & Sylvand, B. (2012). Spatial and temporal interaction between sediment and microphytobenthos in a temperate estuarine macro-intertidal bay. *Marine Ecology Progress Series*. https://doi.org/10.3354/meps09698

Orvain, Francis, Sauriau, P. G., Sygut, A., Joassard, L., & Le Hir, P. (2004). Interacting effects of Hydrobia ulvae bioturbation and microphytobenthos on the erodibility of mudflat sediments. *Marine Ecology Progress Series*. https://doi.org/10.3354/meps278205

Orvain, Francis, Guizien, K., Lefebvre, S., Bréret, M., & Dupuy, C. (2014). Relevance of macrozoobenthic grazers to understand the dynamic behaviour of sediment erodibility and microphytobenthos resuspension in sunny summer conditions. *Journal of Sea Research*. https://doi.org/10.1016/j.seares.2014.03.004

Pang, M. J., & Wei, J. J. (2011). Analysis of drag and lift coefficient expressions of bubbly flow system for low to medium Reynolds number. *Nuclear Engineering and Design*. https://doi.org/10.1016/j.nucengdes.2011.03.046

Parker, P. J., & Collins, A. G. (1999). Ultra-rapid freezing of water treatment residuals. *Water Research*, *33*(10), 2239–2246. https://doi.org/10.1016/S0043-1354(98)00449-7

Passow, U, De La Rocha, C. L., Fairfield, C., & Schmidt, K. (2014). Aggregation as a function of PCO2 and mineral particles. *Limnology and Oceanography*, *59*(2), 532–547. https://doi.org/10.4319/lo.2014.59.2.0532

Passow, Uta, & De La Rocha, C. L. (2006). Accumulation of mineral ballast on organic aggregates. *Global Biogeochemical Cycles*. https://doi.org/10.1029/2005GB002579

Paterson, D. M. (1995). Biogenic structure of early sediment fabric visualized by low-temperature scanning electron microscopy. *Journal of the Geological Society*, *152*(1), 131–140. https://doi.org/10.1144/gsjgs.152.1.0131

Paterson, D. M., & Daborn, G. R. (1991). Sediment stabilization by biological action: significance for coastal engineering.

Paterson, D. M., Tolhurst, T. J., Kelly, J. A., Honeywill, C., De Deckere, E. M. G. T., Huet, V., et al. (2000). Variations in sediment properties, Skeffling mudflat, Humber Estuary, UK. *Continental Shelf Research*, *20*(10–11), 1373–1396. https://doi.org/10.1016/S0278-4343(00)00028-5

Paterson, David M. (1989). Short-term changes in the erodibility of intertidal cohesive sediments related to the migratory behavior of epipelic diatoms. *Limnology and Oceanography*, *34*(1), 223–234. https://doi.org/10.4319/lo.1989.34.1.0223

Paterson, David M., Aspden, R. J., Visscher, P. T., Consalvey, M., Andres, M. S., Decho, A. W., et al. (2008). Light-dependant biostabilisation of sediments by stromatolite assemblages. *PLoS ONE*, *3*(9). https://doi.org/10.1371/journal.pone.0003176

Perkins, R. G., Davidson, I. R., Paterson, D. M., Sun, H., Watson, J., & Player, M. A. (2006). Low-temperature SEM imaging of polymer structure in engineered and natural sediments and the implications regarding stability. *Geoderma*, *134*(1–2), 48–55. https://doi.org/10.1016/j.geoderma.2005.08.017

Perujo, N., Sanchez-Vila, X., Proia, L., & Roman ́ı A. M. (2017). Interaction between Physical Heterogeneity and Microbial Processes in Subsurface Sediments: A Laboratory-Scale Column Experiment. *Environmental Science and Technology*, *51*(11), 6110–6119. https://doi.org/10.1021/acs.est.6b06506

Ploug, H., Iversen, M. H., & Fischer, G. (2008). Ballast, sinking velocity, and apparent diffusivity within marine snow and zooplankton fecal pellets: Implications for substrate turnover by attached bacteria. *Limnology and Oceanography*. https://doi.org/10.4319/lo.2008.53.5.1878

Probandt, D., Eickhorst, T., Ellrott, A., Amann, R., & Knittel, K. (2018). Microbial life on a sand grain: From bulk sediment to single grains. *ISME Journal*, *12*(2), 623–633. https://doi.org/10.1038/ismej.2017.197

Ransom, B., Shea, K. F., Burkett, P. J., Bennett, R. H., & Baerwald, R. (1998). Comparison of pelagic and nepheloid layer marine snow: Implications for carbon cycling. *Marine Geology*, *150*(1–4), 39–50. https://doi.org/10.1016/S0025-3227(98)00052-8

Reid, T., VanMensel, D., Droppo, I. G., & Weisener, C. G. (2016). The symbiotic relationship of sediment and biofilm dynamics at the sediment water interface of oil sands industrial tailings ponds. *Water Research*, *100*, 337–347. https://doi.org/10.1016/j.watres.2016.05.025

Rietkerk, M., Dekker, S. C., De Ruiter, P. C., & Van De Koppel, J. (2004). Self-organized patchiness and catastrophic shifts in ecosystems. *Science*. https://doi.org/10.1126/science.1101867

Van Rijn, L.C. (1993). *Principles of sediment transport in rivers, estuaries and coastal seas*. *Amsterdam: Aqua publications.*

van Rijn, Leo C. (2007). Unified view of sediment transport by currents and waves. I: Initiation of motion, bed roughness, and bed-load transport. *Journal of Hydraulic Engineering*, *133*(6), 649–667. https://doi.org/10.1061/(ASCE)0733-9429(2007)133:6(649)

Roe, S. (2007a). *A laboratory study of the derivation of the suspensionthreshold of fine and very fine sand*. University of Sounthampton.

Roe, S. (2007b). *A laboratory study of the derivation of the suspensionthreshold offine and very fine sand.* University of Southampton.

Roman ́ı A. M., Giorgi, A., Acu ̃na, V., & Sabater, S. (2004). The influence of substratum type and nutrient supply on biofilm organic matter utilization in streams. *Limnology and Oceanography*, *49*(5), 1713–1721. https://doi.org/10.4319/lo.2004.49.5.1713

Rusconi, R., Guasto, J. S., & Stocker, R. (2014). Bacterial transport suppressed by fluid shear. *Nature Physics*, *10*(3), 212–217. https://doi.org/10.1038/NPHYS2883

Saravanan, V., & Sreekrishnan, T. R. (2005). Hydrodynamic study of biogranules obtained from an anaerobic hybrid reactor. *Biotechnology and Bioengineering*. https://doi.org/10.1002/bit.20567

Schindelin, J., Arganda-Carreras, I., Frise, E., Kaynig, V., Longair, M., Pietzsch, T., et al. (2012). Fiji: An open-source platform for biological-image analysis. *Nature Methods*. https://doi.org/10.1038/nmeth.2019

Schmitt, J., & Flemming, H. C. (1999). Water binding in biofilms. In *Water Science and Technology* (Vol. 39, pp. 77–82). https://doi.org/10.1016/S0273-1223(99)00153-5

Shang, Q. Q., Fang, H. W., Zhao, H. M., He, G. J., & Cui, Z. H. (2014). Biofilm effects on size gradation, drag coefficient and settling velocity of sediment particles. *International Journal of*

Sediment Research, *29*(4), 471–480. https://doi.org/10.1016/S1001-6279(14)60060-3

Sharma, S., Lin, C. L., & Miller, J. D. (2017). Multi-scale features including water content of polymer induced kaolinite floc structures. *Minerals Engineering*, *101*, 20–29. https://doi.org/10.1016/j.mineng.2016.11.003

Shi, B. W., Yang, S. L., Wang, Y. P., Bouma, T. J., & Zhu, Q. (2012). Relating accretion and erosion at an exposed tidal wetland to the bottom shear stress of combined current-wave action. *Geomorphology*. https://doi.org/10.1016/j.geomorph.2011.10.004

Shields, I. A. (1936). Application of similarity principles and turbulence research to bed-load movement, U.S. Soil Conservation Service Coop. Lab. In *Ott, W.P., van Uchelen, J.C. (Eds.), (Translators), Hydrodynamics Laboratory Publication, vol. 167. California Institute of Technology, Pasadena*.

Smith, D. J., & Underwood, G. J. C. (2000). The production of extracellular carbohydrates by estuarine benthic diatoms: The effects of growth phase and light and dark treatment. *Journal of Phycology*. https://doi.org/10.1046/j.1529-8817.2000.99148.x

Soulsby, R. L. (1997). *Dynamics of marine sands: a manual for practical applications*. *Dynamics of marine sands: a manual for practical applications*.

Staats, N., Stal, L. J., De Winder, B., & Mur, L. R. (2000). Oxygenic photosynthesis as driving process in exopolysaccharide production of benthic diatoms. *Marine Ecology Progress Series*. https://doi.org/10.3354/meps193261

Sternberg, R. W., Berhane, I., & Ogston, A. S. (1999). Measurement of size and settling velocity of suspended aggregates on the northern California continental shelf. *Marine Geology*, *154*(1–4), 43–53. https://doi.org/10.1016/S0025-3227(98)00102-9

Stone, M., Krishnappan, B. G., & Emelko, M. B. (2008). The effect of bed age and shear stress on the particle morphology of eroded cohesive river sediment in an annular flume. *Water Research*, *42*(15), 4179–4187. https://doi.org/10.1016/j.watres.2008.06.019

Sutherland, I. W. (2001). The biofilm matrix - An immobilized but dynamic microbial environment. *Trends in Microbiology*, *9*(5), 222–227. https://doi.org/10.1016/S0966-842X(01)02012-1

Sutherland, T. F., Amos, C. L., & Grant, J. (1998). The effect of buoyant biofilms on the erodibility of sublittoral sediments of a temperate microtidal estuary. *Limnology and Oceanography*, *43*(2), 225–235. https://doi.org/10.4319/lo.1998.43.2.0225

Sutherland, T. F., Grant, J., & Amos, C. L. (1998). The effect of carbohydrate production by the diatom Nitzschia curvilineata on the erodibility of sediment. *Limnology and Oceanography*. https://doi.org/10.4319/lo.1998.43.1.0065

Tang, F. H. M. (2017). *Microbiological modulation of suspended particulate matter dynamics : A study of biological flocculation in nutrient-enriched waters*. The University of Sydney.

Thompson, C. E. L., Amos, C. L., Lecouturier, M., & Jones, T. E. R. (2004). Flow deceleration as a method of determining drag coefficient over roughened flat beds. *Journal of Geophysical Research: Oceans*, *109*(C3). https://doi.org/10.1029/2001jc001262

Thompson, C. E.L., Couceiro, F., Fones, G. R., & Amos, C. L. (2013). Shipboard measurements of sediment stability using a small annular flume-core mini flume (cmf). *Limnology and Oceanography: Methods*. https://doi.org/10.4319/lom.2013.11.604

Thompson, C. E.L., Williams, M. E., Amoudry, L., Hull, T., Reynolds, S., Panton, A., & Fones, G. R. (2017). Benthic controls of resuspension in UK shelf seas: Implications for resuspension frequency. *Continental Shelf Research*, (May), 0–1. https://doi.org/10.1016/j.csr.2017.12.005

Thompson, Charlotte E. L., Amos, C. L., Jones, T. E. R., & Chaplin, J. (2003). The manifestation of fluid-transmitted bed shear stress in a smooth annular flume - a comparison of methods. *Journal of Coastal …*, *19*(4), 1094–1103. https://doi.org/10.2307/4299251

Thomsen, L., & Gust, G. (2000). Sediment erosion thresholds and characteristics of resuspended aggregates on the western European continental margin. *Deep-Sea Research Part I: Oceanographic Research Papers*, *47*(10), 1881–1897. https://doi.org/10.1016/S0967-0637(00)00003-0

Thornton, D. C. O., & Visser, L. A. (2009). Measurement of acid polysaccharides (APS) associated with microphytobenthos in salt marsh sediments, *54*(February), 185–198. https://doi.org/10.3354/ame01265

Tolhursf, T. J., Gust, G., & Paterson, D. M. (2002). The influence of an extracellular polymeric substance (EPS) on cohesive sediment stability. In *Proceedings in Marine Science*. https://doi.org/10.1016/S1568-2692(02)80030-4

Tolhurst, T. J., Black, K. S., Shayler, S. A., Mather, S., Black, I., Baker, K., & Paterson, D. M. (1999). Measuring the in situ erosion shear stress of intertidal sediments with the cohesive strength meter (CSM). *Estuarine, Coastal and Shelf Science*. https://doi.org/10.1006/ecss.1999.0512

Tolhurst, T. J., Black, K. S., Paterson, D. M., Mitchener, H. J., Termaat, G. R., & Shayler, S. A. (2000). A comparison and measurement standardisation of four in situ devices for determining the erosion shear stress of intertidal sediments. *Continental Shelf Research*, *20*(10–11), 1397–1418. https://doi.org/10.1016/S0278-4343(00)00029-7

Tolhurst, T. J., Defew, E. C., De Brouwer, J. F. C., Wolfstein, K., Stal, L. J., & Paterson, D. M. (2006). Small-scale temporal and spatial variability in the erosion threshold and properties of cohesive intertidal sediments. *Continental Shelf Research*. https://doi.org/10.1016/j.csr.2005.11.007

Turner, J. T. (2015). Zooplankton fecal pellets, marine snow, phytodetritus and the ocean's biological pump. *Progress in Oceanography*, *130*, 205–248. https://doi.org/10.1016/j.pocean.2014.08.005

Tuson, H. H., & Weibel, D. B. (2013). Bacteria-surface interactions. *Soft Matter*. https://doi.org/10.1039/c3sm27705d

Underwood, G. J. C., & Barnett, M. (2006). What determines species composition in microphytobenthic biofilms? *Royal Netherlands Academy of Arts and Sciences*.

Underwood, Graham J.C., & Paterson, D. M. (1993). Seasonal changes in diatom biomass, sediment stability and biogenic stabilization in the severn estuary. *Journal of the Marine Biological Association of the United Kingdom*, *73*(4), 871–887. https://doi.org/10.1017/S0025315400034780

Vahedi, A., & Gorczyca, B. (2011). Application of fractal dimensions to study the structure of flocs formed in lime softening process. *Water Research*, *45*(2), 545–556. https://doi.org/10.1016/j.watres.2010.09.014

Vignaga, E., Sloan, D. M., Luo, X., Haynes, H., Phoenix, V. R., & Sloan, W. T. (2013). Erosion of biofilm-bound fluvial sediments. *Nature Geoscience*, *6*(9), 770–774. https://doi.org/10.1038/ngeo1891

Villatoro, M. (2010). *Sand transport in Chioggia Inlet, Venice Lagoon and resulting morphodynamic evolution*. University of Southampton.

Villatoro, M. M., Amos, C. L., Umgiesser, G., Ferrarin, C., Zaggia, L., Thompson, C. E. L., & Are, D. (2010). Sand transport measurements in Chioggia inlet, Venice lagoon: Theory versus observations. *Continental Shelf Research*, *30*(8), 1000–1018. https://doi.org/10.1016/j.csr.2009.06.008

Virolle, M., Brigaud, B., Bourillot, R., Féniès, H., Portier, E., Duteil, T., et al. (2019). Detrital clay grain coats in estuarine clastic deposits: origin and spatial distribution within a modern sedimentary system, the Gironde Estuary (south-west France). *Sedimentology*. https://doi.org/10.1111/sed.12520

Virolle, M., Brigaud, B., Luby, S., Portier, E., Féniès, H., Bourillot, R., et al. (2019). Influence of sedimentation and detrital clay grain coats on chloritized sandstone reservoir qualities: Insights from comparisons between ancient tidal heterolithic sandstones and a modern estuarine system. *Marine and Petroleum Geology*. https://doi.org/10.1016/j.marpetgeo.2019.05.010

Voulgaris, G., & Meyers, S. T. (2004). Temporal variability of hydrodynamics, sediment concentration and sediment settling velocity in a tidal creek. *Continental Shelf Research*, *24*(15), 1659–1683. https://doi.org/10.1016/j.csr.2004.05.006

van der Wal, D., Wielemaker-van den Dool, A., & Herman, P. M. J. (2010). Spatial synchrony in intertidal benthic algal biomass in temperate coastal and estuarine ecosystems. *Ecosystems*. https://doi.org/10.1007/s10021-010-9322-9

Ward, S. L., Neill, S. P., Van Landeghem, K. J. J., & Scourse, J. D. (2015). Classifying seabed sediment type using simulated tidal-induced bed shear stress. *Marine Geology*. https://doi.org/10.1016/j.margeo.2015.05.010

Watermann, F., Hillebrand, H., Gerdes, G., Krumbein, W. E., & Sommer, U. (1999). Competition between benthic cyanobacteria and diatoms as influenced by different grain sizes and temperatures. *Marine Ecology Progress Series.* https://doi.org/10.3354/meps187077

Weerman, E. J., Herman, P. M. J., & Van De Koppel, J. (2011). Top-down control inhibits spatial self-organization of a patterned landscape. *Ecology*. https://doi.org/10.1890/10-0270.1

Wheatland, J. A. T., Bushby, A. J., & Spencer, K. L. (2017). Quantifying the Structure and Composition of Flocculated Suspended Particulate Matter Using Focused Ion Beam Nanotomography. *Environmental Science & Technology*, *51*(16), 8917–8925. https://doi.org/10.1021/acs.est.7b00770

Widdows, J., Brinsley, M. D., Bowley, N., & Barrett, C. (1998). A benthic annular flume for in situ measurement of suspension feeding/biodeposition rates and erosion potential of intertidal cohesive sediments. *Estuarine, Coastal and Shelf Science*. https://doi.org/10.1006/ecss.1997.0259

Widdows, J., Friend, P. L., Bale, A. J., Brinsley, M. D., Pope, N. D., & Thompson, C. E. L. (2007). Inter-comparison between five devices for determining erodability of intertidal sediments. *Continental Shelf Research*, *27*(8), 1174–1189. https://doi.org/10.1016/j.csr.2005.10.006

Wilson, J. D., Barker, S., & Ridgwell, A. (2012). Assessment of the spatial variability in particulate organic matter and mineral sinking fluxes in the ocean interior: Implications for the ballast hypothesis. *Global Biogeochemical Cycles*, *26*(4), 1–15. https://doi.org/10.1029/2012GB004398

Wimpenny, J. W. T., & Colasanti, R. (1997). A unifying hypothesis for the structure of microbial biofilms based on cellular automaton models. *FEMS Microbiology Ecology*. https://doi.org/10.1016/S0168-6496(96)00078-5

De Winder, B., Staats, N., Stal, L. J., & Paterson, D. M. (1999). Carbohydrate secretion by

phototrophic communities in tidal sediments. *Journal of Sea Research*, *42*(2), 131–146. https://doi.org/10.1016/S1385-1101(99)00021-0

Winterwerp, J. C., Manning, A. J., Martens, C., de Mulder, T., & Vanlede, J. (2006). A heuristic formula for turbulence-induced flocculation of cohesive sediment. *Estuarine, Coastal and Shelf Science*, *68*(1), 195–207. https://doi.org/10.1016/j.ecss.2006.02.003

Winterwerp, J C. (2002). on the Flocculation and Settling Velocity of Esturine Mud.Pdf, *22*(October 2001), 1339–1360.

Winterwerp, Johan C. (1998). A simple model for turbulence induced flocculation of cohesive sediment. *Journal of Hydraulic Research*, *36*(3), 309–326. https://doi.org/10.1080/00221689809498621

Winterwerp, Johan C., & van Kesteren, W. G. M. (2004). *Introduction to the physiscs of cohesive sediment in the marine environment*.

Wurl, O., Ekau, W., Landing, W. M., & Zappa, C. J. (2017). Sea surface microlayer in a changing ocean - A perspective. *Elementa*. https://doi.org/10.1525/elementa.228

Yallop, M. L., Paterson, D. M., & Wellsbury, P. (2000). Interrelationships between rates of microbial production, exopolymer production, microbial biomass, and sediment stability in biofilms of intertidal sediments. *Microbial Ecology*, *39*(2), 116–127. https://doi.org/10.1007/s002489900186

Yao, P., Hu, Z., Su, M., Chen, Y., & Ou, suying. (2018). Erosion Behavior of Sand-silt Mixtures: the Role of Silt Content. *Journal of Coastal Research*, *85*, 1171–1175. https://doi.org/10.2112/si85-235.1

Ye, L., Manning, A. J., Hsu, T. J., Morey, S., Chassignet, E. P., & Ippolito, T. A. (2018). Novel application of laboratory instrumentation characterizes mass settling dynamics of oil-mineral aggregates (OMAs) and oil-mineral-microbial interactions. *Marine Technology Society Journal*, *52*(6), 87–90. https://doi.org/10.4031/MTSJ.52.6.14

Zhang, N., Thompson, C. E. L., Townend, I. H., Rankin, K. E., Paterson, D. M., & Manning, A. J.

(2018). Nondestructive 3D Imaging and Quantification of Hydrated Biofilm-Sediment Aggregates Using X-ray Microcomputed Tomography. *Environmental Science and Technology*, *52*(22), 13306–13313. https://doi.org/10.1021/acs.est.8b03997

Zhao, B., & Wang, J. (2016). 3D quantitative shape analysis on form, roundness, and compactness with μCT. *Powder Technology*, *291*, 262–275. https://doi.org/10.1016/j.powtec.2015.12.029

Zhao, H., Fang, H., & Chen, M. (2011). Floc architecture of bioflocculation sediment by ESEM and CLSM. *Scanning*, *33*(6), 437–445. https://doi.org/10.1002/sca.20247

Zhou, G., Zhang, Q., Bai, R., & Ni, G. (2016). Characterization of Coal Micro-Pore Structure and Simulation on the Seepage Rules of Low-Pressure Water Based on CT Scanning Data. *Minerals (2075-163X)*, *6*(3), 1–16. https://doi.org/10.3390/min6030078